2017-10-01

Development of a Performance-Based Procedure for Assessment of Liquefaction-Induced Lateral Spread Displacements Using the Cone Penetration Test

Tyler Blaine Coutu
Brigham Young University

Development of a Performance-Based Procedure for Assessment of Liquefaction-Induced Lateral Spread Displacements Using the Cone Penetration Test

Tyler Blaine Coutu

A thesis submitted to the faculty of
Brigham Young University
in partial fulfillment of the requirements for the degree of

Master of Science

Kevin W. Franke, Chair
Kyle M. Rollins
W. Spencer Guthrie

Department of Civil and Environmental Engineering

Brigham Young University

ABSTRACT

Development of a Performance-Based Procedure for Assessment of
Liquefaction-Induced Lateral Spread Displacements
Using the Cone Penetration Test

Tyler Blaine Coutu
Department of Civil and Environmental Engineering, BYU
Master of Science

Liquefaction-induced lateral spread displacements cause severe damage to infrastructure, resulting in large economic losses in affected regions. Predicting lateral spread displacements is an important aspect in any seismic analysis and design, and many different methods have been developed to accurately estimate these displacements. However, the inherent uncertainty in predicting seismic events, including the extent of liquefaction and its effects, makes it difficult to accurately estimate lateral spread displacements. Current conventional methods of predicting lateral spread displacements do not completely account for uncertainty, unlike a performance-based earthquake engineering (PBEE) approach that accounts for the all inherent uncertainty in seismic design. The PBEE approach incorporates complex probability theory throughout all aspects of estimating liquefaction-induced lateral spread displacements.

A new fully-probabilistic PBEE method, based on results from the cone penetration test (CPT), was created for estimating lateral spread displacements using two different liquefaction triggering procedures. To accommodate the complexity of all probabilistic calculations, a new seismic hazard analysis tool, *CPTLiquefY*, was developed. Calculated lateral spread displacements using the new fully-probabilistic method were compared to estimated displacements using conventional methods. These comparisons were performed across 20 different CPT profiles and 10 cities of varying seismicity.

The results of this comparison show that the conventional procedures of estimating lateral spread displacements are sufficient for areas of low seismicity and for lower return periods. However, by not accounting for all uncertainties, the conventional methods under-predict lateral spread displacements in areas of higher seismicity. This is cause for concern as it indicates that engineers in industry using the conventional methods are likely under-designing structures to resist lateral spread displacements for larger seismic events.

Key words: cone penetration test (CPT), *CPTLiquefY*, deterministic, earthquake, lateral spread displacement, liquefaction, performance-based, probabilistic, seismic hazard

ACKNOWLEDGEMENTS

I first express my gratitude to my graduate advisor, Dr. Kevin W. Franke, for inspiring me to begin and then leading me to the finish. He opened my eyes to geotechnical engineering, a field for which I have developed such a passion, and then assisted me as I developed my skills and expanded my knowledge. I also thank my graduate committee members, Dr. Kyle M. Rollins and Dr. W. Spencer Guthrie. They have taught me so much throughout my time at BYU, and they have provided their time and knowledge to assist in finishing my work.

While this work may be my own, I could not have gotten to where I am today without help from Mikayla Hatch and Alex Arndt. Countless hours were spent together in understanding theory and developing software. I began by depending on them as colleagues, and now I look to them as friends. I thank them for their patience, example, and friendship.

This research was funded by a Federal Highway Administration Pooled Fund Study Award No. TPF-5(338), with participation from the Utah, Oregon, South Carolina, and Connecticut Departments of Transportation. I acknowledge the support of these sponsors and thank them for their guidance and suggestions over the course of this project.

Most of all, I thank my lovely wife Lindy. She has been with me through it all, supporting me in times of triumph and defeat. She has sacrificed so much to allow me to follow my passion. Without her love and support, I would not be the man that I am today.

TABLE OF CONTENTS

LIST OF TABLES

LIST OF FIGURES

1 INTRODUCTION

Soil liquefaction has been triggered by earthquakes throughout history, but it was not until investigations of the 1964 Niigata and Alaska earthquakes that this phenomenon was studied and understood. The effects of liquefaction are what interest engineers, as they are the cause of damage to infrastructure throughout the world. Lateral spread displacement is one of these effects and has cumulatively caused more damage than any other liquefaction-induced ground failure (National Research Council, 1985). Lateral spread is the horizontal displacement of soil as a result of liquefaction in a subsurface layer, commonly seen in gently sloping ground and level ground near a free face. While these failures do not directly incur loss of life, they cause significant damage to structures, transportation infrastructure, utilities, and lifelines during a seismic event. These damages have a large economic toll, and therefore efforts have been made in the prevention and prediction of lateral spread displacements from large earthquakes.

As liquefaction and lateral spread displacements are relatively new areas of research, predictive analytical and empirical models are continually being developed and refined. The original method to predict liquefaction effects was deterministic, which involved use of a single controlling earthquake to determine the input ground motion. In more recent years, a pseudo-probabilistic approach has been adopted in an attempt to account for some uncertainty in the seismic loading selection using the deterministic method. This pseudo-probabilistic approach

uses probability theory to select a single input ground motion but computes the liquefaction effects using a deterministic approach.

Performance-based earthquake engineering (PBEE) methods have the ability to account for all uncertainty in the seismic loading/ground motions and the soil parameters at a site. This method therefore produces more accurate and consistent hazard estimates than the pseudo-probabilistic approach (Kramer and Mayfield, 2007). PBEE applies a fully-probabilistic analysis in the prediction of liquefaction effects and presents these results in terms of levels of hazard. This presentation empowers stakeholders, such as engineers and government officials, to make informed decisions on seismic design and preparation. PBEE methods are not commonly used in practice due to their natural complexity and extensive calculations. However, efforts are being made to incorporate these methods into common practice.

In recent years, fully-probabilistic PBEE methods have been developed based on the standard penetration test (SPT), which is one of the most common in-situ testing methods. Another in-situ testing method that is gaining popularity is the cone penetration test (CPT). The CPT creates a continuous soil profile and is a repeatable test, both of which contribute to it being more reliable than the SPT. With the increase in popularity of the CPT, there has been development of deterministic and pseudo-probabilistic procedures for the prediction of liquefaction effects using the CPT, but there has yet to be development of a fully-probabilistic procedure. This study seeks to fill this void.

There are three purposes of this study: first, to create a new performance-based (fully-probabilistic) procedure for the estimation of liquefaction-induced lateral spread displacements for the CPT; second, to develop an analysis tool to perform and simplify the necessary

probabilistic calculations; and, third, to assess and quantify the differences between the performance-based and pseudo-probabilistic post-liquefaction lateral spread analyses.

As the conventional standards of practice generally follow pseudo-probabilistic procedures, by comparing the results from this procedure to results using the full-performance based procedures, this research will show where the conventional methods fall short. If the conventional methods are found to be under-predicting lateral spread displacements, many structures have been, and are continuing to be, under-designed for seismic events. There is a need to implement a fully-probabilistic performance-based procedure for predicting lateral spread displacements and preventing damage to structures and potential loss of life.

2 REVIEW OF SEISMIC LOADING

2.1 Introduction

Liquefaction and lateral spreading are primarily the results of seismic events. To better understand the phenomenon of liquefaction, one must first be familiar with the driving force behind it, which is seismic loading. Earthquake engineering is constantly developing as new discoveries are made and new theories are tested. Every year more earthquakes occur, adding to the studied case histories and providing a deeper understanding of this phenomenon. As new methods are tested and tools are developed, the ground motions produced can be better understood, quantified, and even predicted.

2.2 Earthquakes

Throughout history, earthquakes have been one of the most common and devastating natural disasters occurring across the world. Cities, ancient and modern, have been destroyed, countless lives have been lost, and countless dollars have been spent to recover from these disasters. As such, it is now in the hands of engineers to plan and make preparations for more earthquakes to occur. For these preparations to be successful, earthquakes must be quantified in a way that is accurate and measurable.

With the development of seismic instruments, such as seismographs and accelerometers, quantitative measurements of an earthquake's size, termed its "magnitude," could be performed. Different measures of magnitude have been created over the years, one of the original and most

well-known being the Richter local magnitude scale. The Richter scale defines an earthquake magnitude for shallow earthquakes using a Wood-Anderson seismometer (Richter, 1935). The Richter local magnitude is not used in design as it only applies to shallow depths, and it does not distinguish between surface and body seismic waves. Surface and body wave magnitude scales were developed to combat the downfalls of the Richter magnitude scale. However, the surface and body wave magnitude scales have difficulty distinguishing between large earthquakes due to saturation in the recordings and are therefore not as reliable as engineers had hoped. The magnitude scale most widely used in practice is the moment magnitude scale.

The moment magnitude scale is the only magnitude scale not subject to saturation, as it is based on the seismic moment, which is a direct measure of the factors that produce rupture along the fault (Kanamori, 1977; Kanamori, 1983). As the moment magnitude is the most widely used in industry today, this study refers to this scale whenever the general term *magnitude* is mentioned.

2.3 Ground Motion Parameters

Modern instruments measuring ground motions from an earthquake generally report results in a time history, showing the acceleration, velocity, or displacement with time over the duration of the earthquake. The ground motion itself is characterized using ground motion parameters (GMPs). To fully characterize a ground motion record, multiple GMPs that quantify the motion's amplitude, frequency content, and duration are considered.

2.3.1 Amplitude Parameters

Amplitude is the measurement of the maximum value recorded in the time history (for acceleration, velocity, or duration). The most common amplitude parameter used is that of

acceleration, usually reported as peak ground acceleration (PGA) or peak ground surface acceleration (a_{max}). PGA is commonly used to characterize the size of a seismic event; however, this can be misleading. Two earthquakes may have the same PGA, but they may have very different energies released. An example of this is presented in Figure 2-1, which shows two time histories for two different earthquakes. Both time histories have the same maximum amplitude, but the second earthquake has a higher frequency and longer duration. Looking at the amplitude alone, one would think that these earthquakes released the same amount of energy, when in reality the second earthquake was likely much more devastating. For this reason, multiple GMPs are considered.

Figure 2-1: Two time histories for earthquakes with similar amplitudes but different frequencies and durations.

2.3.2 Frequency Parameters

Another GMP that is useful in determining the magnitude of an earthquake is the frequency, which describes how rapidly a specific ground motion at a specific amplitude is repeated. It is important to note this repetition because it can cause damage in a few ways. First, it can increase the energy of an earthquake; as a ground motion is repeated, more damage is

caused. However, the main reasoning behind understanding the frequency of an earthquake loading is that it may correspond to the natural frequency of a structure. All structures have a natural frequency at which they oscillate inherently. When these frequencies correspond, the oscillation of the structure is compounded, resulting in resonance that leads to larger deformations and damage.

Mathematics is used to better understand the frequency content of ground motions; more specifically, a function known as the Fourier series is used. The Fourier series is a sum of simple harmonic terms of different frequency, amplitude, and phase. By plotting the amplitude versus frequency, it can be seen how the amplitude of a ground motion is distributed with respect to frequency. The result of this plot is known as the Fourier spectrum and is used today to see which frequencies are being most commonly repeated by the earthquake loading. An example of two Fourier spectra are depicted in Figure 2-2, which shows two different combinations of frequency ("Period") and amplitude ("Fourier amplitude"). The first spectrum shows high

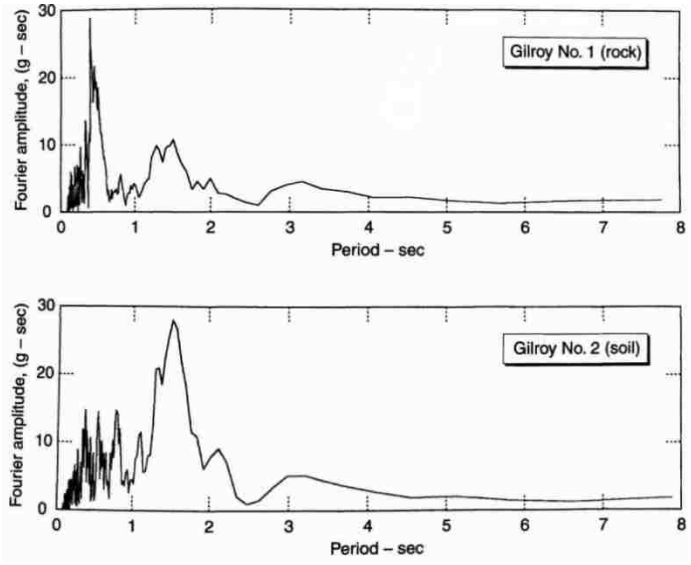

Figure 2-2: Fourier amplitude spectra for Gilroy No. 1 (rock) and Gilroy No. 2 (soil) strong motion records (after Kramer 1996).

amplitude at a low frequency (around 0.5), while the second spectrum shows high amplitude at a higher frequency (around 1.6). The difference in frequency indicates that different structures would be affected depending on their natural frequency.

2.3.3 Duration Parameters

The damage caused by large amplitudes and frequencies corresponding to the natural frequency of a structure are dependent on the duration of the earthquake loading. A large duration of an earthquake means that these ground motions compound over time and can cause significant damage. A short duration could mean that strong ground motions simply do not have enough time to cause significant damage. A large duration of a low amplitude earthquake can cause much more damage than a short duration of a high amplitude earthquake. One duration parameter that is used is known as bracketed duration, which is the time between the first and last exceedances of a specific acceleration (Bolt, 1969). A visual representation of bracketed duration is shown in the time history in Figure 2-3.

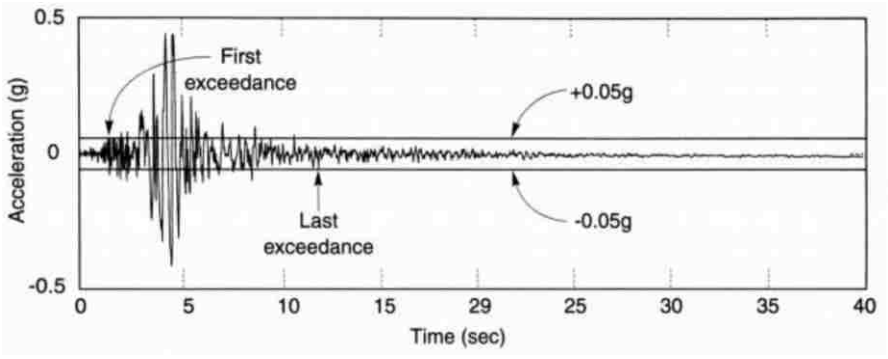

Figure 2-3: Visual representation of bracketed duration using a threshold value of 0.05 g (after Kramer, 1996).

2.3.4 Other Parameters

Efforts have been made to develop GMPs that describe multiple characteristics of ground motions. Examples of these combined GMPs include Arias intensity (I_a) (Arias, 1970), root mean square (RMS) acceleration (a_{rms}) (Kramer, 1996), and cumulative absolute velocity (CAV) (Benjamin, 1988). Each of these GMPs describes multiple characteristics of the ground motion with a single value. The use of these parameters is more efficient than applying multiple GMPs that only characterize one aspect of a ground motion, such as amplitude, frequency content, or duration.

2.4 Ground Motion Prediction Equations

The previous section discussed different GMPs, such as amplitude, frequency, and duration, and how they can help characterize earthquake ground motions. While these data are very useful, they only apply to earthquakes that have already occurred and have been recorded. Engineers are more interested in earthquakes that have not yet happened but may occur during the life of their structure. To perform this prediction, the GMPs that will be used in engineering design must be estimated a priori. Ground motion prediction equations (GMPEs), also known as attenuation relationships, have been created to accomplish this estimation.

GMPEs use predictive relationships between the GMPs and variables that affect them, such as earthquake magnitude, distance, and local site effects. Different researchers have developed relationships to relate these variables to GMPs using previously recorded earthquake time history data. These relationships use different inputs to decrease scatter in the results. To further improve accuracy, five research teams were given the same set of ground motion data and separately developed relationships to fit this data. The results from this endeavor are known as the Next Generation Attenuation (NGA) Relationships (Abrahamson and Silva, 2008; Boore and

Atkinson, 2008; Cambell and Bozorgnia, 2008; Chiou and Youngs, 2008; Idriss, 2008). In 2014 the NGA relationships were updated, known as NGA-West2 (Bozorgnia et al., 2014). All of these attenuation relationships are approximations, and care should be taken to understand the scope of locations and seismic events to which they apply. With caution taken, these relationships are very useful in preparing for future ground motions.

2.5 Local Site Effects

Attenuation relationships previously described rely heavily on magnitude and distance to predict future GMPs. Another consideration that must be made when estimating these parameters is the local site effects. While two sites may experience similar earthquake magnitudes at similar distances, the ground motions felt at the two sites could be entirely different. Local site effects are the cause of these differences, and they include effects such as soil type, directivity, topography, and basin effects.

Soil properties at a site have a large influence on the ground motions felt. As the energy from earthquake waves propagate through the soil, toward the site, the soil has the ability to amplify or dampen these waves. In general, stiff soil or rock amplifies waves of high frequency, while soft soil amplifies waves of low frequency. One example of this effect occurred during the Loma Prieta earthquake in the San Francisco Bay area in 1989. Multiple seismographs and accelerometers were located throughout the area, recording accelerations during this earthquake. Two instruments of interest recorded accelerations on Yerba Buena Island and Treasure Island (two small islands in the San Francisco Bay). Both sites were approximately the same distance from the earthquake epicenter, but felt significantly different accelerations (as illustrated in Figure 2-4). Treasure Island is mostly loose soil, consisting of man-made hydraulic fill over loose alluvial mud. Yerba Buena Island is a natural rock outcrop. The loose soil on Treasure

Island amplified the low-frequency earthquake waves, resulting in accelerations three to four times stronger than those felt on Yerba Buena Island, showing the effect of soil properties on ground motions (Kramer 1996).

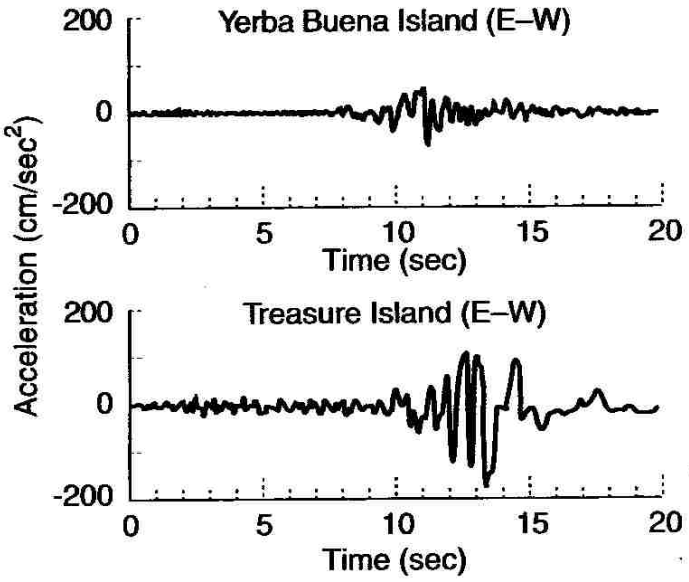

Figure 2-4: The difference in acceleration on Yerba Buena Island and Treasure Island during the Loma Prieta earthquake (after Kramer, 1996).

Directivity is another cause for an alteration of ground motions felt at a site. As a fault ruptures, its directivity refers to the direction along the fault in which it is rupturing. The ground motions could be significantly different depending on the site's location relative to the directivity of an earthquake. Directivity is caused by constructive interferences of waves produced by successive ruptures that create strong pulses of large displacements, illustrated in Figure 2-5 (Benioff, 1955; Singh, 1985).

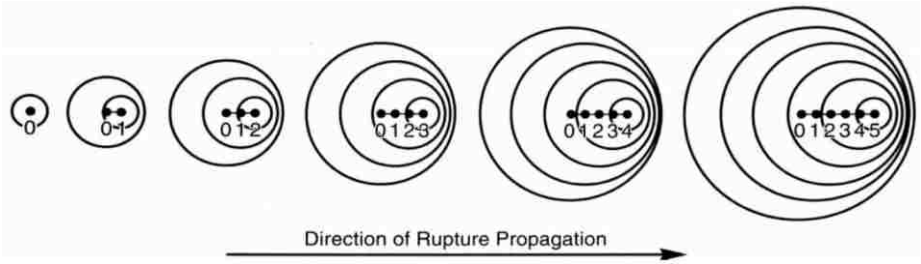

Figure 2-5: Illustration of the directivity effect as a fault ruptures toward a site.

Site topography, including basin effects, has also been shown to affect the ground motions felt at a site. Research shows that ground motions tend to amplify as they move up a peak, showing an increase up to 2.5 times the base acceleration (Jibson, 1987). Calculating the result of these effects can be very complicated, and they are not often accounted for since there are few critical structures built along steep slopes and ridges.

Basin effects occur as earthquake body waves can be "trapped" in curved alluvial valleys. These trapped body waves cause an increase in surface waves, resulting in stronger shaking and longer duration than would have normally been predicted (Vidale and Helmberger, 1988). These basin effects are important to note because alluvial valleys are a common place for cities to be built.

2.6 Seismic Hazard Analysis

With earthquake ground motions understood, the parameters can be estimated using a process known as seismic hazard analysis (SHA) to determine the demand that a structure will experience during an earthquake. SHA involves the quantitative estimation of ground-shaking hazards at a particular site, using the previously discussed attenuation relationships (Kramer, 1996). SHA can be accomplished with a deterministic approach, known as deterministic seismic

hazard analysis (DSHA), or a probabilistic approach, known as probabilistic seismic hazard analysis (PSHA). When a DSHA is implemented, a particular earthquake scenario is assumed. When a PSHA is implemented, the uncertainties in earthquake size and location are considered.

2.6.1 Deterministic Seismic Hazard Analysis

In the early development of earthquake engineering, DSHA was the main analysis method. DSHA is the analysis process in which a single seismic scenario is used for design. The GMPs are then based on this specific seismic scenario. Caution must be taken, as this seismic design scenario may under-predict or over-predict an actual seismic event. In a DSHA, the probability of the design seismic scenario occurring, as well as the uncertainty in size, location, and recurrence of the earthquake, is not used as an input in the analysis. However, a DSHA is still useful in understanding past earthquake case histories, as well as estimating ground motions for structures for which choosing a single seismic scenario is sufficient for design.

The process of implementing a DSHA can be broken into four steps, as described by Reiter (1990) and as illustrated in Figure 2-6. The first step is the identification and characterization of any earthquake sources that are capable of producing significant ground motion at the site, which involves definition of the source's geometry and its seismic potential. The second step is the determination of the shortest source-to-site distance for each of the sources identified in step one. These distances can be hypocentral or epicentral, depending on the predictive relationships that are used. The third step is the selection of the controlling earthquake, which is the one that produces the largest ground motions. This selection is done by comparing the ground motions from sources found in step one and distances found in step two. Once the controlling earthquake is selected, the fourth step is the definition of the seismic hazard at the site, expressed as one or more GMPs.

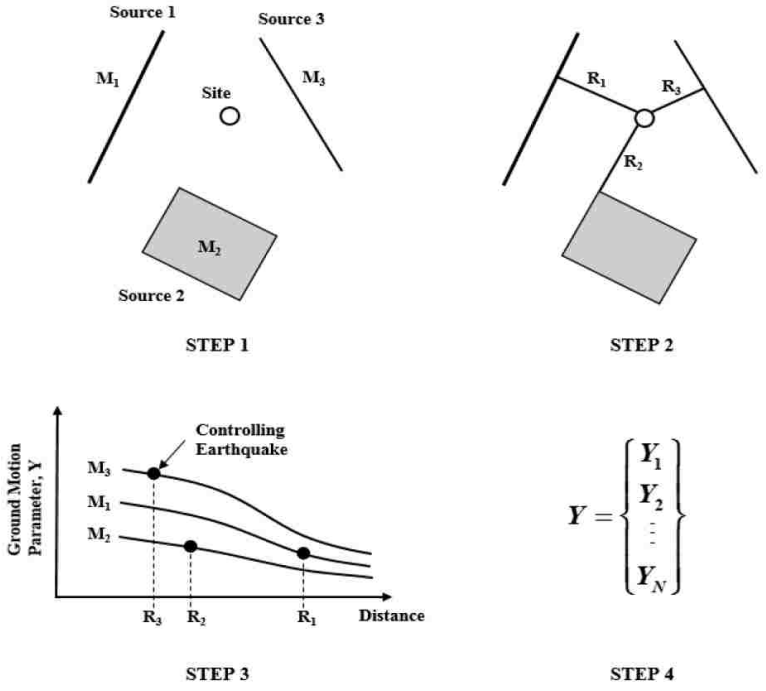

Figure 2-6: Illustration of the four steps in implementing a DSHA (after Kramer, 1996).

2.6.2 Probabilistic Seismic Hazard Analysis

A PSHA uses probability concepts to address the uncertainties inherent in the DSHA (uncertainty in size, location, and rate of recurrence of earthquakes). A PSHA provides the framework in which these uncertainties can be identified, quantified, and combined in a rational manner to provide a more complete picture of the seismic hazard (Kramer, 1996).

Similar to the DSHA, the PSHA procedure can be broken into four steps, as introduced by Reiter (1990) and illustrated in Figure 2-7. The first step is the identification and characterization of earthquake sources, which is identical to the first step in the DSHA, except that the probability distribution of potential rupture locations within the source is characterized. For this first step, a uniform distribution is usually used, suggesting that there is equal probability that the earthquake will occur at any point within the source. With more data, it can be determined if a different type

of probability distribution needs to be used, indicating that the earthquake is more likely to originate at a certain point within the source. The second step is to characterize the seismicity of the source, which is completed by accounting for the probability of the recurrence of a specific level of earthquake. This second step is accomplished using a recurrence relationship, which specifies the average rate at which an earthquake of some size will be exceeded. In a DSHA, this can only be done for the controlling earthquake, but for a PSHA this is done for all possible earthquakes from a specific source. The third step is to determine the ground motions at the site created by earthquakes of all possible sizes and at all possible locations, which is done using attenuation relationships. The inherent uncertainty of the attenuation relationships must be included in the analysis. The fourth step is to combine the uncertainties in earthquake location, size, and GMP prediction to determine the probability that the GMP will be exceeded during a particular time period.

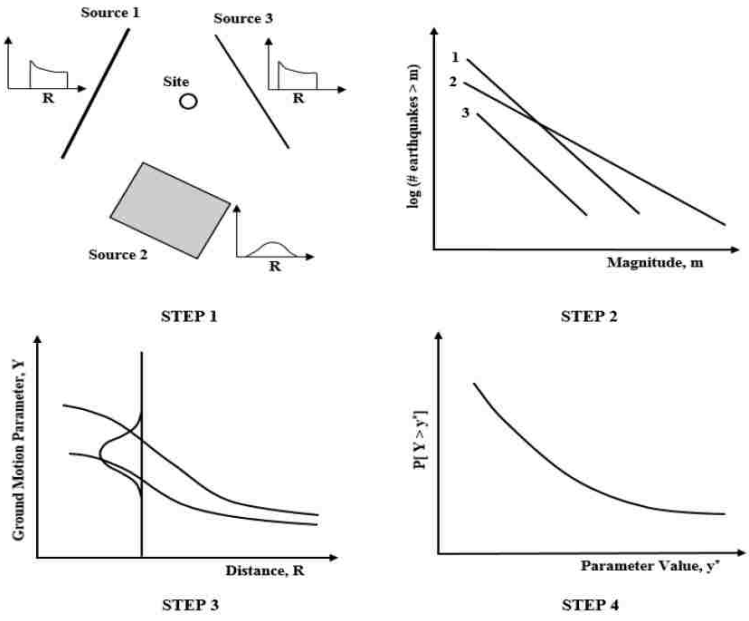

Figure 2-7: Illustration of the four steps in implementing a PSHA (after Kramer, 1996).

Because a PSHA takes into account all possible seismic events, it has the ability to produce a range of results. The results from a PSHA are unlike the results from a DSHA, which outputs a single value, such as factor of safety. A PSHA outputs an annual rate of exceedance (λ), which is the probability that a specific event will be exceeded in a given year. All of the annual rates of exceedance are combined and presented in a seismic hazard curve.

2.6.3 Seismic Hazard Curves

The seismic hazard curve graphically indicates the annual probability of exceeding different values of a selected GMP at a particular site. With this curve, the probability of exceeding some parameter in a given amount of time can be calculated. A seismic hazard curve can be developed using Equation 2-1:

$$\lambda_{y^*} = \sum_{i=1}^{N_S} \nu_i \iint P\left[Y > y^* \mid m, r\right] f_M(m) f_R(r)\, dm\, dr \tag{2-1}$$

where

$$\nu_i = e^{\alpha_i - \beta_i m_o} \tag{2-2}$$

The expression $P\,[Y > y^* \mid m, r]$ is obtained from the attenuation relationships, representing the probability that a specific GMP (y^*) is exceeded given a certain magnitude (m) and distance (r). The functions $f_M(m)$ and $f_R(r)$ are the probability density functions for magnitude and distance, respectively. The variable ν_i is the average rate of threshold magnitude exceedance, with $\alpha = 2.303a$ and $\beta = 2.303b$ (a and b are Gutenberg-Richter coefficients). The

average rate of threshold magnitude exceedance is used to limit the earthquake sources to a specific range of magnitudes at which an earthquake will actually cause damage. Equation 2-1 represents a site that is in a region of N_s potential seismic sources.

The integrals in Equation 2-1 are too complicated to be calculated analytically; therefore, numerical integration is used to develop the hazard curve. The simplest way that this is done is to divide the possible ranges of magnitude and distance into equal segments of N_M and N_R. With this adjustment, Equation 2-1 can be approximated using Equations 2-3 to 2-7:

$$\lambda_{y^*} = \sum_{i=1}^{N_S} \sum_{j=1}^{N_M} \sum_{k=1}^{N_R} v_i P\left[Y > y^* \mid m_j, r_k \right] f_{Mi}(m) f_{Ri}(r) \Delta m \Delta r \tag{2-3}$$

$$m_j = m_o + (j - 0.5) \frac{\left(m_{\max} - m_o \right)}{N_M} \tag{2-4}$$

$$r_k = r_{\min} + (k - 0.5) \frac{\left(r_{\max} - r_{\min} \right)}{N_R} \tag{2-5}$$

$$\Delta m = \frac{\left(m_{\max} - m_o \right)}{N_M} \tag{2-6}$$

$$\Delta r = \frac{\left(r_{\max} - r_{\min} \right)}{N_R} \tag{2-7}$$

where $\left(m_{\max} - m_o\right)$ represents the difference between the magnitudes of the largest and smallest earthquakes and $\left(r_{\max} - r_{\min}\right)$ similarly represents the difference between the largest and smallest distances.

Equation 2-3 assumes that each source is only able to produce N_M earthquakes at different magnitudes and N_R different source-to-site distances. With this assumption, Equation 2-3 can be rewritten as Equation 2-8 as follows:

$$\lambda_{y^*} = \sum_{i=1}^{N_S} \sum_{j=1}^{N_M} \sum_{k=1}^{N_R} v_i P\left[Y > y^* \mid m_j, r_k\right] P\left[M = m_j\right] P\left[R = r_k\right] \tag{2-8}$$

Equation 2-8 calculates a single point on the seismic hazard curve, which is repeated for all increments of y^* until a full hazard curve is formed. When all of the points have been calculated, they can then be plotted together to generate a complete seismic hazard curve.

2.7 Chapter Summary

Earthquakes and their ensuing effects, such as liquefaction, have occurred throughout history. It has only been in recent decades that they have been successfully understood and quantified. Different methods of measuring earthquake intensities have been used through the years, but the moment magnitude scale is one of the most reliable and was used in this study. The ground motions produced by earthquakes can be measured using GMPs such as amplitude, frequency, and duration. Efforts have been made to accurately predict these ground motions using ground motion prediction equations, also known as attenuation relationships. With these relationships, seismic hazard analyses can be performed.

Seismic hazard analyses are used to estimate the demand that a structure will experience during a seismic event. Two types of analyses are used today, a DSHA in which a controlling earthquake is used and a PSHA that considers all possible earthquakes along with their uncertainty in size and location. A DSHA results in a single value, such as a factor of safety. A PSHA results in a seismic hazard curve, which is used to determine the annual probability of exceeding different values of a selected GMP at a particular site. With this information, the ground motions at a site can be accurately predicted.

3 REVIEW OF LIQUEFACTION

3.1 Introduction

Lateral spread displacements can cause major damage to infrastructure, and, while such damage does not usually cause loss of life, the economic repercussions have a serious effect. Large lateral spread displacements are usually caused by soil liquefaction during a seismic event. Because of this, a review of liquefaction is provided in this chapter. The text *Geotechnical Earthquake Engineering* by Kramer (1996) has an excellent summary of liquefaction and is heavily referenced in the following sections.

3.2 Liquefaction

In seismically active zones, soil liquefaction is always a concern when dealing with structures on saturated sandy soil, or soil with similar characteristics. Lateral spreading and other effects of liquefaction cause devastating damage to infrastructure throughout the world. While being an important and complex topic to geotechnical engineers, liquefaction is a relatively new field of study. The phenomenon of liquefaction has surely occurred throughout history, but it was not until the Niigata, Japan, earthquake of 1964 that it was recognized and recorded. In that same year, liquefaction was also evident in the Good Friday earthquake that struck Portage, Alaska. Both of these earthquakes had many examples of liquefaction-induced damage.

As liquefaction has been studied, its definition has changed over the years. The term "liquefaction" was first used by Mogami and Kubo (1953). The general definition of

liquefaction is a loss of shear strength in cohesionless soils. This strength reduction is a result of excess pore pressure that develops in undrained conditions due to rapid (earthquake) loading. These pore pressures lead to a decrease in effective stress and overall strength of the soil. Strength decrease then results in different forms of soil deformation. These deformations are usually manifest in two general ways: flow liquefaction and cyclic mobility.

Flow liquefaction is the less frequent but more dramatic of the two types of liquefaction. Flow liquefaction occurs when the shear strength of the liquefied soil decreases enough to where it becomes less than the shear stress required for equilibrium. The shear stress is usually a combination of factors such as the soil's own weight and its level of saturation. When the shear strength decreases to the point where it is less than the shear stress applied, the soil is unstable and can form flow failures that can result in large soil masses displacing very rapidly. While these types of failures are not as common as those found with cyclic mobility, they can be very dangerous.

Cyclic mobility is the more common form of liquefaction that also can have large deformations. While these deformations may not be extremely life-threatening, they are very common and have large economic impact. The deformations produced by cyclic mobility failures develop incrementally during earthquake shaking (Kramer, 1996). These incremental deformations can be thought of as a ratcheting effect. When considering the effect of lateral spreading, a subsurface soil layer liquefies and causes surficial layers to deform closer and closer toward the free face, or further and further down a ground slope as the earthquake progresses. Soil liquefaction refers to both flow liquefaction and cyclic mobility. For this study, emphasis is made on cyclic mobility, as lateral spread displacements result from that form of liquefaction.

Analysis of soil liquefaction can be broken up into three parts: liquefaction susceptibility, initiation, and effects.

3.3 Liquefaction Susceptibility

Liquefaction will not occur at all sites or in any soil profile. The first step in analyzing the liquefaction hazard is determining the susceptibility of the soil to liquefaction. If the soil proves to not be susceptible to liquefaction, there is no need to continue the investigation. However, if the soil is susceptible, then liquefaction initiation and its effects must be determined. Liquefaction susceptibility is a function of four criteria: historical criteria, geologic criteria, compositional criteria, and state criteria.

3.3.1 Historical Criteria

When it comes to earthquakes and the determination of liquefaction hazards, recorded information from past earthquakes can be very useful. As time goes on, more and more data are recorded, which aid in susceptibility determination. It has been shown that liquefaction often recurs at the same location when soil and groundwater conditions are unchanged (Youd, 1984). Knowing this, case histories can be used to identify locations (or types of soil profiles) where liquefaction can be expected given certain earthquake loading conditions.

3.3.2 Geologic Criteria

One of the largest factors contributing to liquefaction susceptibility is the soil itself. Geologic criteria such as the depositional environment, hydrological environment, and age play a large role in susceptibility (Youd and Hoose, 1977). Geologic formations with high liquefaction susceptibility are those that deposit the soil in a loose state with uniform grain-size distributions.

These types of deposits often correspond to fluvial, colluvial, and aeolian deposits that, when saturated, have a high susceptibility to liquefaction. As the geologic age of a deposit increases, the susceptibility decreases due to an increased densification of the soil. Man-made soil deposits also have the possibility of being susceptible to liquefaction. Examples of man-made deposits that are susceptible to liquefaction include hydraulic fill and poorly-compacted fill, which both result in loose material.

In any geologic environment, a soil must be saturated to liquefy. Because of this, the elevation of the water table can often determine the susceptibility of a soil profile. If the water table is extremely low, the soil is unlikely to liquefy, even if all other criteria are met. Liquefaction is most commonly observed at sites where groundwater is within a few meters of the ground surface (Kramer, 1996).

3.3.3 Compositional Criteria

Liquefaction occurs as the soil is loaded during an earthquake and excess positive pore pressures are developed. In order for these excess pore pressures to develop, the soil must densify and decrease in volume. A decrease in volume will essentially push the water through the pore space. The volume change is, in part, a function of the compositional criteria of the soil, which includes characteristics such as grain size, particle shape, and gradation.

The general understanding is that liquefaction hazards are primarily associated with loose sands. Soils with smaller particles (e.g. silts and clays) have difficulty generating high pore pressures, and soils with larger particles (e.g. gravels) have difficulty sustaining positive pore pressure long enough to induce liquefaction due to their high permeability. However, there are cases of liquefaction of non-plastic silts (Ishihara, 1984; Ishihara, 1985), as well as evidence of liquefaction found in gravelly soils (Chen et al., 2009; Coulter and Migliaccio, 1966; Wong et

al., 1974). Wang (1979) provided criteria (the "Chinese Criteria") for determining the susceptibility of clays based on Atterberg limits and moisture content. The "Chinese Criteria" were adopted by geotechnical engineers, as recommended by Youd (2001). Idriss and Boulanger (2008) stated that low-plasticity clays may undergo a similar process to liquefaction (known as "cyclic softening"), but it is not nearly as destructive as true liquefaction. The results presented by Idriss and Boulanger (2008) have led to many engineers disregarding the "Chinese Criteria" (Bray and Sancio, 2006).

When it comes to gradation, poorly-graded soils are more susceptible to liquefaction than well-graded soils. Well-graded soils have more particles of varying sizes, which allows for smaller particles to fill the voids between larger particles. The consequence of this is a lower change in volume and less excess pore pressure as the soil particles take up the pore space. In poorly-graded soils, this pore space is open, and the excess pore pressure is able to be sustained.

Particle shape also has an effect on liquefaction susceptibility, as it determines how the particles interact with one another. Particles with rounded shapes and smooth edges densify more easily than particles with angular shapes and more jagged edges. Round particles can easily slide past one another, while the angular particles tend to cause friction and interlock between each other.

3.3.4 State Criteria

While all of the preceding criteria may indicate that a soil has the potential to liquefy, it still may not be susceptible to liquefaction. Among these other criteria, liquefaction susceptibility also depends on the initial confining pressure and the initial density of the soil at the time of an earthquake. In other words, liquefaction susceptibility is dependent upon the initial state of the

soil. Unlike the previously discussed criteria, the state criteria is different for flow liquefaction and cyclic mobility.

In 1936, Casagrande reported on his findings after performing drained, strain-controlled triaxial tests on soils in an initially loose state and soils in an initially dense state. It was found that all soil specimens tested at the same confining pressure approached the same density when sheared. Loose specimens contracted (densified) during this shearing, and dense specimens first contracted but then quickly dilated (expanded). The constant density approached is known as the critical void ratio, e_c. As the triaxial tests were performed at different confining pressures, the value of the critical void ratio could be plotted. By plotting these critical void ratios with their corresponding confining pressures, the *critical void ratio* (CVR) line is formed. The CVR line as plotted is shown in Figure 3-1 and is essentially the boundary between loose (dilative) and dense (contractive) soil specimens.

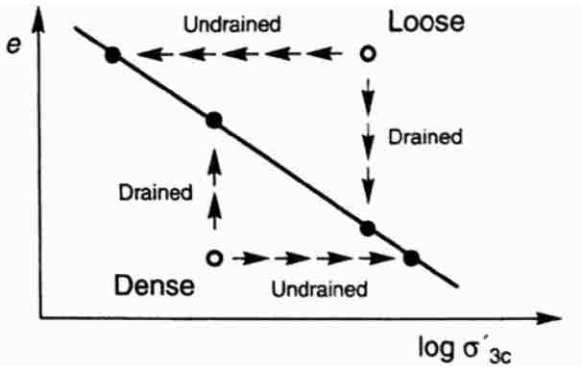

Figure 3-1: Behavior of loose or dense soil specimens under drained or undrained loading (after Kramer, 1996).

Because the CVR line defines the boundary between dilative and contractive behavior of soils, it was thought to also define the boundary between soil specimens that are susceptible and

not susceptible to liquefaction (as illustrated in Figure 3-2). This definition was found to not be entirely accurate after the case of the Fort Peck Dam failure (Middlebrooks, 1942). In 1938 the Fort Peck Dam in Montana failed during construction due to a flow liquefaction failure. The initial state of the liquefied soil in the Fort Peck Dam would have plotted below the CVR line, indicating that it was not susceptible to liquefaction. Casagrande attributed this inconsistency to the inability of the strain-controlled drained test to replicate all of the phenomena that contribute to an actual flow liquefaction failure. After this realization, a more refined state criteria for liquefaction was needed.

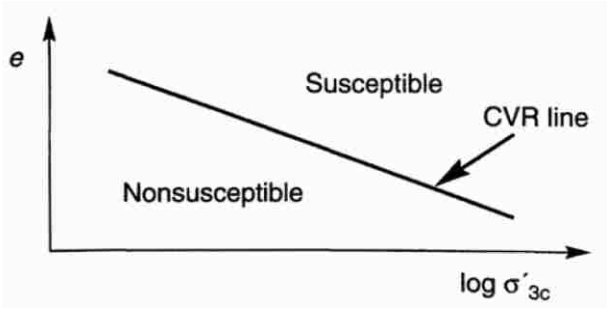

Figure 3-2: The CVR line as a definition of liquefaction susceptibility (after Kramer, 1996).

In 1969, Castro, a student of Casagrande, presented results of further stress-controlled triaxial tests, with the added benefit of now being able to perform these tests in an undrained condition. These tests were able to replicate flow liquefaction and led to the discovery of the steady state of deformation (Castro, 1977; Poulos, 1981). The steady state of deformation describes the state in which the soil flows continuously under constant shear stress and constant confining pressure at a constant volume and constant velocity. Similar to the CVR line, there is a steady-state line (SSL) that can be plotted to show the relationship between void ratio and

confining pressure, but first it must be understood that the SSL is really a three-dimensional curve in e – σ′ – τ space, as shown in Figure 3-3.

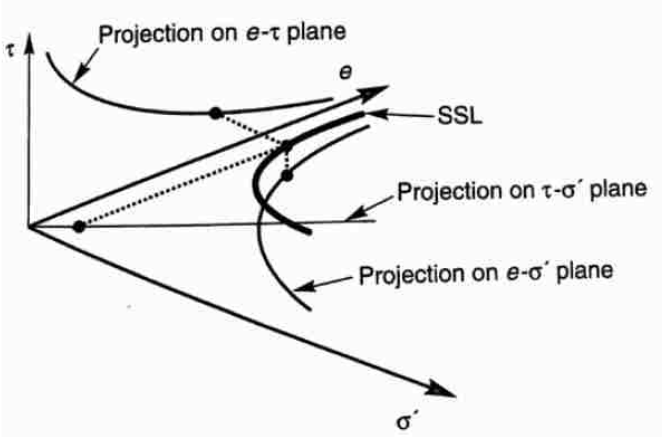

Figure 3-3: Steady-state line (SSL) shown in three dimensions (after Kramer, 1996).

The SSL can be projected into two-dimensional e – σ′ space or e – τ space, which both have equivalent linear slopes when plotted logarithmically. The SSL is useful for identifying conditions under which a certain soil may be susceptible to flow liquefaction. Soils with an initial state plotted below the SSL are not susceptible to flow liquefaction, but soils with an initial state plotted above the SSL are susceptible to flow liquefaction if the state shear stress is greater than the steady-state strength, as presented in Figure 3-4. When plotted together, the SSL is slightly below and parallel to the previously discussed CVR line, which is consistent with the case of the Fort Peck Dam (the initial state likely fell between the two lines).

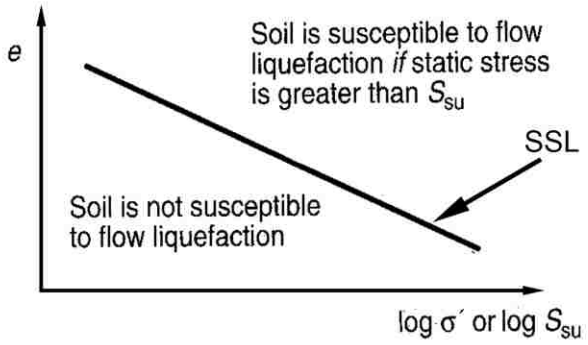

Figure 3-4: State criteria for flow liquefaction susceptibility using the steady-state line (after Kramer, 1996).

It should be noted that, while the SSL was an improvement on the CVR line, it still only applies to susceptibility of flow liquefaction. Cyclic mobility can still occur whether the initial state of the soil falls above or below the SSL; therefore, cyclic mobility has the potential to occur in loose and dense soils.

3.4 Liquefaction Initiation

If a soil meets the susceptibility criteria discussed above, there is a potential liquefaction hazard. However, the next step in liquefaction hazard evaluation is liquefaction initiation. An earthquake must create sufficient strain in the soil as to trigger, or initiate, liquefaction. Flow liquefaction and cyclic mobility are both triggered by sufficient strain but are initiated under separate conditions that can be described using the stress path space (Hanzawa et al., 1979). The flow liquefaction surface is defined in the stress path space and is used to understand initiation of flow liquefaction as well as cyclic mobility.

3.4.1 Flow Liquefaction Surface

To understand the definition of a flow liquefaction surface, one must first begin with an example of a loose, saturated sand specimen under monotonic loading, which is shown in Figure 3-5, with the stress path beginning at point A and progressing to point C. Initially, before any loading, there is no strain or excess pore pressure (as depicted in parts (a) and (c) of Figure 3-5). As the loading is applied, there is an initial increase in the shear strength, shown with a peak at point B. As the stress exceeds the peak shear strength, the soil loses strength, collapses, and reaches a residual strength at point C, far lower than the peak strength at point B. As the peak shear strength reaches a residual strength, the excess pore pressure continues to increases to point C. As the excess pore pressures increase, part (d) of Figure 3-5 shows that the loose soil contracts and reaches the SSL at point C. This instability is the occurrence of flow liquefaction.

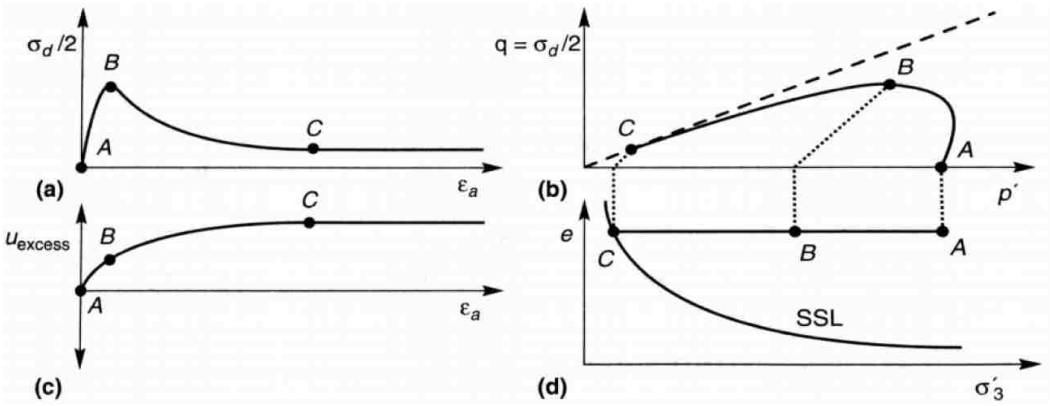

Figure 3-5: Response of isotropically consolidated specimen of loose, saturated sand: (a) stress-strain curve, (b) effective stress path, (c) excess pore pressure, (d) effective confining pressure (after Kramer, 1996).

Figure 3-5 demonstrates the stress path of an initial state of a single soil specimen. The response of multiple specimens can be considered as they are consolidated to the same void ratio

at different confining pressures. Because all of the specimens have the same void ratio, they will reach the same stress conditions at the SSL, but through different stress paths (Kramer, 1996), as illustrated in Figure 3-6.

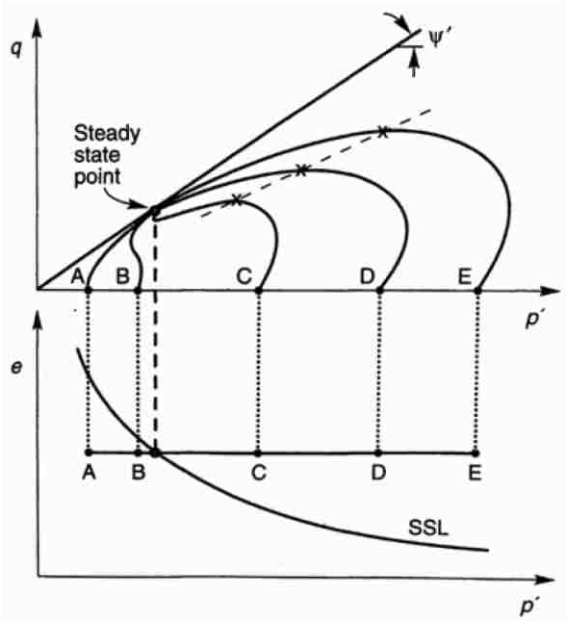

Figure 3-6: Response of five specimens consolidated to the same void ratio but at different confining pressures, with the initiation of flow liquefaction indicatd with an x on stress paths for specimens C, D, and E (after Kramer, 1996).

Specimens A and B on Figure 3-6 have an initial state below the SSL and therefore exhibit dilation upon shearing. Specimens C, D, and E all exhibit contractive behavior and reach a peak undrained strength before shearing rapidly toward the steady state point. The peak undrained strength is the point at which flow liquefaction is initiated (indicated by an x on Figure 3-6). When combining the points for specimens of different initial states (such as C, D, and E), a straight line connecting the point of flow liquefaction initiation is formed, known as the flow liquefaction surface (FLS). The FLS marks the boundary between stable and unstable states in undrained shear. If the stress conditions of a specimen reach the FLS, flow liquefaction is

initiated. Since flow liquefaction cannot occur if the stress path is below the steady-state point (such as in the case of points A and B), the FLS is stopped to the right of that point in the stress path space, as illustrated in Figure 3-7.

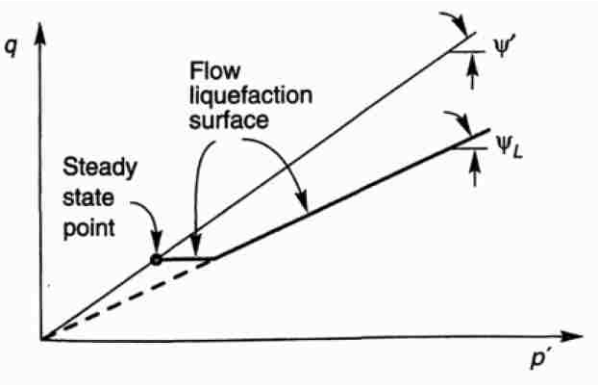

Figure 3-7: Orientation of the FLS in the stress path space (after Kramer, 1996).

In the examples that have been discussed in this section, monotonic loading was considered, but the concept of the FLS also holds true for cyclic loading, such as earthquake shaking. Both monotonic and cyclic loading, if causing enough displacement, can force the stress path of a soil specimen to move toward the FLS and initiate flow liquefaction.

For flow liquefaction to occur, there are two conditions that both have to be met. First, the stress path of the soil must reach the FLS, as discussed previously. The second condition is that the soil must already be experiencing some driving force that is pushing the soil to its steady-state strength. These driving forces for flow liquefaction are usually the static stresses of its own weight due to gravity. The zone in which these two conditions are met and in which a soil is susceptible to flow liquefaction is illustrated in Figure 3-8. Cyclic mobility uses the FLS but has a different zone of susceptibility and initiation mechanism, as discussed in the next section.

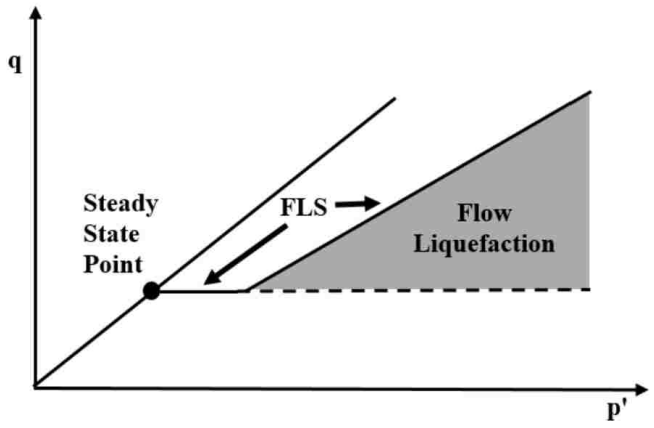

Figure 3-8: Zone of susceptibility to flow liquefaction (after Kramer, 1996).

3.4.2 Cyclic Mobility

When a soil specimen does not meet the conditions required for initiation of flow liquefaction, there is still a possibility of the initiation of liquefaction via cyclic mobility. Similar to flow liquefaction, there is a zone of initial stress in which a soil specimen is susceptible to flow liquefaction, as illustrated in Figure 3-9. This zone includes the possibility of an initial state

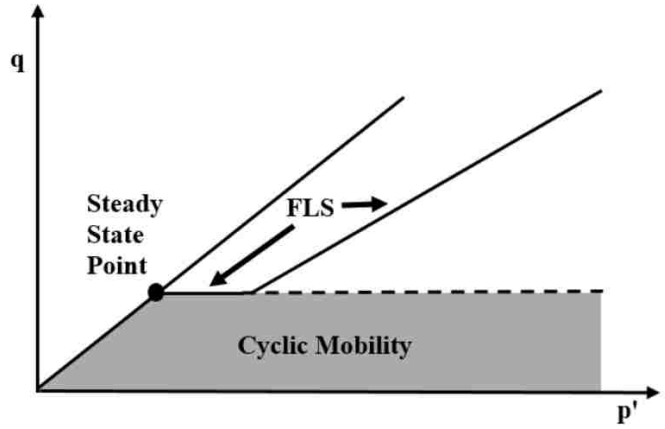

Figure 3-9: Zone of susceptibility to cyclic mobility (after Kramer, 1996).

being to the left of the steady-state point and therefore having a dilative behavior, indicating that both loose and dense soils are subject to cyclic mobility. There are three combinations of initial conditions and cyclic loading conditions that generally produce cyclic mobility (Kramer, 1996). These three conditions are shown in Figure 3-10.

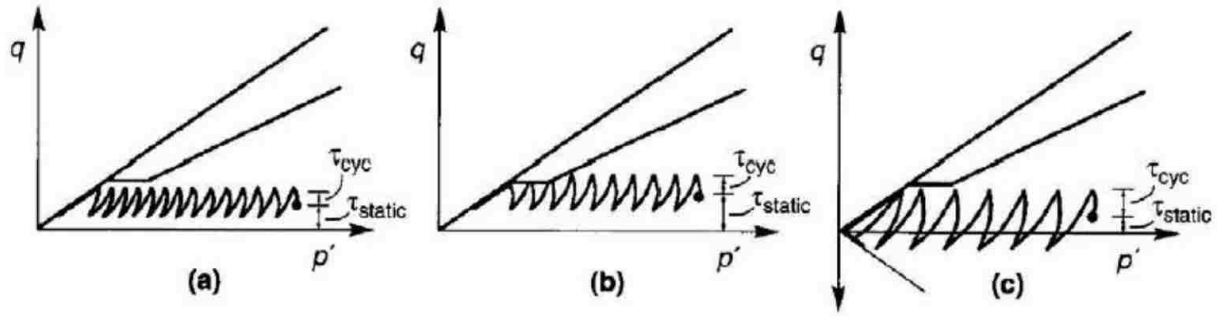

Figure 3-10: Three cases of cyclic mobility: (a) no stress reversal and no exceedance of the steady-state strength, (b) no stress reversal with momentary periods of steady-state strength exceedance, (c) stress reversal with no exceedance of steady-state strength (after Kramer, 1996).

All three conditions in Figure 3-10 show the stress path, the point at which static loading ends and cyclic loading begins, and how the cyclic loading progresses toward the steady-state point. The first condition in which cyclic mobility can occur is when there is no stress reversal ($\tau_{static} - \tau_{cyc} > 0$) and no exceedance of the steady-state strength ($\tau_{static} + \tau_{cyc} < S_{su}$) (Figure 3-10 (a)). The stress path moves left until it passes the FLS and reaches the drained failure envelope. The confining pressure decreases, and the corresponding low stiffness allows for permanent strains/deformations to develop with each loading cycle.

The second condition occurs when there is no stress reversal ($\tau_{static} - \tau_{cyc} > 0$), but unlike the first condition there are momentary periods of steady-state strength exceedance ($\tau_{static} + \tau_{cyc} > S_{su}$) (Figure 3-10 (b)). The stress path moves to the left, but in this condition it touches the FLS,

which cause momentary instability. Permanent strains develop during these moments, but they stop once the stress falls below the FLS.

The third condition occurs when, unlike conditions 1 or 2, there is a stress reversal ($\tau_{static} - \tau_{cyc} < 0$), and there is no exceedance of the steady-state strength ($\tau_{static} + \tau_{cyc} < S_{su}$) (Figure 3-10 (c)). As the stress path in this cycle drops below zero on the y-axis, there is both compressional and extensional loading within each cycle. The rate of pore pressure generation increases with each increasing degree of stress reversal (Dobry and Vucetic, 1987; Mohamad and Dobry, 1986). Because of this, the stress path moves rather quickly to the left and ends up going back and forth between the compression and extension portions of the failure envelope. Each time the stress path goes from compression to extension it crosses the origin, putting the specimen in a state of zero effective stress, which in turn causes large permanent deformations.

Cyclic mobility initiation is much different than that of flow liquefaction because there is no specific point at which it is initiated. The deformations caused by cyclic mobility gradually accumulate as the earthquake loading progresses. The magnitude of the deformations are directly related to the magnitude and duration of the earthquake loading. With higher-magnitude loading, more deformations will accumulate as the loading progresses.

3.5 Evaluation of Liquefaction Initiation

Now that the theory behind liquefaction hazard initiation is understood, procedures used in practice today can be discussed. There are several approaches in analyzing the liquefaction hazard at a site, the most common being known as the cyclic stress approach. In this approach a factor of safety against liquefaction (FS_L) is determined, and, like other factors of safety used in engineering, it is a ratio of the capacity to the demand. In the case of FS_L, the earthquake-induced loading is compared to the liquefaction resistance of the soil. When the loading is greater than

the resistance of the soil, liquefaction is expected to occur. Both the loading and the resistance of the soil are expressed in terms of cyclic shear stress (hence the name *cyclic stress approach*). The earthquake-induced loading is known as the cyclic stress ratio (*CSR*), and the soil's resistance to liquefaction is known as the cyclic resistance ratio (*CRR*). The *CRR* is determined from the cyclic shear stress required to initiate liquefaction ($\tau_{cyc,L}$), and the *CSR* is determined from the cyclic shear stress induced by earthquake loading (τ_{cyc}). The comparison of these two ratios determines the FS_L, as calculated in Equation 3-1:

$$FS_L = \frac{Capacity}{Demand} = \frac{Resistance}{Loading} = \frac{\tau_{cyc,L}}{\tau_{cyc}} = \frac{CRR}{CSR} \tag{3-1}$$

This relationship between *CRR* and *CSR* is frequently referred to as the simplified procedure (Seed, 1979). For most methods, determination of the *CSR* is calculated using Equation 3-2, originally after Seed and Idriss (1971):

$$CSR = 0.65 \frac{a_{\max}}{g} \frac{\sigma_v}{\sigma'_v} (r_d) \left(\frac{1}{MSF} \right) \left(\frac{1}{K_\sigma} \right) \tag{3-2}$$

where $\frac{a_{\max}}{g}$ is the peak acceleration caused by the earthquake in terms of gravity (g), σ_v is the total vertical stress, σ'_v is the effective vertical stress, r_d is the depth-dependent shear stress reduction factor, *MSF* is the magnitude scaling factor, and K_σ is the overburden correction factor (which in some cases, along with the *MSF*, is part of the *CRR* term).

There are a variety of different methods to determine the *CRR*. As it is a measurement of the soil's resistance to liquefaction, strength parameters from in-situ tests are often used to correlate to *CRR*. The standard penetration test (SPT), CPT, shear wave velocity test, and dilatometer index are tests commonly used to measure the *CRR* of a given soil profile. The SPT procedures are very popular, as the test is used often for a variety of purposes. However, there are shortcomings to the SPT procedure, such as limited repeatability and a non-continuous profile. The CPT is becoming a more widely used and trusted in-situ test, making up for the shortcomings of the SPT. This study focuses on an analysis using the CPT. There are two prominent CPT procedures for analyzing liquefaction initiation that are discussed in the following sections, including Robertson and Wride (1998) and Boulanger and Idriss (2016).

3.5.1 Deterministic CPT-Based Evaluation of Liquefaction Initiation (Robertson and Wride, 1998)

One of the most widely used procedures for determining the liquefaction resistance from the CPT comes from Robertson and Wride (1998) along with the updated Robertson (2009) (these are collectively referred to as the Robertson and Wride procedure in this thesis). As the cone is pushed into the soil, the cone tip resistance (*qc*), sleeve friction (*fs*), and pore water pressure (*u*) are recorded with depth. All three of these variables are used to determine the corrected clean sand cone tip resistance, Q_{tncs} (also written as q_{c1Ncs} in other procedures). With the corrected cone tip resistance known, the *CRR* can be calculated as it is primarily a function of Q_{tncs}. The Robertson and Wride procedure determines the FS_L with depth for each soil increment (with the CPT being continuous, values are recorded every few centimeters, defining a soil increment). The relationship between *CRR* and *CSR* for the Robertson and Wride procedure is presented in Figure 3-11, which shows the liquefaction triggering curve developed from all of

the case histories studied. The curve in Figure 3-11 is the approximate boundary between soils that will and will not liquefy given Q_{tncs} (or *CRR*) and *CSR*. The full Robertson and Wride procedure is mapped out in Figure 3-12.

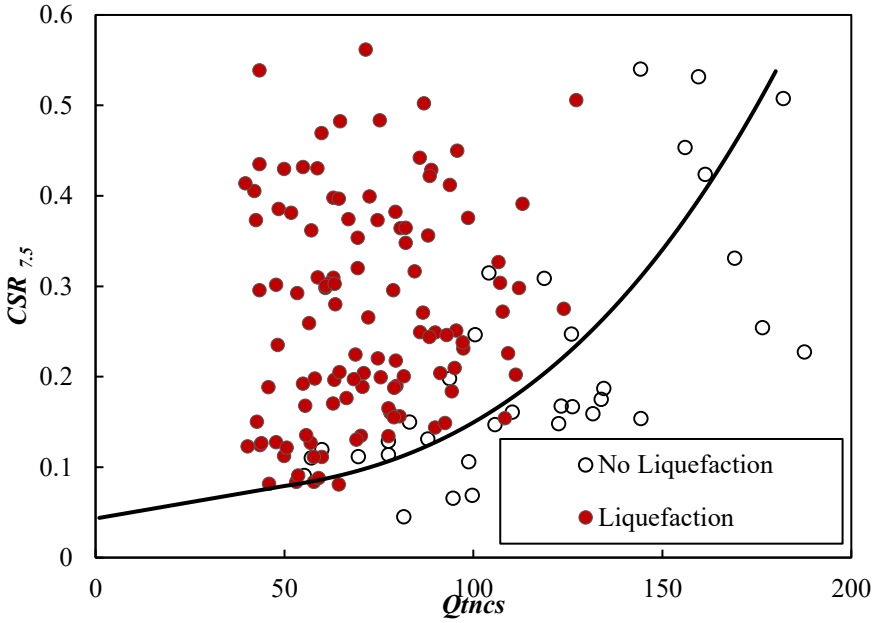

Figure 3-11: Deterministic liquefaction triggering *CRR* curve developed using the Robertson and Wride procedure.

In order to determine Q_{tncs} it must be understood that the Robertson and Wride procedure is iterative. The iterative portion is the determination of the stress exponent, *n*, as calculated in Equation 3-3:

$$n = 0.381(I_c) + 0.05\left(\frac{\sigma'_{vo}}{p_a}\right) - 0.15 \tag{3-3}$$

where I_c is the soil behavior type index, σ'_{vo} is the effective vertical stress, and p_a is the

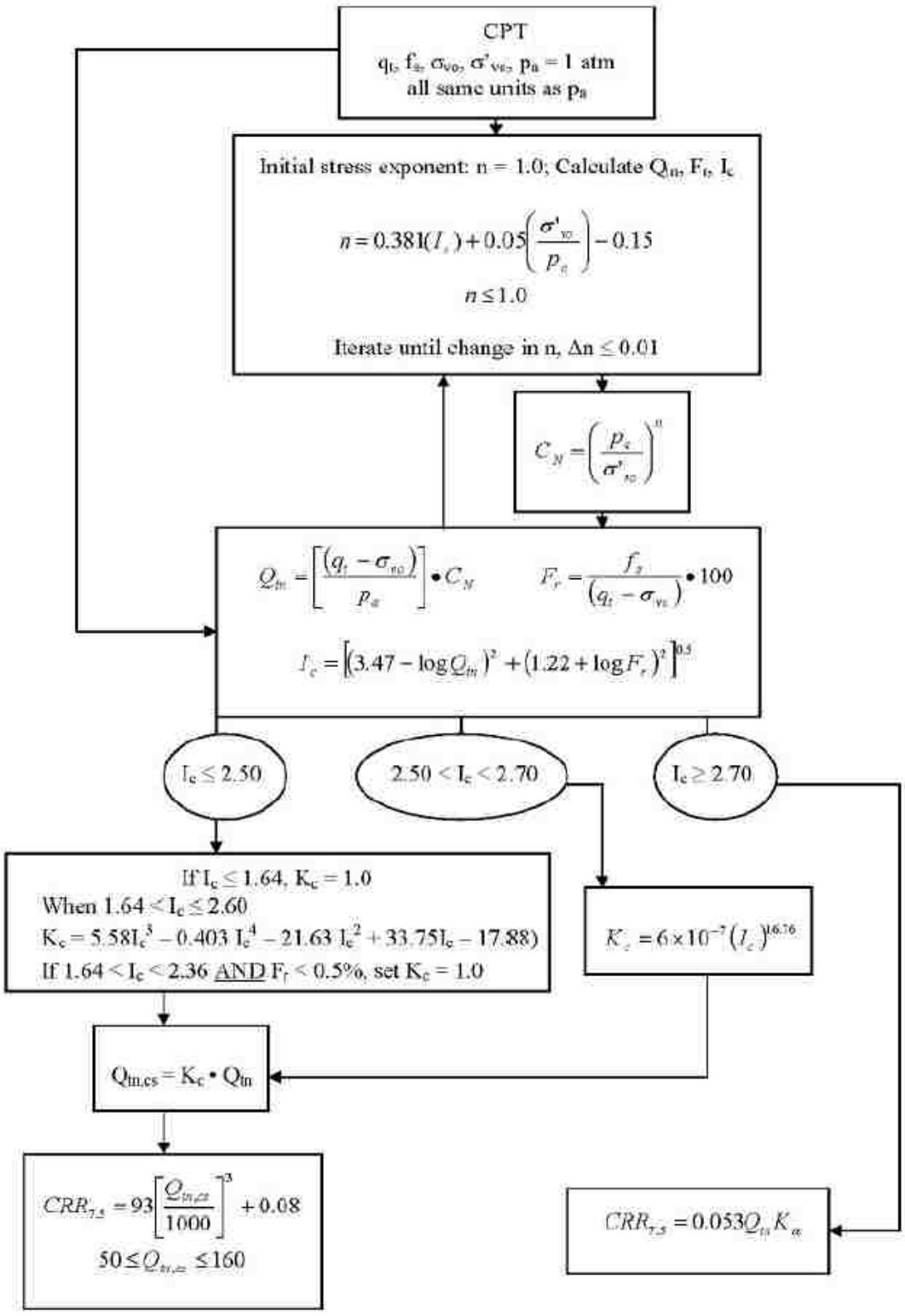

Figure 3-12: Procedure for determining CRR using the Robertson and Wride (1998) procedure.

atmospheric pressure. With the stress exponent calculated, the soil behavior type index can be determined. The soil behavior type index is used as a means to classify the soil from the given CPT data. A chart such as that found in Figure 3-13 is used to determine the soil behavior type index, with each different zone/number representing a different soil type as a function of the normalized cone resistance and the normalized friction ratio. The value of I_c is important in liquefaction triggering evaluation since the soil type is a large factor in the determination of the soil's susceptibility to liquefaction. In the Robertson and Wride procedure, the soil behavior type

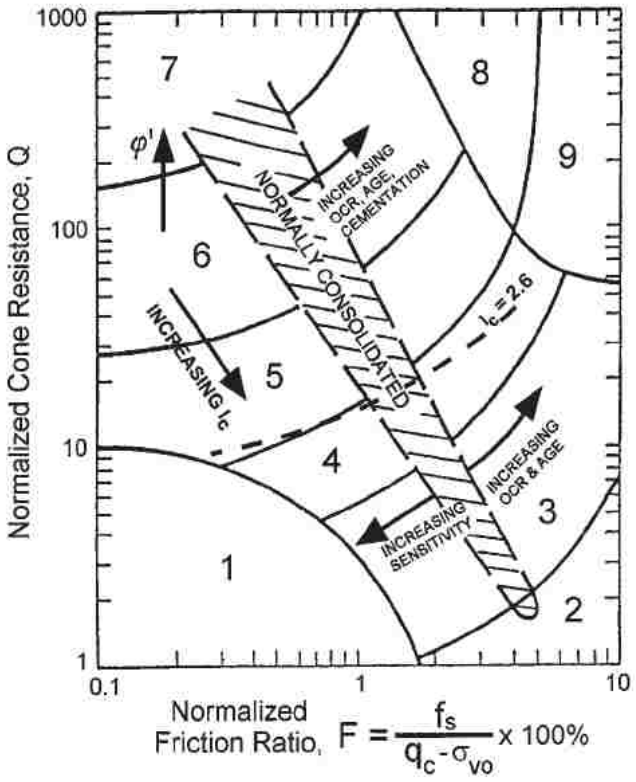

Figure 3-13: Soil behavior type index, I_c, determined using the normalized soil behavior chart, as proposed by Robertson (1990), with soil types as follows: 1, sensitive, fine grained; 2, peats; 3, silty clay to clay; 4, clayey silt to silty clay; 5, silty sand to sandy silt; 6, clean sand to silty sand; 7, gravelly sand to dense sand; 8, very stiff sand to clayey sand; 9, very stiff, fine grained.

index, I_c, is calculated as shown in Equation 3-4:

$$I_c = \left[\left(3.47 - \log Q_{tn}\right)^2 + \left(1.22 + \log F_r\right)^2 \right]^{0.5} \tag{3-4}$$

where Q_{tn} is the dimensionless corrected cone tip resistance (sometimes denoted as Q, as in Figure 3-13), and F_r is the normalized friction ratio (sometimes denoted as F, as in Figure 3-13). The equations for Q_{tn} and F_r are shown in Equations 3-5 and 3-6, respectively:

$$Q_{tn} = \left[\frac{q_t - \sigma_{vo}}{p_a} \right] \left(\frac{p_a}{\sigma'_{vo}} \right)^n \tag{3-5}$$

$$F_r = \left(\frac{f_s}{q_t - \sigma_{vo}} \right) \tag{3-6}$$

In Equation 3-5 it is evident that the stress exponent, n, is a variable in the calculation of Q_{tn}, and Q_{tn} is used to calculate I_c (Equation 3-4), which is in turn used to calculate n. As a result of these relationships, the process is iterative. The iteration is completed by beginning with a seed value of n = 1.0. The value of n is recalculated until the change in n is less than 0.01. With negligible change in n, the iteration process is complete, and the value of I_c is now the true value for this soil increment.

With the values of I_c and then Q_{tn} known, Q_{tncs} can be calculated as presented in Equation 3-7:

$$Q_{tncs} = K_c \cdot Q_{tn} \tag{3-7}$$

where K_c is a function of I_c, as shown in Equation 3-8:

$$K_c = \begin{cases} 1.0 & \text{if } I_c \le 1.64 \\ 1.0 & \text{if } 1.64 < I_c < 2.36 \text{ and } F_r < 0.5\% \\ 5.58 I_c^{\,3} - 0.403 I_c^{\,4} - 21.63 I_c^{\,2} + 33.75 I_c - 17.88 & \text{if } 1.64 < I_c < 2.50 \\ 6 \times 10^{-7} \left(I_c\right)^{16.76} & \text{if } 2.50 < I_c < 2.70 \end{cases} \tag{3-8}$$

With Q_{tncs} calculated, the *CRR* for each soil increment in the CPT profile can be determined. For soil increments with an I_c less than 2.70, the *CRR* is calculated following Equation 3-9:

$$CRR_{7.5} = 93\left[\frac{Q_{tncs}}{1000}\right]^3 + 0.08 \tag{3-9}$$

For soil increments with an I_c greater than 2.70, the *CRR* is calculated as presented in Equation 3-10:

$$CRR_{7.5} = 0.053 Q_{tncs} \tag{3-10}$$

After this process is repeated for every point in the CPT profile, there is a value of *CRR* for every soil increment. By comparing the value to the *CSR*, a value for FS_L can be calculated.

With the *CRR* calculated, the *CSR* must be determined to calculate the FS_L. The Robertson and Wride procedure calculates *CSR* as previously outlined in Equation 3-2. The *MSF* has multiple variations of its calculation (Seed and Idriss, (1982); Ambraseys, (1988) Youd et al., (2001)). The Robertson and Wride procedure follows the *MSF* calculation presented by Youd et al. (2001), as shown in Equation 3-11:

$$MSF = \frac{10^{2.24}}{M_W{}^{2.56}} \tag{3-11}$$

where M_w is the moment magnitude of the given earthquake loading. The depth-dependent shear stress reduction factor, r_d, is a function of the depth of the soil increment and is calculated following the work of Liao and Whitman (1986), Robertson and Wride (1998), and Seed and Idriss (1971), as presented in Equation 3-12:

$$r_d = \begin{cases} 1.0 - 0.00765z & \text{if } z \le 9.15m \\ 1.174 - 0.0267\,\text{z} & \text{if } 9.15\text{m} < z \le 23m \\ 0.774 - 0.008z & \text{if } 23\text{m} < z \le 30m \\ 0.5 & \text{if } z > 30m \end{cases} \tag{3-12}$$

where z is the depth to the soil increment in question, in terms of meters. The overburden correction factor, K_σ, is calculated by following Youd et al. (2001), as shown in Equation 3-13:

$$K_\sigma = \left(\frac{\sigma'_{vo}}{p_a} \right)^{(f-1)} \tag{3-13}$$

where f is a constant value, determined as a function of the site characteristics. With these variables known, the CSR can be calculated. With the CSR and CRR values calculated, the FS_L can be calculated following Equation 3-1.

3.5.2 Probabilistic CPT-Based Evaluation of Liquefaction Initiation (Ku et al., 2012)

As the deterministic Robertson and Wride procedure gained popularity, a probabilistic version of this procedure was needed. Ku et al. (2012) developed a probabilistic model of the Robertson and Wride (1998) procedure by running a statistical analysis of the liquefaction triggering case histories provided by Robertson and Wride (1998). This new probabilistic procedure can be used for more in-depth probabilistic or performance-based analyses.

The main result of the work done by Ku et al. was the development of a function that relates the FS_L, determined from the Robertson and Wride procedure, to a probability of liquefaction, P_L. Using the principal of maximum likelihood and a Bayesian statistical analysis, the expression shown in Equation 3-14 was created:

$$P_L = 1 - \Phi\left[\frac{0.102 + \ln(FS_L)}{\sigma_m}\right] \tag{3-14}$$

where Φ is the cumulative distribution function and σ_m is the model-based uncertainty. Using this function, a P_L can be determined for any FS_L calculated using the Robertson and Wride procedure. This relationship between P_L and FS_L is depicted in Figure 3-14. Similar to the liquefaction triggering curve in Figure 3-11, the P_L can plotted as a curve showing the relationship between Q_{tncs} and CSR, as shown in Figure 3-15. The curves in Figure 3-15 show

that the deterministic curve (denoted by "RW" in Figure 3-15) is approximately equal to a P_L of 0.35.

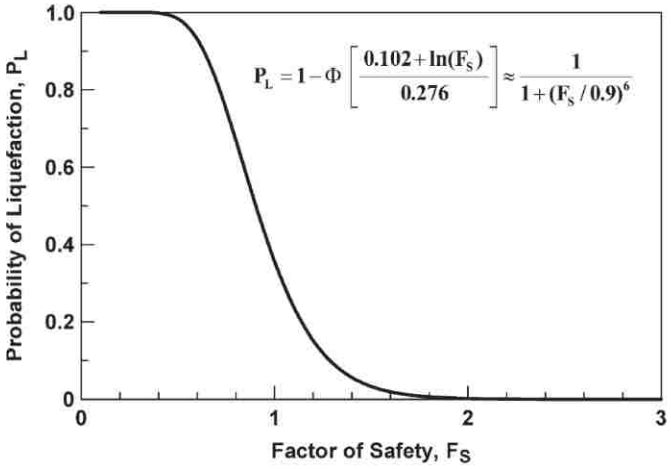

Figure 3-14: Relationship between P_L and FS_L as determined by Ku et al. (2012) and Robertson and Wride (1998) (after Ku et al., 2012).

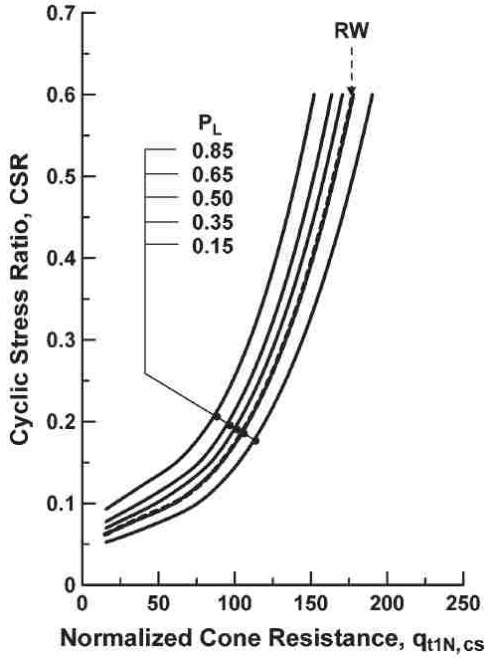

Figure 3-15: Probabilistic liquefaction triggering curves at various levels, determined by the Ku et al. probabilistic procedure (after Ku et al., 2012).

3.5.3 Deterministic CPT-Based Evaluation of Liquefaction Initiation (Boulanger and Idriss, 2016)

Another well-received procedure for the evaluation of liquefaction initiation is the procedure presented by Boulanger and Idriss (2016) (referred to as the Boulanger and Idriss procedure in this thesis), which is mapped out in . The Boulanger and Idriss procedure follows the same calculation of FS_L as shown in Equation 3-1. However, there are some differences in the calculation of the *CSR* and *CRR*. While the Robertson and Wride procedure uses Q_{tncs} to represent the final corrected cone tip resistance, the Boulanger and Idriss procedure uses q_{c1Ncs}, which represents the same parameter.

The first step in determining the *CRR* in the Boulanger and Idriss procedure is to correct the CPT cone tip resistance (*qc*). This correction is calculated in Equation 3-15:

$$q_{c1N} = C_N \frac{q_c}{p_a} \tag{3-15}$$

where p_a is the atmospheric pressure and C_N is the overburden correction factor. C_N is calculated as shown in Equation 3-16:

$$C_N = \left(\frac{p_a}{\sigma'_{vo}} \right)^m \leq 1.7 \tag{3-16}$$

where σ'_{vo} is the effective vertical stress and *m* is calculated following Equation 3-17:

$$m = 1.338 - 0.249(q_{c1Ncs})^{0.264} \tag{3-17}$$

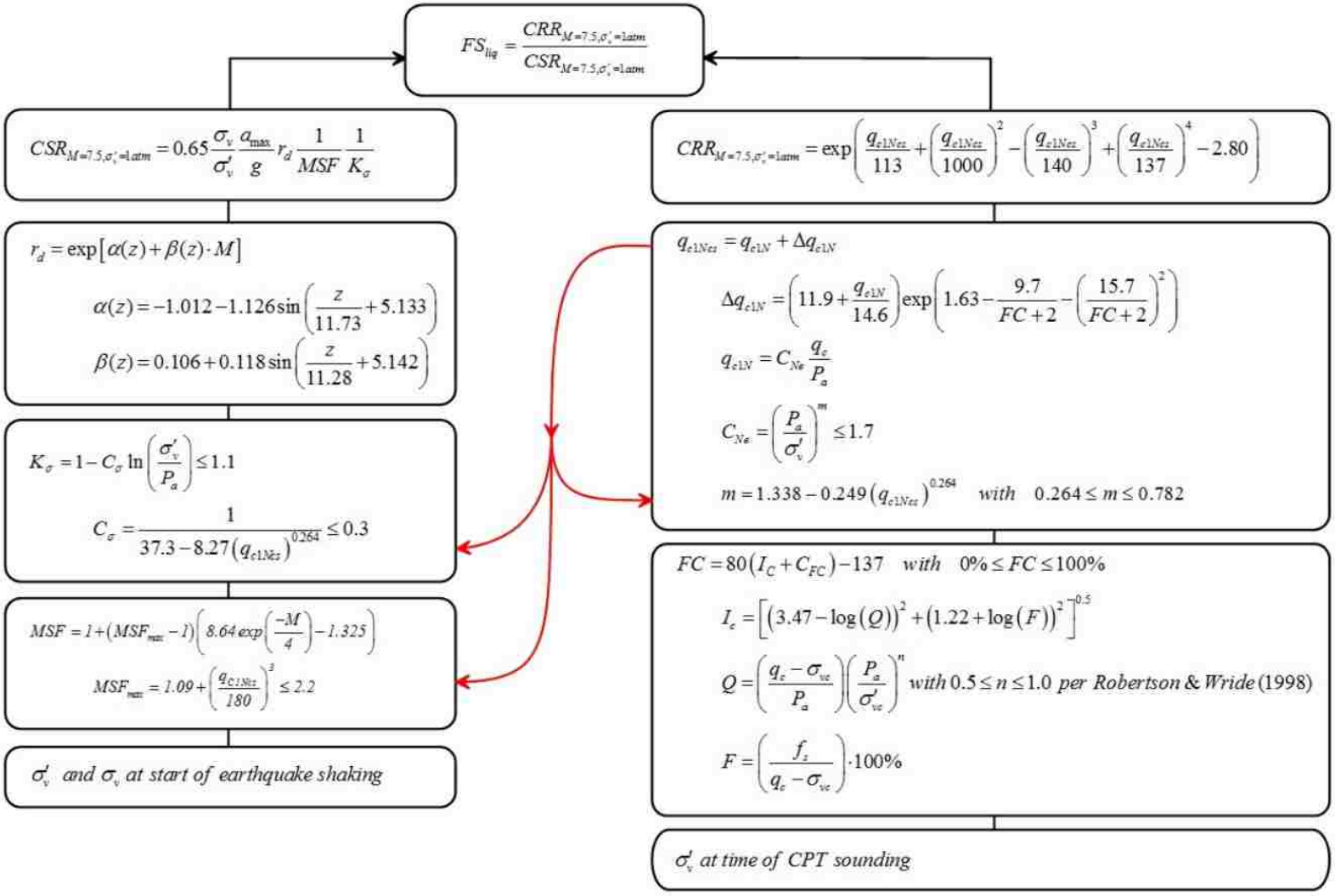

Figure 3-16: Procedure for determining CRR using the Idriss and Boulanger (2016) procedure.

With q_{c1n} being a function of the later calculated q_{c1ncs}, this procedure is iterative, similar to the Robertson and Wride procedure. To first calculate m, a seed value for q_{c1ncs} is needed. Once the seed value is entered, the calculation is repeated until the change in q_{c1ncs} is less than 0.5. The calculation of q_{c1ncs} is shown in Equations 3-18 and 3-19:

$$q_{c1Ncs} = q_{c1N} + \Delta q_{c1N} \tag{3-18}$$

$$\Delta q_{c1N} = \left(11.9 + \frac{q_{c1N}}{14.6}\right)\exp\left(1.63 - \frac{9.7}{FC+2} - \left(\frac{15.7}{FC+2}\right)^2\right) \tag{3-19}$$

where FC is percent fines content.

As the fines content is not specifically measured by the CPT, a correlation has to be made. It is suggested that a correlation be used from the I_c (soil behavior type index). The correlation developed by Boulanger and Idriss is shown in Equation 3-20:

$$FC = 80(I_c + C_{FC}) - 137 \tag{3-20}$$

where FC ranges from 0 to 100%. C_{FC} is a fitting parameter that can be adjusted based on site-specific data when available. C_{FC} can be used to minimize uncertainty when more data are available, which is important because Boulanger and Idriss suggest caution when using this correlation of FC because of data scatter. Figure 3-17 shows the relationship between Ic and FC, with the associated scatter.

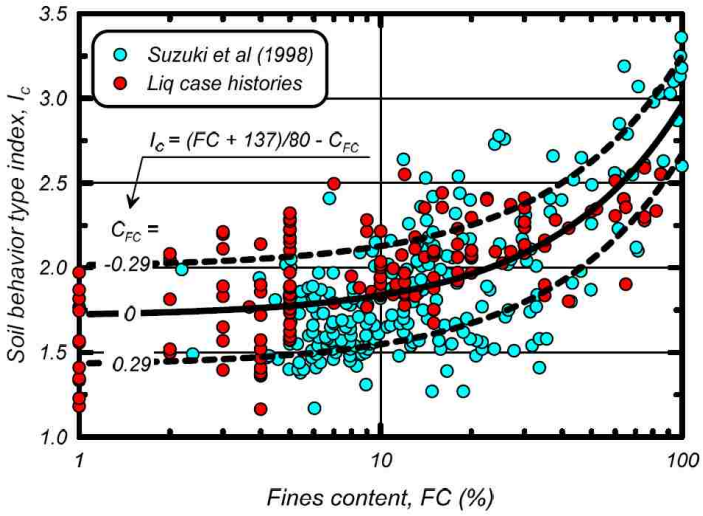

Figure 3-17: Recommended correlation between *FC* and I_c with plus or minus one standard deviation (after Boulanger and Idriss, 2016).

Once all of the previously mentioned calculations are complete, the value of q_{c1ncs} is known, and the *CRR* can be calculated. Similar to the Robertson and Wride procedure, in the Boulanger and Idriss procedure the *CRR* is solely a function of the q_{c1ncs}, as shown in Equation 3-21:

$$CRR_{M=7.5,\ \sigma'_{vo}=1atm} = \exp\left(\frac{q_{c1Ncs}}{113} + \left(\frac{q_{c1Ncs}}{1000}\right)^2 - \left(\frac{q_{c1Ncs}}{140}\right)^3 + \left(\frac{q_{c1Ncs}}{137}\right)^4 - 2.8\right) \qquad (3\text{-}21)$$

As with the Robertson and Wride procedure, with the *CRR* calculated, the *CSR* must be determined to calculate the FS_L. The Boulanger and Idriss procedure also calculates the *CSR* as previously outlined in Equation 3-2, with slight differences from the Robertson and Wride procedure in the determination of the *MSF*, r_d, and K_σ values.

The determination of the *MSF* in the Boulanger and Idriss procedure has gone through multiple changes the relationship presented by Boulanger and Idriss (2016) was developed, as shown in Equations 3-22 and 3-23:

$$MSF = 1 + \left(MSF_{\max} - 1\right)\left(8.64\exp\left(\frac{-M}{4}\right) - 1.325\right) \tag{3-22}$$

$$MSF_{\max} = 1.09 + \left(\frac{q_{c1Ncs}}{180}\right)^3 \leq 2.2 \tag{3-23}$$

where *M* is the moment magnitude of the given earthquake. Using this relationship, the soil is characterized using the corrected cone tip resistance, rather than defining it more broadly as was done in previous *MSF* relationships (Idriss and Boulanger, 2008).

In the Boulanger and Idriss procedure, the depth-dependent shear stress reduction factor, r_d, is calculated following Equations 3-24, 3-25, and 3-26 developed by Golesorkhi (1989):

$$r_d = \exp[\alpha(z) + \beta(z) * M] \tag{3-24}$$

$$\alpha(\mathrm{z}) = -1.012 - 1.126\sin\left(\frac{z}{11.73} + 5.133\right) \tag{3-25}$$

$$\beta(z) = 0.106 + 0.118\sin\left(\frac{z}{11.28} + 5.142\right) \tag{3-26}$$

where M is the moment magnitude of the given earthquake and z is the depth to the desired soil increment in meters.

The overburden correction factor, K_σ, as calculated in the Boulanger and Idriss procedure follows the correlation developed by Boulanger (2003), as shown in Equation 3-27:

$$K_\sigma = 1 - C_\sigma \ln\left(\frac{\sigma'_{vo}}{p_a}\right) \leq 1.1 \tag{3-27}$$

where σ'_{vo} is the effective vertical stress and p_a is the atmospheric pressure. The C_σ coefficient is a function of q_{c1ncs}, as shown in Equation 3-28:

$$C_\sigma = \frac{1}{37.3 - 8.27\left(q_{c1Ncs}\right)^{0.264}} \leq 0.3 \tag{3-28}$$

With all variables known, the *CSR* can be determined. With the *CSR* and *CRR* values calculated, the FS_L for the Boulanger and Idriss procedure can be calculated following Equation 3-1, just as was done in the Robertson and Wride procedure. Figure 3-18 shows the deterministic liquefaction triggering curve for Boulanger and Idriss (2016) (with the *CRR* line indicated as "This study" in Figure 3-18).

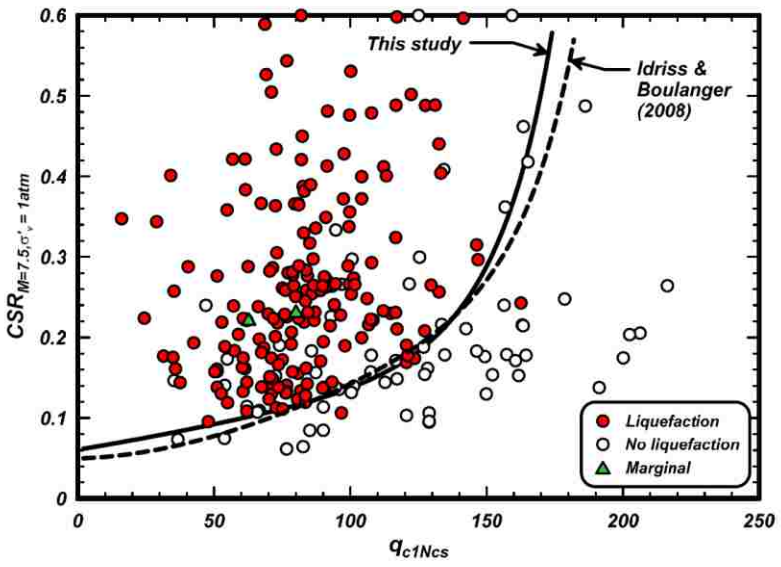

Figure 3-18: Deterministic liquefaction triggering *CRR* curves plotted with the case histories (after Boulanger and Idriss, 2016).

3.5.4 Probabilistic CPT-Based Evaluation of Liquefaction Initiation (Boulanger and Idriss, 2016)

Along with the deterministic liquefaction triggering procedure, Boulanger and Idriss (2016) also outlines a probabilistic procedure. Similar to the Ku et al. (2012) procedure, this probabilistic procedure uses the case history database from the corresponding deterministic procedure to estimate the probability of liquefaction, P_L. However, unlike the Ku et al. probabilistic procedure, the Boulanger and Idriss probabilistic procedure does not provide a relationship between P_L and FS_L. Rather, the Boulanger and Idriss probabilistic procedure provides a relationship between P_L, q_{c1Ncs}, and CSR, as shown in Equation 3-29:

$$P_L = \Phi\left[-\frac{\frac{q_{c1Ncs}}{113}+\left(\frac{q_{c1Ncs}}{1000}\right)^2-\left(\frac{q_{c1Ncs}}{140}\right)^3+\left(\frac{q_{c1Ncs}}{137}\right)^4-2.60-\ln\left(CSR_{M=7.5,\sigma'_v=1atm}\right)}{\sigma_{\ln(R)}}\right] \quad (3\text{-}29)$$

where Φ is the cumulative distribution function, q_{c1Ncs} is the corrected cone tip resistance, $CSR_{M=7.5,\ \sigma'v=1atm}$ is the corrected *CSR* value for standardized magnitude and overburden pressure, and $\sigma_{ln(R)}$ is the model-based uncertainty. It should be noted that the uncertainty that is inherent in the input parameters (q_{c1Ncs} and $CSR_{M=7.5,\ \sigma'v=1atm}$) is greater than the model uncertainty accounted for in this relationship. For this reason, further treatment of these uncertainties needs to be addressed (Boulanger and Idriss, 2016).

As with the Ku et al. procedure, the P_L can be plotted as a curve showing the relationship between q_{c1Ncs} and *CSR* for the Boulanger and Idriss probabilistic procedure, as shown in Figure 3-19. For this procedure, the deterministic curve is approximately equal to a P_L of 0.16.

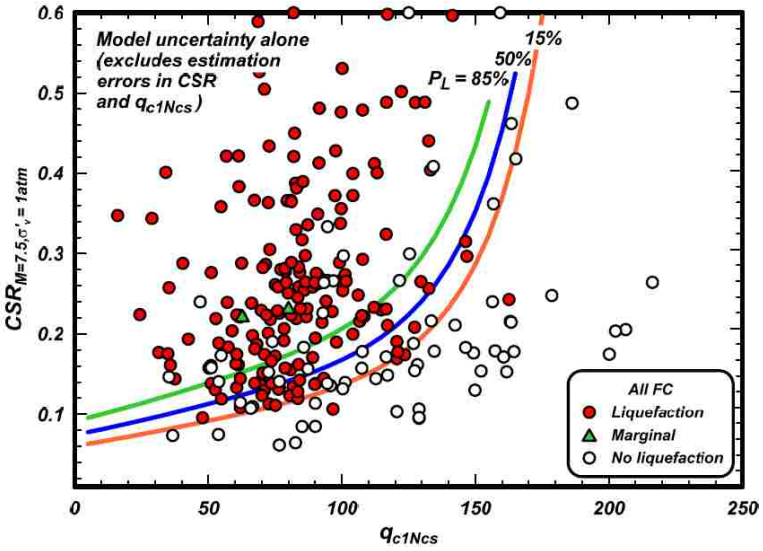

Figure 3-19: Probabilistic liquefaction triggering curves at various levels, determined by the Boulanger and Idriss probabilistic procedure (after Boulanger and Idriss, 2016).

3.6 Liquefaction Effects

Once it is determined that liquefaction will be initiated, the possible liquefaction effects must be evaluated. The effects of liquefaction are what concern engineers, since the effects are the cause of damage to infrastructure such as roads, bridges, buildings, utilities, ports, etc. There are multiple effects of liquefaction. A few common effects that are discussed in this section are lateral spread, settlement, loss of bearing capacity, increased lateral pressure on walls, alteration of ground motions, and flow failures.

3.6.1 Lateral Spread

Lateral spreading is one of the biggest concerns when it comes to liquefaction; as such, it is the main focus of this study and is discussed in more detail in Chapter 4. Lateral spread displacements occur as a shear plane develops in a subsurface layer of liquefied soil. This plane causes blocks of soil above to be displaced down a gentle slope or toward a free face. The movement of the surficial soil layers can range from a few centimeters to multiple meters. Lateral spreading can cause extensive damage to infrastructure near shore lines such as ports and piers, as well as ground along slopes and near river banks. Figure 3-20 shows a small example of lateral spreading that occurred along a shoreline in Washington after the Nisqually earthquake in 2001.

Figure 3-20: Example of lateral spread displacements causing cracking of pavement after an earthquake that occurred in Olympia, WA, in 2001 (after Bray et al. (2001)).

3.6.2 Settlement

A common result of liquefaction is the densification of loose, saturated sands. As pore pressures increase, the water between sand particles is forced upward, and soil particles take its place in the voids. As the soil fills the void space, the soil densifies, and in turn causes settlement at the ground surface. This settlement (specifically differential settlement) can sever utilities and cause damage to building foundations. Liquefaction-induced settlement has a large economic impact on the area affected by an earthquake.

3.6.3 Loss of Bearing Capacity

Loss of bearing capacity was exhibited many times in the Niigata 1964 earthquake, which sparked the study of liquefaction. As depicted in Figure 3-21, the overturned apartment buildings in Niigata are a famous representation of loss of bearing capacity due to liquefaction. As the soil

loses shear strength during liquefaction, it can lose its resistance to the vertical pressure applied by a building. When this resistance is lost, a global bearing capacity failure can occur.

Figure 3-21: Example of a loss of bearing capacity failure causing apartment buildings to collapse in Niigata, Japan, after the 1964 earthquake (after Kramer (1996)).

3.6.4 Increased Lateral Pressure on Walls

As liquefaction occurs, there is a rapid increase in pore water pressure that is manifested as the ground water rises toward the surface. As the ground water rises, it has a detrimental effect on soil already applying lateral pressure to retaining walls. As the backfill soil liquefies and the pore pressure increases, the static lateral pressure increases, which, combined with earthquake motion, can lead to failure of the wall.

3.6.5 Alteration of Ground Motions

Ground motion alteration is caused during seismic loading after a soil has begun to liquefy. As the soil liquefies, its stiffness decreases, and the loose soil alters ground motions such as the

amplitude and frequency of the earthquake loading. This alteration of ground motions allows for only low-frequency waves to reach the surface. The low-frequency waves can result in large, rolling displacements that can be especially destructive to soft structures with low natural frequencies.

3.6.6 Flow Failures

As mentioned previously, two types of liquefaction can occur, including cyclic mobility and flow liquefaction. Flow failures are more dangerous than the other discussed liquefaction effects since they occur rapidly, have large displacements, and occur with little to no warning. The majority of flow failures occur on sloping ground with an existing static shear stress providing a driving force for failure. Once a flow failure is initiated, large masses of fluid-like soil will move, or flow, downslope until reaching equilibrium. With speeds up to a few meters per second, this movement can destroy structures in its path and deposit large volumes of soil downslope.

3.7 Chapter Summary

Liquefaction is the rapid generation of pore water pressure in a loose saturated soil as it is seismically loaded. This phenomenon leads to a loss of shear strength and detrimental effects to surrounding infrastructure. Liquefaction susceptibility is dependent on historical criteria, geologic criteria, compositional criteria, and state criteria. Once a given soil is determined to be susceptible, there are different procedures that can be used to determine if and to what extent liquefaction will be triggered (by calculating the FS_L or the P_L). Using results from the CPT, Robertson and Wride (1998) and Boulanger and Idriss (2016) outline deterministic liquefaction triggering procedures using the CPT, and Ku et al. (2012) and Boulanger and Idriss (2016)

outline their corresponding probabilistic liquefaction triggering procedures. The effects of liquefaction are what truly concern engineers since these effects are what cause damage to infrastructure and lifelines. Some of these effects include lateral spreading, settlement, loss of bearing capacity, increased lateral pressure on walls, and alteration of ground motions.

4 LATERAL SPREAD

4.1 Introduction

Lateral spreading refers to permanent horizontal deformations at the ground surface that occur during an earthquake. These deformations commonly occur at sites located on sloping ground or on level ground near a free face. Lateral spreading is initiated by seismically-induced soil liquefaction at shallow depths. The horizontal deformations can vary in size, ranging from a few millimeters to several meters in some cases. These deformations are dependent on the soil properties, site geometry, and seismic loading. Lateral spreading is most commonly seen near rivers and open bodies of water; therefore, it imposes particular risk on adjacent structures such as buildings, bridges, ports, etc.

This chapter provides a review of lateral spread displacements and the theory behind their occurrence. Historical examples and experimental studies are discussed, as well as methods of estimating lateral spread displacements. Emphasis is made on the Zhang et al. (2004) procedure for predicting lateral spread displacements, as it is used in the comparative study found in Chapter 6.

4.2 Understanding Lateral Spread Displacement

As mentioned previously, lateral spread displacements occur at sites with gently sloping ground and at sites with level ground near a free face, or a combination of the two. For lateral

spreading to occur, the soil must first liquefy. Liquefaction occurs in a layer of soil at or below the ground surface, which then causes horizontal displacements in all soil above the liquefied layer. This liquefaction occurs in the form of cyclic mobility, which causes blocks of soil in the more shallow soil layers to displace down the slope or toward the free face. The magnitude of these displacements is largely dependent upon the thickness and stiffness of the liquefiable layer, the geometry of the site, and the intensity and duration of the accelerations at the ground surface from the seismic loading (Zhang et al., 2004).

When lateral spreading occurs, it causes extensive damage and has major economic impacts. While lateral spreading does not cause immediate life-threatening danger due to its relatively slow nature, it can be a danger to the lives of people nearby as the displacements could sever important lifelines such as power and water. Most damage caused by lateral spreading occurs near rivers and bodies of water, since these sites have the typical geometry that is needed for lateral spreading and high amounts of saturation needed for liquefaction. Therefore, it is common for infrastructure such as bridges and ports to be damaged by lateral spread displacements. Figure 4-1 shows an example of where lateral spreading can push foundations out

Figure 4-1: Example of lateral spread displacements causing bridge spans of the Showa Bridge in Niigata, Japan, to lose support and collapse in after the 1964 earthquake (after Bhattacharya et al. (2014)).

of place to the point where the bridge spans lose support and collapse. Figure 4-2 shows an example of the damage that lateral spreading can cause to a pier.

Figure 4-2: Example of lateral spread displacements causing fissures along a port in Haiti after the 2010 earthquake (after Eberhard et al. (2013)).

4.2.1 Historical Examples of Lateral Spread Displacements

To better understand lateral spread displacements, different examples of the phenomenon have been observed and studied. The main sources of information are historical case studies. In the 1906 San Francisco earthquake, seismic forces caused major damage to structures throughout the city. The infamous fires that ravaged the city in the aftermath of the San Francisco earthquake were ultimately caused by lateral spreading and liquefaction-induced settlement that sheared water lines, preventing firefighters from controlling the fires as they spread throughout the city (Youd and Hoose, 1978). In 1964, the earthquake in Prince William Sound triggered

lateral spreading that damaged multiple ports and facilities along the coast (Coulter and Migliaccio, 1966). Also in 1964, Niigata, Japan, was struck by an earthquake that resulted in large lateral spread displacements due to liquefiable river channel deposits. These displacements in Niigata, Japan, were most notable along the banks of the Shinano River as they moved the soil multiple meters toward the water, which caused major damage to infrastructure such as bridges (Hamada et al., 1986). The 1995 earthquake in Kobe, Japan, caused large displacements in port facilities, misaligning train rails and displacing quay walls. The result of the lateral spreading and other liquefaction-induced effects caused the 1995 Kobe earthquake to be one of the most expensive natural disasters in history. These examples, and many more, have helped increase understanding of lateral spreading.

4.2.2 Experimental Studies of Lateral Spread Displacements

To further understand the mechanics of lateral spread displacements, researchers have developed methods to simulate liquefaction and its effects in the laboratory. As the mechanics behind lateral spreading are very complicated, each of these experiments only shed light on small aspects of this effect of soil liquefaction. However, the information from these experiments is very valuable. Different types of experiments have been run, such as shake table testing, centrifuge testing, and other small-scale tests.

Shake tables have been used to study earthquake engineering for over 60 years. Shake tables can range in size, but for testing of lateral spread displacements a table as large as 6 m in length is used. To perform a test, the specimen is placed on the table (with the desired site geometry and soil strata), and the table is vibrated to simulate the acceleration of the ground during an earthquake. Miyajima et al. (1991) performed shake table testing of lateral spread displacements using multiple slope angles and varying soil thicknesses. The result of the testing

by Miyajima et al. (1991) was the understanding that the magnitude of the surface displacements is closely correlated to the thickness of the liquefied sand layer and the slope angle. Another shake table experiment was performed by Sasaki et al. (1991), which used multiple soil layers (dense sand on bottom, loose sand in the middle, and gravel on top). The results of the testing performed by Sasaki et al. (1991) indicated that the largest displacements occurred near the bottom of the liquefied layer and that the displacements were only observed as the table was shaking.

Centrifuge testing of soil liquefaction has been performed since the 1970s and is accomplished by simulating gravity-induced stresses in soil through centrifugal loading. While this procedure is advantageous in its ability to use small models, scaling effects cause potential limitations. In the 1990s, multiple institutions collaborated to perform centrifuge-based liquefaction testing in a study known as the Verification of Liquefaction Analysis by Centrifuge Studies (VELACS). One of the nine configurations in the VELACS was used to study lateral spread displacements. This configuration led to the understanding that the lateral spread displacements correlated more with the geometry and composition of the soil than they did with the loading conditions (Popescu and Prevost, 1995). In 1998, Taboada-Urtuzuastegui and Dobry (1998) performed 11 centrifuge tests to specifically study lateral spread displacements (not just liquefaction in general). These 11 tests led to the conclusion that, as the slope increases, the pore pressures decreased or remained constant, and shear strain and displacements increased. It was also concluded that, as the accelerations increased, the displacements increased; however, as the frequency increased, the displacements decreased. A final conclusion made by Taboada-Urtuzuastegui and Dobry (1998) was that the downward spikes in pore pressures corresponded to acceleration spikes and strain deformations.

Small-scale laboratory tests have been performed such as torsional tests (Shamoto et al., 1997; Yasuda et al., 1994), undrained triaxial tests (Nagase, 1997), and undrained cyclic direct simple shear tests (Wu, 2002). These tests confirmed many of the conclusions previously discussed using shake table and centrifuge testing. Wu (2002) presented results showing how the direction of loading in some samples may have an effect on the behavior of the soils. When loaded in one direction, the sample may experience cyclic mobility, while loaded in another direction the sample may experience flow liquefaction. Wu (2002) concluded that the directivity of the earthquake ground motions has an effect on the behavior of the liquefied soil and the resulting lateral spread displacements.

4.3 Estimating Lateral Spread Displacements

By combining the knowledge gained from historical examples as well as experimental studies, different methods have been developed to estimate the extent of lateral spread displacements at a given site. There are two main categories of procedures used in industry today to estimate lateral spread displacements, analytical methods and empirical methods.

4.3.1 Analytical Methods

Analytical methods are developed using an understanding of soil mechanics and behavior. Analytical methods usually involve closed-form mathematical solutions. A few common analytical methods include finite element analysis, elastic beam model, and Newmark sliding block analysis.

Finite element analysis is a type of numerical model that is accomplished by viewing the soil profile as a two- or three-dimensional mesh. The strains are calculated iteratively at each of the nodes and/or elements of the mesh, and the resulting lateral spread displacement can be

determined. This type of analysis allows for complex scenarios of complicated geometries and pore pressure distributions. To perform a finite element analysis, a complex model must be used in a finite element computer program. As this analysis method relies heavily on computer calculations, it was not until the late 1970s that finite element models were developed and implemented (Finn et al., 1986; Shiomi et al., 1987; Zienkiewicz et al., 1978; Zienkiewicz and Shiomi, 1984). More recent finite element models are available (Gu et al., 1994; Valsamis et al., 2010; Yang, 2000; Yang et al., 2003; Zhang and Wang, 2012), and, with advancing technology, more models are being created and refined.

The elastic beam model was first proposed by Hamada et al. (1987) and was further developed by researchers in the 1990s (Towhata et al., 1992; Towhata et al., 1991; Yasuda et al., 1990). This model makes the assumption that the liquefied soil acts as a fluid and the surficial soil layers act as a board or an elastic beam floating on the fluid. With the assumption that there is no friction between the two bodies, the movement of the elastic beam is controlled by gravity and the boundary conditions of the site. Very little additional research has been performed on this analytical method.

The Newmark Sliding Block Analysis was first proposed by Newmark (1965). This analysis method considers a block on a sliding plane being held in place by frictional forces. With enough external force, the block will overcome the friction and slide down the plane. This method was originally introduced in earthquake engineering to analyze seismic slope stability but has also been incorporated into the analysis of lateral spread displacements (Baziar et al., 1992; Byrne, 1991; Byrne et al., 1992; Dobry and Baziar, 1990; Taboada et al., 1996). Some more recent semi-empirical models have been developed to predict seismic slope displacements

(Bray and Travasarou, 2007; Saygili and Rathje, 2008) and have also been applied to predict lateral spread displacements.

4.3.2 Empirical Methods

Empirical methods use large databases of earthquake case histories to create a predictive relationship. These relationships are developed using a statistical procedure known as a multi-linear regression. Unlike analytical methods, empirical methods do not directly account for any specific soil behavior or mechanics. While there is some error inherent in these predictive models, as they are based on actual earthquake events, they are widely used in the engineering industry. Caution must be taken when using empirical methods to ensure that the predictive relationships are being used within the recommended range. Extrapolation of an empirical model can lead to large amounts of error.

While there are some limitations to empirical methods, they are almost universally used because they are reliable, easy to understand, and easy to use and incorporate into engineering software. Multiple empirical predictive relationships have been created over the years; some common relationships recognized in industry today are Youd et al. (2002), Bardet et al. (2002), Baska (2002), and Zhang et al. (2004). This study focuses on the Zhang et al. (2004) procedure, as it is the most common procedure for predicting lateral spread displacements using the CPT.

4.3.3 Zhang et al. Procedure

The predictive relationships for lateral spread displacements as laid out by Zhang et al. (2004) are the first that incorporate both SPT and CPT case histories. The equations were developed using 13 earthquake case histories throughout the western continental United States, Alaska, and Japan, with test results from 150 SPTs and 41 CPTs. With far fewer case histories

for the CPT, caution must be taken as to not extrapolate outside the bounds of the data. While this procedure primarily uses case histories, it is considered semi-empirical as it also incorporates soil mechanics in the determination of the shear strain of the soil. With a CPT sounding of tip resistance, sleeve friction, and pore pressure with depth, an estimate of lateral spread displacements at any site can be made using this procedure.

The following procedure is for a deterministic analysis; the application to different probabilistic analyses are discussed in Chapter 5. To begin the calculation, an estimate of relative density (D_r) must be made for every soil increment. Zhang et al. (2004) uses the relationship presented by Tatsuoka et al. (1990) to determine D_r as shown in Equation 4-1:

$$D_r = -85 + 76\log(q_{c1N}) \tag{4-1}$$

where q_{c1N} is the corrected cone tip resistance. In the Robertson and Wride (1998) liquefaction triggering procedure, this value is referred to as Q_{tn}, while in the Boulanger and Idriss (2016) liquefaction triggering procedure this value is simply q_{c1N}.

With a known value of D_r as well as the FS_L from the liquefaction triggering procedure, the maximum cyclic shear strain (γ_{max}) can be determined. This is done using the plot shown in Figure 4-3, which presents the relationship between maximum cyclic shear strain and factor of safety for different relative densities. These curves are based on data from Ishihara and Yoshimine (1992) and Seed (1979).

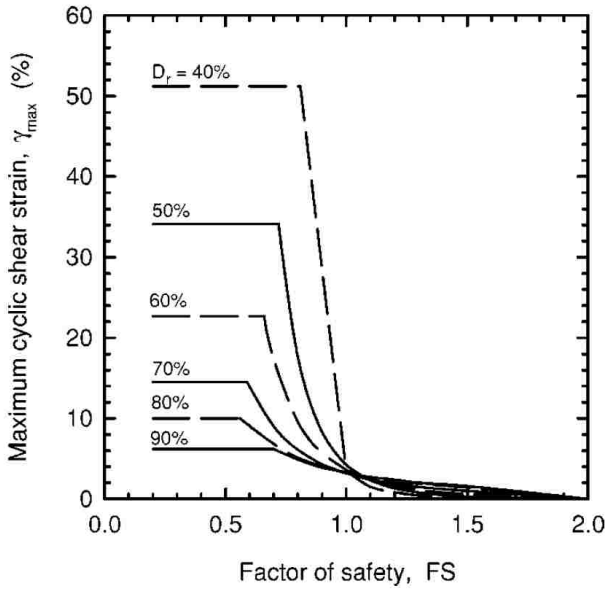

Figure 4-3: The relationship between maximum cyclic shear strain and factor of safety for different relative densities (after Zhang et al. (2004)).

With values of γ_{max} known for each soil increment, the lateral displacement index (*LDI*) is then calculated. The *LDI* is a measure of displacement independent from site geometry; it provides an index to quantify potential lateral spread displacements for a given soil profile, soil properties, and earthquake characteristics. As such, the actual value of the lateral displacement (*LD*) is a function of *LDI* and the site geometry. The *LDI* is calculated by integrating γ_{max} with depth, as presented in Equation 4-2:

$$LDI = \int_0^{Z_{max}} \gamma_{max} dz \tag{4-2}$$

where Z_{max} is the maximum depth below all the potential liquefiable layers with an FS_L less than 2.0.

As mentioned, the *LD* is a function of both *LDI* and the site geometry. There are three types of site geometries considered: (1) gently sloping ground, (2) level ground near a free face, and (3) gently sloping ground near a free face. For sites with gently sloping ground, *LD* is calculated using Equation 4-3:

$$LD = (S + 0.2) \cdot LDI \qquad (for\ \ 0.2\% < S < 3.5\%) \tag{4-3}$$

where *S* is the ground slope measure in percent. For sites with level ground near a free face, *LD* is calculated using Equation 4-4:

$$LD = 6 \cdot (L / H)^{-0.8} \cdot LDI \qquad (for\ \ 4 < L / H < 40) \tag{4-4}$$

where *L* is the distance to the free face and *H* is the height of the free face. The units of both *L* and *H* are irrelevant as a ratio is used in the equation. However, the same units must be used for *L* and *H* to not cause an error; meters are commonly used for consistency. For sites with gently sloping ground near a free face, Equation 4-4 is used because the data points for gently sloping ground with a free face lie generally within the scatter of the results for nearly level ground with a free face (Zhang et al, 2004). Once *LD* is calculated, this value is the final result for the lateral spread displacement at the ground surface of the site in question.

4.4 Chapter Summary

Liquefaction-induced lateral spread displacements cause major damage to infrastructure throughout the world. These damages may not be directly life-threatening, but they have a large

economic impact on communities. Researchers and engineers are constantly working to better understand lateral spreading in order to prepare for future earthquakes. Multiple analytical and empirical procedures have been developed to estimate lateral spreading based on input ground motions and site geometry. This study focuses on the semi-empirical procedure presented by Zhang et al. (2004), which is the first of these procedures to incorporate case histories of CPT data. With this procedure, lateral spread displacements can be estimated and predicted using data from a CPT.

5 INCORPORATING GROUND MOTIONS TO PREDICT LATERAL SPREAD DISPLACEMENTS

5.1 Introduction

To predict the liquefaction-induced lateral spread displacement at a site, the correct ground motions must be selected. With an understanding of the theory and procedures in estimating liquefaction and lateral spread displacements, the process behind selecting proper design ground motions can be discussed. Ground motions are some of the main factors in determining the extent of liquefaction at a site. If the ground motions are incorrectly selected in a design, any resulting structure may not be able to withstand the earthquake shaking. Due to the inherent uncertainty in predicting earthquake events, there is a high level of difficulty when incorporating ground motions to predict lateral spread displacements. This chapter discusses the most common methods for incorporating these ground motions.

To better understand how the different methods of incorporating ground motions are applied to the liquefaction triggering and lateral spread displacement procedures, an example site and soil profile are used to illustrate the differences between methods. This example calculation is performed for a site located in Provo, UT, with a longitude and latitude of 40.2469 and -111.6481, respectively. To help further emphasize the difference in methods, the CPT profile used for the example calculations has a high susceptibility to liquefaction. The corrected cone tip resistance (Q_{tncs}) of the CPT profile is plotted with depth in Figure 5-1. For consistency, all

methods are calculated using the Robertson and Wride liquefaction triggering procedure, and the site has a ground slope of 1%.

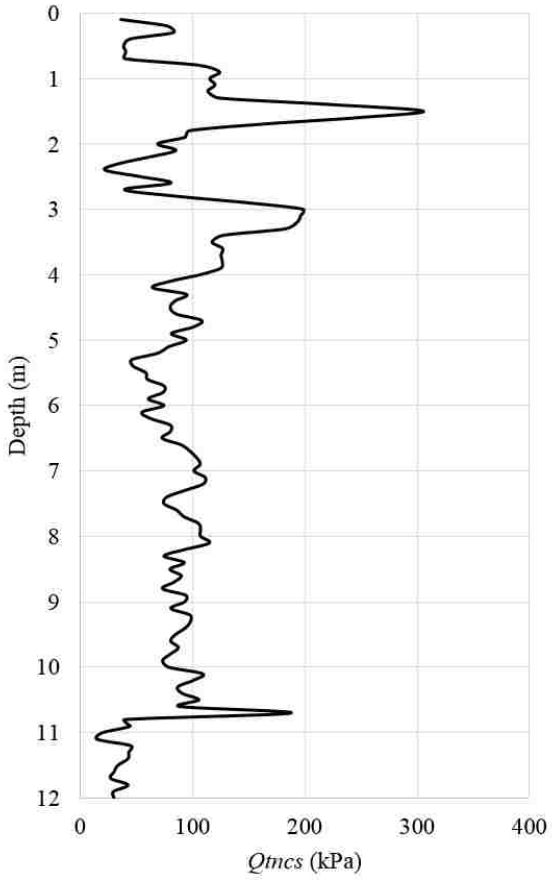

Figure 5-1: Plot of *Qtncs* with depth for example site at Provo, UT.

5.2 Deterministic Method

The original method of incorporating ground motions in a liquefaction hazard analysis is the deterministic method. More information on this method can also be found in Section 2.6.1. The deterministic method uses a single input design earthquake with its corresponding ground motions and magnitude. The chosen ground motions are often the largest that would occur at the

site and result in a conservative estimate of lateral spread displacement. With the chosen earthquake ground motion (a_{max}), and a profile of soil properties (such as Q_{tncs}), the *CRR* and *CSR* can be calculated; these are then used to determine the FS_L (more information on using the liquefaction triggering procedures is found in Section 3.5). The FS_L is then known for each soil increment of the CPT profile, and, with the value of Q_{tncs} for each soil increment known, the lateral spread displacement at the site can be determined (a detailed outline of the Zhang et al. (2004) procedure for estimating lateral spread displacements is presented in Section 4.3.3).

In the calculation example for Provo, UT, using the deterministic method, the design earthquake must first be chosen. For this site, the source chosen for a deterministic analysis would likely be the Wasatch fault. Using the geometry of the fault and the correlations developed by Wells and Coppersmith (1994), an estimated earthquake magnitude of 7.4 is used for the calculation. To calculate the ground motion, the NGA West-2 ground motion prediction database (Ancheta et al., 2014) is used, resulting in an a_{max} of 0.456 g. The magnitude, a_{max}, and the soil parameters from the CPT can then be used to determine the value of FS_L for each soil increment (following the Robertson and Wride liquefaction triggering procedure). With the value of FS_L for each soil increment known, the Zhang et al. (2004) procedure can be used to calculate the lateral spread displacement. For this example, using the deterministic method, the lateral spread displacement is 3.74 m.

5.3 Pseudo-Probabilistic Method

The pseudo-probabilistic method is widely accepted and used by engineers in industry. The pseudo-probabilistic method selects the design ground motion using a PSHA, but applies it to the calculation of lateral spread displacement using a deterministic procedure. Because this method uses probability theory in only part of the calculation, the prefix “pseudo” is used. The ground

motion selection through a PSHA is accomplished using the USGS Unified Hazard Tool (located at https://earthquake.usgs.gov/hazards/interactive/). To determine the magnitude and a_{max}, the PSHA needs an input return period. For the given return period, the PSHA can provide the mean or modal magnitude for a specific site, along with the corresponding a_{max}.

For the calculation example of Provo, UT, using the pseudo-probabilistic method, a return period of 2475 years is used as it represents a large seismic event. Using the 2014 USGS deaggregation, the resulting mean and modal magnitudes for Provo, UT, are 7.05 and 7.09, respectively. For simplicity, the mean magnitude and corresponding a_{max} of 0.650 g is used. Now with the magnitude and a_{max} known, the Robertson and Wride liquefaction triggering procedure can be followed (just as was done in the deterministic method), after which the Zhang et al. (2004) procedure can be used to calculate the lateral spread displacement at the site. The resulting lateral spread displacement for this example, using the pseudo-probabilistic method, is 3.75 m.

The main drawback in using the pseudo-probabilistic method is its neglect of uncertainty in the calculation of liquefaction triggering and lateral spread displacement. By using a PSHA, the pseudo-probabilistic method attempts to account for the inherent uncertainty in the ground motion selection, but this does not compare to the other sources of uncertainty in the seismic hazard analysis. Therefore, the pseudo-probabilistic method assumes that all possible lateral spread displacements are caused by the single return period selected. While the return period selected is associated with the computed ground motions, it does not necessarily apply to the calculated lateral spread displacement. This lack of uncertainty consideration is corrected by the fully-probabilistic method.

5.4 Fully-Probabilistic Method (Performance-Based Earthquake Engineering)

To benefit from the use of a fully-probabilistic method of incorporating ground motions in a seismic hazard analysis, a new seismic hazard design approach has been developed, known as performance-based earthquake engineering (PBEE). This new approach to seismic hazard analysis was developed by the Pacific Earthquake Engineering Research Center (PEER) (Cornell and Krawinkler, 2000; Deierlein et al., 2003). The key benefit to using PBEE is that it seeks to quantify all inherent uncertainty in the prediction of a seismic hazard.

5.4.1 PEER Framework for PBEE

The PEER framework developed for PBEE has the ability to handle a wide range of potential hazards. This framework consists of the following four components:

1. Intensity Measure (*IM*): This represents the ground motion parameter that will be experienced at a site such as a_{max}, PGA, Arias intensity, etc. These values are determined by considering geologic characteristics of the area.
2. Engineering Demand Parameter (*EDP*): This variable represents the response of a system or structure to some *IM*. Some examples of this variable include lateral spread displacement, settlement, or probability of liquefaction.
3. Damage Measure (*DM*): This term describes the resulting effect of the *EDP* to the structure or system and can be things such as size of cracks, structure displacement, or structure collapse.
4. Decision Variable (*DV*): This is a quantifiable value of the risk associated with the *DM*. The *DV* can be values such as cost of repairs, time lost, or number of casualties.

The framework of PBEE follows a process similar to that of PSHA, in that it probabilistically determines the mean annual rate of exceeding some variable. The variables used in PBEE are determined in sequence. For example, the equation to calculate λ_{EDP} is given in Equation 5-1:

$$\lambda_{EDP} = \int P\left[EDP > edp \mid IM = im_j \right] \Delta\lambda_{IM} \tag{5-1}$$

where λ_{EDP} is the mean annual rate of exceeding some *EDP* given some *IM*. Also, $P\left[EDP > edp \mid IM = im_j \right]$ is the probability that some *EDP* will exceed a certain level of *edp*, given that the *IM* is equal to a specific *im*. $\Delta\lambda_{IM}$ represents the incremental mean annual rate of exceedance of the *IM*. This process is then repeated for a range of *edp* values until the total mean annual rate of exceedance of a *DV* (λ_{DV}) is calculated. The complete PBEE framework process is represented in Equation 5-2:

$$\lambda_{DV} = \iiint P\left[DV \mid DM\right] dP\left[DM \mid EDP\right] dP\left[EDP \mid IM\right] d\lambda_{IM} \tag{5-2}$$

Equation 5-2 can be approximated numerically as Equation 5-3:

$$\begin{aligned} \lambda_{DV} = \sum_{k=1}^{N_{DM}} \sum_{j=1}^{N_{EDP}} \sum_{i=1}^{N_{IM}} & P\left[DV > dv \mid DM = dm_k\right] \times \\ & P\left[DM > dm \mid EDP = edp_j \right] \times P\left[EDP > edp \mid IM = im_i\right] \Delta\lambda_{IM} \end{aligned} \tag{5-3}$$

where N_{DM}, N_{EDP}, and N_{IM} are increments of *DM*, *EDP*, and *IM*, respectively. As the number of these increments increases, the accuracy of the calculation is improved. After iterating through a range of values for *DV*, a hazard curve is formed that represents the mean annual rate of exceeding a *DV* (λ_{DV}) for the specified range of *DV* values. An example of one of these hazard curves is shown in Figure 5-2. With this hazard curve, stakeholders (such as engineers, owners, or government officials) can specify a certain value of *DV* (along the x-axis) such as cost, which then corresponds to a specific λ_{DV} (along the y-axis). The λ_{DV} helps engineers understand the level of seismic hazard that needs to be incorporated in the design.

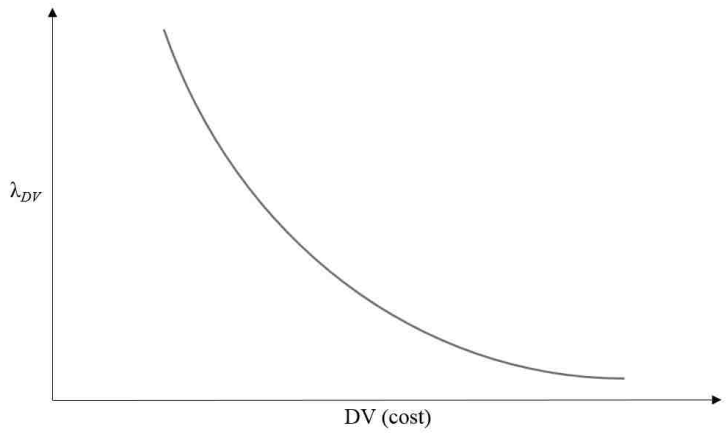

Figure 5-2: Example hazard curve for a specific *DV*.

5.4.2 Performance-Based Liquefaction Triggering Procedure

To incorporate ground motions using a fully-probabilistic method, the framework of PBEE must first be applied to liquefaction triggering, which is done by creating hazard curves for FS_L

using the approach described by Kramer and Mayfield (2007). The framework of PBEE is followed by using FS_L as the *EDP* and the magnitude (M) and a_{max} together as the *IM*. By using FS_L as the *EDP*, it is more appropriate to use an annual rate of *non*-exceedance because, unlike other *EDP* values, a larger FS_L indicates less damage. This relationship is presented in Equation 5-4:

$$\Lambda_{FS_L^*} = \sum_{k=1}^{N_M} \sum_{j=1}^{N_{a_{max}}} P\left[FS_L < FS_L^* \mid a_{max,j}, m_k \right] \Delta\lambda_{a_{max,j}, m_k} \tag{5-4}$$

where $\Lambda_{FS_L^*}$ is the mean annual rate of not exceeding some given FS_L^* value and N_M and Na_{max} are the number of increments for M and a_{max}, respectively. $\Delta\lambda_{a_{max,j}, m_k}$ is the incremental mean annual rate of exceedance for both $a_{max,j}$ and m_{kj}.

A more common way to perform the PBEE liquefaction triggering calculations is to use a value from in-situ testing in place of FS_L. Kramer and Mayfield (2007) do this by using N_{req}, which is the SPT resistance (number of blow counts) required to prevent liquefaction triggering (which is considered to occur when FS_L falls below 1.0). As this study focuses on the CPT, for this process N_{req} is replaced with q_{req}, the cone tip resistance required to prevent liquefaction triggering (Arndt, 2017). The process outlined by Kramer and Mayfield (2007) can be modeled using Equations 5-5 and 5-6:

$$\lambda_{q_{req}^*} = \sum_{k=1}^{N_M} \sum_{j=1}^{N_{a_{max}}} P\left[q_{req} > q_{req}^* \mid a_{max,j}, m_k \right] \Delta\lambda_{a_{max,j}, m_k} \tag{5-5}$$

$$P\left[q_{req} > q_{req}^{*} \mid a_{max,j}, m_k\right] = P_L\left(q_{req}^{*}\right) \tag{5-6}$$

As the previous equation now includes the probability of liquefaction (P_L), this value must be calculated using the liquefaction triggering procedures presented in Section 3.5.2 and 3.5.4. The two procedures outlined in this study are Robertson and Wride (1998) (with its corresponding probabilistic procedure by Ku et al. (2012)) and Boulanger and Idriss (2016) (which includes a deterministic and probabilistic procedure). The Robertson and Wride procedure uses Equation 5-7 to calculate P_L:

$$P_L = 1 - \Phi\left[\frac{0.102 + \ln\left(\frac{CRR}{CSR}\right)}{\sigma_{total}}\right] \tag{5-7}$$

where Φ is the cumulative distribution function and σ_{total} is the parameter- and model-based uncertainty (equal to 0.3537 for the Robertson and Wride procedure). The *CRR* and *CSR* are calculated using the steps laid out in Section 3.5.1 and 3.5.2, but the Q_{tncs} in those steps is replaced with q_{req}^{*}. For the Boulanger and Idriss procedure, P_L is calculated following Equation 5-8:

$$P_L = \Phi\left[-\frac{\frac{q_{c1Ncs}^{*}}{113} + \left(\frac{q_{c1Ncs}^{*}}{1000}\right)^2 - \left(\frac{q_{c1Ncs}^{*}}{140}\right)^3 + \left(\frac{q_{c1Ncs}^{*}}{137}\right)^4 - 2.60 - \ln\left(CSR_{M=7.5,\sigma'_v=1atm}\right)}{\sigma_{total}}\right] \tag{5-8}$$

where σ_{total} is the parameter- and model-based uncertainty (equal to 0.506 for the Boulanger and Idriss procedure), q_{c1Ncs}^{*} is equal to q_{req}^{*}, and $CSR_{M=7.5,\sigma'_v=1atm}$ is calculated following the steps laid out in Section 3.5.4.

To complete the PBEE analysis, Equation 5-5 must be repeated for a wide range of q_{req}^{*} values for the selected liquefaction triggering procedure. After this is done, the result is a range of $\lambda_{q_{req}^{*}}$ with corresponding values of q_{req}^{*}, developing a q_{req} hazard curve. To acquire a hazard curve of FS_L, a conversion must be made from q_{req} to FS_L. A conversion is provided by Kramer and Mayfield (2007), except that the N value has been replaced with a q (changing the relationship from using the SPT to the CPT) as shown in Equation 5-9:

$$FS_L^{site} = \frac{CRR}{CSR} = \frac{CRR\left(q^{site}\right)}{CSR\left(q_{req}^{site}\right)} \tag{5-9}$$

where q^{site} is the measured CPT cone tip resistance at the site and q_{req}^{site} is the calculated cone tip resistance required to resist liquefaction at the site. This equation converts the q_{req} hazard curve to a FS_L hazard curve. The conversion will automatically change the annual rate of exceeding q_{req}^{*} ($\lambda_{q_{req}^{*}}$) to the annual rate of not exceeding FS_L^{*} ($\Lambda_{FS_L^{*}}$). The resulting hazard curve of FS_L corresponds to one soil increment of the CPT profile, and this process is then repeated for each soil increment.

In the calculation example for Provo, UT, using the fully-probabilistic method, the FS_L must first be calculated for each soil increment using the PBEE framework. As with the pseudo-probabilistic method, for this example a return period of 2475 years is used. Each soil increment has its own FS_L hazard curve, like the one shown in Figure 5-4. Each of these hazard curves can be used to plot the FS_L with depth for the entire soil profile (at a given return period). For the calculation example of Provo, UT, using the fully-probabilistic method, the values of FS_L with depth are shown in Figure 5-3.

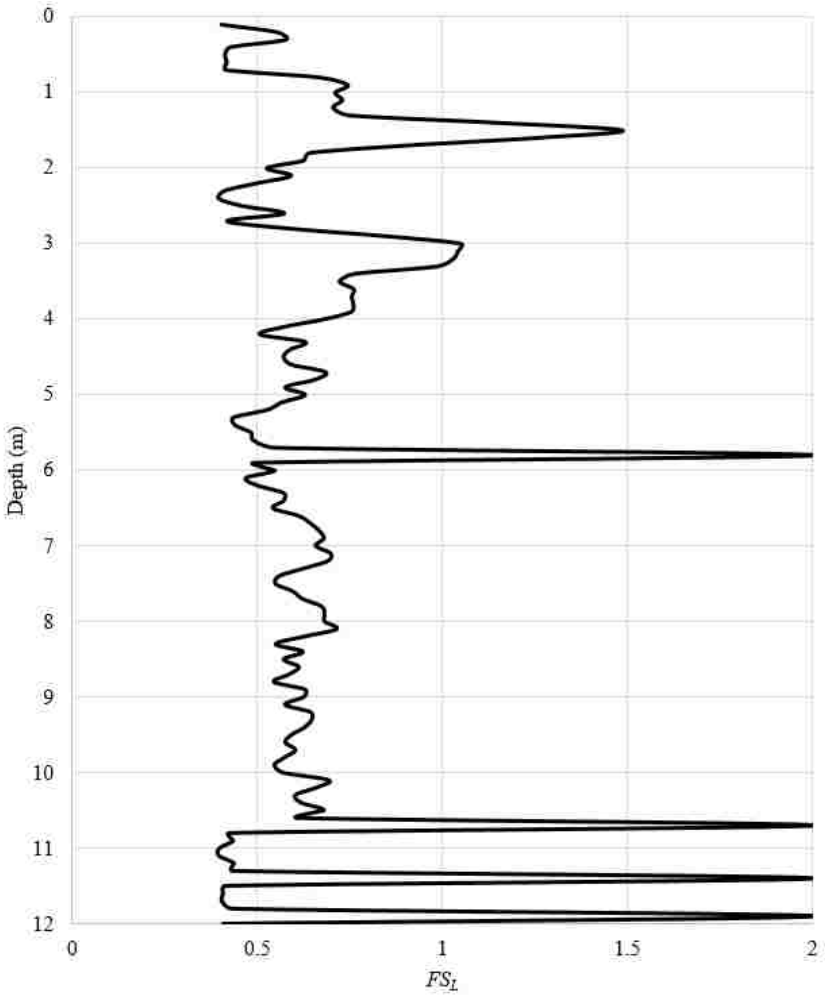

Figure 5-3: Plot of FS_L with depth for example site at Provo, UT, using the fully-probabilistic method at the 2475-year return period.

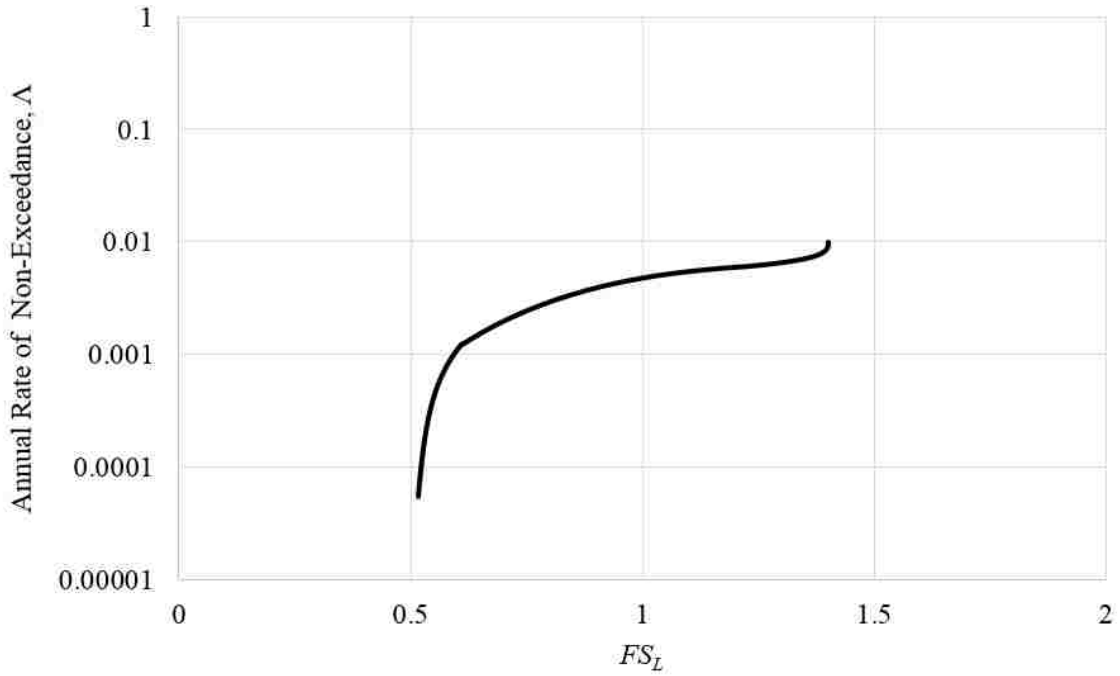

Figure 5-4: FS_L hazard curve for soil increment located at a depth of 6 m for example site in Provo, UT.

5.4.3 Performance-Based Lateral Spread Procedure

With the fully-probabilistic method complete for liquefaction triggering, this method can now be applied to the estimation of lateral spread displacements using the PBEE framework. The next step, which is the focus of this study, is the development of a fully-probabilistic procedure for predicting lateral spread displacements. The unique aspect of this developed method is that it is the only one of its kind using input values from the CPT. The following steps use the Zhang et al. (2004) procedure and may differ slightly if using a different lateral spread displacement procedure. The first step is to create hazard curves of maximum cyclic shear strain (γ_{max}) for each soil increment using Equation 5-10:

$$\lambda_{\gamma_{max^*}} = \sum_{j=1}^{N_{FS_L}} P\left[\overline{\gamma_{max}} > \gamma_{max^*} \mid q_{c1Ncs_i}, FS_{L_j}\right] \Delta\lambda_{FS_{L_j}} \tag{5-10}$$

where $\lambda_{\gamma_{max^*}}$ is the mean annual rate of exceeding a specified strain value, γ_{max^*}, $\overline{\gamma_{max}}$ is the calculated strain using the Zhang et al. (2004) procedure multiplied by the probability of liquefaction (P_L), N_{FS_L} is the number of FS_L increments in the soil layer's FS_L hazard curve, q_{c1Ncs} is the soil layer's corrected cone tip resistance, $\Delta\lambda_{FS_{L_j}}$ is the incremental mean annual rate of exceedance of FS_L, and $P\left[\overline{\gamma_{max}} > \gamma_{max^*} \mid q_{c1Ncs_i}, FS_{L_j}\right]$ is the probability that the calculated strain ($\overline{\gamma_{max}}$) will exceed the specified strain (γ_{max^*}). The probability function can be calculated with Equation 5-11:

$$P\left[\overline{\gamma_{max}} > \gamma_{max^*} \mid q_{c1Ncs_i}, FS_{L_j}\right] = \Phi\left[\frac{\ln\left(\overline{\gamma_{max}}\right) - \ln\left(\gamma_{max^*}\right)}{\sigma_{\ln(\gamma_{max})}}\right] \tag{5-11}$$

where $\sigma_{\ln(\gamma_{max})}$ represents the model-based uncertainty for the Zhang et al. (2004) procedure.

As the Zhang et al. (2004) procedure does not explicitly state its level of uncertainty, this value was calculated from the reported prediction residuals by Zhang et al. (2004). While the uncertainty was computed using values of displacement, it is also applicable to the strain values used in this performance-based procedure as there is a direct linear relationship between strain and displacement. This calculation was done separately for the three different types of site geometries, resulting in $\sigma_{\ln(\gamma_{max})}$ values of 0.473 for a site with gently sloping ground, 0.460 for a

site with level ground near a free face, and 0.560 for a site with gently sloping ground near a free face.

The process outlined in Equations 5-10 and 5-11 is repeated for a range of γ_{max^*} values (this study used a range of 0 to 60%). With this complete, all of the γ_{max^*} values and corresponding $\lambda_{\gamma_{max^*}}$ values create a hazard curve of strain for each depth of soil where CPT data are recorded. This step is then repeated for each soil depth until there is a hazard curve of strain for each increment in the CPT profile. For the calculation example of Provo, UT, one hazard curve of γ_{max^*} for a single soil increment (located at a depth of 6 m) is shown in Figure 5-5.

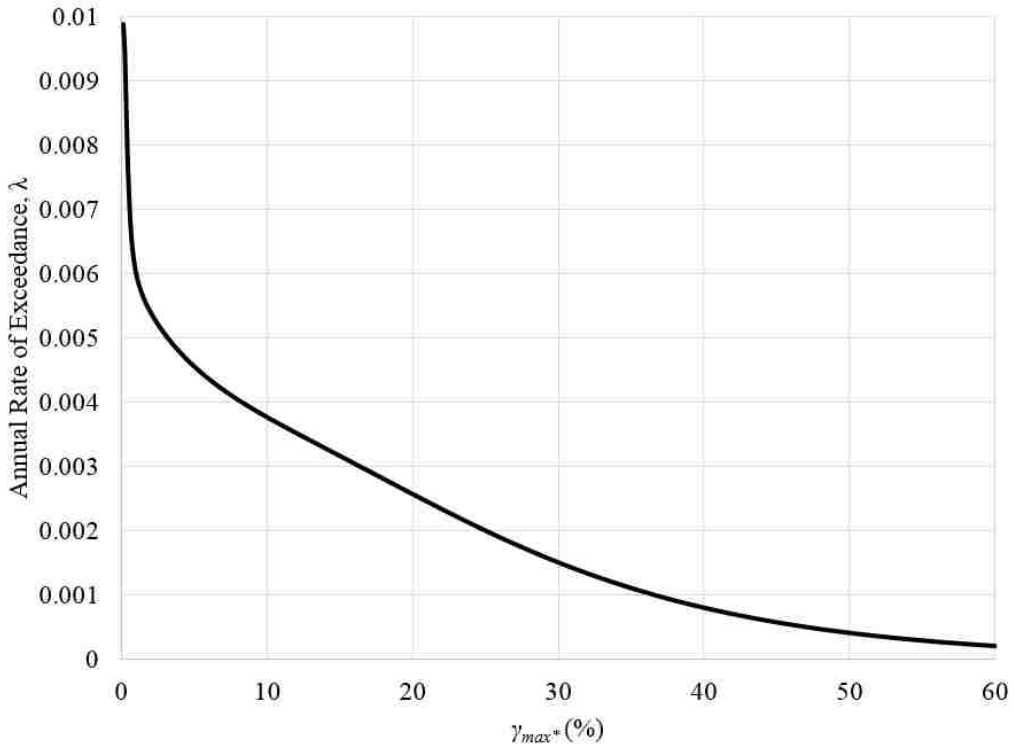

Figure 5-5: Hazard curve of γ_{max} for example site at Provo, UT, for a single soil increment at a depth of 6m.

With strain hazard curves for every soil increment in the CPT profile, the lateral spread displacement can be calculated. The strains from each soil increment are used to create a hazard curve of lateral spread displacement, which is done following the calculation steps laid out by the Zhang et al. (2004) procedure (found in Section 4.3.3); however, the inputs of FS_L and γ_{max} come from the fully-probabilistic method. For a specific return period, corresponding γ_{max} and FS_L values are selected from their respective hazard curves for each soil increment. After γ_{max} and FS_L values are selected for every soil increment, profiles of γ_{max} and FS_L with depth can then be created, and the lateral spread displacement for the specified return period can be calculated, creating a single point on the lateral spread displacement hazard curve. This process is repeated for a range of return periods (this study uses a range of 100 to 10,000 years) until the entire hazard curve is built.

For the calculation example of Provo, UT, using the fully-probabilistic method, the lateral spread displacement hazard curve can be made using the process previously outlined. With the data of γ_{max} and FS_L for each soil increment and return period, the hazard curve can be created, as shown in Figure 5-6. With this hazard curve, the lateral spread displacement for the 2475-year return period can be determined, as illustrated by the dashed red line. For this example, the fully-probabilistic method calculates a lateral spread displacement of 4.25 m.

For this example, the fully-probabilistic method results in a value of lateral spread displacement higher than the value estimated with the pseudo-probabilistic method. This result only applies to the 2475-year return period; at other return periods, it is possible that the fully-probabilistic method results in a lower value than the pseudo-probabilistic method. The difference between these two methods is a result of the pseudo-probabilistic method

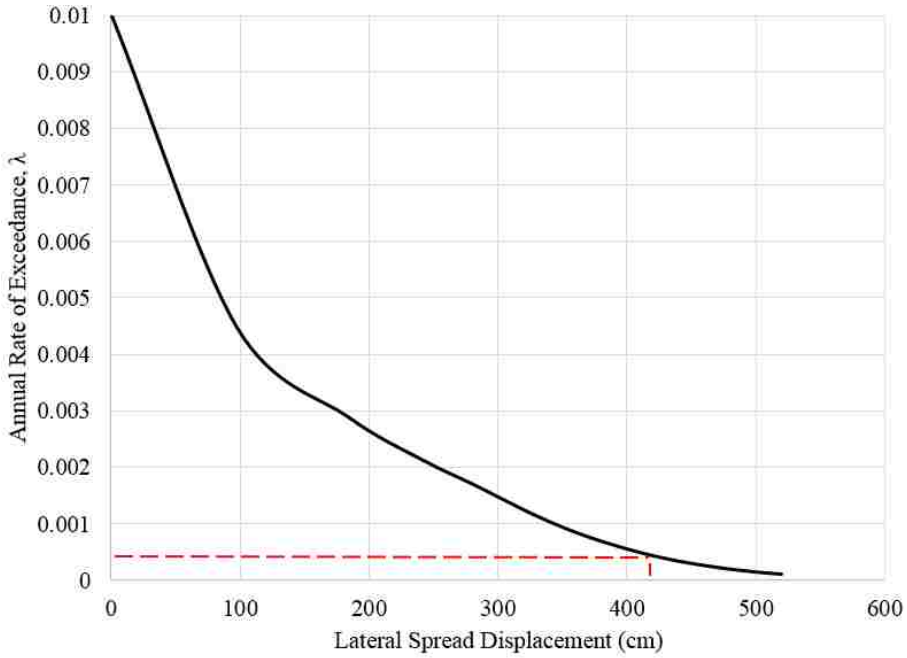

Figure 5-6: Hazard curve of lateral spread displacement for the example site at Provo, UT, using the fully-probabilistic method

neglecting many of the uncertainties involved in seismic hazard analysis. By accounting for all uncertainty, the fully-probabilistic method is providing a more accurate estimate of lateral spread displacement.

5.5 Semi-Probabilistic Method

The semi-probabilistic method was created in an attempt to benefit from the accuracy of the fully-probabilistic method but to do so with less calculations. The semi-probabilistic method calculates the FS_L using fully-probabilistic methods but calculates the lateral spread displacement deterministically. By calculating the FS_L using fully-probabilistic methods, the semi-probabilistic method accounts for the inherent uncertainty in the liquefaction triggering procedure and therefore accurately calculates the return period of soil liquefaction. However, it does not account for uncertainty in the lateral spread displacement procedure

For the calculation example of Provo, UT, the semi-probabilistic method calculates the lateral spread displacement using the procedure described above. The input FS_L values for the Zhang et al. (2004) procedure at the 2475-year return period are determined from the fully-probabilistic method (shown visually in Figure 5-3). These values are then used to calculate the lateral spread displacement in a deterministic manner. The result of these calculations with the semi-probabilistic method is a lateral spread displacement of 3.54 m.

5.6 Chapter Summary

A crucial step in seismic analysis of liquefaction-induced lateral spread displacements is the input ground motion selection. Different methods have been developed that incorporate varying levels of probability and uncertainty. The deterministic method is the original method used, which is accomplished by manually selecting a design earthquake and ground motion and using the corresponding magnitude and acceleration in the estimation of the lateral spread displacement. The pseudo-probabilistic method incorporates probability by performing a PSHA to determine the input ground motions, which are then used deterministically in the lateral spread displacement calculation.

The fully-probabilistic method accounts for uncertainty in the liquefaction triggering and lateral spread displacement procedures as it follows the PBEE framework. PBEE was created to improve risk-based decision making by allowing stakeholders to quantify and communicate their desired level of risk in seismic analysis and design. This chapter presented a new fully-probabilistic method for calculating lateral spread displacements following PBEE framework. One final method discussed is the semi-probabilistic method, which accounts for the uncertainty in the liquefaction triggering procedure but not in the lateral spread displacement procedure.

These different methods are recognized in industry, but it is not generally known how they compare to one another. It is not understood if the more conventional pseudo- and semi-probabilistic methods are a sufficient approximation of the more complicated fully-probabilistic method. To address this gap in understanding, Chapter 6 provides a comparison of these different methods.

6 COMPARISON OF RESULTS BETWEEN PERFORMANCE-BASED, PSEUDO-PROBABILISTIC, AND SEMI-PROBABILISTIC ANALYSIS OF LATERAL SPREAD

6.1 Introduction

With an understanding of seismic loading, liquefaction, lateral spread displacements, and the different analysis methods used, a comparative study can now be performed to observe the performance of the different methods. This study compares the difference in lateral spread displacements using the pseudo-probabilistic, semi-probabilistic, and fully-probabilistic (performance-based) methods across multiple sites representing different tectonic environments and for various soil profiles. These comparisons show the shortcomings of the conventional methods (pseudo-probabilistic and semi-probabilistic) and demonstrate how uncertainties accounted for in the fully-probabilistic method can have significant influence on the calculation of lateral spread displacements.

6.2 Methodology

To complete this comparison study, a tool was created to run the complex analyses. *CPTLiquefY* was created to run calculations for all different analysis methods, especially making it possible to run a complicated fully-probabilistic analysis. This comparative study evaluated 20 soil profiles, 10 site locations, and 3 return periods of interest. It was also determined to use two

different site geometries in the analysis to represent the different types of sites susceptible to lateral spreading. The details of the analysis process are outlined in the following sections.

6.2.1 CPTLiquefY

Due to the complicated nature of the fully-probabilistic method, there was a need to create an analysis tool to automate the calculations. *CPTLiquefY* was created to fill this need and can run the desired calculations, including the application of all necessary probability theory. This complicated probability theory is the main reason these procedures are not widely used in the industry today. *CPTLiquefY* is a research tool that is not meant to replace conventional liquefaction analysis tools used in the industry but to aid in the demonstration of the difference between analysis methods.

CPTLiquefY was created by Tyler Coutu, Mikayla Hatch, and Alex Arndt, under the direction of Dr. Kevin Franke at Brigham Young University. It was created using Microsoft Visual Studio in C++. *CPTLiquefY* has the ability to run fully-probabilistic, semi-probabilistic, pseudo-probabilistic, and deterministic procedures for liquefaction triggering, post-liquefaction settlement, and liquefaction-induced lateral spread displacements. As evident in the name, *CPTLiquefY* runs these calculations using input from the CPT. A fully-probabilistic analysis of a single soil increment takes less than 10 seconds, and, depending on the size of the CPT profile, *CPTLiquefY* completes its fully-probabilistic analysis of lateral spread in 10 to 20 minutes, which is quite fast considering the complexity of the calculations required. All results presented in this chapter were developed using this tool. A basic tutorial on how these analyses were run using *CPTLiquefY* is available in Appendix A.

6.2.2 Soil Profiles

To represent as many different soil types as possible, the same 20 CPT soundings were analyzed at each location. These CPT soundings were collected from a United States Geological Survey (USGS) database that is available online. The CPT soundings were selected because together they represent a range of soil type and stiffness, as measured by Q_{tncs}. A summary of the selected soil profiles is found in Table 6-1.

Table 6-1: Summary of Soil Profiles

Profile	Name	Location	Latitude	Longitude	Source	Sand Content	Stiffness	Full Depth (m)	Date Collected
1	SFO029	San Francisco, CA	37.824	-122.364	USGS	Medium	Soft/Very Soft	17	1/21/1994
2	LWE001	Lawrenceville, Il	38.747	-87.511	USGS	High	Med./Hard	12.5	10/6/2004
3	HNC005	Evansville, IN	37.872	-87.702	USGS	Medium	Medium	20	12/6/2003
4	BDY002	Arkansas	33.278	-92.333	USGS	Medium	Medium	12	12/14/2005
5	SBC030	Riverside,CA	34.070	-117.290	USGS	High	Med./Hard	19	3/24/2001
6	BKY006	Charleston, SC	32.905	-79.924	USGS	High	Soft	20	11/6/2004
7	MGA003	Matagorda, TX	28.765	-95.787	USGS	Low	Soft	18.15	1/5/2006
8	SCR001	East St. Louis, Il	38.620	-90.162	USGS	High	Medium	24	10/6/2008
9	SOC024	Oceano, CA	35.104	-120.631	USGS	High	Med./Hard	15	3/2/2004
10	POR006	Chesterton, IN	41.660	-87.051	USGS	Medium	Soft/Med.	15	9/24/2004
11	HTN003	Upper peninsula, MI	47.159	-88.245	USGS	High	Soft to Hard	17	9/15/2004
12	SYC001	Memphis, TN	35.195	-89.987	USGS	Medium	Soft/Med.	20	10/29/2003
13	BZA001	Freeport, TX	28.979	-95.285	USGS	Low	Soft	30	1/3/2006
14	CMN002	Rio grande valley, TX	25.953	-97.560	USGS	Medium	Soft	20	1/14/2005
15	LAC076	Northridge, CA	34.227	-118.560	USGS	Low	Soft	14	6/18/1996
16	RCD052	Fargo, ND	46.471	-96.834	USGS	Very Low	Very Soft	18	9/8/2008
17	SCC097	Santa Clara, CA	37.427	-122.041	USGS	Low	Soft	18	6/26/2000
18	Oak061	Oakland, CA	37.818	-122.281	USGS	Very Low	Very Soft	20	3/30/1999
19	SCS001	St. Charles, MO	38.856	-90.212	USGS	Very High	Medium	24	10/6/2008
20	BKY021	North Charleston, SC	33.036	-79.736	USGS	Low	Medium	20	11/14/2004

The data in Table 6-1 show how the stiffness and sand content varied between CPT soundings. To visually reinforce that the soil profiles represent a full range of soil stiffness, each soil profile was plotted as Q_{tncs} versus depth. The combined plot of all 20 profiles is shown in Figure 6-1. At first glance Figure 6-1 seems to be completely random; however, this plot is demonstrating that with all 20 profiles a full range of stiffness values is achieved throughout the entire profile, shown by the lack of white space in the plot. It is difficult to find a CPT sounding

with values of Q_{tncs} lower than 50 kPa, as very few soils are soft enough to have so little resistance. Also, values of Q_{tncs} beyond 250 kPa are considered too dense to liquefy by both Boulanger and Idriss (2016) and Robertson and Wride (1998). Therefore, it was unnecessary to include profiles with comprehensive coverage of Q_{tncs} lower than 50 kPa and higher than 250 kPa.

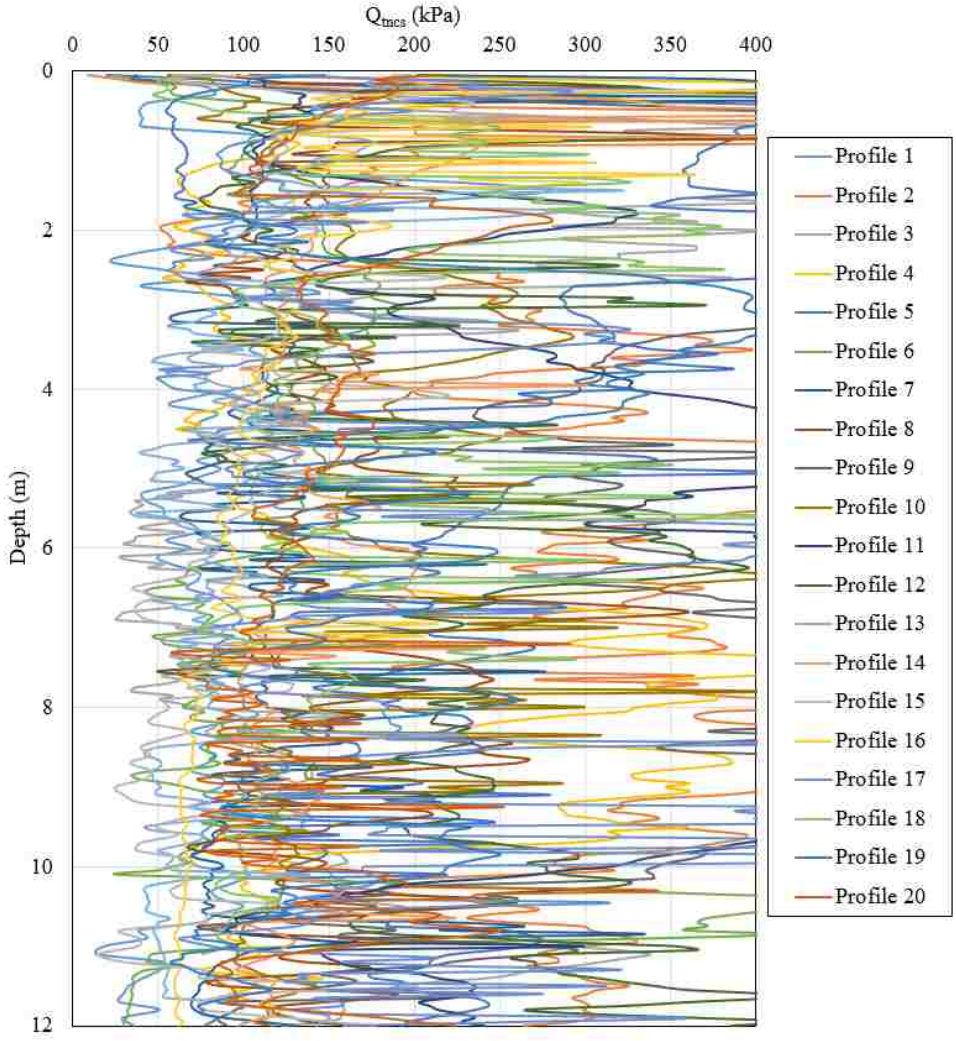

Figure 6-1: The stiffness of all 20 CPT profiles plotted with depth.

To compare differences in analysis methods, a few variables in the CPT profiles were standardized. This standardization gives the ability to attribute differences in the results to different analysis methods rather than variability in the soil profiles. A standard maximum depth of 12 m was applied to all soil profiles. As presented in Table 6-1, the true maximum depth of the soil profiles varied from 12 to 30 m. The value of 12 m for the maximum depth was chosen because most liquefaction triggering case histories occur at depths of less than 12 m. As discussed in the section on liquefaction susceptibility (Section 3.3), a soil must be saturated to liquefy. In the case of the chosen soil profiles, this would mean that the soil increment of interest must be below the water table. The CPT soundings reported varying water table depths (as would be expected), as well as many with no water table depth reported. It was decided to place the water table at the ground surface for all profiles, indicating that the entire soil profile is saturated. A final standardization was made in the measurement of the pore pressure from the cone. The pore pressure value is used in the tip resistance correction procedure. None of the CPT soundings had pore pressure readings; therefore, it was assumed that this value was zero for each soil increment. Each of these changes in the depth, water table, and pore pressure measurements can have significant consequences on the results of the liquefaction triggering and lateral spread evaluations. However, as this is a comparative study, it was determined that a consistent application of these changes to all of the analysis methods being evaluated was appropriate.

6.2.3 Site Location

To represent different levels of seismicity, 10 locations/cities were examined in this study. These 10 cities were chosen because of their range in seismic activity, as well as the fact that they have been used in other performance-based analysis studies (Franke et al., 2014; Kramer and Mayfield, 2007). These 10 cities are located throughout the United States, as

depicted on the map in Figure 6-2. The different cities represent different seismic regions and are distributed as follows: four cities on the west coast along the San Andreas fault, two cities in the Rocky Mountains near the Wasatch fault, two cities in the Pacific Northwest in the Cascadia subduction zone, one city within the New Madrid fault zone, and one city near the Charleston liquefaction features.

Figure 6-2: Map of 10 cities throughout the United States that are used in this study.

To determine the seismic loading for each city, the 2014 USGS seismic source model was used. The most recent release, which provides several updates to the probabilistic earthquake hazard calculation for areas throughout the United States, was used for this study (Petersen et al., 2015). The 2014 seismic source model of the National Seismic Hazard Mapping Project (NSHMP) was integrated directly in *CPTLiquefY* to aid in the calculation process. The model provides the earthquake magnitude (mean or modal) and maximum acceleration (a_{max}) at each site for a specified return period. The exact locations used are listed in Table 6-2 along with

their respective latitude and longitude. Table 6-2 also presents the seismic loading data for two of the return periods used in this study. These data include mean and modal magnitude, as well as PGA, which is used to calculate a_{max}, with site amplification factors for an AASHTO site class D. These values of magnitude and PGA are examples of the seismic loading inputs used in the pseudo-probabilistic analysis.

Table 6-2: List of 10 Cities Used, Including Their Corresponding Latitude, Longitude, Mean Magnitude, Modal Magnitude, and PGA from 2014 USGS PSHA Values

City	Latitude	Longitude	Mean Magnitude (475 T_R / 2475 T_R)	Modal Magnitude (475 T_R / 2475 T_R)	PGA (g) (475 T_R / 2475 T_R)
Butte, MT	46.0038	-112.535	6.03 / 6.05	5.20 / 6.20	0.0834 / 0.1785
Charleston, S.C.	32.7765	-79.9311	6.61 / 7.00	7.36 / 7.37	0.1513 / 0.7287
Eureka, CA	40.8021	-124.164	7.33 / 7.45	6.99 / 6.99	0.6154 / 1.4004
Memphis, TN	35.1495	-90.049	6.98 / 7.24	7.70 / 7.70	0.1604 / 0.5711
Portland, OR	45.5231	-122.677	7.24 / 7.31	9.00 / 9.00	0.199 / 0.4366
Salt Lake City, UT	40.7608	-111.891	6.75 / 6.90	6.99 / 6.99	0.2126 / 0.6717
San Fran, CA	37.7749	-122.419	7.31 / 7.44	7.99 / 7.98	0.4394 / 0.7254
San Jose, CA,	37.3382	-121.886	6.66 / 6.66	6.60 / 6.60	0.456 / 0.6911
Santa Monica, CA	34.0195	-118.491	6.74 / 6.84	7.21 / 7.22	0.3852 / 0.7415
Seattle, WA	47.6062	-122.332	6.75 / 6.88	6.60 / 6.80	0.311 / 0.6432

6.2.4 Return Periods

Along with areas of differing levels of seismicity, three different return periods of interest were analyzed at each location. Return periods are often used to specify the level of earthquake loading that a structure can withstand. For critical and important structures, a requirement to resist a larger seismic event with a high return period may be specified, while for more common, less critical structures a requirement to resist a smaller seismic event with a far lower return period may be specified. The return periods chosen for this study are 475 years, 1039 years, and 2475 years, corresponding to probabilities of exceedance of 10% in 50 years, 2% in 21 years,

and 2% in 50 years, respectively. These return periods represent low, medium, and high levels of seismic loading and therefore span a full range of ground motions at each site.

6.2.5 Site Geometry

As lateral spread displacements are a function of the geometry of the site in question, it was determined that two different geometries should be used in the analysis. The two main types of geometries discussed by Zhang et al. (2004) are a site with a gently sloping ground and a site with level ground near a free face. One geometry from each of these types was used in this analysis. The first geometry was a gently sloping ground, with a ground slope (S) of 3% (referred to from this point on as lateral spread geometry 1). The second geometry was a level ground near a free face, with a free face height (H) of 6 m and a distance to the free face (L) of 50 m (referred to from this point on as lateral spread geometry 2).

6.3 Analysis Methods

As mentioned, this study compares the results of two conventional methods (pseudo-probabilistic and semi-probabilistic) of predicting liquefaction-induced lateral spread displacements to the fully-probabilistic method. A more detailed explanation of each of these methods can be found in Chapter 5.

6.4 Presentation of Comparison between Different Methods

This section presents the results of the lateral spread analysis for all sites, soil profiles, return periods, and site geometries, resulting in a total of 9,600 data points. More importantly, it is a presentation of the comparison between the different analysis methods mentioned above: fully-probabilistic, pseudo-probabilistic (mean and modal magnitude), and semi probabilistic.

The Zhang et al. (2004) procedure for predicting lateral spread displacements was applied to each different analysis method. The input FS_L values for the Zhang et al. (2004) procedure were determined from both the Robertson and Wride and the Boulanger and Idriss liquefaction triggering procedures. Results of this comparative study, including a discussion of any trends observed, using the two different liquefaction triggering procedures, are presented in this section.

6.4.1 Presentation of Robertson and Wride Results

Table 6-3 to Table 6-22 present the results of the lateral spread analysis using the Robertson and Wride liquefaction triggering procedure for both site geometries. Each table contains the results for the fully-probabilistic, pseudo-probabilistic (mean and modal magnitude), and semi-probabilistic methods. The results of all 10 soil profiles are shown, as well as the results for all three return periods (475 years, 1039 years, and 2475 years). Each value represents the lateral spread displacement at the specified site in centimeters.

Table 6-3: Lateral Spread Displacements in Butte Calculated with the Robertson and Wride Liquefaction Triggering Procedure (Lateral Spread Geometry 1)

	Full Probabilistic			Mean Magnitude			Modal Magnitude			Semi-Probabilistic		
Profile	475	1039	2475	475	1039	2475	475	1039	2475	475	1039	2475
1	263.5	550.1	762.7	466.7	735.2	902.6	53.7	365.1	740.1	587.3	690.0	800.9
2	20.9	48.1	75.5	36.4	68.0	78.6	8.7	20.2	68.4	59.9	74.0	84.3
3	112.7	329.6	532.1	244.5	464.1	596.0	3.6	155.3	467.4	386.8	503.7	603.5
4	29.9	181.7	393.0	96.2	333.6	587.9	1.3	22.9	336.5	243.2	367.7	562.4
5	9.8	22.7	44.4	13.5	30.7	52.3	8.3	10.3	31.2	35.7	56.9	79.1
6	169.0	445.8	699.8	339.9	644.3	786.6	28.4	225.7	648.5	520.8	654.4	763.3
7	10.4	49.6	93.7	36.1	78.0	117.3	0.2	8.1	78.6	66.2	89.6	116.5
8	3.9	24.5	60.9	7.0	30.5	102.1	0.1	1.7	31.4	54.7	80.9	128.2
9	8.7	12.7	16.1	10.6	13.1	15.6	8.4	9.4	13.2	14.8	18.9	23.2
10	7.7	29.9	61.9	14.5	53.6	92.1	0.3	9.9	54.6	48.1	74.4	105.8
11	1.6	11.4	27.9	2.2	13.8	43.9	0.0	0.5	14.1	25.5	39.1	58.7
12	4.1	40.5	118.7	8.8	85.5	181.6	0.1	2.2	87.0	61.7	130.2	219.9
13	55.2	232.4	422.7	145.7	426.8	526.0	2.3	59.9	431.0	293.5	402.4	500.2
14	2.2	15.5	43.6	1.5	13.4	75.2	0.0	0.4	13.9	34.7	57.2	95.7
15	54.7	118.4	169.4	96.3	146.8	193.4	11.5	83.9	148.0	125.6	152.8	196.8
16	0.1	0.8	4.9	0.0	1.0	8.6	0.0	0.0	1.2	1.6	5.5	10.7
17	3.5	18.0	50.7	12.2	27.0	77.8	0.1	3.0	27.5	26.0	47.6	101.3
18	0.0	0.4	2.2	0.0	0.1	1.9	0.0	0.0	0.1	2.6	4.4	10.7
19	89.9	240.5	375.9	233.1	322.0	420.7	2.2	134.5	323.8	302.6	349.3	409.4
20	2.8	50.4	161.2	6.4	98.3	270.7	0.0	1.4	101.5	78.5	173.2	305.8

Table 6-4: Lateral Spread Displacements in Eureka Calculated with the Robertson and Wride Liquefaction Triggering Procedure (Lateral Spread Geometry 1)

	Full Probabilistic			Mean Magnitude			Modal Magnitude			Semi-Probabilistic		
Profile	475	1039	2475	475	1039	2475	475	1039	2475	475	1039	2475
1	1129.4	1285.6	1433.9	1001.6	1002.4	1002.6	999.3	1002.0	1002.5	955.7	962.0	968.7
2	121.1	135.8	148.4	127.9	136.5	143.5	118.8	131.3	137.4	102.0	103.5	105.0
3	803.5	870.2	925.8	857.9	866.2	875.0	847.1	862.6	867.6	744.1	754.1	764.8
4	869.9	1002.1	1096.4	845.7	851.3	854.0	837.3	847.6	851.9	788.5	795.1	800.8
5	124.2	152.8	181.1	233.7	265.7	273.1	207.1	246.7	267.8	156.4	163.6	170.4
6	1020.9	1122.5	1195.7	952.9	954.2	954.9	950.4	953.2	954.4	869.0	874.4	880.1
7	169.2	189.3	203.6	185.7	187.4	188.3	184.4	186.6	187.5	167.3	170.3	172.6
8	205.9	263.7	322.8	365.7	373.9	375.9	347.8	369.6	374.5	243.3	251.5	259.7
9	30.4	37.9	46.2	61.3	68.8	72.7	54.0	64.8	69.6	38.1	39.7	41.4
10	165.1	208.2	245.6	287.5	308.4	317.0	262.6	294.8	310.1	189.4	197.4	204.8
11	107.2	143.1	180.9	189.8	201.5	205.3	179.7	194.1	202.6	133.6	138.6	143.5
12	353.9	418.1	469.5	464.4	486.7	495.6	447.9	473.6	489.2	387.6	396.3	407.4
13	700.1	787.1	848.9	633.8	633.9	633.9	630.0	633.9	633.9	597.8	601.4	605.1
14	202.0	276.7	356.6	396.0	405.9	408.2	377.5	400.4	406.7	265.7	279.0	291.5
15	295.6	334.5	356.0	306.0	318.5	321.6	304.7	307.4	321.4	290.9	294.0	295.9
16	18.1	22.9	28.1	51.4	58.6	58.6	50.2	54.2	58.6	27.4	30.1	33.2
17	204.3	249.4	279.4	318.0	330.2	336.9	305.7	325.6	330.7	241.0	249.5	257.4
18	29.4	41.9	51.0	101.5	140.8	150.6	80.0	109.3	143.6	49.5	53.5	58.0
19	560.4	636.8	709.9	586.1	594.5	595.9	577.3	589.7	595.0	518.0	523.2	529.0
20	530.3	649.3	752.8	772.1	808.4	820.8	737.4	788.4	811.0	584.4	602.7	620.8

Table 6-5: Lateral Spread Displacements in Santa Monica Calculated with the Robertson and Wride Liquefaction Triggering Procedure (Lateral Spread Geometry 1)

	Full Probabilistic			Mean Magnitude			Modal Magnitude			Semi-Probabilistic		
Profile	475	1039	2475	475	1039	2475	475	1039	2475	475	1039	2475
1	1057.2	1204.0	1342.0	992.8	997.0	1001.3	995.7	999.2	1001.8	933.8	942.9	952.1
2	112.8	126.9	138.3	98.9	110.2	125.1	105.9	118.6	129.0	97.9	99.6	101.5
3	748.7	817.2	868.6	762.9	829.5	854.6	810.8	846.8	859.6	712.8	725.6	739.0
4	770.6	921.6	1024.3	816.9	829.7	844.1	825.3	837.1	846.3	765.3	775.2	785.6
5	98.6	123.6	146.9	139.8	185.5	224.9	173.0	206.4	238.2	138.0	144.8	153.6
6	967.7	1069.3	1149.1	921.0	943.9	952.6	940.3	950.2	953.0	852.5	859.9	866.6
7	151.2	171.5	186.8	172.8	183.8	185.2	182.8	184.4	186.0	158.2	162.2	166.1
8	162.6	216.6	266.3	271.8	329.6	361.4	312.4	347.3	367.2	220.3	229.8	239.6
9	25.3	31.2	37.9	34.0	44.7	59.4	40.7	53.8	62.4	33.8	35.5	37.5
10	134.1	173.2	205.8	195.4	246.9	280.2	232.9	262.2	290.5	168.4	177.0	186.4
11	80.7	110.6	143.7	144.6	168.6	186.7	162.1	179.5	191.4	118.4	124.5	130.8
12	294.8	360.6	409.0	395.1	436.7	458.4	426.9	447.7	467.6	355.4	368.0	382.2
13	653.3	741.5	808.1	614.5	624.7	633.4	622.5	629.8	633.9	587.3	592.4	596.5
14	143.5	203.3	267.7	316.7	360.3	389.6	349.7	377.2	398.0	222.9	238.6	258.5
15	263.9	304.7	330.8	285.3	301.8	305.4	293.6	304.7	306.4	274.2	281.5	288.3
16	13.0	16.6	19.9	26.7	42.2	51.2	39.6	50.0	51.5	20.5	22.9	26.0
17	158.8	206.5	239.0	248.3	298.1	311.1	285.8	305.6	321.6	214.9	225.1	236.5
18	18.7	28.6	38.3	46.6	65.1	96.2	56.1	79.5	103.4	38.8	42.6	47.5
19	513.9	584.7	651.9	545.4	567.7	583.6	562.0	577.1	587.4	499.7	508.2	515.5
20	430.7	545.9	641.0	638.9	709.5	760.2	690.1	736.7	778.0	531.4	552.2	576.3

Table 6-6: Lateral Spread Displacements in Portland Calculated with the Robertson and Wride Liquefaction Triggering Procedure (Lateral Spread Geometry 1)

	Full Probabilistic			Mean Magnitude			Modal Magnitude			Semi-Probabilistic		
Profile	475	1039	2475	475	1039	2475	475	1039	2475	475	1039	2475
1	696.1	934.7	1128.9	972.2	991.7	996.1	994.8	999.3	1001.8	880.9	914.0	933.4
2	64.3	94.9	120.2	88.2	96.4	107.5	102.8	118.7	128.8	90.0	94.4	97.7
3	465.5	674.2	791.4	679.1	748.0	818.6	792.1	847.1	859.3	659.7	690.8	712.7
4	341.1	636.2	858.1	757.0	809.2	826.8	821.9	837.2	846.2	681.8	740.2	764.5
5	40.4	77.6	114.9	72.6	126.7	177.8	160.6	206.7	237.5	102.3	124.3	137.7
6	610.1	862.0	1019.9	838.2	907.3	941.3	935.6	950.3	953.0	813.8	838.6	852.5
7	79.5	131.5	164.4	142.7	165.3	183.3	180.9	184.4	185.9	136.6	150.3	158.1
8	57.2	126.0	194.6	165.5	252.4	319.1	297.1	347.6	367.1	171.4	201.3	219.7
9	15.5	21.4	28.5	18.5	30.1	42.0	38.0	53.9	62.2	26.5	30.8	33.7
10	57.1	106.2	156.8	127.9	182.9	238.3	217.7	262.4	290.0	131.0	152.6	168.3
11	26.2	61.3	98.8	100.3	137.2	164.2	155.4	179.6	191.1	82.5	106.6	118.6
12	106.3	235.8	337.2	301.7	377.0	431.1	415.0	447.8	467.1	286.7	328.6	354.4
13	360.7	569.6	698.6	571.4	609.6	623.2	620.3	629.9	633.9	553.0	575.0	587.2
14	42.2	106.3	180.6	191.2	298.8	353.3	338.8	377.3	397.9	139.3	190.0	221.9
15	155.5	230.7	288.6	247.3	284.8	296.6	286.8	304.7	306.3	239.6	262.1	274.6
16	4.6	9.8	15.7	9.8	18.1	40.3	38.1	50.1	51.5	12.5	15.9	20.3
17	45.8	121.1	190.6	151.8	238.5	291.1	271.3	305.6	321.2	157.7	192.6	214.4
18	2.3	12.4	25.2	15.5	41.6	59.4	51.9	79.8	103.0	20.8	31.8	38.6
19	323.1	461.1	552.8	483.2	536.7	564.4	556.1	577.3	587.2	452.6	482.8	499.7
20	146.3	337.0	502.2	450.6	616.7	696.7	672.4	737.1	777.0	413.7	488.5	530.2

Table 6-7: Lateral Spread Displacements in Salt Lake City Calculated with the Robertson and Wride Liquefaction Triggering Procedure (Lateral Spread Geometry 1)

	Full Probabilistic			Mean Magnitude			Modal Magnitude			Semi-Probabilistic		
Profile	475	1039	2475	475	1039	2475	475	1039	2475	475	1039	2475
1	739.4	982.2	1179.0	976.0	993.5	999.1	981.7	994.0	999.4	905.4	928.9	944.6
2	68.6	100.5	125.5	88.9	100.2	117.9	89.9	101.3	119.2	93.1	96.9	100.0
3	504.2	711.9	821.7	686.0	772.2	845.5	696.7	781.3	847.8	682.7	706.3	728.0
4	399.3	701.8	915.4	765.9	818.8	836.4	776.4	820.0	837.5	727.2	758.9	777.1
5	46.8	91.2	129.5	77.0	146.7	204.8	84.7	153.0	208.1	118.3	134.5	146.6
6	652.9	902.8	1054.1	844.5	927.2	949.7	853.7	931.7	950.6	832.4	848.9	861.2
7	88.8	143.1	174.4	144.1	176.4	184.3	145.6	178.7	184.4	146.9	156.4	162.7
8	71.5	148.7	220.9	172.1	281.2	346.3	182.2	288.6	348.8	193.8	215.1	232.0
9	16.5	23.8	31.8	18.9	35.4	53.2	19.7	36.5	54.3	29.3	32.9	36.0
10	66.3	122.6	176.2	131.4	202.8	261.2	138.0	210.1	263.4	146.8	164.3	178.8
11	32.8	74.9	115.2	103.1	148.4	178.9	108.3	151.5	180.2	99.0	115.5	125.5
12	132.6	272.4	370.6	309.3	402.3	446.9	320.5	407.9	448.5	318.5	347.6	371.2
13	396.3	605.4	729.3	574.7	617.4	629.4	580.1	618.7	630.3	570.9	584.1	592.8
14	54.6	134.2	216.3	201.2	325.3	376.3	218.7	331.6	378.1	177.5	213.2	243.3
15	169.5	250.8	308.1	251.9	285.9	304.6	255.5	286.2	304.7	257.0	271.8	282.6
16	5.7	11.8	18.5	10.1	31.2	49.5	10.6	34.6	50.5	14.3	19.2	23.4
17	59.8	146.8	215.7	160.7	255.8	305.1	173.3	262.8	305.9	183.6	208.8	227.7
18	3.9	17.9	31.6	17.0	48.6	78.3	18.4	49.9	80.8	29.5	37.0	43.7
19	347.8	487.5	582.7	488.6	549.6	576.6	496.3	552.6	577.7	476.2	495.4	509.8
20	184.9	395.3	561.1	464.3	651.0	735.0	487.9	661.3	738.8	470.2	519.6	557.7

Table 6-8: Lateral Spread Displacements in San Francisco Calculated with the Robertson and Wride Liquefaction Triggering Procedure (Lateral Spread Geometry 1)

	Full Probabilistic			Mean Magnitude			Modal Magnitude			Semi-Probabilistic		
Profile	475	1039	2475	475	1039	2475	475	1039	2475	475	1039	2475
1	1100.9	1247.8	1388.1	995.6	999.0	1001.7	997.9	1000.6	1002.0	939.6	947.5	955.2
2	117.6	130.9	142.4	105.8	117.4	128.1	113.0	122.5	131.3	99.0	100.5	102.0
3	776.4	839.3	890.0	809.9	844.8	858.2	836.6	851.4	862.7	721.4	731.8	743.2
4	826.6	962.4	1057.1	825.1	835.9	845.8	832.2	841.6	847.7	771.6	780.7	788.4
5	109.7	134.5	158.7	172.5	203.8	234.5	192.7	217.9	247.0	143.0	148.8	156.3
6	1000.2	1097.5	1170.6	940.1	949.3	952.9	946.3	952.3	953.2	857.4	863.2	868.9
7	160.0	179.5	192.8	182.7	184.3	185.7	184.1	184.8	186.6	160.8	164.1	167.3
8	183.4	236.5	288.8	311.6	345.6	366.0	335.9	356.1	369.6	227.1	234.7	243.1
9	27.5	33.8	40.9	40.5	52.7	61.4	48.1	57.3	64.8	35.0	36.6	38.1
10	149.0	187.4	220.4	232.2	260.5	288.0	253.3	273.3	294.9	174.2	181.7	189.3
11	92.7	124.2	158.8	161.8	178.2	190.1	172.6	184.2	194.2	122.3	127.6	133.3
12	323.1	384.6	431.0	426.3	446.4	465.1	441.3	454.1	473.7	364.7	374.6	386.7
13	681.1	766.1	827.2	622.4	629.0	633.9	626.1	632.7	633.9	590.5	594.3	597.8
14	168.7	231.7	299.6	349.3	375.7	396.5	366.7	384.4	400.5	234.1	248.5	265.2
15	280.3	318.0	339.5	293.3	304.6	306.1	304.4	305.1	307.4	279.0	285.3	290.9
16	15.1	18.6	22.2	39.5	49.1	51.4	45.5	51.0	54.3	22.1	24.2	27.2
17	180.5	223.5	252.8	285.2	304.7	318.6	300.9	308.2	325.7	221.6	230.5	240.3
18	23.2	33.6	42.0	55.8	77.5	101.8	70.5	90.0	109.6	41.4	45.0	49.3
19	538.3	608.8	677.4	561.7	576.1	586.4	571.2	581.4	589.7	505.4	511.9	517.7
20	477.6	588.7	682.8	689.3	733.8	773.0	720.3	750.3	788.7	545.8	563.7	584.7

Table 6-9: Lateral Spread Displacements in San Jose Calculated with the Robertson and Wride Liquefaction Triggering Procedure (Lateral Spread Geometry 1)

	Full Probabilistic			Mean Magnitude			Modal Magnitude			Semi-Probabilistic		
Profile	475	1039	2475	475	1039	2475	475	1039	2475	475	1039	2475
1	1184.4	1316.6	1451.8	995.6	999.2	1001.6	995.1	998.4	1001.1	942.5	948.8	955.7
2	125.3	136.6	146.3	105.8	118.4	127.1	104.0	115.1	124.2	99.4	100.8	102.1
3	812.8	863.3	907.7	810.1	846.4	857.0	800.1	840.9	853.6	725.8	733.8	744.0
4	907.6	1010.4	1089.6	825.1	836.8	845.3	823.4	834.0	843.5	774.7	782.1	788.5
5	122.5	144.7	167.4	172.5	205.9	231.4	166.2	198.0	222.8	145.0	150.2	156.4
6	1056.3	1137.8	1196.4	940.1	950.0	952.8	937.5	947.9	952.6	859.7	864.1	869.0
7	170.6	186.0	197.8	182.7	184.4	185.5	181.9	184.2	185.0	161.8	164.7	167.4
8	212.6	259.6	311.4	311.7	347.1	364.8	303.6	340.8	359.7	229.8	236.0	243.6
9	30.7	36.9	43.8	40.5	53.6	60.7	39.0	50.6	58.8	35.6	36.9	38.3
10	170.7	202.8	232.3	232.3	261.8	285.9	224.4	257.0	278.0	176.8	183.1	189.8
11	108.7	139.5	171.7	161.9	179.4	189.0	158.2	175.3	185.9	124.2	128.4	133.4
12	357.5	405.3	447.2	426.4	447.4	462.6	420.4	443.8	457.1	368.0	377.1	388.4
13	730.5	798.7	849.6	622.4	629.6	633.7	621.4	627.4	633.2	591.9	594.9	597.7
14	200.2	260.9	327.3	349.4	376.9	394.3	344.1	371.2	388.1	239.9	251.4	265.4
15	302.5	329.5	346.5	293.3	304.7	305.8	289.6	304.5	305.3	281.4	285.8	290.7
16	16.7	19.9	23.4	39.5	49.8	51.3	38.9	47.4	51.1	23.1	24.7	27.4
17	205.0	237.6	261.6	285.3	305.5	316.0	277.7	303.0	309.9	225.1	232.3	240.9
18	28.4	38.1	44.2	55.8	79.1	100.5	53.3	73.8	94.3	42.8	45.8	49.4
19	577.5	641.4	705.3	561.8	577.1	585.5	558.6	573.5	583.0	507.7	512.9	518.1
20	539.1	631.1	717.2	689.5	736.1	769.2	680.5	727.6	757.2	553.1	567.6	585.7

Table 6-10: Lateral Spread Displacements in Seattle Calculated with the Robertson and Wride Liquefaction Triggering Procedure (Lateral Spread Geometry 1)

	Full Probabilistic			Mean Magnitude			Modal Magnitude			Semi-Probabilistic		
Profile	475	1039	2475	475	1039	2475	475	1039	2475	475	1039	2475
1	936.9	1103.7	1256.7	990.8	994.5	998.2	991.3	995.0	998.4	919.8	932.1	943.6
2	96.8	117.9	131.2	93.7	102.2	114.3	95.1	103.1	115.0	95.4	97.5	99.7
3	673.0	773.7	837.7	735.7	788.1	839.4	743.4	794.5	840.7	696.2	711.0	726.4
4	631.2	823.8	964.8	799.8	821.0	833.5	806.0	822.4	834.0	747.8	763.1	775.9
5	75.5	107.0	132.1	115.5	157.8	196.1	122.4	162.2	197.8	127.7	136.9	145.4
6	866.4	1002.1	1103.3	893.0	934.1	947.3	902.1	936.3	947.8	842.0	851.6	860.3
7	129.9	158.2	178.4	159.6	180.2	184.1	162.9	181.2	184.2	153.2	157.7	162.4
8	121.6	180.1	235.0	232.1	293.9	339.2	244.7	299.0	340.7	205.9	218.1	230.5
9	21.1	27.1	33.6	26.4	37.4	49.7	28.9	38.3	50.5	31.5	33.5	35.7
10	103.8	146.9	185.7	171.9	214.6	255.8	178.9	219.7	256.9	156.5	166.7	177.7
11	58.4	89.8	122.8	128.8	154.0	174.3	134.3	156.1	175.2	109.4	117.9	124.8
12	230.5	318.0	380.9	360.4	412.1	442.7	371.0	416.6	443.7	335.0	351.2	369.1
13	571.4	681.8	769.8	603.3	619.7	626.9	607.2	620.6	627.4	578.2	586.4	592.6
14	100.1	162.3	227.2	277.7	336.1	369.5	291.6	340.4	371.0	197.9	218.2	240.5
15	226.5	277.4	315.9	282.7	286.6	304.5	284.7	287.3	304.5	266.1	274.1	282.0
16	9.6	14.4	17.8	14.5	36.9	46.8	16.2	38.3	47.4	17.1	19.8	23.1
17	114.9	175.8	219.6	222.7	268.1	302.2	233.1	273.1	302.9	198.7	212.8	226.0
18	11.0	21.8	32.4	33.0	51.0	72.6	38.2	52.2	73.6	33.7	38.0	43.1
19	458.3	536.9	610.4	527.0	554.8	572.6	533.3	556.9	573.4	487.2	498.6	508.6
20	326.9	469.0	583.3	591.2	668.2	725.0	607.7	674.9	727.3	498.0	526.3	554.4

Table 6-11: Lateral Spread Displacements in Memphis Calculated with the Robertson and Wride Liquefaction Triggering Procedure (Lateral Spread Geometry 1)

	Full Probabilistic			Mean Magnitude			Modal Magnitude			Semi-Probabilistic		
Profile	475	1039	2475	475	1039	2475	475	1039	2475	475	1039	2475
1	517.5	875.6	1098.2	956.4	991.9	997.5	986.5	995.3	1000.2	855.1	911.4	934.5
2	48.8	84.4	116.0	86.1	97.1	111.7	91.2	104.4	121.8	87.9	94.0	98.0
3	327.7	627.1	782.8	657.9	752.0	833.4	713.0	802.5	850.4	643.3	688.2	714.0
4	209.8	568.1	835.1	725.5	811.6	831.0	786.4	823.9	840.7	648.7	736.7	765.9
5	26.7	69.6	114.3	64.1	130.8	189.0	97.7	167.6	215.8	94.0	122.9	138.5
6	444.0	797.0	997.5	823.5	911.5	945.2	869.6	938.3	952.1	798.7	836.9	853.4
7	53.1	120.6	163.3	136.2	167.6	184.0	150.6	182.2	184.7	129.7	149.3	158.6
8	32.1	113.3	190.7	147.7	259.0	332.9	199.6	305.9	354.3	156.6	199.0	220.7
9	12.3	20.1	28.2	17.4	31.2	46.4	21.6	39.3	56.6	25.1	30.4	33.9
10	36.4	95.6	153.3	118.2	186.6	250.3	150.7	226.4	270.9	121.4	151.3	168.7
11	15.1	54.8	98.0	89.8	139.4	170.6	115.8	159.1	183.2	73.2	105.4	119.2
12	57.3	209.5	333.9	275.3	382.8	439.0	335.5	422.2	452.7	265.9	326.5	355.4
13	250.8	513.3	680.8	561.5	611.1	625.4	588.7	621.6	632.2	535.9	574.3	587.9
14	22.4	95.4	180.8	160.0	304.4	363.5	243.7	345.6	382.4	121.9	187.1	223.3
15	111.0	216.1	285.0	229.3	284.9	304.1	266.4	290.5	305.0	223.8	260.6	275.3
16	2.0	8.7	16.2	9.3	20.7	43.9	11.6	39.0	50.9	11.9	15.4	20.6
17	23.1	108.0	189.2	127.7	241.5	299.7	189.9	279.7	307.6	137.7	190.4	215.2
18	0.8	10.8	25.7	10.8	43.5	67.8	21.2	53.9	87.5	16.5	30.9	39.0
19	234.3	435.7	543.1	467.2	539.6	569.6	507.8	559.4	580.6	438.2	480.9	500.5
20	76.4	299.4	495.7	406.6	623.1	715.3	529.9	682.8	747.2	375.1	484.3	532.4

Table 6-12: Lateral Spread Displacements in Charleston Calculated with the Robertson and Wride Liquefaction Triggering Procedure (Lateral Spread Geometry 1)

	Full Probabilistic			Mean Magnitude			Modal Magnitude			Semi-Probabilistic		
Profile	475	1039	2475	475	1039	2475	475	1039	2475	475	1039	2475
1	461.3	859.9	1096.4	946.1	992.7	1000.7	985.3	995.3	1001.8	850.2	915.7	939.6
2	43.2	81.9	115.3	84.9	98.6	123.0	90.9	104.6	128.9	87.6	94.8	98.9
3	284.0	612.5	786.8	646.1	761.0	852.0	708.3	803.8	859.4	640.6	692.5	721.0
4	174.0	552.1	838.7	702.6	816.1	842.3	784.1	824.1	846.2	642.3	742.9	771.6
5	21.6	68.5	117.6	62.3	138.6	219.3	94.5	168.3	237.7	92.7	125.7	142.1
6	388.8	777.0	996.3	815.9	919.5	952.5	865.0	938.5	953.0	796.5	839.7	857.3
7	45.1	117.1	165.4	131.5	171.9	184.9	149.2	182.3	185.9	128.9	151.4	160.7
8	25.4	111.8	195.4	138.2	269.8	357.2	194.6	306.8	367.1	154.0	202.8	226.3
9	11.0	20.0	28.9	17.0	33.6	57.8	20.9	39.5	62.3	25.0	31.0	34.8
10	29.5	94.0	156.5	111.5	193.7	274.6	147.1	227.5	290.2	120.1	153.7	173.8
11	12.0	54.6	101.8	82.4	143.8	184.6	113.5	159.5	191.2	71.7	107.9	122.2
12	42.9	205.1	340.7	255.5	393.2	455.1	331.2	422.8	467.3	262.2	330.8	362.8
13	214.6	497.2	680.3	556.2	613.8	633.0	586.1	621.8	633.9	533.0	576.1	590.4
14	16.9	95.5	189.7	141.3	314.8	385.6	237.1	346.3	397.9	119.6	192.6	233.0
15	97.8	213.8	288.3	220.0	285.2	305.1	262.5	291.0	306.3	221.7	263.8	279.2
16	1.0	8.5	17.2	9.1	25.6	51.1	11.3	39.1	51.5	11.8	16.3	22.0
17	17.6	106.5	194.8	115.8	246.8	308.6	185.2	280.9	321.4	135.0	194.9	221.5
18	0.5	11.0	27.5	8.3	46.1	91.4	20.3	54.2	103.1	16.0	32.4	41.2
19	207.0	424.7	545.6	457.7	544.4	581.8	504.5	559.8	587.2	435.1	484.2	505.3
20	55.4	294.0	507.2	383.2	636.1	752.0	517.8	684.0	777.3	369.6	491.9	544.9

Table 6-13: Lateral Spread Displacements in Butte Calculated with the Robertson and Wride Liquefaction Triggering Procedure (Lateral Spread Geometry 2)

	Full Probabilistic			Mean Magnitude			Modal Magnitude			Semi-Probabilistic		
Profile	475	1039	2475	475	1039	2475	475	1039	2475	475	1039	2475
1	87.2	184.8	258.5	160.5	252.8	310.4	18.5	125.5	254.5	198.2	234.7	272.8
2	6.8	16.2	25.4	12.5	23.4	27.0	3.0	6.9	23.5	20.1	25.3	28.9
3	36.3	110.0	179.7	84.1	159.6	204.9	1.2	53.4	160.7	130.8	169.6	205.1
4	8.8	60.1	130.4	33.1	114.7	202.1	0.5	7.9	115.7	81.3	123.1	188.9
5	3.3	7.5	14.8	4.6	10.5	18.0	2.8	3.5	10.7	12.0	19.2	26.7
6	54.9	149.2	236.7	116.9	221.5	270.5	9.8	77.6	223.0	175.7	222.2	260.6
7	3.1	16.5	31.4	12.4	26.8	40.3	0.1	2.8	27.0	22.2	30.4	39.4
8	1.1	8.0	20.0	2.4	10.5	35.1	0.0	0.6	10.8	18.4	27.0	43.1
9	2.9	4.3	5.4	3.7	4.5	5.4	2.9	3.2	4.5	5.0	6.4	7.9
10	2.5	9.8	20.6	5.0	18.4	31.7	0.1	3.4	18.8	15.9	24.7	35.5
11	0.5	3.7	9.2	0.8	4.7	15.1	0.0	0.2	4.8	8.5	13.1	19.8
12	1.2	13.0	39.1	3.0	29.4	62.4	0.0	0.8	29.9	19.7	42.9	73.9
13	17.3	77.2	141.8	50.1	146.7	180.9	0.8	20.6	148.2	97.5	136.2	170.5
14	0.6	5.0	14.3	0.5	4.6	25.9	0.0	0.1	4.8	11.6	19.0	31.8
15	18.1	39.7	57.3	33.1	50.5	66.5	4.0	28.9	50.9	42.5	51.7	66.9
16	0.0	0.2	1.6	0.0	0.3	2.9	0.0	0.0	0.4	0.5	1.8	3.6
17	1.0	5.9	16.6	4.2	9.3	26.8	0.0	1.0	9.5	8.6	15.7	33.6
18	0.0	0.1	0.7	0.0	0.0	0.6	0.0	0.0	0.0	0.8	1.4	3.5
19	28.8	80.6	127.6	80.2	110.7	144.7	0.8	46.3	111.3	102.8	118.9	139.2
20	0.8	16.1	52.9	2.2	33.8	93.1	0.0	0.5	34.9	25.2	56.4	102.5

Table 6-14: Lateral Spread Displacements in Eureka Calculated with the Robertson and Wride Liquefaction Triggering Procedure (Lateral Spread Geometry 2)

	Full Probabilistic			Mean Magnitude			Modal Magnitude			Semi-Probabilistic		
Profile	475	1039	2475	475	1039	2475	475	1039	2475	475	1039	2475
1	385.0	437.7	487.2	344.4	344.7	344.7	343.6	344.5	344.7	328.2	330.7	332.9
2	41.2	46.3	50.6	44.0	46.9	49.3	40.9	45.1	47.2	35.1	35.6	36.1
3	274.7	297.7	316.5	295.0	297.8	300.8	291.3	296.6	298.3	255.4	259.1	262.7
4	296.1	341.6	373.8	290.8	292.7	293.6	287.9	291.4	292.9	271.0	273.3	275.2
5	42.2	51.9	61.4	80.4	91.4	93.9	71.2	84.8	92.1	53.8	56.3	58.4
6	348.6	383.3	408.7	327.6	328.1	328.3	326.8	327.7	328.2	298.6	300.4	302.4
7	57.8	64.7	69.5	63.8	64.4	64.8	63.4	64.1	64.5	57.6	58.5	59.3
8	69.7	89.3	108.9	125.7	128.6	129.3	119.6	127.1	128.8	83.4	86.3	89.1
9	10.3	12.8	15.6	21.1	23.6	25.0	18.6	22.3	23.9	13.1	13.6	14.3
10	55.9	70.6	83.3	98.8	106.1	109.0	90.3	101.4	106.6	65.1	67.7	70.3
11	36.3	48.3	61.0	65.3	69.3	70.6	61.8	66.7	69.7	45.6	47.5	49.3
12	120.5	142.5	159.9	159.7	167.3	170.4	154.0	162.8	168.2	132.8	136.2	139.4
13	238.8	268.6	289.7	217.9	218.0	218.0	216.6	217.9	218.0	205.5	206.6	208.1
14	68.4	93.4	119.9	136.2	139.6	140.3	129.8	137.7	139.8	90.7	95.3	100.0
15	100.9	114.4	121.7	105.2	109.5	110.6	104.8	105.7	110.5	99.7	100.9	101.6
16	6.2	7.8	9.5	17.7	20.2	20.2	17.2	18.6	20.2	9.3	10.3	11.3
17	69.4	85.0	95.2	109.3	113.5	115.8	105.1	112.0	113.7	82.5	85.5	88.3
18	9.9	14.2	17.2	34.9	48.4	51.8	27.5	37.6	49.4	16.8	18.3	19.8
19	191.3	217.0	241.4	201.5	204.4	204.9	198.5	202.8	204.6	177.9	179.8	181.7
20	180.2	220.8	255.5	265.5	278.0	282.2	253.5	271.1	278.8	200.6	206.8	213.3

Table 6-15: Lateral Spread Displacements in Santa Monica Calculated with the Robertson and Wride Liquefaction Triggering Procedure (Lateral Spread Geometry 2)

	Full Probabilistic			Mean Magnitude			Modal Magnitude			Semi-Probabilistic		
Profile	475	1039	2475	475	1039	2475	475	1039	2475	475	1039	2475
1	359.7	409.2	455.3	341.4	342.8	344.3	342.3	343.6	344.4	320.6	323.7	326.9
2	38.3	43.2	47.1	34.0	37.9	43.0	36.4	40.8	44.4	33.6	34.1	34.8
3	255.4	279.2	296.6	262.3	285.2	293.8	278.8	291.2	295.5	244.4	248.8	253.4
4	260.9	312.9	348.3	280.9	285.3	290.2	283.7	287.8	291.0	262.7	266.0	269.6
5	33.2	41.8	49.5	48.1	63.8	77.3	59.5	71.0	81.9	47.2	49.4	52.4
6	329.8	364.5	392.2	316.7	324.5	327.5	323.3	326.7	327.7	292.8	295.3	297.6
7	51.5	58.4	63.7	59.4	63.2	63.7	62.9	63.4	63.9	54.3	55.6	56.9
8	54.6	72.8	89.3	93.5	113.3	124.3	107.4	119.4	126.2	75.1	78.5	81.9
9	8.5	10.5	12.7	11.7	15.4	20.4	14.0	18.5	21.4	11.6	12.1	12.8
10	45.1	58.4	69.4	67.2	84.9	96.3	80.1	90.1	99.9	57.4	60.5	63.6
11	27.1	37.0	48.0	49.7	58.0	64.2	55.8	61.7	65.8	40.4	42.6	44.6
12	99.7	122.3	138.7	135.9	150.1	157.6	146.8	153.9	160.8	121.3	125.7	130.7
13	222.4	252.3	275.6	211.3	214.8	217.8	214.0	216.5	217.9	201.6	203.4	204.9
14	47.8	67.8	89.0	108.9	123.9	134.0	120.2	129.7	136.9	75.6	81.1	87.9
15	89.7	103.6	113.0	98.1	103.8	105.0	101.0	104.8	105.3	94.1	96.6	99.0
16	4.4	5.6	6.7	9.2	14.5	17.6	13.6	17.2	17.7	6.9	7.7	8.8
17	53.4	69.8	81.0	85.4	102.5	107.0	98.3	105.1	110.6	73.3	76.8	80.7
18	6.2	9.5	12.9	16.0	22.4	33.1	19.3	27.3	35.5	13.2	14.4	16.1
19	174.9	198.8	221.2	187.5	195.2	200.7	193.2	198.4	202.0	171.3	174.4	176.9
20	145.2	184.4	216.4	219.7	244.0	261.4	237.3	253.3	267.5	181.7	188.6	196.9

Table 6-16: Lateral Spread Displacements in Portland Calculated with the Robertson and Wride Liquefaction Triggering Procedure (Lateral Spread Geometry 2)

	Full Probabilistic			Mean Magnitude			Modal Magnitude			Semi-Probabilistic		
Profile	475	1039	2475	475	1039	2475	475	1039	2475	475	1039	2475
1	238.8	320.5	385.9	334.3	341.0	342.5	342.0	343.6	344.4	302.9	314.3	320.9
2	22.1	32.4	41.1	30.3	33.1	37.0	35.3	40.8	44.3	30.9	32.5	33.6
3	159.9	231.3	271.5	233.5	257.2	281.5	272.4	291.3	295.4	226.8	237.5	245.0
4	117.4	218.1	293.3	260.3	278.2	284.3	282.6	287.9	290.9	234.4	254.5	262.9
5	13.9	26.6	39.3	25.0	43.6	61.1	55.2	71.1	81.7	35.2	42.8	47.3
6	209.6	295.5	349.2	288.2	312.0	323.6	321.7	326.7	327.7	279.8	288.3	293.1
7	27.3	45.1	56.4	49.0	56.8	63.0	62.2	63.4	63.9	47.0	51.7	54.4
8	19.7	43.3	66.4	56.9	86.8	109.7	102.2	119.5	126.2	58.9	69.2	75.5
9	5.3	7.4	9.8	6.4	10.4	14.4	13.1	18.5	21.4	9.1	10.6	11.6
10	19.7	36.4	53.5	44.0	62.9	81.9	74.9	90.2	99.7	45.0	52.5	57.9
11	9.0	21.0	33.8	34.5	47.2	56.5	53.4	61.8	65.7	28.4	36.7	40.8
12	36.7	80.9	115.5	103.7	129.6	148.2	142.7	154.0	160.6	98.6	113.0	121.9
13	124.1	195.2	239.0	196.5	209.6	214.3	213.3	216.6	217.9	190.1	197.7	201.9
14	14.5	36.5	61.7	65.7	102.7	121.5	116.5	129.7	136.8	47.9	65.3	76.3
15	53.4	79.3	98.9	85.0	97.9	102.0	98.6	104.8	105.3	82.4	90.1	94.4
16	1.6	3.4	5.4	3.4	6.2	13.8	13.1	17.2	17.7	4.3	5.5	7.0
17	15.8	41.6	65.3	52.2	82.0	100.1	93.3	105.1	110.5	54.2	66.2	73.7
18	0.8	4.3	8.6	5.3	14.3	20.4	17.8	27.4	35.4	7.1	10.9	13.3
19	110.9	158.3	189.2	166.1	184.5	194.1	191.2	198.5	201.9	155.6	166.0	171.8
20	50.4	115.7	171.8	154.9	212.0	239.6	231.2	253.4	267.2	142.2	168.0	182.3

Table 6-17: Lateral Spread Displacements in Salt Lake City Calculated with the Robertson and Wride Liquefaction Triggering Procedure (Lateral Spread Geometry 2)

	Full Probabilistic			Mean Magnitude			Modal Magnitude			Semi-Probabilistic		
Profile	475	1039	2475	475	1039	2475	475	1039	2475	475	1039	2475
1	253.8	336.6	402.9	335.6	341.6	343.5	337.6	341.8	343.6	311.3	319.4	324.8
2	23.6	34.3	42.9	30.6	34.5	40.5	30.9	34.8	41.0	32.0	33.3	34.4
3	173.2	244.2	281.9	235.9	265.5	290.7	239.6	268.6	291.5	234.8	242.8	250.3
4	137.5	240.5	313.0	263.3	281.5	287.6	267.0	282.0	288.0	250.0	260.9	267.2
5	16.1	31.3	44.3	26.5	50.4	70.4	29.1	52.6	71.6	40.7	46.3	50.4
6	224.3	309.4	360.8	290.4	318.8	326.5	293.5	320.3	326.9	286.2	291.9	296.1
7	30.5	49.1	59.8	49.6	60.7	63.4	50.1	61.4	63.4	50.5	53.8	55.9
8	24.6	51.0	75.4	59.2	96.7	119.1	62.6	99.2	119.9	66.6	74.0	79.8
9	5.7	8.2	10.9	6.5	12.2	18.3	6.8	12.6	18.7	10.1	11.3	12.4
10	22.8	42.1	60.1	45.2	69.7	89.8	47.4	72.2	90.6	50.5	56.5	61.5
11	11.3	25.7	39.3	35.4	51.0	61.5	37.2	52.1	62.0	34.1	39.7	43.2
12	45.7	93.5	126.9	106.3	138.3	153.7	110.2	140.2	154.2	109.5	119.5	127.6
13	136.3	207.5	249.5	197.6	212.3	216.4	199.5	212.7	216.7	196.3	200.8	203.8
14	18.8	46.1	73.8	69.2	111.9	129.4	75.2	114.0	130.0	61.0	73.3	83.7
15	58.2	86.1	105.6	86.6	98.3	104.7	87.8	98.4	104.8	88.4	93.5	97.2
16	2.0	4.0	6.4	3.5	10.7	17.0	3.6	11.9	17.4	4.9	6.6	8.1
17	20.6	50.4	73.9	55.3	88.0	104.9	59.6	90.4	105.2	63.1	71.8	78.3
18	1.3	6.2	10.8	5.9	16.7	26.9	6.3	17.2	27.8	10.1	12.7	15.0
19	119.4	167.3	199.4	168.0	189.0	198.2	170.7	190.0	198.6	163.7	170.3	175.3
20	63.8	135.7	191.9	159.6	223.8	252.7	167.8	227.4	254.0	161.7	178.7	191.8

Table 6-18: Lateral Spread Displacements in San Francisco Calculated with the Robertson and Wride Liquefaction Triggering Procedure (Lateral Spread Geometry 2)

	Full Probabilistic			Mean Magnitude			Modal Magnitude			Semi-Probabilistic		
Profile	475	1039	2475	475	1039	2475	475	1039	2475	475	1039	2475
1	376.5	426.1	472.8	342.3	343.5	344.4	343.1	344.0	344.5	323.1	325.8	328.4
2	40.2	44.8	48.7	36.4	40.4	44.0	38.8	42.1	45.2	34.0	34.6	35.1
3	266.2	287.7	304.9	278.5	290.5	295.1	287.6	292.7	296.6	248.0	251.6	255.5
4	282.7	329.0	361.2	283.7	287.4	290.8	286.1	289.4	291.4	265.3	268.4	271.1
5	37.6	46.0	54.1	59.3	70.1	80.6	66.3	74.9	84.9	49.2	51.2	53.7
6	342.4	375.5	400.6	323.2	326.4	327.6	325.4	327.4	327.7	294.8	296.8	298.8
7	54.9	61.5	66.0	62.8	63.4	63.9	63.3	63.6	64.1	55.3	56.4	57.5
8	62.6	80.5	97.9	107.2	118.8	125.8	115.5	122.5	127.1	78.1	80.7	83.6
9	9.4	11.5	13.9	13.9	18.1	21.1	16.5	19.7	22.3	12.0	12.6	13.1
10	50.9	64.0	75.1	79.8	89.6	99.0	87.1	94.0	101.4	59.9	62.5	65.1
11	31.7	42.3	53.8	55.6	61.3	65.4	59.4	63.3	66.8	42.0	43.9	45.8
12	110.7	131.6	147.2	146.6	153.5	159.9	151.7	156.1	162.9	125.4	128.8	133.0
13	233.1	261.9	282.8	214.0	216.3	217.9	215.3	217.5	217.9	203.0	204.3	205.5
14	57.7	78.8	101.4	120.1	129.2	136.3	126.1	132.2	137.7	80.5	85.4	91.2
15	96.1	109.0	116.3	100.8	104.7	105.2	104.7	104.9	105.7	95.9	98.1	100.0
16	5.2	6.4	7.6	13.6	16.9	17.7	15.7	17.5	18.7	7.6	8.3	9.4
17	61.8	76.5	86.5	98.1	104.8	109.5	103.5	106.0	112.0	76.2	79.2	82.6
18	8.0	11.4	14.3	19.2	26.7	35.0	24.2	31.0	37.7	14.2	15.5	16.9
19	184.3	208.1	231.1	193.1	198.1	201.6	196.4	199.9	202.8	173.8	176.0	178.0
20	163.5	201.1	232.8	237.0	252.3	265.8	247.7	258.0	271.2	187.7	193.8	201.1

Table 6-19: Lateral Spread Displacements in San Jose Calculated with the Robertson and Wride Liquefaction Triggering Procedure (Lateral Spread Geometry 2)

	Full Probabilistic			Mean Magnitude			Modal Magnitude			Semi-Probabilistic		
Profile	475	1039	2475	475	1039	2475	475	1039	2475	475	1039	2475
1	404.6	449.1	494.1	342.3	343.6	344.4	342.2	343.3	344.2	324.1	326.2	328.6
2	42.9	46.7	50.0	36.4	40.7	43.7	35.8	39.6	42.7	34.2	34.7	35.1
3	278.8	295.9	310.8	278.5	291.0	294.7	275.1	289.1	293.5	249.6	252.3	255.8
4	310.2	345.3	372.2	283.7	287.7	290.6	283.1	286.8	290.0	266.4	268.9	271.1
5	42.0	49.4	56.9	59.3	70.8	79.6	57.1	68.1	76.6	49.8	51.6	53.8
6	361.5	389.3	409.4	323.2	326.6	327.6	322.3	325.9	327.5	295.6	297.1	298.8
7	58.5	63.8	67.7	62.8	63.4	63.8	62.6	63.3	63.6	55.6	56.6	57.6
8	72.5	88.2	105.4	107.2	119.4	125.4	104.4	117.2	123.7	79.0	81.1	83.8
9	10.5	12.5	14.8	13.9	18.4	20.9	13.4	17.4	20.2	12.2	12.7	13.2
10	58.2	69.1	79.0	79.9	90.0	98.3	77.1	88.4	95.6	60.8	63.0	65.3
11	37.1	47.3	58.1	55.7	61.7	65.0	54.4	60.3	63.9	42.7	44.1	45.9
12	122.4	138.6	152.7	146.6	153.8	159.0	144.5	152.6	157.2	126.5	129.7	133.5
13	249.8	273.1	290.4	214.0	216.5	217.9	213.6	215.7	217.7	203.5	204.6	205.5
14	68.3	88.6	110.5	120.1	129.6	135.6	118.3	127.6	133.4	82.5	86.5	91.3
15	103.6	112.9	118.6	100.9	104.8	105.2	99.6	104.7	105.0	96.8	98.3	100.0
16	5.7	6.8	8.0	13.6	17.1	17.6	13.4	16.3	17.6	7.9	8.5	9.4
17	70.2	81.3	89.4	98.1	105.0	108.6	95.5	104.2	106.6	77.4	79.9	82.8
18	9.7	13.0	15.1	19.2	27.2	34.6	18.3	25.4	32.4	14.7	15.8	17.0
19	197.6	219.0	240.3	193.2	198.4	201.3	192.1	197.2	200.4	174.6	176.3	178.2
20	184.3	215.4	244.2	237.1	253.1	264.5	234.0	250.2	260.3	190.2	195.2	201.4

Table 6-20: Lateral Spread Displacements in Seattle Calculated with the Robertson and Wride Liquefaction Triggering Procedure (Lateral Spread Geometry 2)

	Full Probabilistic			Mean Magnitude			Modal Magnitude			Semi-Probabilistic		
Profile	475	1039	2475	475	1039	2475	475	1039	2475	475	1039	2475
1	321.1	377.4	429.0	340.7	342.0	343.3	340.9	342.1	343.3	316.3	320.5	324.4
2	33.0	40.3	44.9	32.3	35.2	39.6	32.8	35.5	39.8	32.8	33.5	34.3
3	230.9	265.3	287.1	253.3	271.5	289.2	255.9	273.7	289.6	239.4	244.5	249.8
4	216.3	281.6	329.7	275.2	282.4	286.8	277.3	282.9	287.0	257.1	262.4	266.8
5	25.9	36.6	45.1	40.0	54.7	68.2	42.3	56.1	68.8	43.9	47.1	50.0
6	296.8	343.1	377.3	307.4	321.3	325.9	310.5	322.0	326.1	289.5	292.8	295.8
7	44.6	54.3	61.1	55.1	62.1	63.3	56.1	62.4	63.3	52.7	54.2	55.8
8	41.7	61.4	80.0	80.3	101.4	117.2	84.6	103.2	117.7	70.8	75.0	79.2
9	7.2	9.2	11.4	9.2	12.9	17.4	10.0	13.2	17.7	10.8	11.5	12.3
10	35.6	50.1	63.3	59.5	74.1	88.4	61.8	75.9	88.8	53.8	57.3	61.1
11	20.0	30.7	41.7	44.5	53.1	60.3	46.4	53.9	60.7	37.6	40.5	42.9
12	79.0	108.9	130.3	124.3	142.0	152.6	128.0	143.6	152.9	115.2	120.8	126.9
13	195.8	233.3	263.2	207.6	213.1	215.7	208.9	213.5	215.9	198.8	201.6	203.8
14	34.3	55.5	77.2	96.0	115.9	127.7	100.7	117.4	128.2	68.0	75.0	82.7
15	77.8	95.1	108.3	97.3	98.6	104.7	97.9	99.0	104.7	91.5	94.3	97.0
16	3.3	5.0	6.1	5.0	12.9	16.3	5.6	13.2	16.5	5.9	6.8	7.9
17	39.5	60.2	75.1	77.0	92.6	104.2	80.5	94.3	104.4	68.3	73.2	77.7
18	3.8	7.5	11.0	11.5	17.6	25.4	13.3	18.0	25.8	11.6	13.1	14.8
19	157.3	183.8	208.5	181.5	190.9	197.2	183.6	191.6	197.5	167.5	171.4	174.9
20	112.1	160.5	199.2	204.0	230.2	250.3	209.5	232.6	251.0	171.2	181.0	190.6

Table 6-21: Lateral Spread Displacements in Memphis Calculated with the Robertson and Wride Liquefaction Triggering Procedure (Lateral Spread Geometry 2)

	Full Probabilistic			Mean Magnitude			Modal Magnitude			Semi-Probabilistic		
Profile	475	1039	2475	475	1039	2475	475	1039	2475	475	1039	2475
1	178.3	300.6	375.8	328.8	341.1	343.0	339.2	342.2	343.9	294.2	313.4	321.3
2	16.8	28.9	39.6	29.6	33.4	38.4	31.4	35.9	41.9	30.2	32.3	33.7
3	113.2	215.3	268.5	226.2	258.5	286.6	245.2	275.9	292.4	221.2	236.7	245.5
4	72.6	195.3	285.9	249.5	279.1	285.7	270.4	283.3	289.1	223.3	253.4	263.4
5	9.2	24.0	39.2	22.0	45.0	65.0	33.6	57.6	74.3	32.3	42.3	47.7
6	153.2	273.5	341.7	283.1	313.4	325.0	299.0	322.6	327.4	274.8	287.8	293.4
7	18.4	41.4	56.0	46.8	57.6	63.3	51.8	62.6	63.5	44.6	51.3	54.6
8	11.1	39.0	65.2	50.8	89.0	114.5	68.7	105.2	121.9	53.9	68.4	75.9
9	4.2	6.9	9.7	6.0	10.7	16.0	7.4	13.5	19.5	8.7	10.5	11.7
10	12.5	32.9	52.4	40.7	64.2	86.1	51.8	77.9	93.2	41.7	52.0	58.0
11	5.2	18.9	33.6	30.9	47.9	58.7	39.8	54.7	63.0	25.2	36.2	41.0
12	19.8	72.1	114.4	94.7	131.6	151.0	115.4	145.2	155.7	91.4	112.2	122.3
13	86.8	176.2	233.2	193.1	210.1	215.0	202.4	213.7	217.4	184.2	197.5	202.1
14	7.7	32.9	61.9	55.0	104.7	125.0	83.8	118.8	131.5	42.0	64.3	76.7
15	38.3	74.3	97.7	78.9	98.0	104.5	91.6	99.9	104.9	76.9	89.6	94.6
16	0.7	3.0	5.6	3.2	7.1	15.1	4.0	13.4	17.5	4.1	5.3	7.1
17	8.0	37.2	64.8	43.9	83.0	103.0	65.3	96.2	105.8	47.4	65.5	74.2
18	0.3	3.7	8.8	3.7	15.0	23.3	7.3	18.5	30.2	5.7	10.6	13.4
19	80.9	149.5	186.1	160.6	185.5	195.8	174.6	192.4	199.7	150.7	165.4	172.2
20	26.4	103.1	169.9	139.8	214.2	245.9	182.2	234.8	257.0	129.1	166.5	183.0

Table 6-22: Lateral Spread Displacements in Charleston Calculated with the Robertson and Wride Liquefaction Triggering Procedure (Lateral Spread Geometry 2)

	Full Probabilistic			Mean Magnitude			Modal Magnitude			Semi-Probabilistic		
Profile	475	1039	2475	475	1039	2475	475	1039	2475	475	1039	2475
1	159.3	295.6	375.6	325.3	341.3	344.1	338.8	342.2	344.4	292.7	314.9	323.2
2	14.9	28.1	39.4	29.2	33.9	42.3	31.3	36.0	44.3	30.1	32.6	34.0
3	98.3	210.6	270.2	222.2	261.7	292.9	243.6	276.4	295.5	220.2	238.3	248.1
4	60.2	190.1	287.3	241.6	280.6	289.6	269.6	283.3	291.0	221.3	255.4	265.4
5	7.5	23.7	40.5	21.4	47.7	75.4	32.5	57.9	81.7	31.9	43.2	49.1
6	134.4	266.8	341.4	280.5	316.2	327.5	297.4	322.7	327.7	273.9	288.9	294.9
7	15.6	40.2	56.8	45.2	59.1	63.6	51.3	62.7	63.9	44.3	52.0	55.3
8	8.8	38.6	67.0	47.5	92.8	122.8	66.9	105.5	126.2	53.1	69.8	78.1
9	3.8	6.9	9.9	5.9	11.5	19.9	7.2	13.6	21.4	8.6	10.7	12.0
10	10.2	32.4	53.7	38.3	66.6	94.4	50.6	78.2	99.8	41.3	53.0	60.0
11	4.2	18.9	35.0	28.3	49.4	63.5	39.0	54.8	65.7	24.8	37.2	42.1
12	14.9	70.7	117.0	87.8	135.2	156.5	113.9	145.4	160.7	90.4	113.8	125.3
13	74.3	170.8	233.1	191.2	211.0	217.6	201.5	213.8	217.9	183.4	198.2	203.1
14	5.8	33.0	65.2	48.6	108.2	132.6	81.5	119.1	136.8	41.2	66.3	80.6
15	33.7	73.5	98.9	75.7	98.1	104.9	90.3	100.1	105.3	76.2	90.6	96.0
16	0.3	2.9	5.9	3.1	8.8	17.6	3.9	13.5	17.7	4.1	5.6	7.6
17	6.1	36.8	66.9	39.8	84.9	106.1	63.7	96.6	110.5	46.4	67.1	76.4
18	0.2	3.8	9.5	2.8	15.8	31.4	7.0	18.6	35.5	5.5	11.1	14.3
19	71.6	145.7	187.2	157.4	187.2	200.1	173.5	192.5	201.9	149.9	166.6	173.8
20	19.1	101.5	174.2	131.7	218.7	258.6	178.0	235.2	267.3	127.1	169.5	188.1

6.4.2 Presentation of Idriss and Boulanger Results

Table 6-23 to Table 6-42 present the results of the lateral spread analysis using the Boulanger and Idriss liquefaction triggering procedure for both site geometries. The same process and organization that was used with the Robertson and Wride procedure was also used with the Boulanger and Idriss procedure. Each table contains the results for the fully-probabilistic, pseudo-probabilistic (mean and modal magnitude), and semi-probabilistic methods. The results of all 10 soil profiles are shown, as well as the results for all three return periods (475 years, 1039 years, and 2475 years). Each value represents the lateral spread displacement at the specified site in centimeters.

Table 6-23: Lateral Spread Displacements in Butte Calculated with the Boulanger and Idriss Liquefaction Triggering Procedure (Lateral Spread Geometry 1)

	Full Probabilistic			Mean Magnitude			Modal Magnitude			Semi-Probabilistic		
Profile	475	1039	2475	475	1039	2475	475	1039	2475	475	1039	2475
1	422.0	889.5	1206.1	766.3	982.7	1023.8	605.6	909.3	1017.2	918.7	1006.3	1026.3
2	61.9	112.6	150.0	95.6	117.3	128.8	83.8	110.8	122.8	112.0	122.4	136.9
3	177.6	624.5	949.5	500.0	792.9	874.5	273.1	689.9	847.1	725.9	841.0	896.5
4	156.1	564.7	943.0	403.2	786.2	865.1	274.3	554.2	845.2	658.2	839.2	878.2
5	16.2	63.4	123.2	30.9	94.1	127.8	18.5	61.7	112.5	75.3	111.8	148.9
6	261.8	741.7	1073.5	635.7	879.3	932.8	306.2	814.6	909.8	840.9	907.1	959.5
7	49.9	143.1	200.0	130.0	167.7	180.0	79.8	155.2	175.1	158.9	174.6	184.6
8	25.9	139.6	259.5	92.1	209.9	265.3	41.5	160.1	239.6	178.1	238.1	293.6
9	14.6	20.2	26.2	17.3	18.5	21.6	17.1	17.5	19.6	18.4	20.1	25.1
10	32.1	141.0	272.6	89.0	217.2	279.6	53.0	140.2	255.7	172.5	252.0	308.6
11	9.8	52.4	125.9	25.9	95.6	145.0	16.8	55.8	123.3	61.0	118.7	157.9
12	38.3	291.8	504.8	162.8	422.2	478.3	59.7	351.5	465.8	378.7	456.3	485.6
13	177.9	530.6	768.1	445.3	635.5	664.3	275.2	597.9	654.1	607.2	650.7	672.0
14	4.7	73.7	241.8	25.8	134.9	310.9	6.1	66.2	231.4	99.8	214.4	375.1
15	100.7	279.1	375.8	242.4	322.1	326.1	164.7	302.5	325.6	307.7	325.6	327.1
16	7.0	34.6	58.2	28.6	44.2	58.1	11.6	42.1	50.4	43.1	49.1	61.5
17	28.2	203.3	362.5	99.4	302.1	348.6	39.2	212.0	332.2	259.5	329.9	359.5
18	4.1	83.3	172.6	29.1	136.2	177.5	3.5	93.9	164.7	111.8	159.2	183.9
19	176.6	400.9	558.1	311.4	469.1	517.1	268.7	393.8	496.9	419.0	493.5	537.7
20	15.0	306.3	643.6	111.3	481.3	672.2	13.2	365.5	585.5	416.7	573.8	750.4

Table 6-24: Lateral Spread Displacements in Eureka Calculated with the Boulanger and Idriss Liquefaction Triggering Procedure (Lateral Spread Geometry 1)

	Full Probabilistic			Mean Magnitude			Modal Magnitude			Semi-Probabilistic		
Profile	475	1039	2475	475	1039	2475	475	1039	2475	475	1039	2475
1	1502.2	1669.8	1822.5	1034.7	1038.6	1039.0	1031.8	1035.7	1038.7	1038.0	1038.7	1039.1
2	204.5	231.0	258.7	157.7	161.4	167.6	155.6	158.3	163.5	160.0	163.1	166.3
3	1172.1	1245.9	1314.3	933.4	936.1	938.1	930.7	933.7	935.9	935.4	936.6	938.0
4	1246.1	1347.1	1433.8	909.4	912.2	915.8	907.6	910.0	913.4	911.5	912.9	915.4
5	244.8	297.5	348.2	225.5	246.2	263.7	212.5	228.6	245.2	239.4	253.0	264.5
6	1353.1	1469.9	1576.4	1006.6	1006.7	1007.2	1006.6	1006.6	1006.8	1006.6	1006.8	1007.1
7	238.8	256.7	272.1	198.7	198.7	198.7	197.9	198.7	198.7	198.7	198.7	198.7
8	472.4	575.0	678.0	382.6	391.0	398.1	372.0	384.8	392.4	389.2	392.7	397.5
9	52.3	70.3	89.4	54.6	63.8	67.8	46.1	57.2	63.7	62.4	65.9	68.5
10	471.7	556.6	633.2	383.9	392.0	399.8	379.0	385.7	392.9	389.7	394.9	400.2
11	263.1	330.7	389.4	203.4	209.7	214.9	196.9	204.8	211.0	208.4	211.4	214.6
12	627.5	668.0	697.8	514.8	523.3	532.7	509.7	516.0	523.9	520.6	525.7	531.1
13	926.1	976.6	1007.5	686.0	686.0	686.0	686.0	686.0	686.0	686.0	686.0	686.0
14	600.8	748.8	891.8	463.1	463.4	463.4	461.1	463.4	463.4	463.4	463.4	463.4
15	406.8	412.7	416.9	333.0	334.7	335.5	331.0	334.4	334.7	334.5	335.0	335.9
16	78.9	87.9	94.7	64.5	64.5	64.5	64.5	64.5	64.5	64.5	64.5	64.5
17	466.2	489.6	505.5	378.0	381.7	382.5	376.2	379.1	382.3	380.8	381.9	382.1
18	254.8	279.6	295.9	208.4	209.9	210.1	206.2	209.0	209.9	209.8	210.0	210.3
19	773.4	874.0	976.5	586.8	592.4	599.1	582.4	588.0	593.7	591.1	594.4	597.9
20	1119.5	1304.2	1474.9	913.6	923.6	927.5	901.0	915.5	924.6	921.8	925.2	927.3

Table 6-25: Lateral Spread Displacements in Santa Monica Calculated with the Boulanger and Idriss Liquefaction Triggering Procedure (Lateral Spread Geometry 1)

	Full Probabilistic			Mean Magnitude			Modal Magnitude			Semi-Probabilistic		
Profile	475	1039	2475	475	1039	2475	475	1039	2475	475	1039	2475
1	1467.8	1634.3	1788.4	1028.2	1030.3	1033.4	1029.7	1031.8	1034.8	1031.3	1033.7	1036.8
2	192.5	217.5	243.2	150.1	154.3	156.9	153.2	155.6	157.8	155.1	156.8	158.7
3	1138.4	1212.1	1280.3	924.4	929.7	932.3	928.4	930.8	933.3	930.3	932.0	934.2
4	1213.3	1318.5	1407.1	903.1	906.8	908.7	905.7	907.8	909.5	907.3	908.6	910.5
5	210.9	253.2	292.2	188.0	204.3	219.5	198.4	212.6	225.7	209.3	219.4	231.7
6	1314.1	1434.7	1541.9	1005.9	1006.6	1006.6	1006.5	1006.6	1006.6	1006.6	1006.6	1006.6
7	229.8	246.5	261.2	192.6	195.7	198.7	193.9	197.6	198.7	197.0	198.7	198.7
8	420.3	512.5	605.2	351.7	365.7	377.8	362.2	372.1	382.8	369.5	377.5	386.0
9	41.6	52.2	64.1	36.3	42.9	49.9	40.8	46.3	54.7	44.9	49.6	60.0
10	428.9	509.8	584.9	364.1	375.0	381.7	371.3	379.2	384.1	378.0	381.6	387.2
11	232.1	294.8	350.8	182.0	191.6	201.1	188.8	196.8	203.5	194.2	201.2	206.0
12	606.9	645.4	672.4	497.2	505.3	512.4	502.1	509.7	514.7	508.4	512.6	517.6
13	907.1	963.1	996.7	684.3	686.0	686.0	685.1	686.0	686.0	686.1	686.0	686.0
14	524.5	671.6	817.2	441.2	457.5	462.5	451.8	461.1	463.3	459.6	462.4	463.4
15	404.0	409.7	412.0	329.9	330.4	332.0	330.1	330.9	333.4	330.8	331.8	334.4
16	75.6	84.6	93.0	64.5	64.5	64.5	64.5	64.5	64.5	64.5	64.5	64.5
17	452.4	476.3	493.8	372.3	375.3	377.2	374.1	376.2	378.2	376.0	377.2	379.8
18	239.2	262.7	279.9	197.9	203.9	207.5	201.4	206.2	208.6	205.2	207.6	209.3
19	730.8	827.7	925.8	569.4	578.1	585.0	575.4	582.4	586.9	580.0	584.7	589.1
20	1017.8	1193.6	1364.9	868.7	891.8	909.1	883.9	901.3	913.7	897.6	909.1	917.3

Table 6-26: Lateral Spread Displacements in Portland Calculated with the Boulanger and Idriss Liquefaction Triggering Procedure (Lateral Spread Geometry 1)

	Full Probabilistic			Mean Magnitude			Modal Magnitude			Semi-Probabilistic		
Profile	475	1039	2475	475	1039	2475	475	1039	2475	475	1039	2475
1	1000.9	1275.8	1494.9	1026.3	1027.7	1030.0	1031.0	1035.0	1038.3	1027.2	1029.1	1031.7
2	122.2	167.3	201.3	135.5	146.5	153.4	152.0	158.0	160.9	142.5	150.5	155.6
3	759.1	1043.0	1165.2	897.6	921.9	929.2	930.2	934.4	936.1	915.6	926.3	930.8
4	729.4	1059.1	1239.6	876.9	900.6	906.1	905.1	909.4	911.8	892.4	903.5	907.7
5	94.3	174.0	232.5	149.5	184.3	200.8	202.0	227.0	245.1	175.2	190.7	211.9
6	872.6	1171.8	1346.9	957.3	1004.1	1006.6	1005.7	1006.6	1006.7	992.0	1006.0	1006.6
7	166.4	215.0	236.0	184.7	192.0	194.2	193.1	197.7	198.7	190.3	192.8	197.0
8	196.2	338.9	457.5	293.5	343.8	363.7	363.8	383.4	390.8	326.4	354.7	371.5
9	21.6	33.1	47.7	25.8	33.5	41.9	43.6	54.9	63.1	29.9	37.7	46.2
10	201.5	354.3	461.3	303.9	355.9	372.5	368.1	383.5	390.9	334.8	365.3	378.7
11	90.6	173.4	254.6	157.4	177.2	189.9	189.3	203.5	209.1	168.4	184.3	196.2
12	377.0	555.9	621.4	484.3	494.2	503.1	503.0	515.8	522.5	489.9	498.4	509.1
13	611.0	817.6	922.5	671.1	682.2	685.2	683.7	686.0	686.0	678.4	684.2	686.0
14	174.4	397.4	583.5	375.6	433.7	453.6	448.0	462.4	463.4	415.5	443.2	460.4
15	316.2	388.0	406.1	326.8	329.8	330.2	330.4	332.2	334.6	328.6	330.0	330.8
16	42.9	67.7	78.6	61.1	64.4	64.5	64.5	64.5	64.5	63.1	64.5	64.5
17	280.3	414.6	463.1	360.8	370.6	374.4	373.1	377.8	381.0	368.5	372.4	376.1
18	126.6	206.7	250.4	183.4	194.7	202.0	200.1	207.8	209.9	188.7	198.4	205.9
19	471.4	633.8	761.9	537.5	564.9	576.4	575.5	587.6	592.0	555.5	570.8	582.1
20	467.7	849.1	1093.5	740.7	854.6	886.8	881.1	914.0	923.0	820.6	872.3	900.8

Table 6-27: Lateral Spread Displacements in Salt Lake City Calculated with the Boulanger and Idriss Liquefaction Triggering Procedure (Lateral Spread Geometry 1)

	Full Probabilistic			Mean Magnitude			Modal Magnitude			Semi-Probabilistic		
Profile	475	1039	2475	475	1039	2475	475	1039	2475	475	1039	2475
1	1035.6	1302.9	1520.0	1027.0	1028.9	1031.6	1027.2	1029.0	1031.9	1027.8	1030.2	1033.4
2	130.8	176.9	210.1	140.2	150.8	155.6	140.9	151.4	155.6	146.6	153.6	156.9
3	816.2	1075.6	1186.2	906.9	925.4	930.5	909.8	926.2	930.7	921.4	928.5	932.1
4	784.4	1097.5	1264.7	885.9	903.5	907.6	888.5	904.0	907.8	900.8	906.2	908.7
5	110.5	191.5	252.2	161.3	189.6	211.6	165.3	191.2	212.8	184.3	200.7	218.6
6	916.4	1208.6	1376.6	979.1	1006.0	1006.6	983.9	1006.1	1006.6	1004.3	1006.6	1006.6
7	175.9	220.1	242.6	187.9	192.9	197.8	188.6	193.1	198.1	192.2	194.7	198.7
8	226.3	370.5	489.4	310.0	354.0	371.3	315.1	355.9	372.3	343.0	363.8	377.6
9	23.2	36.8	53.0	27.4	37.5	45.6	27.9	38.3	46.2	33.3	41.7	50.2
10	236.2	388.7	492.8	321.8	365.8	378.8	326.6	367.2	379.3	356.8	372.9	381.6
11	110.6	194.1	276.3	162.0	183.9	196.4	163.7	185.2	197.3	176.9	190.4	200.8
12	417.5	576.1	637.1	487.3	498.2	509.2	488.1	498.9	509.8	494.3	503.4	512.3
13	645.8	837.3	936.1	675.2	684.4	686.0	676.4	684.6	686.0	682.2	685.5	686.0
14	230.0	447.8	632.1	399.0	443.4	461.0	404.5	445.3	461.4	433.7	453.9	462.5
15	327.5	392.8	408.0	327.8	329.9	330.9	328.1	330.0	331.0	329.8	330.3	331.9
16	50.0	71.2	81.7	62.2	64.5	64.5	62.5	64.5	64.5	64.4	64.5	64.5
17	306.0	428.1	471.3	363.8	372.8	376.1	365.1	373.0	376.3	371.0	374.6	377.2
18	144.8	220.2	261.0	185.3	198.6	206.1	186.3	199.2	206.3	195.3	202.5	207.4
19	501.4	659.3	787.0	547.2	570.7	581.9	549.8	571.8	582.7	564.3	576.6	585.0
20	553.4	923.8	1158.4	789.5	872.3	899.9	801.5	875.1	901.5	855.4	887.3	908.3

Table 6-28: Lateral Spread Displacements in San Francisco Calculated with the Boulanger and Idriss Liquefaction Triggering Procedure (Lateral Spread Geometry 1)

	Full Probabilistic			Mean Magnitude			Modal Magnitude			Semi-Probabilistic		
Profile	475	1039	2475	475	1039	2475	475	1039	2475	475	1039	2475
1	1489.1	1655.2	1806.9	1029.7	1031.6	1034.6	1031.0	1033.1	1036.4	1032.9	1034.8	1037.8
2	198.1	223.7	249.9	153.1	155.6	157.5	154.7	156.8	158.7	156.1	157.9	160.0
3	1156.5	1229.4	1296.7	928.3	930.7	933.2	930.4	932.4	934.5	932.0	933.8	935.4
4	1231.7	1333.7	1420.2	905.6	907.5	909.3	907.1	908.6	910.3	908.4	909.7	911.5
5	225.0	269.7	311.3	198.2	211.4	224.6	208.0	218.7	232.3	217.0	226.9	239.6
6	1336.1	1454.1	1560.6	1006.5	1006.6	1006.6	1006.6	1006.6	1006.6	1006.6	1006.6	1006.6
7	233.8	250.9	266.1	193.9	197.2	198.7	195.7	198.4	198.7	198.2	198.7	198.7
8	444.9	539.8	635.4	361.9	371.4	382.1	368.8	377.5	386.5	375.7	383.4	389.2
9	45.5	57.6	70.6	40.7	45.9	53.9	44.9	49.7	60.0	48.6	56.2	62.3
10	449.1	530.8	604.8	371.1	378.6	383.6	376.3	380.9	386.8	380.4	384.4	389.7
11	246.7	310.3	366.1	188.6	196.1	203.2	193.6	200.5	205.9	199.3	203.9	208.4
12	616.2	654.5	681.5	502.0	509.2	514.3	507.2	512.3	517.5	511.5	515.2	520.7
13	918.0	970.4	1002.2	685.0	686.0	686.0	685.9	686.0	686.0	686.0	686.0	686.0
14	563.1	710.5	854.5	451.6	460.5	463.1	458.5	462.2	463.4	461.9	463.3	463.4
15	405.5	410.5	413.0	330.1	330.8	333.0	330.6	331.5	334.4	331.3	333.8	334.5
16	77.4	86.3	93.9	64.5	64.5	64.5	64.5	64.5	64.5	64.5	64.5	64.5
17	459.5	482.5	497.9	374.1	376.1	377.9	375.5	376.9	379.5	376.7	378.4	381.1
18	246.2	269.8	286.0	201.3	205.9	208.3	204.5	207.2	209.2	207.1	208.8	209.9
19	752.7	850.2	949.4	575.4	581.9	586.6	579.8	584.7	589.3	584.3	587.2	591.3
20	1066.2	1243.7	1412.3	883.6	900.2	913.1	896.4	908.2	917.9	905.9	914.0	922.2

Table 6-29: Lateral Spread Displacements in San Jose Calculated with the Boulanger and Idriss Liquefaction Triggering Procedure (Lateral Spread Geometry 1)

	Full Probabilistic			Mean Magnitude			Modal Magnitude			Semi-Probabilistic		
Profile	475	1039	2475	475	1039	2475	475	1039	2475	475	1039	2475
1	1582.5	1735.5	1867.1	1029.7	1031.7	1034.1	1029.4	1031.1	1033.2	1033.6	1035.5	1038.1
2	212.8	237.1	262.3	153.3	155.6	157.2	152.7	155.2	156.8	156.8	158.2	160.5
3	1198.1	1263.7	1324.2	928.3	930.6	932.8	927.6	930.2	932.0	932.2	933.7	935.5
4	1292.8	1381.1	1455.9	905.8	907.6	909.1	905.2	907.3	908.6	908.7	910.0	911.6
5	248.9	288.0	325.9	198.6	212.0	221.9	196.0	208.8	218.4	220.4	228.8	239.9
6	1407.0	1511.2	1610.2	1006.6	1006.6	1006.6	1006.4	1006.6	1006.6	1006.6	1006.6	1006.6
7	243.8	258.6	271.7	194.2	197.7	198.7	193.8	197.1	198.7	198.6	198.7	198.7
8	497.1	585.8	677.3	362.1	371.7	379.9	360.3	369.4	377.2	378.1	384.7	389.0
9	51.1	62.8	73.4	40.7	45.9	52.0	39.9	44.6	49.2	49.7	55.9	62.1
10	497.2	571.2	635.0	371.6	378.9	383.0	370.6	377.6	381.2	381.8	385.2	390.4
11	283.4	339.6	386.6	188.9	196.6	202.3	187.8	194.5	200.5	201.2	204.4	208.2
12	639.9	669.0	689.9	502.4	509.5	513.2	501.1	508.0	512.0	512.7	515.6	520.4
13	951.9	988.2	1013.7	685.2	686.0	686.0	685.1	686.0	686.0	686.0	686.0	686.0
14	646.9	784.5	913.5	452.4	461.0	463.0	450.4	459.9	462.4	462.5	463.4	463.4
15	408.9	411.7	414.2	330.1	330.9	332.4	330.1	330.7	331.8	331.8	334.2	334.6
16	82.8	91.4	95.9	64.5	64.5	64.5	64.5	64.5	64.5	64.5	64.5	64.5
17	472.9	491.4	502.2	374.3	376.2	377.6	374.0	375.9	377.1	377.2	379.1	381.2
18	260.6	279.5	290.9	201.7	206.1	208.0	201.0	205.4	207.4	207.8	208.8	209.9
19	806.7	899.6	993.1	575.5	582.1	585.9	574.4	580.4	584.7	585.1	587.9	591.2
20	1166.9	1331.6	1470.2	884.4	900.5	911.3	881.6	897.0	908.2	909.8	915.0	921.7

Table 6-30: Lateral Spread Displacements in Seattle Calculated with the Boulanger and Idriss Liquefaction Triggering Procedure (Lateral Spread Geometry 1)

	Full Probabilistic			Mean Magnitude			Modal Magnitude			Semi-Probabilistic		
Profile	475	1039	2475	475	1039	2475	475	1039	2475	475	1039	2475
1	1323.2	1510.4	1688.4	1027.3	1029.2	1031.0	1027.6	1029.3	1031.1	1029.4	1031.1	1033.9
2	171.7	199.0	226.1	145.6	151.7	155.1	146.4	152.2	155.2	152.0	155.0	157.1
3	1061.2	1160.0	1237.2	920.1	926.6	930.2	921.4	927.1	930.3	927.1	930.1	932.6
4	1096.3	1244.1	1350.7	899.5	904.4	907.2	900.7	904.7	907.2	904.7	907.1	909.0
5	175.4	223.2	267.9	181.7	192.5	208.1	183.4	193.9	208.7	195.3	208.6	221.9
6	1200.1	1347.4	1472.7	1003.2	1006.1	1006.6	1004.1	1006.2	1006.6	1006.3	1006.6	1006.6
7	216.5	234.6	251.8	191.9	193.2	196.7	192.0	193.4	196.8	193.3	196.4	198.7
8	346.8	446.0	545.3	338.7	356.9	368.8	342.7	358.5	369.3	358.6	368.7	379.4
9	33.6	44.5	56.4	32.0	38.9	44.6	33.0	39.5	44.8	39.2	44.7	51.1
10	362.5	451.3	537.9	352.7	368.0	377.1	355.6	369.0	377.4	368.6	377.3	382.6
11	180.7	249.6	316.0	174.6	186.1	193.9	176.5	186.9	194.3	186.6	193.2	201.6
12	567.2	618.4	656.1	492.8	499.5	507.5	494.1	500.2	507.8	500.0	507.7	513.0
13	839.1	924.8	975.8	681.5	684.6	686.0	682.3	684.8	686.0	684.7	686.1	686.0
14	406.7	566.5	724.4	430.0	446.5	459.4	433.0	448.1	459.6	448.5	459.3	462.7
15	392.8	405.9	410.4	329.7	330.0	330.6	329.8	330.0	330.7	330.1	330.5	332.1
16	68.4	78.0	87.8	64.3	64.5	64.5	64.4	64.5	64.5	64.5	64.5	64.5
17	420.9	460.2	483.8	370.2	373.3	375.7	370.5	373.6	375.8	373.4	375.7	377.5
18	211.7	246.4	270.0	193.7	199.6	205.1	194.7	200.1	205.3	200.3	205.0	207.8
19	648.5	757.7	861.9	562.4	572.4	580.0	564.3	573.3	580.3	573.5	579.7	585.7
20	864.1	1068.5	1256.4	849.6	876.9	896.4	854.5	879.0	897.1	880.4	897.1	911.2

Table 6-31: Lateral Spread Displacements in Memphis Calculated with the Boulanger and Idriss Liquefaction Triggering Procedure (Lateral Spread Geometry 1)

	Full Probabilistic			Mean Magnitude			Modal Magnitude			Semi-Probabilistic		
Profile	475	1039	2475	475	1039	2475	475	1039	2475	475	1039	2475
1	828.8	1199.3	1435.8	1025.8	1027.7	1030.5	1027.2	1029.5	1032.7	1027.0	1028.6	1031.3
2	103.0	158.2	196.5	135.6	148.2	154.6	141.6	152.7	156.6	140.1	148.5	155.1
3	608.0	997.5	1145.0	895.3	923.0	929.9	912.2	927.8	931.9	906.3	923.5	930.3
4	575.8	981.5	1205.1	876.0	902.3	906.9	889.4	905.1	908.1	885.9	902.5	907.2
5	69.9	158.0	224.8	146.2	185.7	205.5	168.9	196.2	216.9	162.8	186.9	208.5
6	711.2	1110.1	1310.7	956.8	1005.1	1006.6	985.5	1006.3	1006.6	976.1	1005.1	1006.6
7	135.3	209.7	232.2	184.3	192.3	196.1	189.2	193.5	198.3	187.6	192.5	196.8
8	147.2	309.1	437.0	290.9	347.8	366.8	319.3	360.4	376.0	310.0	349.2	369.1
9	18.7	29.8	45.4	24.7	34.6	43.5	28.9	40.2	48.6	27.7	34.9	44.8
10	150.2	324.6	447.0	303.5	360.6	375.9	328.4	369.9	380.3	320.2	360.9	377.3
11	62.0	155.3	240.0	156.1	179.4	192.5	165.5	187.7	199.4	162.6	181.0	194.1
12	295.9	527.8	612.3	484.3	495.8	505.9	488.7	501.2	511.7	487.7	496.2	507.5
13	499.4	776.2	900.0	670.9	683.8	686.1	677.2	684.8	686.0	675.0	683.7	686.1
14	102.5	353.3	551.5	371.2	437.4	458.3	408.0	449.4	461.9	398.5	438.4	459.3
15	260.9	378.0	403.0	326.8	329.8	330.5	328.3	330.1	331.4	327.7	329.9	330.7
16	33.3	65.1	77.1	61.3	64.5	64.5	62.5	64.5	64.5	62.1	64.5	64.5
17	214.6	390.8	456.8	359.4	371.4	375.5	366.3	373.7	376.7	363.8	372.0	375.8
18	92.7	192.1	245.6	183.1	196.5	204.4	187.0	200.6	206.9	185.9	196.9	205.3
19	380.8	596.5	734.2	535.9	567.5	578.8	551.6	574.3	583.9	546.2	567.9	580.1
20	336.8	781.9	1058.4	738.3	862.4	893.5	806.3	881.2	906.3	785.5	863.4	895.8

Table 6-32: Lateral Spread Displacements in Charleston Calculated with the Boulanger and Idriss Liquefaction Triggering Procedure (Lateral Spread Geometry 1)

	Full Probabilistic			Mean Magnitude			Modal Magnitude			Semi-Probabilistic		
Profile	475	1039	2475	475	1039	2475	475	1039	2475	475	1039	2475
1	819.0	1201.0	1438.9	1026.1	1028.1	1032.9	1027.1	1029.5	1034.8	1027.1	1029.1	1032.1
2	102.2	160.1	199.3	136.8	150.1	156.6	141.8	152.9	157.6	141.4	150.7	155.7
3	611.5	1005.9	1151.4	896.6	924.3	931.5	912.9	927.8	933.3	909.5	925.2	930.9
4	581.2	990.4	1211.3	877.6	903.0	908.2	891.0	905.3	909.4	889.3	903.8	907.9
5	71.5	163.7	232.6	147.1	187.8	217.0	169.9	196.6	225.5	165.4	190.1	213.5
6	707.2	1117.2	1317.3	961.4	1005.9	1006.6	988.4	1006.4	1006.6	982.8	1005.8	1006.6
7	134.8	211.1	234.4	184.7	192.7	198.7	189.5	193.7	198.7	188.8	193.0	198.0
8	150.6	317.6	447.8	293.2	351.5	376.1	320.8	360.7	382.7	315.4	353.4	372.9
9	18.2	30.6	47.6	24.7	36.2	48.3	28.5	40.2	54.6	28.4	36.8	46.5
10	153.8	333.8	457.0	306.8	364.1	380.7	331.7	370.6	384.0	327.5	364.8	379.6
11	64.9	160.2	247.1	156.9	182.0	199.8	165.7	188.0	203.4	163.9	183.5	197.4
12	301.7	533.7	617.4	484.7	497.2	511.7	488.8	501.3	514.6	488.7	498.4	510.4
13	497.9	779.6	903.1	671.7	684.3	686.0	677.7	685.0	686.0	675.8	684.4	686.0
14	110.3	367.4	567.4	375.4	441.2	462.3	410.2	450.5	463.2	404.7	443.0	461.2
15	258.6	378.9	403.8	327.0	329.9	331.6	328.4	330.1	333.3	328.1	329.9	331.1
16	33.8	66.2	77.9	61.4	64.5	64.5	62.8	64.5	64.5	62.7	64.5	64.5
17	217.5	395.0	459.5	359.4	372.4	376.9	366.7	373.9	378.2	365.5	372.8	376.4
18	95.4	195.7	249.5	183.3	197.9	207.2	187.4	201.0	208.6	186.6	198.3	206.4
19	379.2	602.7	742.2	537.4	569.4	584.1	552.4	574.8	586.8	550.4	570.3	582.4
20	347.9	804.1	1080.7	747.3	868.8	906.8	812.6	882.0	913.6	803.1	870.0	901.8

Table 6-33: Lateral Spread Displacements in Butte Calculated with the Boulanger and Idriss Liquefaction Triggering Procedure (Lateral Spread Geometry 2)

	Full Probabilistic			Mean Magnitude			Modal Magnitude			Semi-Probabilistic		
Profile	475	1039	2475	475	1039	2475	475	1039	2475	475	1039	2475
1	139.1	299.6	409.5	263.5	337.9	352.0	208.2	312.6	349.8	312.7	344.6	352.8
2	20.6	38.0	50.9	32.9	40.3	44.3	28.8	38.1	42.2	38.2	41.9	46.7
3	55.5	208.9	323.1	171.9	272.6	300.7	93.9	237.2	291.3	244.8	287.2	307.4
4	49.4	187.8	318.8	138.6	270.3	297.5	94.3	190.6	290.6	218.3	286.6	301.2
5	5.3	21.0	41.4	10.6	32.3	43.9	6.3	21.2	38.7	24.9	37.8	50.2
6	83.7	249.6	364.9	218.6	302.3	320.7	105.3	280.1	312.8	286.5	310.9	328.7
7	15.8	48.1	68.4	44.7	57.7	61.9	27.4	53.4	60.2	54.3	59.8	63.3
8	7.8	46.2	87.2	31.7	72.2	91.2	14.3	55.0	82.4	59.5	80.8	99.8
9	4.9	6.9	8.8	5.9	6.4	7.4	5.9	6.0	6.7	6.3	6.8	8.4
10	10.0	46.6	91.6	30.6	74.7	96.1	18.2	48.2	87.9	55.8	85.1	104.9
11	3.1	17.1	42.1	8.9	32.9	49.9	5.8	19.2	42.4	19.9	39.6	53.9
12	11.1	97.3	171.2	56.0	145.2	164.5	20.5	120.9	160.2	125.3	155.4	166.8
13	56.6	178.2	261.2	153.1	218.5	228.4	94.6	205.6	224.9	206.3	223.0	230.7
14	1.4	23.7	79.8	8.9	46.4	106.9	2.1	22.8	79.6	31.8	69.5	126.8
15	32.5	93.9	128.5	83.3	110.8	112.1	56.6	104.0	111.9	105.0	111.9	112.4
16	2.0	11.6	19.7	9.8	15.2	20.0	4.0	14.5	17.3	14.8	16.6	21.0
17	8.6	67.3	122.4	34.2	103.9	119.9	13.5	72.9	114.2	86.6	112.5	123.1
18	1.1	27.4	58.1	10.0	46.8	61.0	1.2	32.3	56.6	37.0	53.7	63.1
19	58.6	134.4	189.6	107.1	161.3	177.8	92.4	135.4	170.9	140.7	168.6	184.1
20	4.2	101.3	215.7	38.3	165.5	231.1	4.5	125.7	201.3	139.1	193.2	255.1

Table 6-34: Lateral Spread Displacements in Eureka Calculated with the Boulanger and Idriss Liquefaction Triggering Procedure (Lateral Spread Geometry 2)

	Full Probabilistic			Mean Magnitude			Modal Magnitude			Semi-Probabilistic		
Profile	475	1039	2475	475	1039	2475	475	1039	2475	475	1039	2475
1	511.3	567.2	619.0	355.8	357.1	357.2	354.8	356.1	357.1	356.8	357.1	357.2
2	69.8	78.6	87.7	54.2	55.5	57.6	53.5	54.4	56.2	55.0	55.9	57.2
3	401.2	426.0	449.1	320.9	321.9	322.5	320.0	321.0	321.8	321.6	322.1	322.5
4	425.3	459.7	489.2	312.7	313.6	314.9	312.1	312.9	314.1	313.4	313.9	314.7
5	83.3	101.1	118.1	77.5	84.6	90.7	73.0	78.6	84.3	82.1	86.7	91.0
6	462.0	501.5	537.3	346.1	346.1	346.3	346.1	346.1	346.2	346.1	346.2	346.2
7	81.7	87.8	93.0	68.3	68.3	68.3	68.0	68.3	68.3	68.3	68.3	68.3
8	160.4	194.7	229.1	131.6	134.4	136.9	127.9	132.3	134.9	133.8	135.1	136.6
9	17.8	23.8	30.2	18.8	21.9	23.3	15.8	19.7	21.9	21.3	22.4	23.5
10	160.6	189.0	215.2	132.0	134.8	137.5	130.3	132.6	135.1	134.0	135.5	137.5
11	89.0	111.8	131.8	69.9	72.1	73.9	67.7	70.4	72.5	71.6	72.6	73.7
12	214.8	228.7	239.0	177.0	179.9	183.2	175.2	177.4	180.1	179.0	180.8	182.3
13	316.5	334.5	345.3	235.9	235.9	235.9	235.9	235.9	235.9	235.9	235.9	235.9
14	203.6	253.1	301.1	159.2	159.3	159.3	158.6	159.3	159.3	159.3	159.3	159.3
15	139.6	141.8	143.2	114.5	115.1	115.4	113.8	115.0	115.1	115.0	115.2	115.5
16	27.0	29.9	32.4	22.2	22.2	22.2	22.2	22.2	22.2	22.2	22.2	22.2
17	159.7	167.7	173.4	130.0	131.2	131.5	129.4	130.4	131.5	131.0	131.3	131.4
18	87.1	95.5	101.4	71.6	72.2	72.3	70.9	71.9	72.2	72.2	72.2	72.3
19	263.5	297.1	331.2	201.8	203.7	206.0	200.3	202.2	204.1	203.1	204.2	205.6
20	381.5	443.3	501.8	314.1	317.6	318.9	309.8	314.8	317.9	316.7	317.9	318.9

Table 6-35: Lateral Spread Displacements in Santa Monica Calculated with the Boulanger and Idriss Liquefaction Triggering Procedure (Lateral Spread Geometry 2)

	Full Probabilistic			Mean Magnitude			Modal Magnitude			Semi-Probabilistic		
Profile	475	1039	2475	475	1039	2475	475	1039	2475	475	1039	2475
1	499.3	554.8	607.3	353.5	354.3	355.3	354.0	354.8	355.8	354.5	355.2	356.3
2	65.6	73.9	82.4	51.6	53.1	53.9	52.7	53.5	54.2	53.3	53.9	54.5
3	389.3	414.3	437.3	317.8	319.7	320.5	319.2	320.0	320.9	319.8	320.4	321.1
4	413.7	449.7	479.9	310.5	311.8	312.4	311.4	312.1	312.7	311.9	312.3	312.9
5	71.6	85.7	98.8	64.6	70.2	75.5	68.2	73.1	77.6	71.3	74.8	79.0
6	448.1	489.2	525.4	345.8	346.1	346.1	346.1	346.1	346.1	346.1	346.1	346.1
7	78.6	84.2	89.1	66.2	67.3	68.3	66.7	67.9	68.3	67.6	68.3	68.3
8	142.3	173.1	203.9	120.9	125.7	129.9	124.5	128.0	131.6	126.7	129.5	132.5
9	14.0	17.5	21.5	12.5	14.8	17.1	14.0	15.9	18.8	15.2	16.8	20.3
10	145.6	172.7	198.2	125.2	128.9	131.2	127.7	130.4	132.1	129.6	131.0	132.8
11	78.2	99.3	118.4	62.6	65.9	69.1	64.9	67.7	70.0	66.9	68.9	70.6
12	207.6	220.8	230.3	171.0	173.7	176.2	172.7	175.3	177.0	174.4	176.1	177.7
13	309.7	329.5	341.3	235.3	235.9	235.9	235.5	235.9	235.9	235.9	235.9	235.9
14	177.0	226.2	274.8	151.7	157.3	159.0	155.4	158.6	159.3	157.7	159.0	159.3
15	138.5	140.8	141.5	113.4	113.6	114.1	113.5	113.8	114.6	113.7	114.1	114.9
16	25.8	28.8	31.8	22.2	22.2	22.2	22.2	22.2	22.2	22.2	22.2	22.2
17	154.9	163.1	169.2	128.0	129.0	129.7	128.6	129.3	130.0	129.2	129.6	130.6
18	81.6	89.7	95.7	68.0	70.1	71.3	69.2	70.9	71.7	70.3	71.2	71.9
19	248.6	281.0	313.7	195.8	198.8	201.1	197.8	200.2	201.8	199.4	200.9	202.4
20	345.9	404.9	462.5	298.7	306.6	312.6	303.9	309.9	314.2	307.9	311.8	315.0

Table 6-36: Lateral Spread Displacements in Portland Calculated with the Boulanger and Idriss Liquefaction Triggering Procedure (Lateral Spread Geometry 2)

	Full Probabilistic			Mean Magnitude			Modal Magnitude			Semi-Probabilistic		
Profile	475	1039	2475	475	1039	2475	475	1039	2475	475	1039	2475
1	343.5	436.6	510.0	352.9	353.3	354.1	354.5	355.9	357.0	353.2	353.8	354.7
2	41.9	57.4	68.9	46.6	50.4	52.8	52.3	54.3	55.3	49.0	51.7	53.5
3	261.0	358.0	399.5	308.6	317.0	319.5	319.8	321.3	321.9	314.8	318.5	320.1
4	251.1	362.7	423.9	301.5	309.7	311.5	311.2	312.7	313.5	306.8	310.7	312.1
5	32.5	59.8	79.6	51.4	63.4	69.0	69.4	78.0	84.3	60.2	65.6	72.8
6	299.6	401.6	460.8	329.2	345.3	346.1	345.8	346.1	346.1	341.1	345.9	346.1
7	57.2	73.9	80.9	63.5	66.0	66.8	66.4	68.0	68.3	65.4	66.3	67.7
8	67.6	116.2	156.2	100.9	118.2	125.1	125.1	131.8	134.4	112.2	122.0	127.7
9	7.4	11.3	16.3	8.9	11.5	14.4	15.0	18.9	21.7	10.3	13.0	15.9
10	69.4	121.6	157.8	104.5	122.4	128.1	126.6	131.9	134.4	115.1	125.6	130.2
11	31.3	59.4	86.7	54.1	60.9	65.3	65.1	70.0	71.9	57.9	63.4	67.5
12	129.9	190.8	213.1	166.5	169.9	173.0	173.0	177.4	179.7	168.4	171.4	175.1
13	209.9	280.1	315.7	230.7	234.6	235.6	235.1	235.9	235.9	233.3	235.3	235.9
14	60.2	136.5	199.0	129.1	149.1	156.0	154.0	159.0	159.3	142.9	152.4	158.3
15	108.6	133.2	139.5	112.4	113.4	113.5	113.6	114.2	115.0	113.0	113.5	113.7
16	14.8	23.3	26.9	21.0	22.1	22.2	22.2	22.2	22.2	21.7	22.2	22.2
17	96.5	142.3	158.9	124.1	127.4	128.7	128.3	129.9	131.0	126.7	128.1	129.3
18	43.7	70.9	85.8	63.1	67.0	69.5	68.8	71.5	72.2	64.9	68.2	70.8
19	161.9	217.3	260.4	184.8	194.2	198.2	197.9	202.0	203.5	191.0	196.3	200.1
20	161.3	291.7	374.2	254.7	293.8	304.9	302.9	314.3	317.3	282.2	299.9	309.7

Table 6-37: Lateral Spread Displacements in Salt Lake City Calculated with the Boulanger and Idriss Liquefaction Triggering Procedure (Lateral Spread Geometry 2)

	Full Probabilistic			Mean Magnitude			Modal Magnitude			Semi-Probabilistic		
Profile	475	1039	2475	475	1039	2475	475	1039	2475	475	1039	2475
1	355.4	445.6	518.3	353.1	353.8	354.7	353.2	353.8	354.8	353.4	354.2	355.3
2	44.9	60.6	71.9	48.2	51.9	53.5	48.5	52.1	53.5	50.4	52.8	53.9
3	280.5	369.1	406.6	311.8	318.2	319.9	312.8	318.5	320.0	316.8	319.2	320.5
4	269.8	375.6	432.4	304.6	310.7	312.1	305.5	310.8	312.1	309.7	311.6	312.4
5	38.1	65.8	86.3	55.5	65.2	72.8	56.8	65.7	73.2	63.4	69.0	75.2
6	314.6	414.1	470.7	336.6	345.9	346.1	338.3	345.9	346.1	345.3	346.1	346.1
7	60.4	75.6	83.1	64.6	66.3	68.0	64.8	66.4	68.1	66.1	66.9	68.3
8	77.9	127.0	166.9	106.6	121.7	127.7	108.4	122.4	128.0	117.9	125.1	129.8
9	8.0	12.6	18.1	9.4	12.9	15.7	9.6	13.2	15.9	11.5	14.3	17.2
10	81.3	133.4	168.3	110.6	125.8	130.2	112.3	126.2	130.4	122.7	128.2	131.2
11	38.2	66.4	94.0	55.7	63.2	67.5	56.3	63.7	67.8	60.8	65.5	69.1
12	143.7	197.7	218.4	167.6	171.3	175.1	167.8	171.5	175.3	169.9	173.1	176.2
13	221.7	286.9	320.5	232.2	235.3	235.9	232.6	235.4	235.9	234.6	235.7	235.9
14	79.5	153.6	215.3	137.2	152.5	158.5	139.1	153.1	158.6	149.1	156.1	159.0
15	112.4	134.9	140.2	112.7	113.4	113.8	112.8	113.4	113.8	113.4	113.6	114.1
16	17.2	24.5	27.9	21.4	22.2	22.2	21.5	22.2	22.2	22.1	22.2	22.2
17	105.3	147.0	161.7	125.1	128.2	129.3	125.5	128.3	129.4	127.6	128.8	129.7
18	49.9	75.5	89.5	63.7	68.3	70.9	64.0	68.5	70.9	67.2	69.6	71.3
19	172.2	225.9	268.8	188.2	196.2	200.1	189.0	196.6	200.4	194.0	198.3	201.1
20	190.8	317.1	396.1	271.5	299.9	309.4	275.6	300.9	310.0	294.1	305.1	312.3

Table 6-38: Lateral Spread Displacements in San Francisco Calculated with the Boulanger and Idriss Liquefaction Triggering Procedure (Lateral Spread Geometry 2)

	Full Probabilistic			Mean Magnitude			Modal Magnitude			Semi-Probabilistic		
Profile	475	1039	2475	475	1039	2475	475	1039	2475	475	1039	2475
1	508.0	563.2	614.6	354.0	354.7	355.7	354.5	355.2	356.4	355.1	355.8	356.8
2	67.8	76.3	85.0	52.6	53.5	54.1	53.2	53.9	54.6	53.7	54.3	55.0
3	396.6	421.1	443.7	319.2	320.0	320.9	319.9	320.6	321.3	320.4	321.1	321.6
4	421.2	455.8	485.2	311.4	312.0	312.7	311.9	312.4	313.0	312.3	312.8	313.4
5	77.1	92.2	106.2	68.1	72.7	77.2	71.5	75.2	79.9	74.6	78.0	82.4
6	457.1	497.0	532.7	346.1	346.1	346.1	346.1	346.1	346.1	346.1	346.1	346.1
7	80.2	86.0	91.1	66.7	67.8	68.3	67.3	68.2	68.3	68.2	68.3	68.3
8	151.9	183.7	215.6	124.4	127.7	131.4	126.8	129.8	132.9	129.2	131.8	133.8
9	15.6	19.6	24.1	14.0	15.8	18.5	15.4	17.1	20.6	16.7	19.3	21.4
10	153.7	181.0	206.2	127.6	130.2	131.9	129.4	131.0	133.0	130.8	132.2	134.0
11	84.0	105.4	124.4	64.9	67.4	69.9	66.6	68.9	70.8	68.5	70.1	71.6
12	211.3	224.4	233.8	172.6	175.1	176.8	174.4	176.2	177.9	175.9	177.2	179.0
13	314.2	332.6	343.6	235.5	235.9	235.9	235.8	235.9	235.9	235.9	235.9	235.9
14	192.1	241.3	289.5	155.3	158.3	159.2	157.6	158.9	159.3	158.8	159.3	159.3
15	139.3	141.1	141.9	113.5	113.8	114.5	113.7	114.0	115.0	113.9	114.8	115.0
16	26.5	29.5	32.2	22.2	22.2	22.2	22.2	22.2	22.2	22.2	22.2	22.2
17	157.7	165.5	170.9	128.6	129.3	129.9	129.1	129.6	130.5	129.5	130.1	131.0
18	84.4	92.4	98.2	69.2	70.8	71.6	70.3	71.2	71.9	71.2	71.8	72.2
19	257.2	289.8	322.9	197.8	200.1	201.7	199.3	201.0	202.6	200.9	201.9	203.3
20	365.0	424.5	481.8	303.8	309.5	313.9	308.2	312.3	315.6	311.5	314.3	317.1

Table 6-39: Lateral Spread Displacements in San Jose Calculated with the Boulanger and Idriss Liquefaction Triggering Procedure (Lateral Spread Geometry 2)

	Full Probabilistic			Mean Magnitude			Modal Magnitude			Semi-Probabilistic		
Profile	475	1039	2475	475	1039	2475	475	1039	2475	475	1039	2475
1	539.0	590.4	636.2	354.0	354.7	355.5	354.0	354.5	355.3	355.4	356.0	356.9
2	72.7	80.8	89.3	52.7	53.5	54.0	52.5	53.4	53.9	53.9	54.4	55.2
3	410.6	432.7	453.0	319.2	320.0	320.7	318.9	319.8	320.5	320.5	321.0	321.6
4	442.0	471.8	497.3	311.4	312.1	312.6	311.2	312.0	312.4	312.5	312.9	313.4
5	85.1	98.4	111.1	68.3	72.9	76.3	67.4	71.8	75.1	75.8	78.7	82.5
6	480.9	516.2	549.5	346.1	346.1	346.1	346.0	346.1	346.1	346.1	346.1	346.1
7	83.6	88.6	93.1	66.8	68.0	68.3	66.6	67.8	68.3	68.3	68.3	68.3
8	169.4	199.1	229.5	124.5	127.8	130.6	123.9	127.0	129.7	130.0	132.3	133.7
9	17.5	21.4	25.0	14.0	15.8	17.9	13.7	15.3	16.9	17.1	19.2	21.4
10	169.8	194.7	216.3	127.8	130.3	131.7	127.4	129.8	131.1	131.3	132.5	134.2
11	96.3	115.3	131.4	64.9	67.6	69.6	64.6	66.9	68.9	69.2	70.3	71.6
12	219.5	229.4	236.6	172.7	175.2	176.4	172.3	174.7	176.1	176.3	177.3	178.9
13	325.9	338.7	347.7	235.6	235.9	235.9	235.5	235.9	235.9	235.9	235.9	235.9
14	220.1	266.0	309.6	155.5	158.5	159.2	154.9	158.1	159.0	159.0	159.3	159.3
15	140.5	141.5	142.3	113.5	113.8	114.3	113.5	113.7	114.1	114.1	114.9	115.0
16	28.3	31.2	32.8	22.2	22.2	22.2	22.2	22.2	22.2	22.2	22.2	22.2
17	162.3	168.6	172.4	128.7	129.3	129.8	128.6	129.2	129.6	129.7	130.3	131.1
18	89.3	95.9	99.8	69.4	70.9	71.5	69.1	70.6	71.3	71.4	71.8	72.2
19	275.3	306.2	337.6	197.9	200.1	201.5	197.5	199.6	201.0	201.2	202.1	203.3
20	398.8	453.8	501.8	304.1	309.6	313.3	303.1	308.4	312.3	312.8	314.6	316.9

Table 6-40: Lateral Spread Displacements in Seattle Calculated with the Boulanger and Idriss Liquefaction Triggering Procedure (Lateral Spread Geometry 2)

	Full Probabilistic			Mean Magnitude			Modal Magnitude			Semi-Probabilistic		
Profile	475	1039	2475	475	1039	2475	475	1039	2475	475	1039	2475
1	452.3	515.0	574.6	353.2	353.9	354.5	353.3	353.9	354.6	353.9	354.5	355.5
2	58.8	68.1	77.2	50.1	52.3	53.4	50.4	52.4	53.4	52.3	53.3	54.0
3	364.1	397.8	423.7	316.5	318.6	319.9	316.9	318.8	319.9	318.8	319.8	320.7
4	375.1	425.4	461.5	309.4	311.0	311.9	309.7	311.1	312.0	311.1	311.9	312.5
5	60.2	76.4	91.5	62.6	66.3	71.8	63.1	66.8	72.0	67.2	71.7	76.3
6	411.1	460.9	503.1	345.1	345.9	346.1	345.3	346.0	346.1	346.0	346.1	346.1
7	74.4	80.4	86.2	66.0	66.4	67.7	66.0	66.5	67.7	66.5	67.5	68.3
8	118.8	152.2	185.5	116.7	122.8	127.0	118.0	123.4	127.2	123.3	126.8	130.5
9	11.5	15.2	19.2	11.0	13.4	15.4	11.4	13.6	15.5	13.5	15.4	17.6
10	124.3	154.3	183.4	121.5	126.6	129.8	122.4	126.9	129.9	126.7	129.7	131.5
11	61.8	85.0	107.2	60.1	64.0	66.9	60.8	64.3	67.1	64.2	66.4	69.3
12	194.6	212.1	225.0	169.5	171.8	174.6	170.0	172.0	174.8	171.9	174.6	176.4
13	287.4	316.7	334.6	234.4	235.4	235.9	234.6	235.5	235.9	235.4	235.9	235.9
14	139.5	193.2	245.8	148.0	153.7	158.1	149.0	154.2	158.2	154.2	157.9	159.1
15	134.9	139.5	141.1	113.4	113.5	113.7	113.4	113.5	113.7	113.5	113.7	114.2
16	23.5	26.7	30.0	22.1	22.2	22.2	22.2	22.2	22.2	22.2	22.2	22.2
17	144.5	157.9	165.9	127.3	128.4	129.2	127.4	128.5	129.2	128.4	129.2	129.8
18	72.6	84.5	92.5	66.6	68.7	70.6	67.0	68.9	70.7	68.9	70.5	71.4
19	222.2	258.9	293.6	193.5	196.9	199.6	194.2	197.2	199.7	197.2	199.3	201.4
20	296.6	365.8	428.6	292.4	301.7	308.5	294.1	302.4	308.8	302.7	308.4	313.3

Table 6-41: Lateral Spread Displacements in Memphis Calculated with the Boulanger and Idriss Liquefaction Triggering Procedure (Lateral Spread Geometry 2)

	Full Probabilistic			Mean Magnitude			Modal Magnitude			Semi-Probabilistic		
Profile	475	1039	2475	475	1039	2475	475	1039	2475	475	1039	2475
1	285.6	411.1	490.0	352.7	353.4	354.3	353.2	354.0	355.1	353.1	353.7	354.6
2	35.5	54.3	67.3	46.6	51.0	53.2	48.7	52.5	53.8	48.2	51.1	53.3
3	209.9	342.6	392.7	307.8	317.4	319.7	313.6	319.0	320.4	311.6	317.5	319.9
4	199.2	336.6	412.3	301.2	310.3	311.8	305.8	311.2	312.2	304.6	310.3	311.9
5	24.1	54.3	77.1	50.3	63.8	70.6	58.1	67.5	74.6	55.9	64.4	71.8
6	245.3	380.9	448.6	329.0	345.6	346.1	338.9	346.0	346.1	335.7	345.6	346.1
7	46.7	72.1	79.7	63.4	66.1	67.4	65.1	66.5	68.2	64.5	66.2	67.6
8	50.9	106.2	149.5	100.0	119.6	126.1	109.8	123.9	129.3	106.8	120.0	127.0
9	6.4	10.2	15.5	8.5	11.9	15.0	9.9	13.8	16.7	9.5	12.0	15.5
10	52.0	111.5	153.1	104.4	124.0	129.3	112.9	127.2	130.8	110.1	124.1	129.8
11	21.5	53.4	81.8	53.7	61.7	66.2	56.9	64.5	68.6	56.0	62.2	66.8
12	102.4	181.1	210.1	166.5	170.5	174.0	168.0	172.3	175.9	167.7	170.6	174.5
13	172.4	266.2	308.0	230.7	235.1	235.9	232.8	235.5	235.9	232.1	235.1	235.9
14	35.5	121.7	188.5	127.6	150.4	157.6	140.3	154.5	158.8	137.0	150.8	158.0
15	90.0	129.8	138.4	112.4	113.4	113.6	112.9	113.5	113.9	112.7	113.4	113.7
16	11.5	22.4	26.4	21.1	22.2	22.2	21.5	22.2	22.2	21.3	22.2	22.2
17	74.3	134.1	156.8	123.6	127.7	129.1	126.0	128.5	129.5	125.1	127.9	129.2
18	32.2	66.0	84.2	62.9	67.6	70.3	64.3	69.0	71.2	63.9	67.7	70.6
19	131.3	204.8	251.1	184.3	195.1	199.0	189.7	197.5	200.8	187.8	195.2	199.5
20	116.6	268.7	362.6	253.8	296.5	307.2	277.3	303.0	311.6	270.0	296.9	307.9

Table 6-42: Lateral Spread Displacements in Charleston Calculated with the Boulanger and Idriss Liquefaction Triggering Procedure (Lateral Spread Geometry 2)

	Full Probabilistic			Mean Magnitude			Modal Magnitude			Semi-Probabilistic		
Profile	475	1039	2475	475	1039	2475	475	1039	2475	475	1039	2475
1	282.4	411.7	491.1	352.8	353.5	355.1	353.2	354.0	355.8	353.1	353.9	354.9
2	35.2	55.0	68.3	47.0	51.6	53.8	48.8	52.6	54.2	48.6	51.8	53.7
3	211.3	345.5	395.0	308.3	317.8	320.3	313.9	319.0	320.9	312.8	318.1	320.1
4	201.2	339.7	414.4	301.8	310.5	312.3	306.3	311.3	312.7	305.8	310.7	312.2
5	24.8	56.3	79.8	50.6	64.6	74.6	58.4	67.6	77.5	57.7	65.4	73.6
6	244.1	383.4	450.9	330.6	345.9	346.1	339.8	346.0	346.1	337.8	345.9	346.1
7	46.6	72.6	80.5	63.5	66.2	68.3	65.2	66.6	68.3	64.9	66.3	68.1
8	52.2	109.2	153.3	100.8	120.9	129.3	110.3	124.0	131.6	108.6	121.5	128.4
9	6.3	10.5	16.3	8.5	12.5	16.6	9.8	13.8	18.8	9.8	13.0	16.2
10	53.3	114.8	156.6	105.5	125.2	130.9	114.1	127.4	132.0	112.5	125.7	130.6
11	22.5	55.1	84.4	53.9	62.6	68.7	57.0	64.6	69.9	56.4	63.0	68.0
12	104.6	183.2	211.9	166.7	171.0	175.9	168.1	172.4	176.9	168.0	171.5	175.5
13	172.0	267.4	309.1	231.0	235.3	235.9	233.0	235.5	235.9	232.4	235.3	235.9
14	38.2	126.7	194.0	129.1	151.7	158.9	141.0	154.9	159.3	139.5	152.2	158.7
15	89.3	130.1	138.6	112.4	113.4	114.0	112.9	113.5	114.6	112.8	113.4	113.9
16	11.7	22.7	26.7	21.1	22.2	22.2	21.6	22.2	22.2	21.5	22.2	22.2
17	75.4	135.6	157.8	123.6	128.0	129.6	126.1	128.6	130.0	125.6	128.2	129.5
18	33.1	67.2	85.6	63.0	68.1	71.2	64.4	69.1	71.7	64.2	68.3	71.0
19	130.9	207.0	253.9	184.8	195.8	200.8	189.9	197.6	201.8	189.3	196.3	200.5
20	120.5	276.6	370.6	257.0	298.7	311.8	279.4	303.3	314.1	276.8	299.8	310.2

6.5 Discussion of Comparative Study

With 9,600 data points to analyze in this comparative study, the tables presented previously are not sufficient for identifying trends. To better identify trends in the data, different visual representations are presented in the following sections. One-to-one plots, box-and-whisker plots, and a heat map are used to show the trends and patterns in comparing the fully-probabilistic method to the pseudo-probabilistic and semi-probabilistic methods. Before the results are further discussed, it should be noted that only the results from lateral spread geometry 1 are discussed in the comparative study. This is because it was found that lateral spread geometry 2 had the exact same trends as lateral spread geometry 1, only the values were scaled down. Therefore, all comparative analyses presented are for lateral spread geometry 1. The results of the analysis of lateral spread geometry 1 can be applied to all site geometries within the bounds presented by Zhang et al. (2004). One-to-one plots using lateral spread geometry 2 are presented in Appendix B.

6.5.1 Discussion of Robertson and Wride Results

This section discusses the trends observed when comparing lateral spread displacements calculated with the fully-probabilistic method with those calculated with the pseudo-probabilistic and semi-probabilistic methods using the Robertson and Wride liquefaction triggering procedure. The first way in which the trends in these comparisons are presented visually is with one-to-one plots, as shown in Figure 6-3 to Figure 6-11. The 20 different soil profiles for each city are represented by a different marker, which is plotted to represent the lateral spread displacement calculated with the fully-probabilistic method (x-axis) and the conventional method (y-axis). If the two methods are a perfect match, the point will lie on the solid black one-to-one line. The best-fit linear regression line for all points is plotted in blue. If the best-fit line lies above the

one-to-one line, this indicates that the conventional method is calculating higher values, therefore over-predicting lateral spread displacements. If the best-fit line lies below the one-to-one line, this indicates that the conventional method is calculating lower values, therefore under-predicting lateral spread displacements. Both situations can be problematic and demonstrate why the use of the fully-probabilistic method is necessary for accurate prediction of lateral spread displacements.

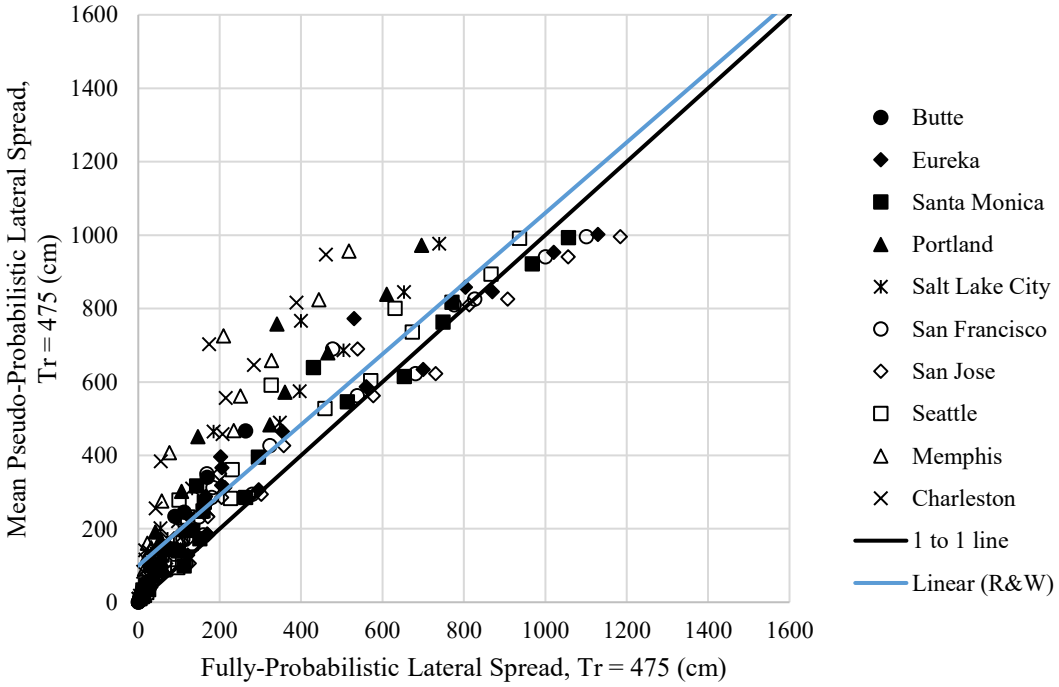

Figure 6-3: Mean magnitude pseudo-probabilistic versus fully-probabilistic for the 475-year return period using the Robertson and Wride liquefaction triggering procedure.

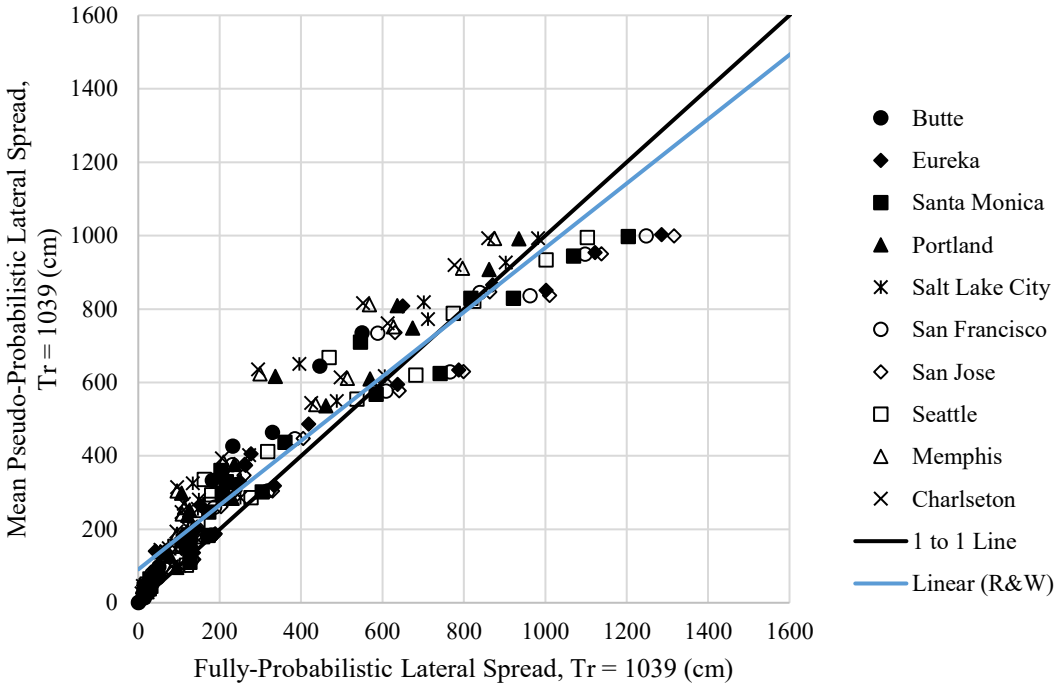

Figure 6-4: Mean magnitude pseudo-probabilistic versus fully-probabilistic for the 1039-year return period using the Robertson and Wride liquefaction triggering procedure.

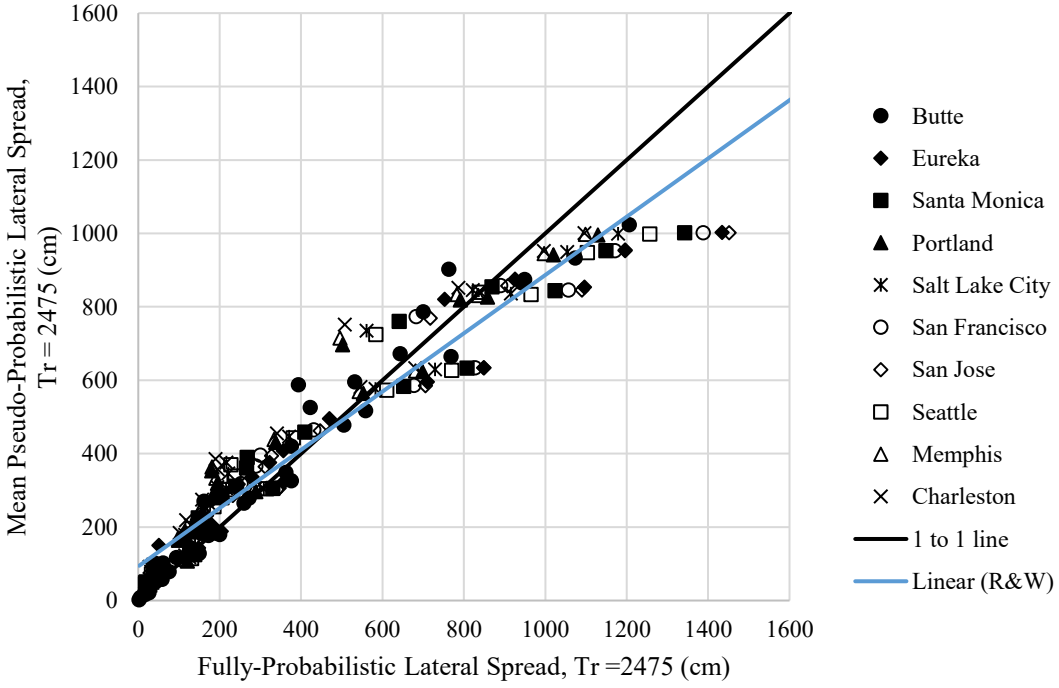

Figure 6-5: Mean magnitude pseudo-probabilistic versus fully-probabilistic for the 2475-year return period using the Robertson and Wride liquefaction triggering procedure.

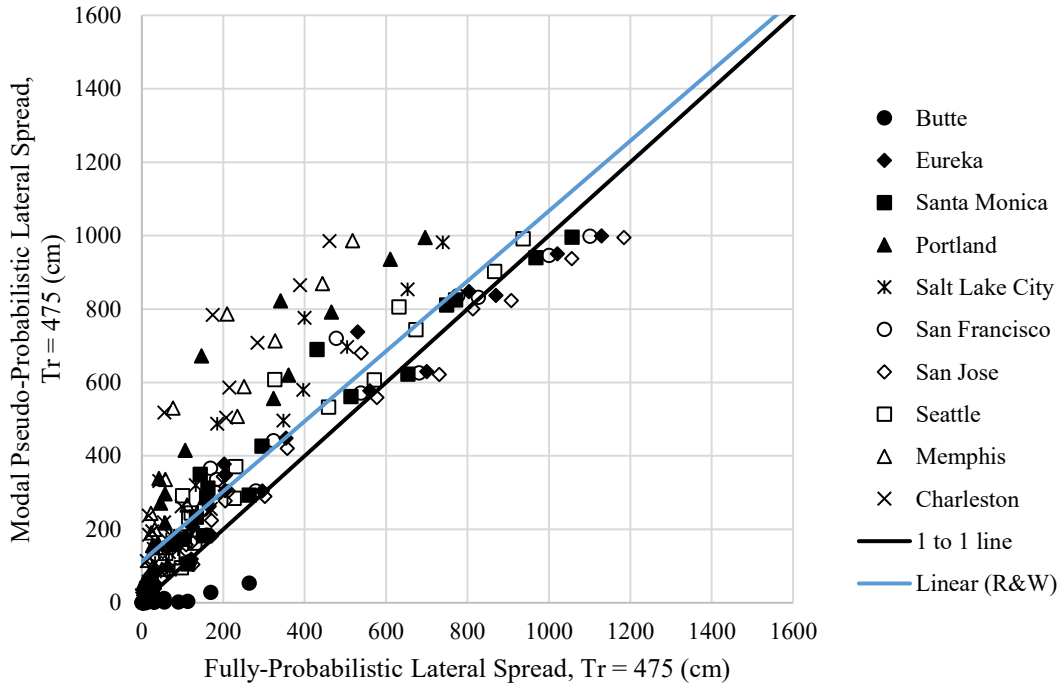

Figure 6-6: Modal magnitude pseudo-probabilistic versus fully-probabilistic for the 475-year return period using the Robertson and Wride liquefaction triggering procedure.

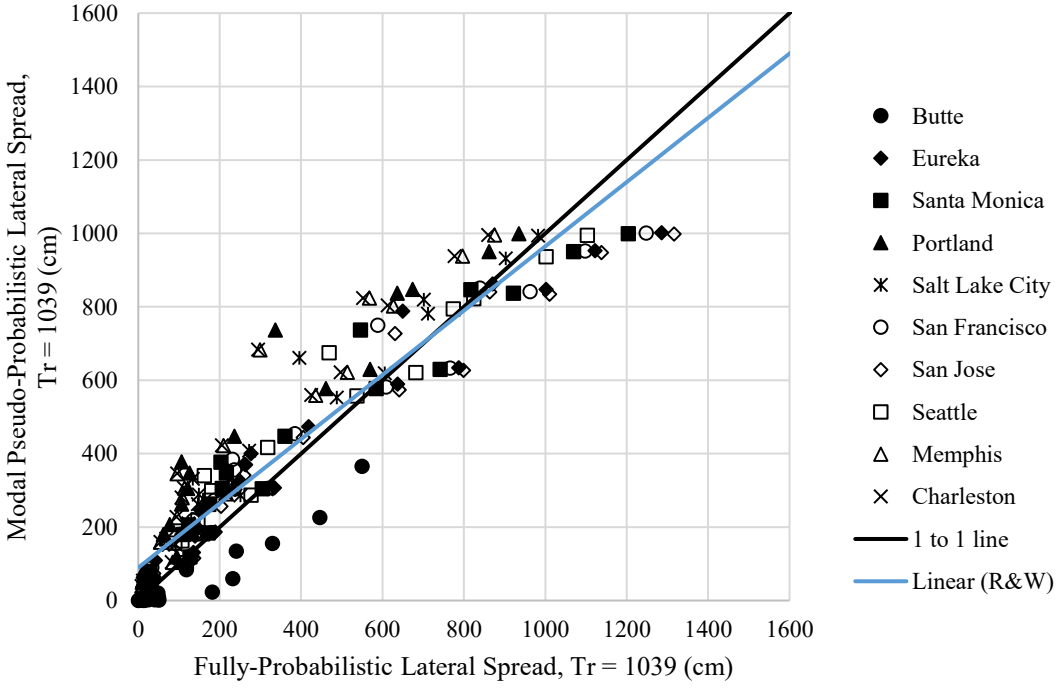

Figure 6-7: Modal magnitude pseudo-probabilistic versus fully-probabilistic for the 1039-year return period using the Robertson and Wride liquefaction triggering procedure.

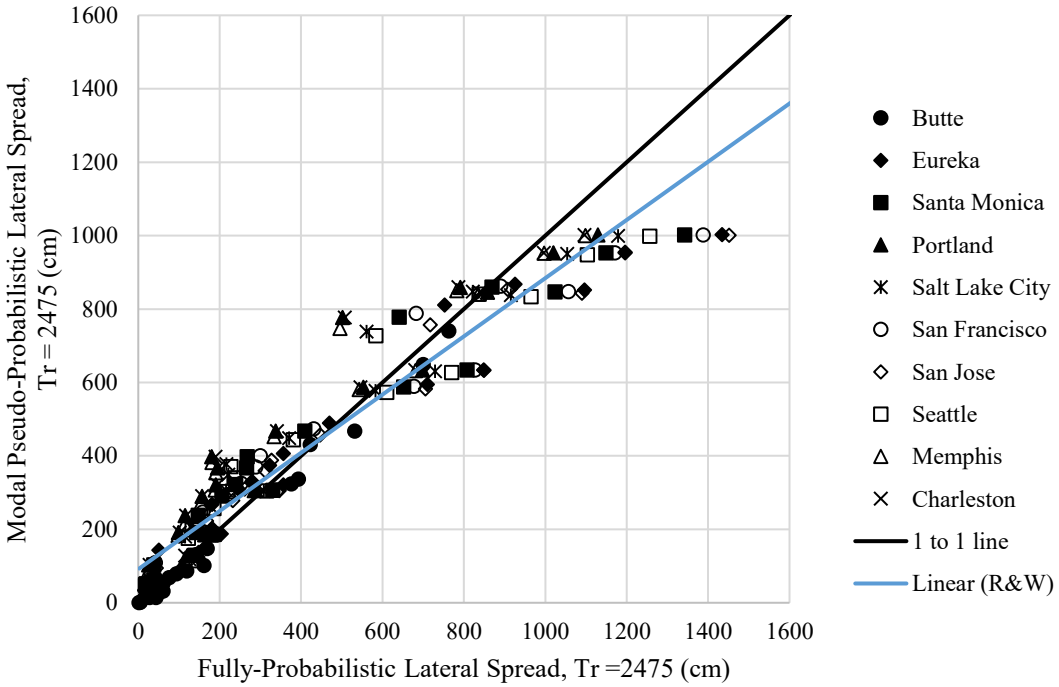

Figure 6-8: Modal magnitude pseudo-probabilistic versus fully-probabilistic for the 2475-year return period using the Robertson and Wride liquefaction triggering procedure.

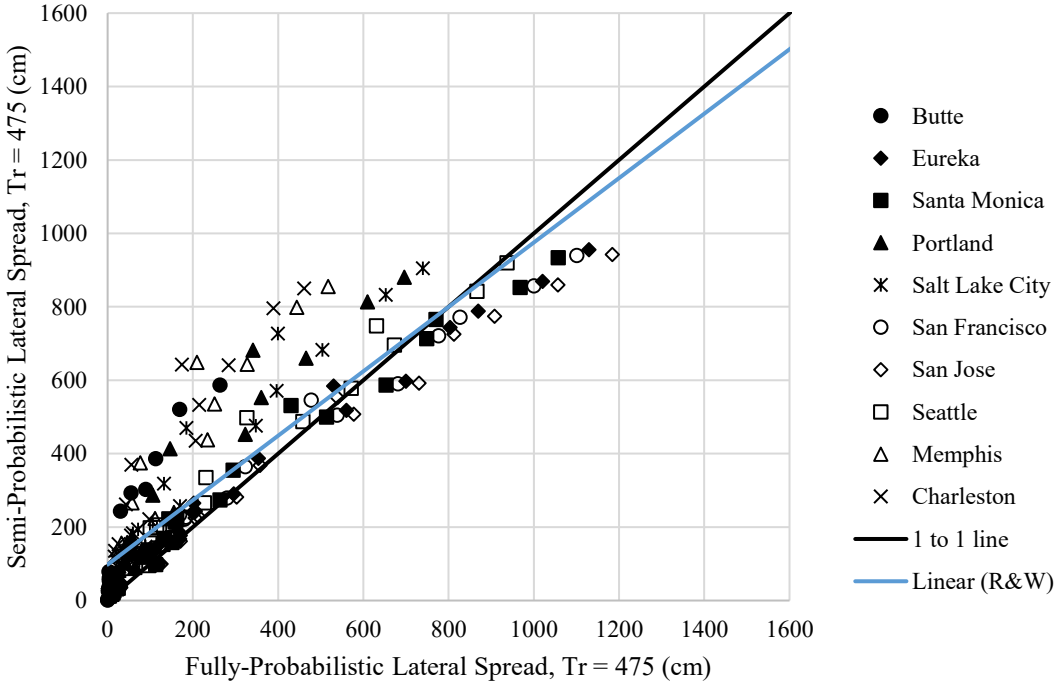

Figure 6-9: Semi-probabilistic versus fully-probabilistic for the 475-year return period using the Robertson and Wride liquefaction triggering procedure.

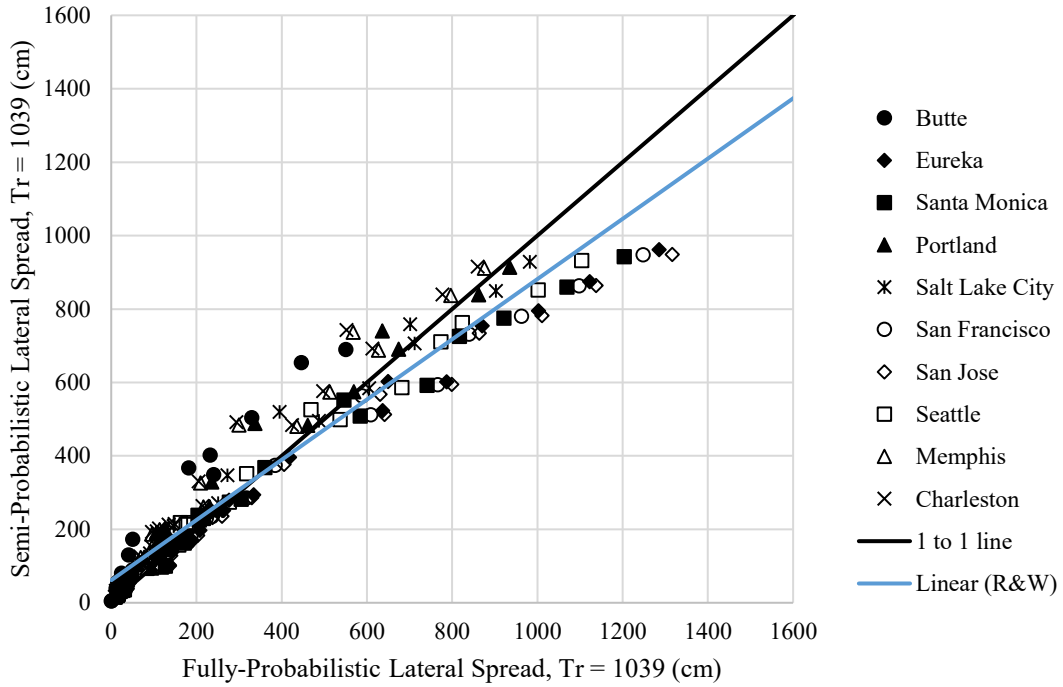

Figure 6-10: Semi-probabilistic versus fully-probabilistic for the 1039-year return period using the Robertson and Wride liquefaction triggering procedure.

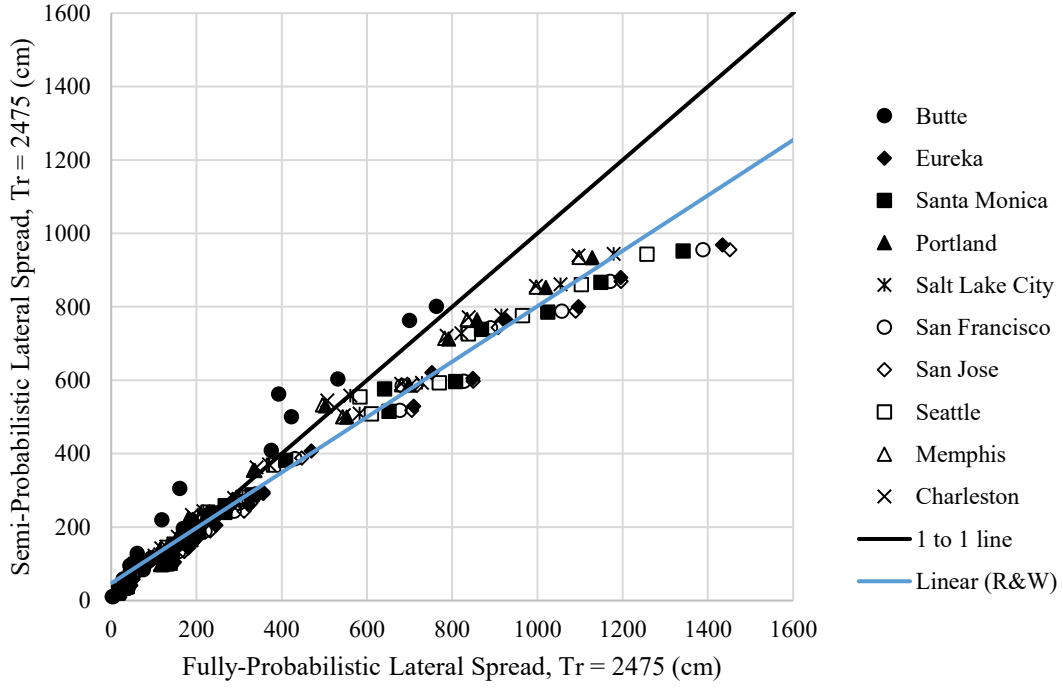

Figure 6-11: Semi-probabilistic versus fully-probabilistic for the 2475-year return period using the Robertson and Wride liquefaction triggering procedure.

The general trend observed from the comparison plots is how the best-fit line goes from above, or near, the one-to-one line at low return periods to farther and farther below the one-to-one line as the return period increases. This trend indicates that the larger the seismic event, the more the conventional methods of predicting lateral spread displacements are under-predicting the amount of displacement that will occur. Also, the sites of lower seismicity and the soil profiles that are less liquefiable tend to have a closer agreement between the fully-probabilistic method and the conventional methods (as visible in the bottom left corner of each one-to-one plot). Another trend to note is that the mean and modal magnitude pseudo-probabilistic methods essentially result in the same trends. The only difference between the two methods that is apparent in the one-to-one plots is how the mean-magnitude pseudo-probabilistic method produces slightly more variability in the displacements calculated. Because of these similarities, these two pseudo-probabilistic methods were analyzed in more detail together.

When comparing the fully-probabilistic method to the pseudo-probabilistic method, the first visible trend is how the best-fit line lies above the one-to-one line for the 475-year return period. Very few data points fall below the one-to-one line at this return period, indicating that for smaller hazard levels the pseudo-probabilistic method slightly over-predicts lateral spread displacement. As the return period increases, the best-fit line goes from above the one-to-one line to crossing it at around 700 cm for the 1039-year return period and at around 450 cm for the 2475-year return period, indicating that as the return period increases, or the size of the seismic event increases, more points are being under-predicted when using the pseudo-probabilistic method. However, for the 1039-year and 2475-year return periods, it seems that a majority of the points still lie fairly close to, and above, the one-to-one line. Areas of high seismicity are

contributing to the points under the one-to-one line and tend to pull down the best-fit line as the displacements increase.

When comparing the fully-probabilistic method to the semi-probabilistic method, the same general trends are observed as those that were found in the comparison with the pseudo-probabilistic method, with one major difference being that the best-fit line does not remain above the one-to-one line for the 475-year return period. For semi-probabilistic method, the best-fit line crosses the one-to-one at 800 cm, 350 cm, and 150 cm for the 475-year, 1039-year, and 2475-year return periods, respectively. For the higher return periods, the same general trends are shown, with the best-fit line going farther under the one-to-one line. One key difference in the higher return periods is that the results from the semi-probabilistic method have much less scatter, indicating slightly more consistent calculations than the pseudo-probabilistic approach, which is likely due to accounting for the uncertainty in the liquefaction triggering analysis.

Another way to visually compare these different methods is through the use of box-and-whisker plots representing the assumed versus actual return period. When a conventional method is used to calculate the lateral spread displacement at a specified return period, that method will likely result in a displacement different from the actual value. This displacement from the conventional method is assumed to be at the correct specified return period when in fact it corresponds to a much different return period. The box-and-whisker plots in Figure 6-12 through Figure 6-14 compare the assumed return period of the conventional method to the actual return period as determined by the fully-probabilistic method. The box-and-whisker plots show the minimum, first quartile, median, third quartile, maximum, and average (marked with an “x”) values of the actual return period. The assumed return period is marked with a dotted red line for reference. All data used to create these box-and-whisker plots can be found in Appendix C.

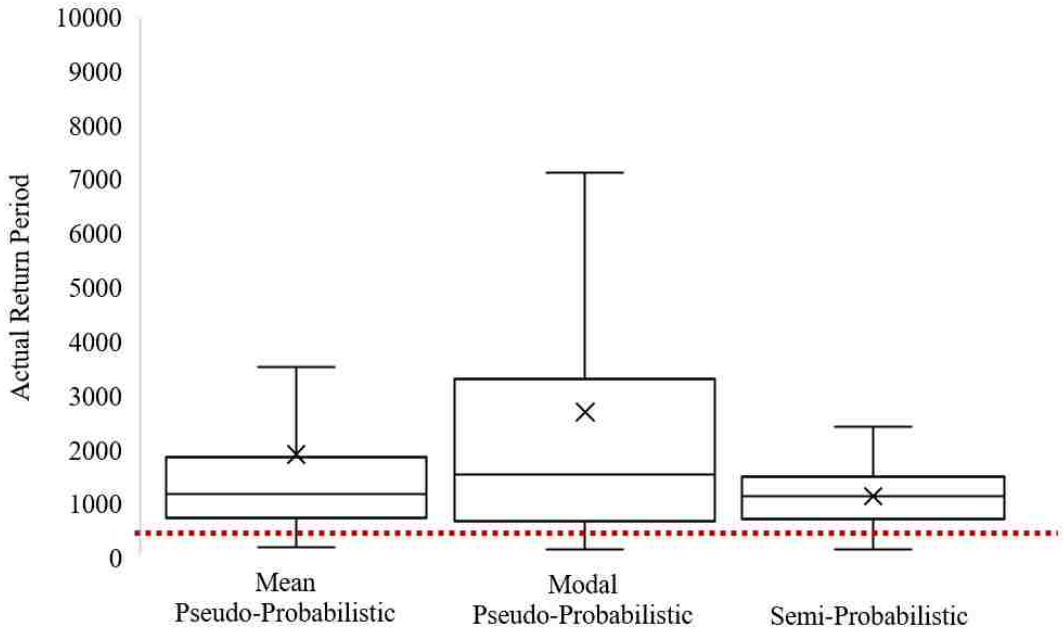

Figure 6-12: Box-and-whisker plots of actual return periods versus assumed 475-year return period using the Robertson and Wride liquefaction triggering procedure.

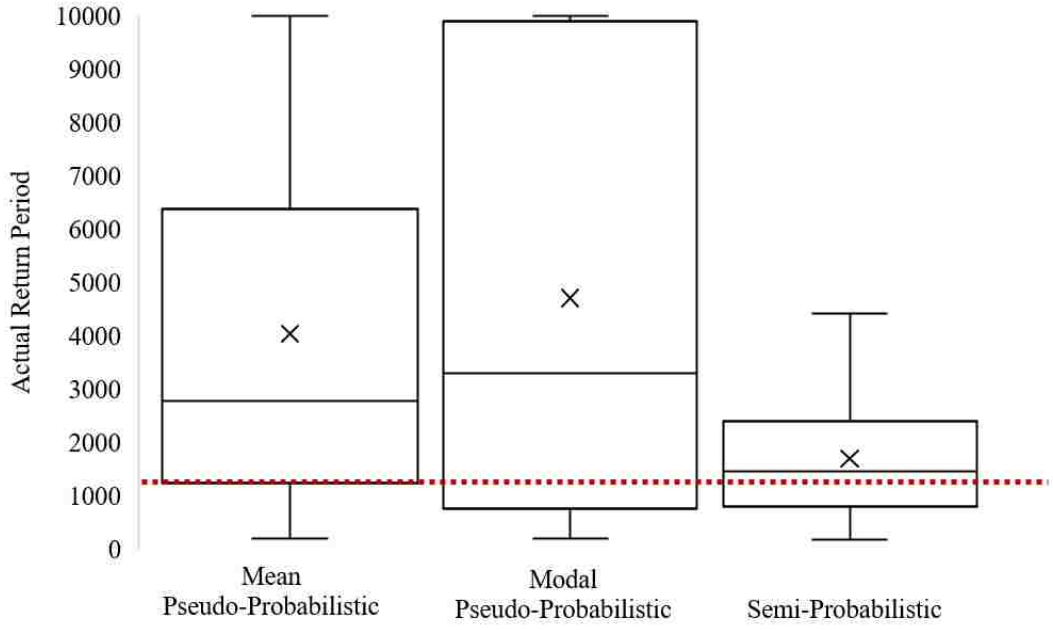

Figure 6-13: Box-and-whisker plots of actual return periods versus assumed 1039-year return period using the Robertson and Wride liquefaction triggering procedure.

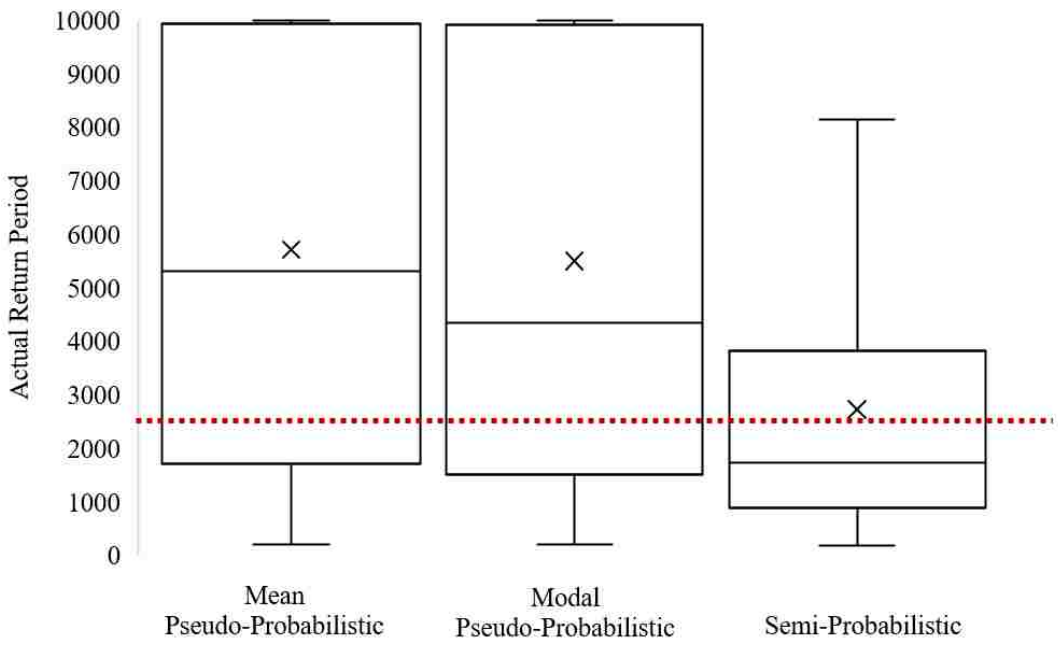

Figure 6-14: Box-and-whisker plots of actual return periods versus assumed 2475-year return period using the Robertson and Wride liquefaction triggering procedure.

As discussed previously, one-to-one plots in Figure 6-3 to Figure 6-11 show the general trend of the conventional methods under-predicting lateral spreading as the return period increases. At first glance the box plots in Figure 6-12 through Figure 6-14 seem to show the opposite trend, with the exception of the semi-probabilistic method, but this can be misleading. While there are many points over-predicting lateral spread displacement for the 1039-year and 2475-year return periods, the over-prediction shown on the box-and-whisker plots seems more extreme than the over-prediction shown on the one-to-one plots. The back-calculated actual return periods are arbitrarily high due to the steepness of the hazard curves when the fully-probabilistic method is used with the Robertson and Wride liquefaction triggering procedure. This is especially true for areas of lower seismicity and for less-liquefiable soil profiles.

Consider the following example of the analysis of profile 9 (medium to hard soil) at Butte (lower seismicity) to demonstrate these steep hazard curves. Over a span of return periods from 100 years to 10,000 years, the calculated lateral spread displacement only ranges from 9 cm to 22 cm. For the 2475-year return period, the pseudo-probabilistic (mean magnitude) method results in a lateral spread displacement of 29 cm. For the same analysis with the fully-probabilistic method, the lateral spread displacement is 17 cm. Using the hazard curve to back-calculate the actual return period from the pseudo-probabilistic method shows that the actual return period is over 10,000 years. While the pseudo-probabilistic method was only over-predicting the displacement by a few centimeters, due to the steepness of the hazard curve, the corresponding actual return period makes it seem like an extreme over-prediction, which was the case for multiple combinations of sites and soil profiles.

The semi-probabilistic box-and-whisker plots in Figure 6-12 through Figure 6-14 show results that are consistent with the one-to-one plots in Figure 6-3 to Figure 6-11. As the return period increases, the median actual return period goes from above the assumed return period of 475 years to below the assumed return period of 2475 years, indicating that the semi-probabilistic method tends to under-predict the lateral spread displacement as the return period increases, as discussed previously.

6.5.2 Discussion of Boulanger and Idriss Results

This section discusses the trends observed when comparing lateral spread displacements calculated with the fully-probabilistic method to those calculated using the pseudo-probabilistic and semi-probabilistic methods using the Boulanger and Idriss liquefaction triggering procedure. This comparison was done using the same visual representations as were used in the Robertson and Wride comparisons, starting with one-to-one plots, as shown in Figure 6-15 to Figure 6-23.

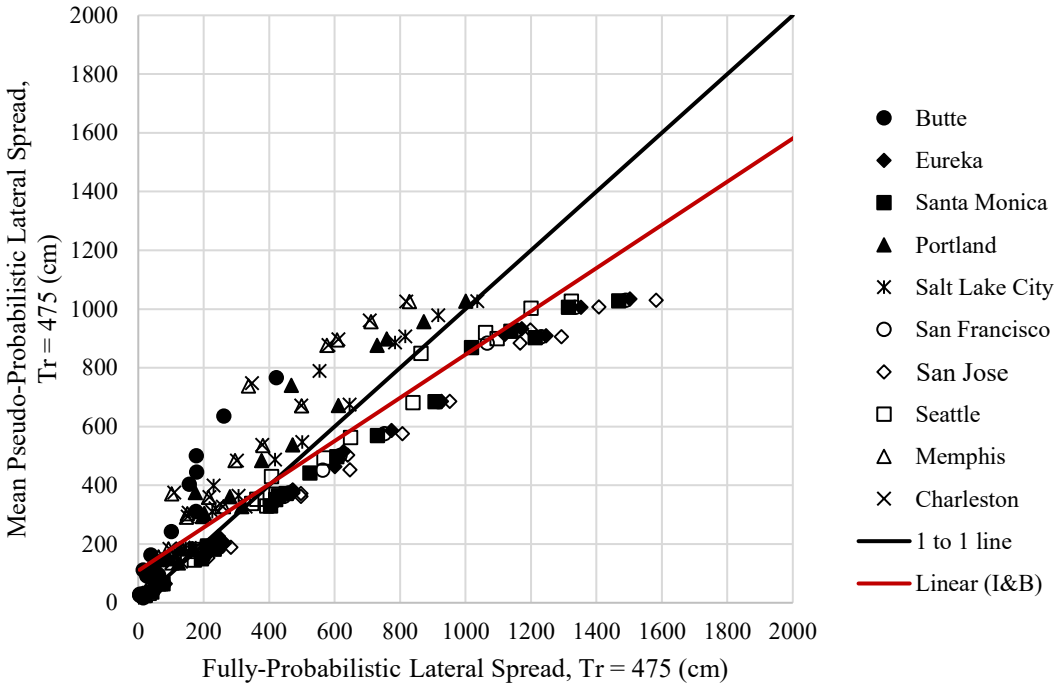

Figure 6-15: Mean magnitude pseudo-probabilistic versus fully-probabilistic for the 475-year return period using the Boulanger and Idriss liquefaction triggering procedure.

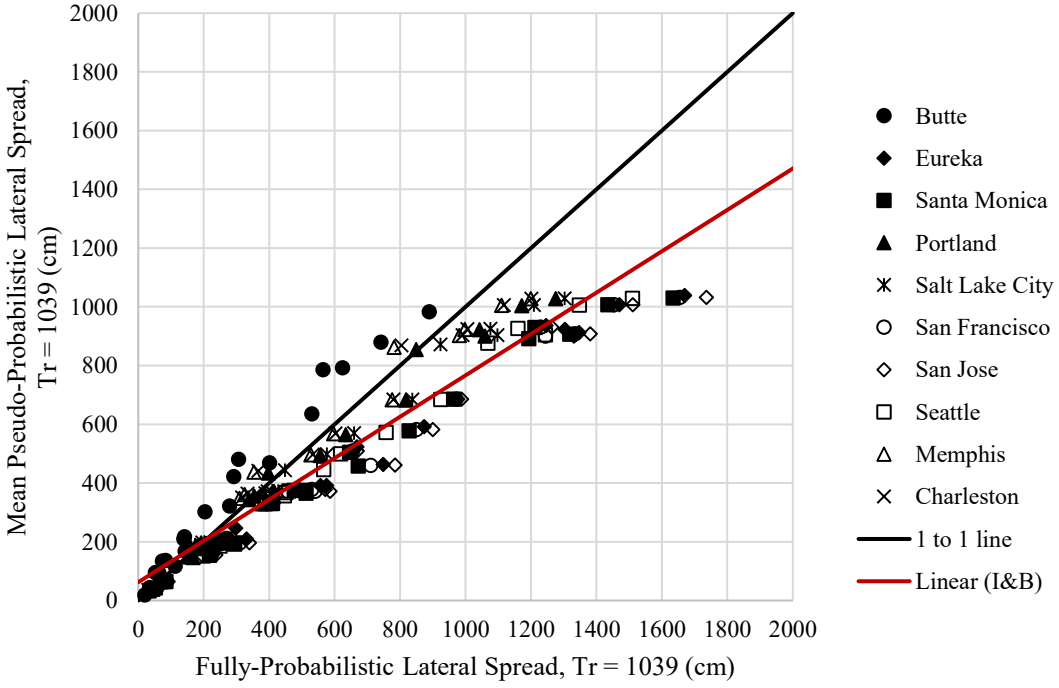

Figure 6-16: Mean magnitude pseudo-probabilistic versus fully-probabilistic for the 1039-year return period using the Boulanger and Idriss liquefaction triggering procedure.

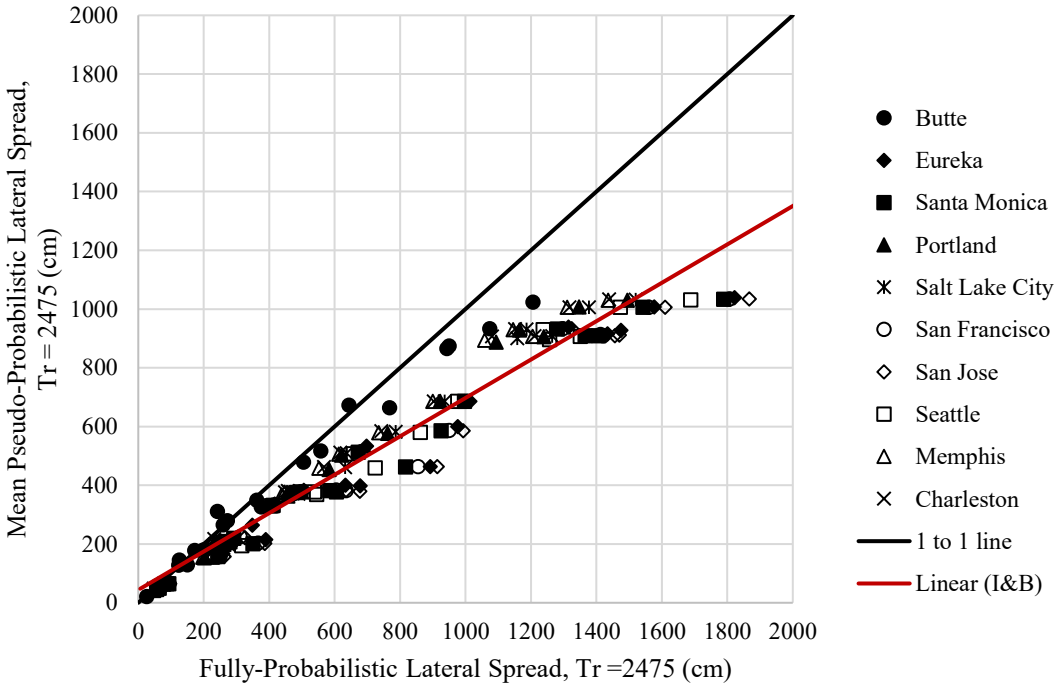

Figure 6-17: Mean magnitude pseudo-probabilistic versus fully-probabilistic for the 2475-year return period using the Boulanger and Idriss liquefaction triggering procedure.

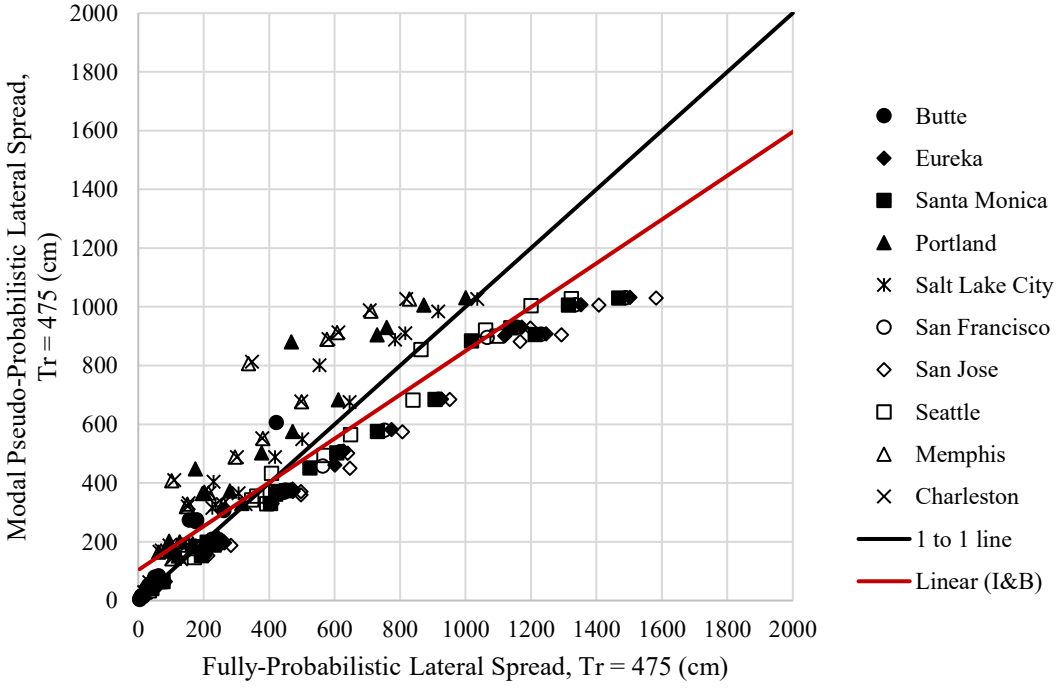

Figure 6-18: Modal magnitude pseudo-probabilistic versus fully-probabilistic for the 475-year return period using the Boulanger and Idriss liquefaction triggering procedure.

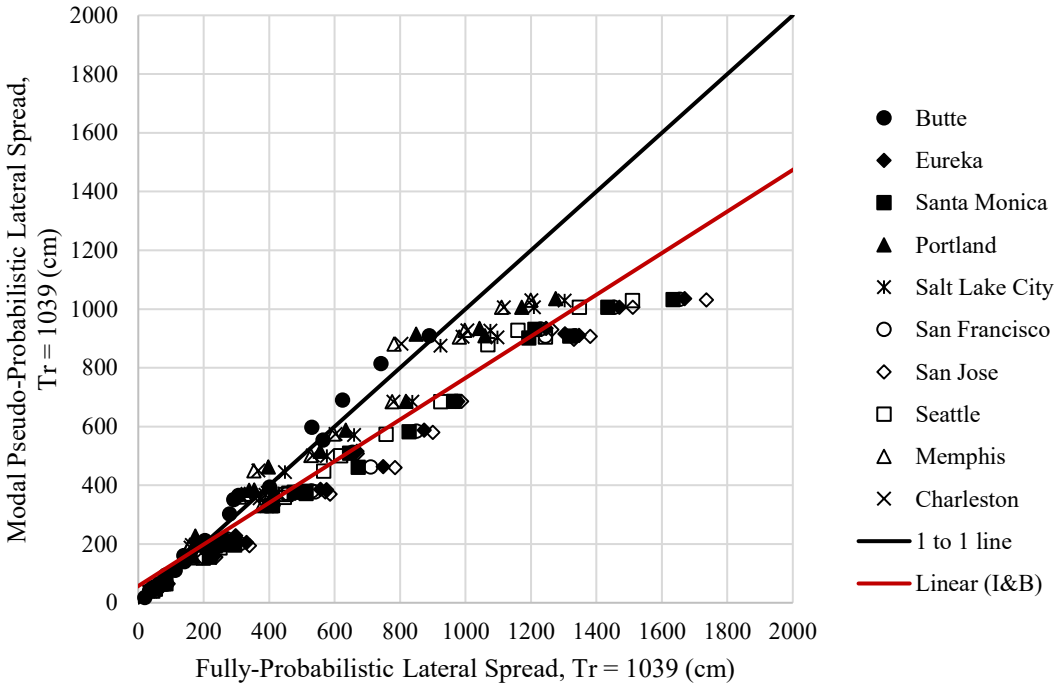

Figure 6-19: Modal magnitude pseudo-probabilistic versus fully-probabilistic for the 1039-year return period using the Boulanger and Idriss liquefaction triggering procedure.

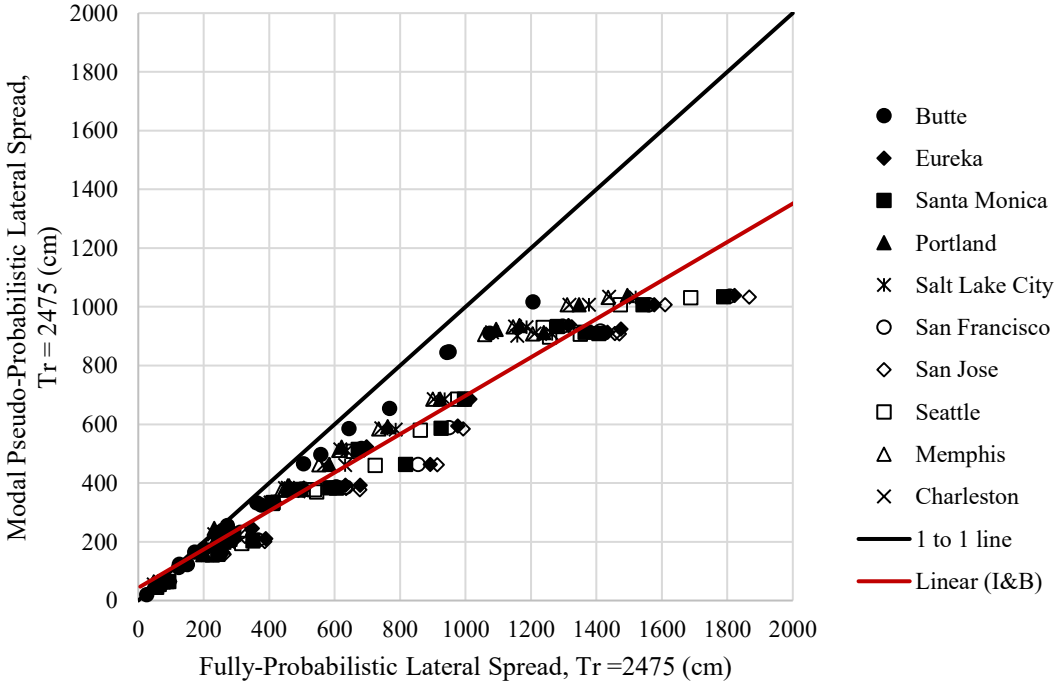

Figure 6-20: Modal magnitude pseudo-probabilistic versus fully-probabilistic for the 2475-year return period using the Boulanger and Idriss liquefaction triggering procedure.

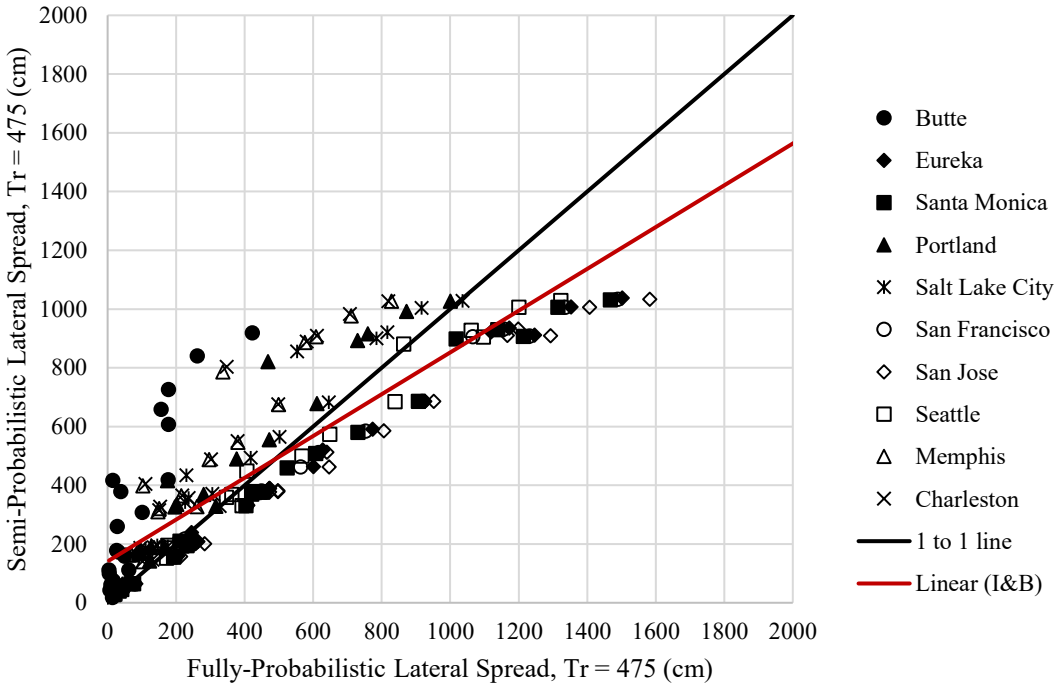

Figure 6-21: Semi-probabilistic versus fully-probabilistic for the 475-year return period using the Boulanger and Idriss liquefaction triggering procedure.

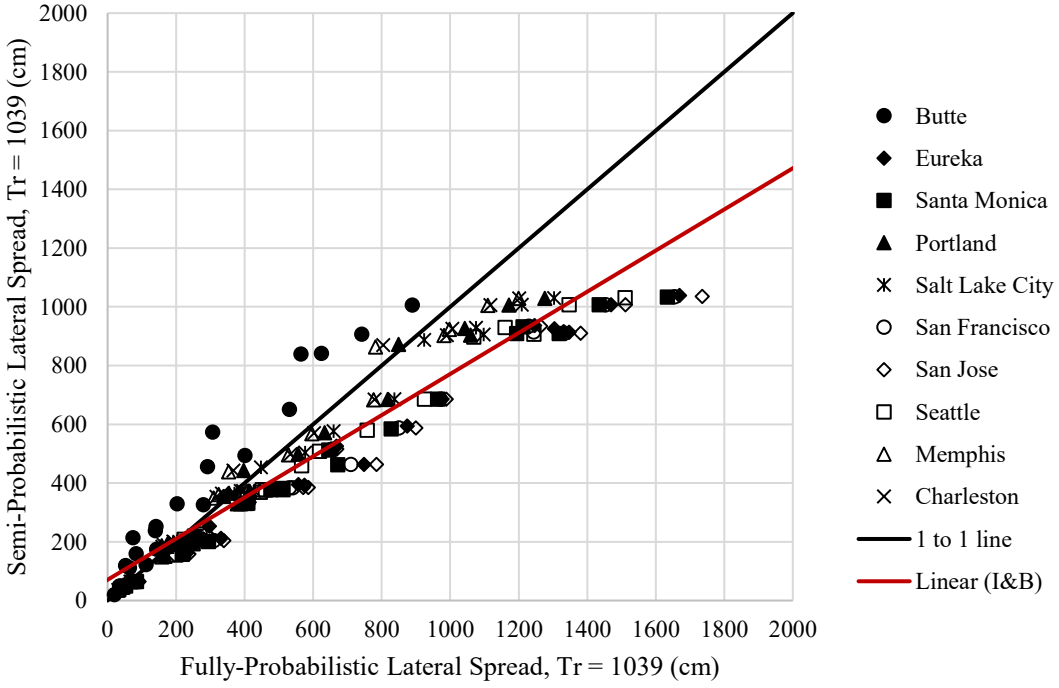

Figure 6-22: Semi-probabilistic versus fully-probabilistic for the 1039-year return period using the Boulanger and Idriss liquefaction triggering procedure.

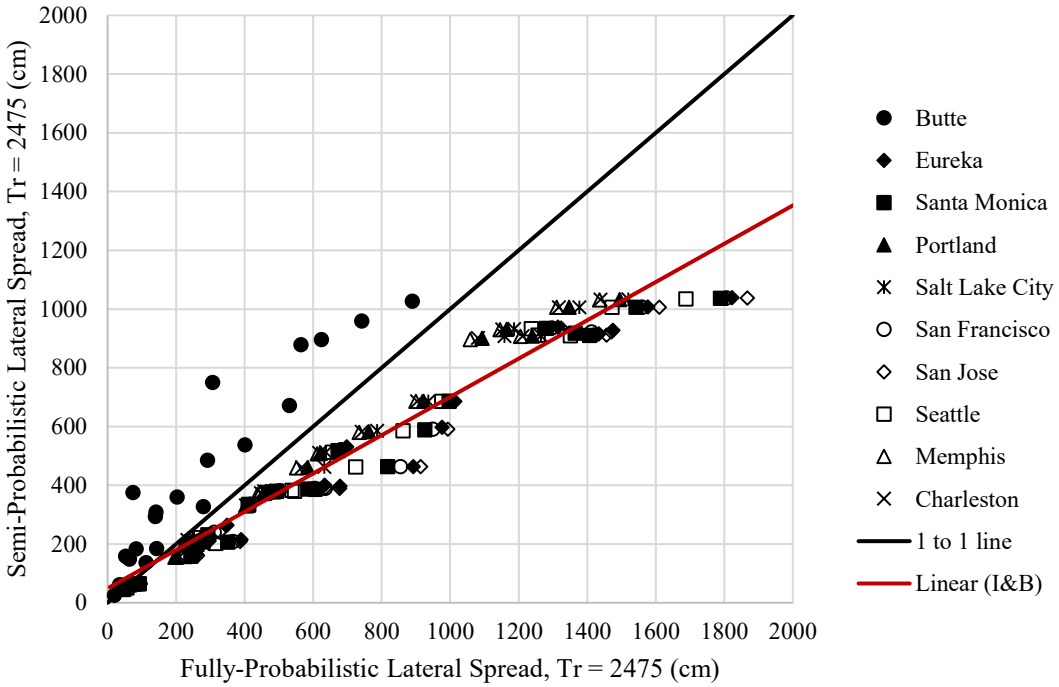

Figure 6-23: Semi-probabilistic versus fully-probabilistic for the 2475-year return period using the Boulanger and Idriss liquefaction triggering procedure.

The general trend that is observed is similar to that found using the Robertson and Wride procedure; specifically, the best-fit line goes farther and farther below the one-to-one line as the return period increases. This general trend indicates that the larger the seismic event, the more the conventional methods of predicting lateral spread displacement are under-predicting the amount of displacement that will occur. However, when using the Boulanger and Idriss procedure, the best-fit line never lies above the one-to-one line like it does for the 475-year return period using the Robertson and Wride procedure. Another trend similar to the results using the Robertson and Wride procedure is that the sites of lower seismicity, and the soil profiles that are less liquefiable, tend to have a closer agreement between the fully-probabilistic method and the conventional methods (visible in the bottom-left corner of each one-to-one plot). Using the Boulanger and Idriss procedure, the two different pseudo-probabilistic methods seem

to show the exact same trends with increasing return period, with the same amount of scatter. Because of these similarities, these two pseudo-probabilistic methods are analyzed in more detail together.

When comparing the fully-probabilistic method to the pseudo-probabilistic method, in general there are more points falling below the one-to-one line when using the Boulanger and Idriss procedure than when using the Robertson and Wride procedure. For the pseudo-probabilistic method, the Boulanger and Idriss procedure predicts lower lateral spread displacements than the Robertson and Wride procedure. The best-fit line crosses the one-to-one line at lower and lower points as the return period increases. The lines cross at approximately 400 cm, 200 cm, and 150 cm for the 475-year, 1039-year, and 2475-year return periods, respectively, indicating that, as the return period increases or the size of the seismic event increases, more points are being under-predicted when using the pseudo-probabilistic method. At the higher return period, almost all of the points are below the one-to-one line, which demonstrates that for larger seismic events the pseudo-probabilistic method will almost always under-predict the lateral spread displacement. This is especially true for areas of high seismicity and for highly liquefiable soil profiles that are being under-predicted by 10 to 50%.

When comparing the fully-probabilistic method to the semi-probabilistic method, almost identical trends are observed as those found with the comparison of the pseudo-probabilistic method. The only visible difference is in the data from the site with the lowest seismicity, Butte. As the return period increases, the majority of the data trends below the one-to-one line, with the exception of the points for Butte, which actually stay above the one-to-one line and are the only ones that remain there for the 2475-year return period. The reason these points stay above the one-to-one line is likely due to the semi-probabilistic method accounting for the uncertainty in

the liquefaction triggering procedure but not in the lateral spread procedure for this very-low-seismicity site.

As with the Robertson and Wride procedure, the results from the Boulanger and Idriss procedure were used to create box-and-whisker plots of the assumed return period versus actual return period. The box-and-whisker plots in Figure 6-24 through Figure 6-26 compare the assumed return period of the conventional method to the actual return period as determined by the fully-probabilistic method. The box-and-whisker plots show the minimum, first quartile, median, third quartile, maximum, and average (marked with an "x") values of the actual return period. The assumed return period is marked with a dotted red line for reference.

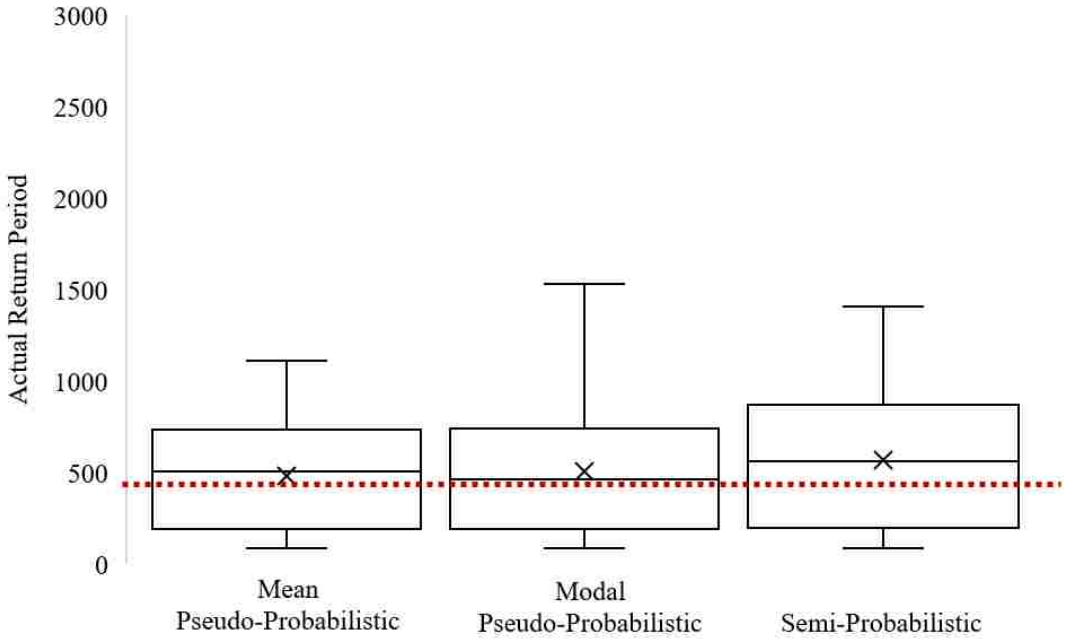

Figure 6-24: Box-and-whisker plots of actual return periods versus assumed 475-year return period using the Boulanger and Idriss liquefaction triggering procedure.

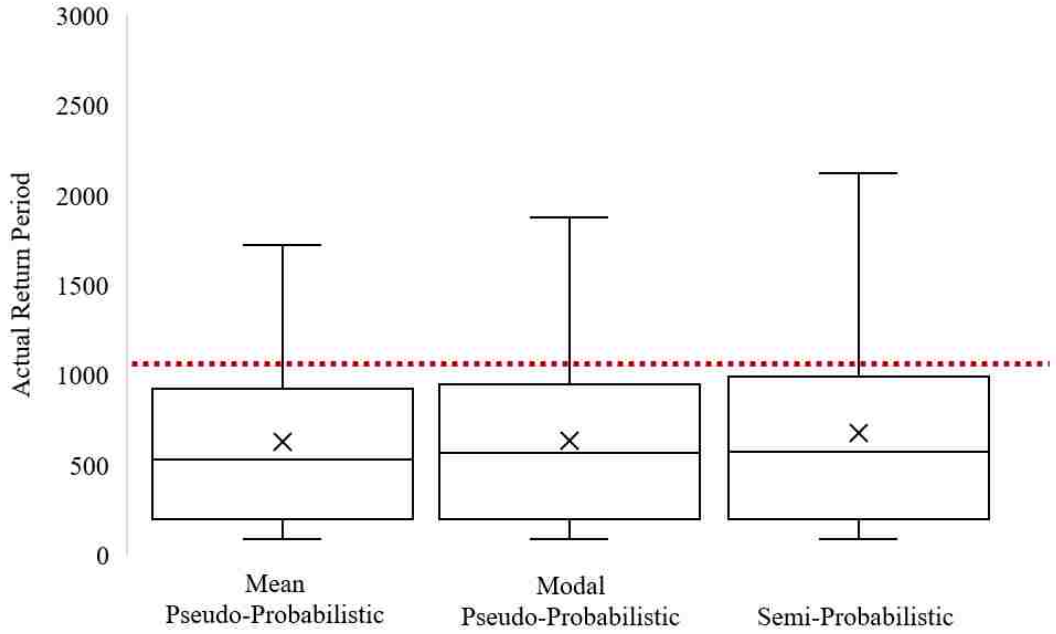

Figure 6-25: Box-and-whisker plots of actual return periods versus assumed 1039-year return period using the Boulanger and Idriss liquefaction triggering procedure.

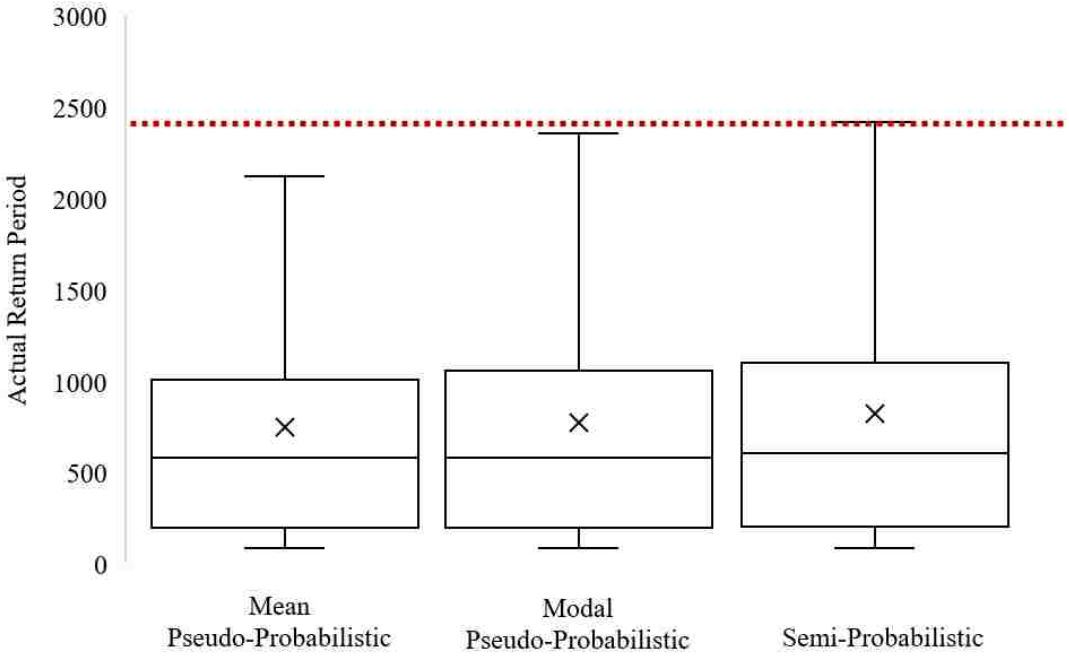

Figure 6-26: Box-and-whisker plots of actual return periods versus assumed 2475-year return period using the Boulanger and Idriss liquefaction triggering procedure.

The trends illustrated in the box-and-whisker plots in Figure 6-24 to Figure 6-26 are consistent with the trends found in the one-to-one plots in Figure 6-15 to Figure 6-23. The results are also consistent across all the different conventional methods at each return period. When using the Boulanger and Idriss liquefaction triggering procedure, the actual return period goes from being approximately equal to the assumed return period to substantially below the assumed return period as the assumed return period increases. This indicates that the conventional methods under-predict lateral spread displacement more as the return period increases.

6.5.3 Further Discussion of Results of Comparative Study

As was discussed in the previous sections, there is a slight difference in the calculation of lateral spread displacement when using the Robertson and Wride or Boulanger and Idriss liquefaction triggering procedures. When looking at the fully-probabilistic method for both liquefaction triggering procedures, the Boulanger and Idriss procedure consistently predicts higher values of lateral spread displacement, making it the more conservative option of the two. This trend, as well as others, is illustrated using a heat map, as shown in Figure 6-27.

To further examine the trends in the different liquefaction triggering procedures, Figure 6-27 shows a heat map that represents the number of CPT soundings (out of 20) at each city for which the pseudo-probabilistic method under-predicted lateral spread displacement by more than 10% (when compared to the fully-probabilistic method). The map is divided by the liquefaction triggering procedure, return period, and mean or modal magnitude input for the pseudo-probabilistic calculation. The cities are in order from lowest to highest seismicity.

City	Robertson & Wride (2009)						Idriss & Boulanger (2014)					
	475		1039		2475		475		1039		2475	
	Mean	Modal	Mean	Modal	Mean	Modal	Mean	Modal	Mean	Modal	Mean	Modal
Butte, MT	2	18	2	20	1	16	0	2	0	2	6	11
Memphis, TN	0	0	0	0	0	0	0	0	3	3	18	18
Charleston, S.C.	0	0	0	0	0	0	0	0	3	3	18	18
Portland, OR	0	0	0	0	3	1	0	0	11	6	20	18
Salt Lake City, UT	0	0	0	0	2	2	0	0	11	11	20	20
Seattle, WA	0	0	1	1	5	5	11	11	20	20	20	20
San Francisco, CA	1	0	5	4	6	5	20	18	20	20	20	20
Santa Monica, CA	1	0	4	3	5	4	20	18	20	20	20	20
Eureka, CA	1	2	4	4	5	5	18	20	19	20	20	20
San Jose, CA,	4	4	6	6	7	7	20	20	20	20	20	20

Figure 6-27: A heat map representing the number of CPT soil profiles, out of the total 20, in which the pseudo-probabilistic method under-predicted fully-probabilistic lateral spread displacements by more than 10%.

Evident in Figure 6-27 is how there are more lateral spread displacements being under-predicted by the Boulanger and Idriss procedure. As the fully-probabilistic method produces higher (more conservative) values with the Boulanger and Idriss procedure, it is therefore logical that, for the pseudo-probabilistic method, the Boulanger and Idriss procedure under-predicts more displacements than the Robertson and Wride procedure. Also evident in the heat map is how the rate of under-prediction increases as the return period and level of seismicity increase.

Figure 6-27 has three outliers at Butte for the modal magnitude pseudo-probabilistic method using the Robertson and Wride procedure. These three points had 16 to 20 profiles under-predict the lateral spread displacement by more than 10%, while the mean magnitude calculation resulted in only one or two under-predictions. This is likely due to the large difference in mean and modal magnitude, resulting in a significant different in the calculation of *MSF* (found in Chapter 3). Since the *MSF* is calculated differently in the Boulanger and Idriss procedure, the outliers are only present in the Robertson and Wride procedure.

6.5.4 Practical Implications of Study Results

Pseudo-probabilistic methods of predicting lateral spread displacements are widely accepted in the engineering industry because they are considered conservative and are simple to perform. This study found that the pseudo-probabilistic method does seem to give reasonable results for lower return periods, even conservative results at times. However, as the size of the seismic event increases, the ability of the pseudo-probabilistic method to accurately predict lateral spread displacements quickly diminishes, which is due to the pseudo-probabilistic method using a deterministic calculation of lateral spreading. The deterministic method does not account for the inherent uncertainty in the calculation of the horizontal strains that are used to determine the lateral spread displacements. This uncertainty can be accredited for lateral spread displacements being under-predicted by up to 80% at large return periods.

This information is concerning, as the common practice for engineers today is to use the pseudo-probabilistic method. Large seismic events are the most problematic in terms of damage, cost, and danger to human lives. Therefore, use of a fully-probabilistic method that accounts for uncertainty in the calculation of lateral spread displacements is essential. As practicing engineers continue to ignore uncertainty in estimating lateral spread displacements, the structures they design may withstand smaller earthquakes but will be under-designed during a larger seismic event. Relying on the pseudo-probabilistic method in designing for higher return periods can lead to disastrous economic loss and potential loss of life in the aftermath of a large earthquake. Lateral spread displacements can only be accurately predicted by implementing this newly developed fully-probabilistic method and accounting for all uncertainty in the seismic hazard analysis.

The semi-probabilistic method showed trends similar to those obtained using the pseudo-probabilistic method. Therefore, the semi-probabilistic method is not an improvement on the pseudo-probabilistic method as this method does not result in displacements any closer to those determined using the fully-probabilistic method. While the semi-probabilistic method accounts for uncertainty in the liquefaction triggering calculations, it does not account for uncertainty in the horizontal strain calculation. It seems that this second source of uncertainty is what contributes far more to the different displacements calculated by the pseudo-probabilistic and fully-probabilistic methods. The fully-probabilistic method accounts for both types of uncertainties and therefore cannot be replaced by a method that only accounts for uncertainty in one aspect of the calculation.

After viewing the results of the comparative study, it should not be mistakenly assumed that this indicates that one liquefaction triggering procedure is better than another. It also should be known that implementation of these procedures in a fully-probabilistic framework does not relate to field validation of the same liquefaction triggering procedures. These results showed that the Boulanger and Idriss procedure is more sensitive to the pseudo-probabilistic method. This does not indicate that the Boulanger and Idriss procedure is a worse predictive model when validating field data with actual case histories. In fact, the Boulanger and Idriss procedure could possibly show better agreement of field observations than the Robertson and Wride procedure. Having a closer agreement with field data does not imply that a liquefaction triggering procedure using a pseudo-probabilistic method has a closer agreement with the fully-probabilistic method. Multiple procedures should be used in any seismic hazard analysis to account for epistemic uncertainty. If site-specific preferences exist, they can be accounted for using tools such as weighting factors between procedures.

It should be mentioned that the scope of this study is not without bounds. This study only focused on lateral spread displacements calculated using the Zhang et al. (2004) procedure. Therefore, it does not apply directly to other lateral spread displacement procedures. Also, only two liquefaction triggering models were used (Robertson and Wride (1998) and Boulanger and Idriss (2016)). All sites and soil profiles were restricted to those found within the United States. As this study emphasized lateral spread displacements, it does not apply directly to other liquefaction effects such as settlement, bearing capacity, slope stability, etc.; however, a study was completed by Hatch (2017) that demonstrates a similar analysis for liquefaction-induced settlement using the same database. Further research should be performed to go beyond the bounds mentioned.

6.6 Correction Factor Sensitivity Analysis

When calculating lateral spread displacements, there are multiple factors affecting the liquefaction susceptibility that can cause an over-prediction of the horizontal strains involved. Some of these factors include failures to account for the effect of depth, thin sand layers, and transition zones between stiff and soft soil layers. Along with the comparative study previously discussed, a separate analysis was conducted to determine the sensitivity of lateral spread displacement calculations to these correction factors.

To perform this analysis, four fully-probabilistic lateral spread calculations were completed using different combinations of correction factors. The first data set is that which was already analyzed, with no corrections applied (referred to as the baseline data set). The second data set is corrected using a depth-weighting factor. The third data set is corrected using a combination of a thin-layer correction and a transition-zone correction. The fourth data set is corrected using both the depth-weighting factor, as well as a combination of a thin-layer

correction and a transition-zone correction. The theory behind these different correction factors is discussed in the following sections.

6.6.1 Depth-Weighting Correction Factor

The susceptibility of a soil to liquefaction decreases with depth (Iwasaki et al., 1982). However, this relationship is not accounted for in the liquefaction triggering procedures previously presented. To account for this, Cetin et al. (2009) has suggested weighting volumetric strains for depths less than 18 m and not accounting for strains at depths greater than 18 m. While the procedure presented by Cetin et al. (2009) is intended for volumetric strains (as used in settlement calculations), it can be assumed that the same depth-weighting factor can be applied to lateral spread displacements as the horizontal shear strains used in those calculations are impacted by the same mechanisms as volumetric strains. The depth-weighting factor calculated at each depth is then multiplied by the strain at the corresponding soil increment. This factor is calculated as shown in Equation 6-1:

$$DF_i = 1 - \frac{d_i}{18m} \tag{6-1}$$

where d_i is the depth at the soil increment of interest.

When applying this depth-weighting factor to lateral spreading, it can be directly applied for displacements occurring on gently sloping ground. Personal communication with Dr. Peter K. Robertson and Dr. T. Leslie Youd (in reference to Chu et al. (2006)) has led to the conclusion that this is an acceptable assumption for gently sloping ground; however, for lateral spread displacements occurring on sites near a free face, no depth correction factor is applied. Rather,

soil increments at depths beyond two times the height of the free face do not contribute to liquefaction triggering.

As there are two different procedures for determining the depth-weighting factor for different site geometries, it was decided that the sensitivity analysis will also include two different site geometries. As with the comparative study, a site with gently sloping ground and a site with level ground near a free face were analyzed. The same gently sloping ground geometry of 3% that was used in the comparative study (lateral spread geometry 1) was also used in the sensitivity analysis. However, level ground near a free face (lateral spread geometry 2) used in the comparative study was not used in the sensitivity analysis. Lateral spread geometry 2 has a free face height (H) of 6 m and a distance to the free face (L) of 50 m. Since all soil profiles used in this study have a maximum depth of 12 m, when applying a depth-weighting factor to lateral spread geometry 2, there is no correction observed as two times the height of the free face is equal to the maximum depth. It was determined that a new site geometry (lateral spread geometry 3) should be created specifically for the sensitivity analysis. Lateral spread geometry 3 has a free face height (H) of 3 m and a distance to the free face (L) of 25 m. Since the Zhang et al. (2004) procedure uses a ratio of L/H to calculate the final displacement, lateral spread geometry 3 has the same results as lateral spread geometry 2. However, since lateral spread geometry 3 has a smaller free-face height, the application of a depth-weighting factor is possible. Lateral spread geometry 1 and lateral spread geometry 3 are used for the entirety of the sensitivity analysis.

6.6.2 Transition-Zone Correction Factor

As the cone tip of the CPT is pushed through a soil profile, it encounters layers of varying stiffness and soil type. Because the CPT provides a continuous profile, the inter-layer boundary

between soil layers is not as easily defined as it may be with the SPT. As a result, the measured cone tip resistance of an inter-layer boundary is influenced by the soil properties both ahead and behind the cone as it is pushed though the soil (Treadwell, 1976). Figure 6-28 shows an example of a transition zone as a cone tip is pushed from a medium dense sand into a soft clay. This transition zone exists from an interface distance of 0 m to approximately -0.25 m, where the tip resistance is decreased gradually until the cone reaches the interface.

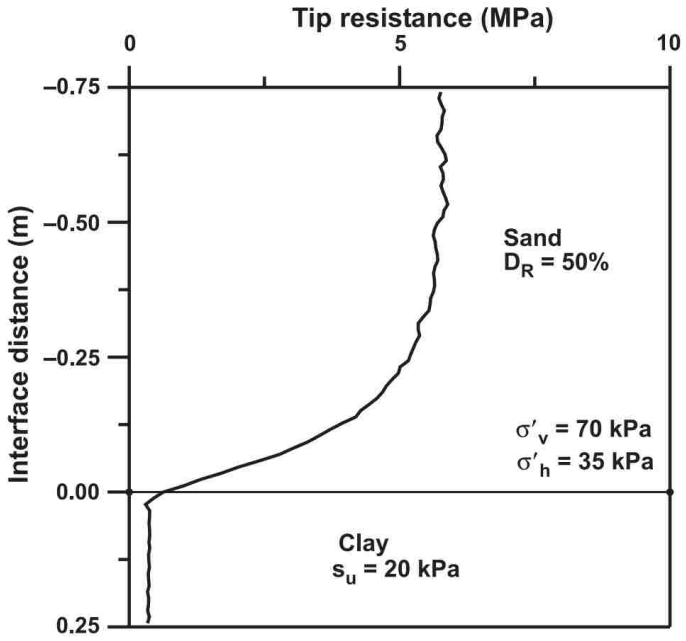

Figure 6-28: Example of a transition zone for medium dense sand overlying soft clay (after Ahmadi and Robertson 2005).

Robertson (2011) defines a transition zone as a steep change in *Ic* between soil increments (usually greater than 0.01). To account for the incorrect measurement of tip resistance found in these transition zones, Robertson (2011) suggests removing these soil increments from the liquefaction triggering analysis. However, it is possible that these transition zones can still contribute to the liquefaction hazard. Rather than entirely disregard the soil increments in these

transition zones, this study uses the correction process outlined for a thin-layer correction, as presented in the following section.

6.6.3 Thin-Layer Correction Factor

A thin sand layer embedded in a soft clay deposit can cause a CPT to record incorrect measurements of tip resistance, similar to what occurs with a transition zone. In this case, the cone tip resistance for the thin sand layer is recorded as being much lower than its actual stiffness. The cone tip resistance is recorded as being much lower because as the cone enters the thin sand layer the recorded cone tip resistance is influenced by the soft clay layer above, and before it exits the thin sand layer the cone tip resistance begins to be influenced by the soft clay layer below. An example of this is shown in Figure 6-29, where "Layer A" is a thin sand layer and "Deposit B" is a soft clay deposit above and below the sand layer. As the cone enters the thin

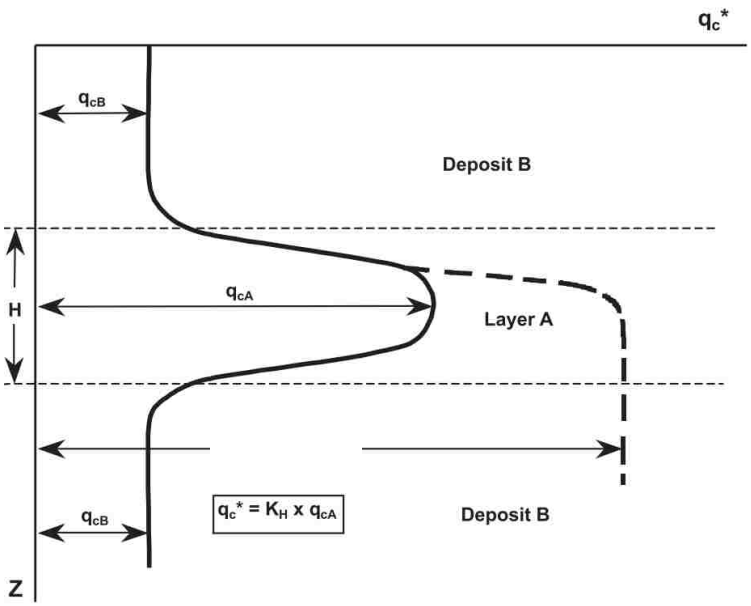

Figure 6-29: Example of the effect of a thin interbedded sand layer (Layer A) between two soft clay deposits (Deposit B) on cone tip resistance (after Ahmadi and Robertson 2005).

sand layer, it takes some distance before it does not feel the influence of the soft clay above. Before the tip resistance records the true stiffness of the sand, it is influenced by the clay layer below and decreases rapidly. As the cone tip is influenced by the clay layer, it causes the sand layer to seem much softer than it truly is, which can lead to the over-prediction of liquefaction-induced lateral spread displacements. Youd et al. (2001) provides a correction factor to account for these thin sand layers in a liquefaction hazard evaluation.

Once a thin sand layer is identified, a correction factor can be applied to the measured cone tip resistance to correct for this effect. As mentioned, Youd et al. (2001) define a correction factor, K_H, which is used as shown in Equations 6-2 and 6-3:

$$q_c^* = K_H q_c \tag{6-2}$$

$$K_H = 0.25\left[\frac{\left(\frac{H}{d_c}\right)}{17} - 1.77\right]^2 + 1.0 \tag{6-3}$$

where q_c* is the corrected cone tip resistance accounting for the thin sand layer, d_c is the diameter of the cone, and H is the thin sand layer thickness.

As mentioned previously, the sensitivity analysis used a data set that was corrected using a combination of a thin-layer correction and a transition-zone correction. This combination is accomplished by correcting the tip resistance using the correction factor for the thin sand layer, while identifying the thin sand layer and transition zones using the definition of a transition zone (as described by Robertson (2011)). As these two corrections are very similar in nature, this

assumption is appropriate. Applying the correction in this manner also aided in the automation of the calculations completed in *CPTLiquefY*.

6.6.4 Results and Discussion of Sensitivity Analysis

With an understanding of the correction factors used in the sensitivity analysis, the results can be presented. This analysis was performed at all 10 locations, for all 20 soil profiles, and at the same three return periods used in the comparative study. The resulting data were combined and are presented in box-and-whisker plots in Figure 6-30 to Figure 6-35. To compare these different levels of correction, a ratio (R) was created, as defined in Equation 6-4:

$$R = \frac{Lateral\ Spread_{Corrected}}{Lateral\ Spread_{Baseline}} \tag{6-4}$$

where $Lateral\ Spread_{Corrected}$ is the calculated fully-probabilistic displacement for one of the corrected data sets, and $Lateral\ Spread_{Baseline}$ is the calculated fully-probabilistic displacement for the baseline data set with no corrections. *R* for any data set can then be multiplied by the baseline value to get the corrected value. If *R* were equal to 1, this would indicate that no correction was calculated. If *R* were equal to 0.5, this would indicate that the corrected displacement results in half of the baseline displacement. The lower the *R* value is, the more sensitive the fully-probabilistic procedure is to that correction.

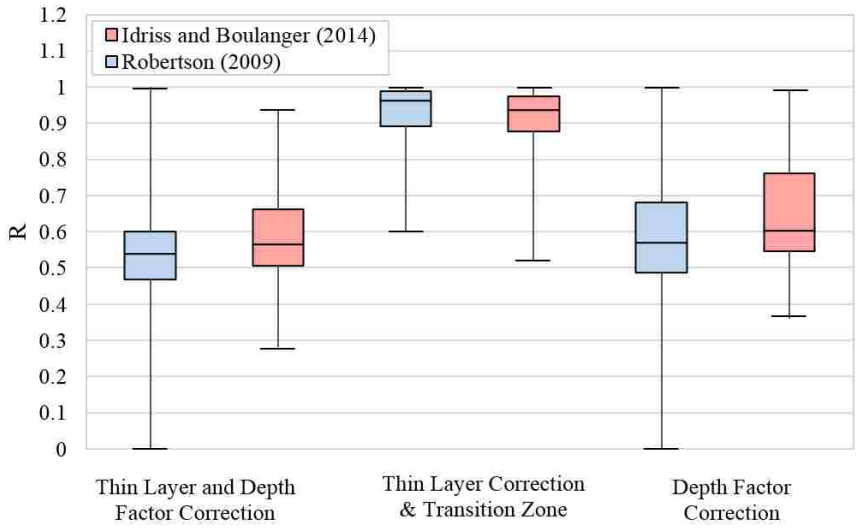

Figure 6-30: Box-and-whisker plots for R at a return period of 475 years (geometry 1).

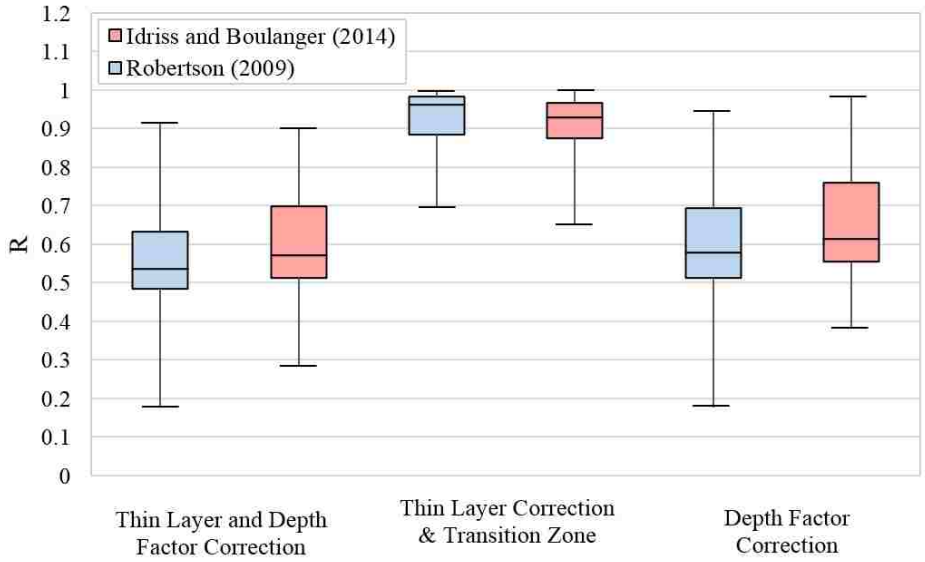

Figure 6-31: Box-and-whisker plots for R at a return period of 1039 years (geometry 1).

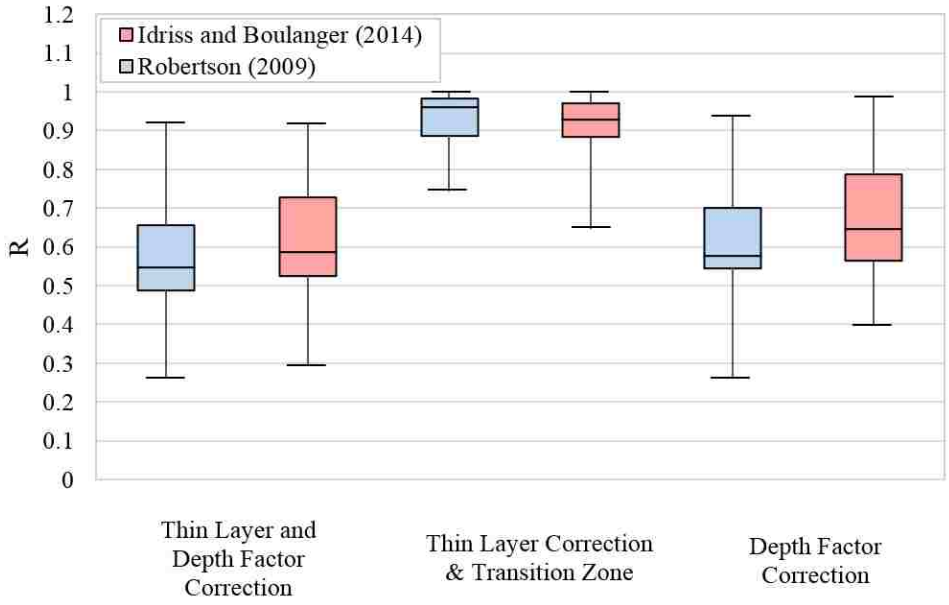

Figure 6-32: Box-and-whisker plots for R at a return period of 2475 years (geometry 1).

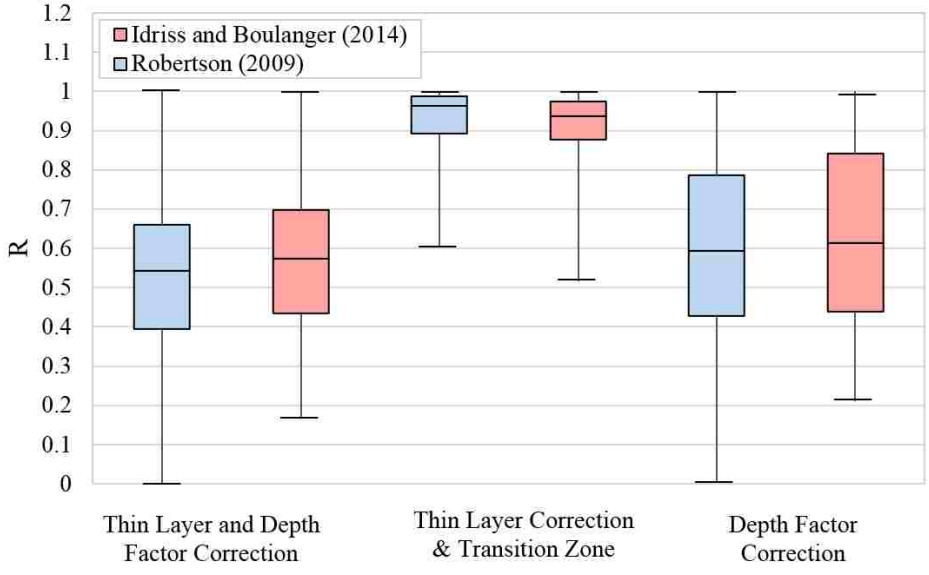

Figure 6-33: Box-and-whisker plots for R at a return period of 475 years (geometry 3).

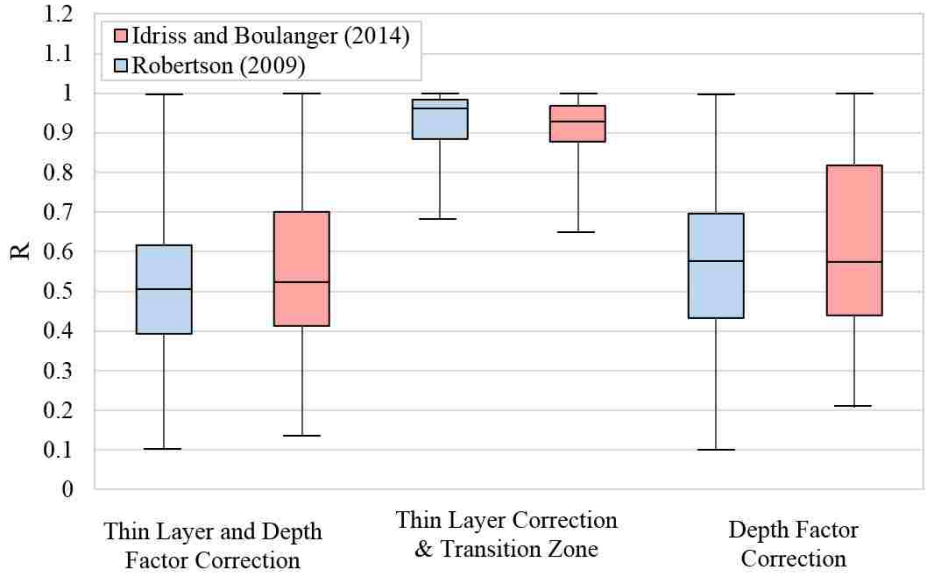

Figure 6-34: Box-and-whisker plots for R at a return period of 1039 years (geometry 3).

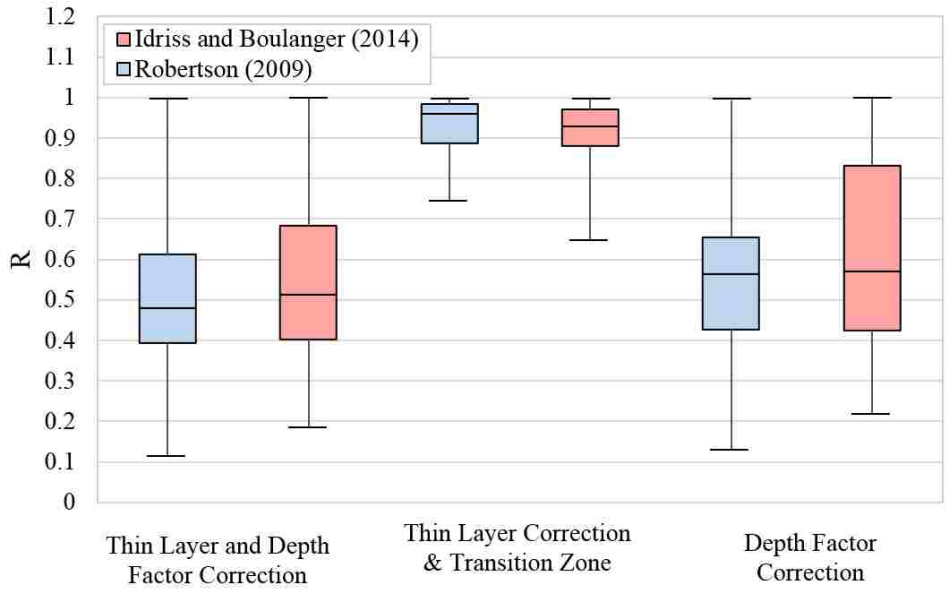

Figure 6-35: Box-and-whisker plots for R at a return period of 2475 years (geometry 3).

The box-and-whisker plots presented above show how sensitive the fully-probabilistic method is to the correction factors discussed previously. As illustrated in Figure 6-30 to Figure

6-35, the box-and-whisker plots have many things in common. The first trend that is easily noticed is how the depth-weighting correction factor has a much greater influence than the thin-layer/transition-zone correction factor. The median value of *R* for the thin-layer/transition-zone correction factor is always close to 0.95, while the median value of *R* for the depth-weighting correction factor is consistently near 0.55 to 0.60, indicating a higher sensitivity to the depth-weighting correction factor. It is likely that there was a higher sensitivity to the depth-weighting correction factor because it is independent of soil parameters. The depth-weighting correction factor is always applied and almost always lowers the calculated displacement. However, the thin-layer/transition-zone correction factor is a function of the change in *Ic*, and, if there is no steep change in *Ic*, there is no thin-layer/transition-zone correction applied, which was the case for a few of the soil profiles used in this study.

While most of the plots are similar between the two geometries, two procedures, and three return periods, there are a few differences to note. When comparing the Robertson and Wride procedure to the Boulanger and Idriss procedure, there is only a slight difference between the two, but it is not consistent. At times the Robertson and Wride procedure has a higher median value of *R* or a larger spread, but at other times it is the Boulanger and Idriss procedure with the higher median value of *R* or a larger spread. When comparing lateral spread geometry 1 to lateral spread geometry 3, the general trends remain the same. While the trends of the thin-layer/transition-zone correction factor are the same, it seems that lateral spread geometry 3 shows a larger spread for the depth-weighting factor correction, especially within the inter-quartile range. One final minor difference to note is that it seems that, as the return period increases, the spread decreases while the median values stay generally in the same area.

Further statistical analysis could be performed on this correction factor sensitivity study to identify sources of uncertainty in the analysis. However, it was determined that an in-depth statistical analysis is beyond the scope of this study. Therefore, the results are limited to those presented previously for demonstrating the sensitivity of the fully-probabilistic method to the observed CPT correction factors.

6.7 Chapter Summary

The fully-probabilistic method of estimating lateral spread displacements was compared to the conventional pseudo-probabilistic and semi-probabilistic methods. In this comparison, 10 cities, 20 CPT profiles, three return periods, and two site geometries were analyzed. These calculations were run using the newly developed research tool, *CPTLiquefY*. By comparing these results, it was found that, for lower seismic areas and for lower return periods, the conventional methods correlated reasonably well to the more precise fully-probabilistic method. However, in general, as the return period increased and the seismicity increased, the conventional method began to under-predict lateral spread displacements. While the semi-probabilistic method accounted for uncertainty in the liquefaction triggering procedure, it still did not perform better than the pseudo-probabilistic method. These results demonstrate that the conventional methods for predicting lateral spread displacement used by engineers are not sufficient as they can lead to the under-prediction of lateral spreading at high return periods and for areas of high seismicity.

A sensitivity study showed how the fully-probabilistic method is affected by a depth-weighting correction factor and a thin-layer/transition-zone correction factor. While the thin-layer/transition-zone correction factor had an effect on the results, the fully-probabilistic method was more sensitive to the depth-weighting correction factor, regardless of liquefaction triggering procedures or return period.

7 SUMMARY AND CONCLUSIONS

Liquefaction occurs in loose soil as it is subjected to seismic loading, such as earthquake shaking. One of the most common effects of liquefaction is lateral spread displacement. Lateral spreading occurs as loose layers of soil liquefy and lose strength, causing all surficial layers to displace down a gentle slope or toward a free face. While lateral spread displacements may not be immediately life-threatening, they cause significant damage to infrastructure, having a large economic impact. To prepare for the potential damages caused by lateral spread displacements, engineers in industry commonly use a pseudo-probabilistic method, which attempts to account for the inherent uncertainty in the ground motion selection but disregards uncertainty in the other aspects of the seismic hazard analysis.

To account for all uncertainty in the estimation of lateral spread displacements, a fully-probabilistic method was developed following the framework of PBEE procedures. This study introduced a new fully-probabilistic method using input data from the CPT. As the fully-probabilistic method is complex in nature, a seismic hazard analysis tool, *CPTLiquefY*, was created to run any type of seismic hazard analysis.

To better understand how conventional methods of predicting lateral spread displacements compare to the more accurate fully-probabilistic method, a comparative study was performed. This comparison was performed with 20 CPT profiles, at 10 sites of varying seismicity, and for three return periods. It was found that the conventional methods showed consistent trends when

compared to the fully-probabilistic methods. For low return periods and areas of low seismicity, the conventional methods of predicting lateral spread displacements seem to match or slightly over-predict the results when compared to the fully-probabilistic method. However, for higher return periods and areas of high seismicity, the conventional methods under-predicted the lateral spread displacement.

Along with the comparative study, a separate analysis was completed that demonstrated the sensitivity of the fully-probabilistic method to a depth-weighting correction factor and a thin-layer/transition-zone correction factor. It was found that the fully-probabilistic method is more sensitive to the depth-weighting correction factor, adjusting displacement values by up to 50%. The thin-layer/transition-zone correction factor influenced the displacement values but not as much as the depth-weighting correction factor. These results demonstrate that correction factors such as these should not be neglected when estimating lateral spread displacements.

The results of the comparative study are cause for concern as they indicate that the conventional methods being used in industry may not be correctly predicting some lateral spread displacements. As engineers commonly use the pseudo-probabilistic method to predict lateral spread displacements, they may accurately design a structure to resist smaller seismic events, but structures designed for larger seismic events with the same practice will not be sufficiently protected from larger earthquakes. There is a need to implement these newly developed fully-probabilistic design practices in industry to account for all uncertainty in predicting lateral spread displacements. By implementing the fully-probabilistic method, more structures will be protected, and large economic losses will be minimized.

REFERENCES

Abrahamson, N., and Silva, W. (2008). "Summary of the Abrahamson & Silva NGA Ground-Motion Relations." *Earthquake Spectra: February 2008*, 24(1), 67-97.

Ahmadi, M. M., and Robertson, P. K. (2005). "Thin-layer effects on the CPT qc measurement." *Canadian Geotechnical Journal*, 42(5), 1302-1317.

Ambraseys, N. N. (1988). "Engineering seismology." *Earthquake Engineering and Structural Dynamics*, 17, 1-105.

Ancheta, T. D., Darragh, R. B., Stewart, J. P., Seyhan, E., Silva, W. J., Chiou, B. S.-J., Wooddell, K. E., Graves, R. W., Kottke, A. R., Boore, D. M., Kihida, T., and Donahue, J. L. (2014). "NGA-West2 Database." *Earthquake Spectra:*, 30(3), 989-1005.

Arias, A. (1970). "A measure of earthquake intensity." *Seismic Design for Nuclear Power Plants*, MIT Press, Cambridge, Massachusetts, 438-483.

Arndt, A. M. (2017). "Performance-Based Liquefaction Triggering Analyses with Two Liquefaction Models Using the Cone Penetration Test." *(Master of Science), Brigham Young University, Provo, UT.*

Bardet, J.-P., Tobita, T., Mace, N., and Hu, J. (2002). "Regional modeling of liquefaction-induced ground deformation." *Earthquake Spectra*, 18(1), 19-46.

Baska, D. (2002). "An analytical model for prediction of lateral spread displacement." Ph. D. dissertation, Univ. of Washington, Seattle., Google Scholar.

Baziar, M., Dobry, R., and Elgamal, A.-W. (1992). "Engineering evaluation of permanent ground deformations due to seismically induced liquefaction."

Benioff, H. (1955). *Mechanism and strain characteristics of the White Wolf fault as indicated by the aftershock sequence*, California Division of Mines, Bulletin 171.

Benjamin, J. R., and Associates (1988). "A criterion for determining exceedance of the Operating Basis Earthquake." *EPRI Report NP-5930*, E. P. R. Institute, ed.Palo Alto, California.

Bhattacharya, S., Tokimatsu, K., Goda, K., Sarkar, R., Shadlou, M., and Rouholamin, M. (2014). "Collapse of Showa Bridge during 1964 Niigata earthquake: A quantitative reappraisal on the failure mechanisms." *Soil Dynamics and Earthquake Engineering*, 65, 55-71.

Bolt, B. A. "Duration of strong motion." *Proc., 4th World Conference on Earthquake Engineering*, 1304-1315.

Boore, D. M., and Atkinson, G. M. (2008). "Ground-Motion Prediction Equations for the Average Horizontal Component of PGA, PGV, and 5%-Damped PSA at Special Periods between 0.01 s and 10.0 s." *Earthquake Spectra: February 2008*, 24(1), 99-138.

Boulanger, R. W. (2003). "Closure to "High Overburden Stress Effects in Liquefaction Analyses," by Ross W. Boulanger." *Journal of geotechnical and geoenvironmental engineering*, 131(8), 1060-1062.

Boulanger, R. W., and Idriss, I. (2016). "CPT-based liquefaction triggering procedure." *Journal of Geotechnical and Geoenvironmental Engineering*, 142(2), 04015065.

Bozorgnia, Y., Abrahamson, N. A., Atik, L. A., Ancheta, T. D., Atkinson, G. M., Baker, J. W., Baltay, A., Boore, D. M., Campbell, K. W., and Chiou, B. S.-J. (2014). "NGA-West2 research project." *Earthquake Spectra*, 30(3), 973-987.

Bray, J. D., and Sancio, R. B. (2006). "Assessment of the liquefaction susceptibility of fine-grained soils." *Journal of geotechnical and geoenvironmental engineering*, 132(9), 1165-1177.

Bray, J. D., Sancio, R. B., Kammerer, A. M., Merry, S., Rodriguez-Marek, A., Khazai, B., Chang, S., and Bastani, A. (2001). "Some Observations of Geotechnical Aspects of the February 28, 2001, Nisqually Earthquake in Olympia, South Seattle, and Tacoma, Washington." <http://peer.berkeley.edu/publications/nisqually/geotech/index.html>.

Bray, J. D., and Travasarou, T. (2007). "Simplified procedure for estimating earthquake-induced deviatoric slope displacements." *Journal of Geotechnical and Geoenvironmental Engineering*, 133(4), 381-392.

Byrne, P. M. (1991). "A model for predicting liquefaction induced displacement."

Byrne, P. M., Jitno, H., and Salgado, F. "Earthquake induced displacements of soil-structures systems." *Proc., Proceedings of 10th World Conference on Earthquake Engineering*, 1407-1412.

Cambell, K. W., and Bozorgnia, Y. (2008). "NGA Ground Motion Model for the Geometric Mean Horizontal Component of PGA, PGV, PGD, and 5% Damped Linear Elastic Response Spectra for Periods Ranging from 0.01 to 10 s." *Earthquake Spectra: February 2008*, 24(1), 139-171.

Casagrande, A. (1936). "Characteristics of cohesionless soils affecting the stability of slopes and earth fills." *Journal of the Boston Society of Civil Engineers*.

Cetin, K., Bilge, H., Wu, J., Kammerer, A., and Seed, R. (2009). "Probabilistic Model for the Assessment of Cyclically Induced Reconsolidation (Volumetric) Settlements." *Journal of Geotechnical and Geoenvironmental Engineering*, 3(135), 387-393.

Chen, L., Yuan, X., Cao, Z., Hou, L., Sun, R., Dong, L., Wang, W., Meng, F., and Chen, H. (2009). "Liquefaction macrophenomena in the great Wenchuan earthquake." *Earthquake Engineering and Engineering Vibration*, 8(2), 219-229.

Chiou, B. S.-J., and Youngs, R. R. (2008). "A NGA Model for the Average Horizontal Component of Peak Ground Motion and Response Spectra." *Earthquake Spectra: February 2008*, 24(1), 173-215.

Chu, D. B., Stewart, J. P., Youd, T. L., and Chu, B. (2006). "Liquefaction-induced lateral spreading in near-fault regions during the 1999 Chi-Chi, Taiwan earthquake." *Journal of geotechnical and geoenvironmental engineering*, 132(12), 1549-1565.

Cornell, C. A., and Krawinkler, H. (2000). "Progress and challenges in seismic performance assessment." *PEER Center News*, 3(2), 1-3.

Coulter, H. W., and Migliaccio, R. R. (1966). "Effects of the earthquake of March 27, 1964, at Valdez, Alaska."

Deierlein, G., Krawinkler, H., and Cornell, C. "A framework for performance-based earthquake engineering." *Proc., Pacific conference on earthquake engineering*, Citeseer, 1-8.

Dobry, R., and Baziar, M. "Evaluation of ground deformation caused by lateral spreading." *Proc., Proceedings of the 3rd Japan–US Workshop on Earthquake Resistant Design of Lifelines Facilities and Countermeasures for Soil Liquefaction, San Francisco, Calif*, 17-19.

Dobry, R., and Vucetic, M. "Dynamic properties and seismic response of soft clay deposits." *Proc., International Symposium on Geotechnical Engineering of Soft Soils*, 51-87.

Eberhard, M. O., Baldridge, S., Marshall, J., Mooney, W., and Rix, G. J. (2013). *Mw 7.0 Haiti Earthquake of January 12, 2010: USGS/EERI Advance Reconnaissance Team Report*, BiblioGov.

Finn, W. L., Yogendrakumar, M., Yoshida, N., and Yoshida, H. (1986). "TARA-3: A program to compute the response of 2-D embankments and soil-structure interaction systems to seismic loadings." *Department of Civil Engineering, University of British Columbia, Vancouver, BC*.

Franke, K. W., Wright, A. D., and Hatch, C. K. "PBLiquefY: A New Analysis tool for the performance-based evaluation of liquefaction triggering." *Proc., 10th National Conference on Earthquake Engineering*.

G. Castro, S. J. P. (1977). "Factors affecting liquefaction and cyclic loading." *Journal of the Geotechnical Engineering Division*, 106(GT6), 501-506.

Golesorkhi, R. (1989). *Factors influencing the computational determination of earthquake-induced shear stresses in sandy soils*, University of California, Berkeley.

Gu, W., Morgenstern, N., and Robertson, P. (1994). "Postearthquake deformation analysis of Wildlife site." *Journal of geotechnical engineering*, 120(2), 274-289.

Hamada, M., Towhata, I., Yasuda, S., and Isoyama, R. (1987). "Study on permanent ground displacement induced by seismic liquefaction." *Computers and Geotechnics*, 4(4), 197-220.

Hamada, M., Yasuda, S., Isoyama, R., and Emoto, K. (1986). "Study on liquefaction induced permanent ground displacements." *Report for the Association for the Development of Earthquake Prediction*.

Hatch, M. S. (2017). "Development of a Performance-Based Procedure to Predict Liquefaction-Induced Free-Field Settlements for the Cone Penetration Test." *(Master of Science), Brigham Young University, Provo, UT.*

Idriss, I., and Boulanger, R. W. (2008). *Soil liquefaction during earthquakes*.

Idriss, I. M. (2008). "An NGA Empirical Model for Estimating the Horizontal Spectral Values Generated By Shallow Crustal Earthquakes." *Earthquake Spectra: February 2008*, 24(1), 217-242.

Ishihara, K. "Post-Earthquake Failure of Tailings Dam due to Liquefaction of the Pond Deposit." *Proc., Int. Conference on Case Histories in Geotechnical Engineering*, 1129-1143.

Ishihara, K. "Stability of natural deposits during earthquakes." *Proc., 11th International Conference on Soil Mechanics and Foundation Engineering*, 321-376.

Ishihara, K., and Yoshimine, M. (1992). "Evaluation of settlements in sand deposits following liquefaction during earthquakes." *SOILS AND FOUNDATIONS*, 32(1), 173-188.

Iwasaki, T., Tokida, K., Tatsuka, F., Wantabe, S., Yasuda, S., and Sato, H. "Miccrozonation for soil liquefaction potential using the simplified methods." *Proc., 3rd International Conference on Microzonation*, 1319-1330.

Jibson, R. (1987). "Summary of research on the effects of topographic amplification of earthquake shaking on slope stability." *Open-File Report 87-268*, U.S. Geologic Survey, Melano Park, California.

Kanamori, H. (1977). "The Energy Release in Great Earthquakes." *Journal of Geophysical Research*, 82, 2981-2987.

Kanamori, H. (1983). "Magnitude scale and quantification of earthquakes." *Tectonophysics*, 93, 185-199.

Kramer, S. L. (1996). *Geotechnical Earthquake Engineering*, Prentice Hall, Inc., Upper Saddle River, NJ.

Kramer, S. L., and Mayfield, R. T. (2007). "Return period of soil liquefaction." *Journal of Geotechnical and Geoenvironmental Engineering*, 133(7), 802-813.

Ku, C.-S., Juang, C. H., Chang, C.-W., and Ching, J. (2012). "Probabilistic version of the Robertson and Wride method for liquefaction evaluation: development and application." *Canadian Geotechnical Journal*, 49(1), 27-44.

Liao, S. S., and Whitman, R. V. (1986). "Overburden correction factors for SPT in sand." *Journal of Geotechnical Engineering*, 112(3), 373-377.

Middlebrooks, T. A. (1942). "For Peck Slide." *ASCE*, 107, 723-764.

Miyajima, M., Kitaura, M., and Ando, K. "Experiments on liquefaction-induced large ground deformation." *Proc., Proceedings of the third Japan–US workshop on earthquake resistant design of lifeline facilities and countermeasures for soil liquefaction*, 269-278.

Mogami, T., and Kubo, K. (1953). "The behaviour of soil during vibration." *Proceedings, 3rd International Conference on Soil Mechanics and Foundation Engineering, Zurich*, 1.

Mohamad, R., and Dobry, R. (1986). "Undrained monotonic and cyclic triaxial strength of sand." *Journal of Geotechnical Engineering*, 112(10), 941-958.

Nagase, H. (1997). "Defromation characteristics of liquefied loose sand by triaxial compression tests." *Proc. Deformation characteristics and progressive failure in geomachanics, IS-Nagoya97*.

Newmark, N. M. (1965). "Effects of earthquakes on dams and embankments." *Geotechnique*, 15(2), 139-160.

Petersen, M. D., Moschetti, M. P., Powers, P. M., Mueller, C. S., Haller, K. M., Frankel, A. D., Zeng, Y., Rezaeian, S., Harmsen, S. C., and Boyd, O. S. (2015). "The 2014 United States national seismic hazard model." *Earthquake Spectra*, 31(S1), S1-S30.

Popescu, R., and Prevost, J. H. (1995). "Comparison between VELACS numerical 'class A'predictions and centrifuge experimental soil test results." *Soil Dynamics and Earthquake Engineering*, 14(2), 79-92.

Poulos, S. J. (1981). "The steady state of deformation." *Journal of Geotechnical Engineering Division*, 107(GT5), 553-562.

Reiter, L. (1990). *Earthquake Hazard Analysis - Issues and Insights*, Columbia University Press, New York.

Richter, C. F. (1935). "An instrumental earthquake scale." *Bulletin of the Seismological Society of America*, 25, 1-32.

Robertson, P. "Performance based earthquake design using the CPT." *Proc., Proceedings of IS-Tokyo 2009: international conference on performance-based design in earthquake geotechnical engineering—from case history to practice, Tokyo, Japan*, 15-18.

Robertson, P. (2011). "Computing in Geotechnical Engineering-Automatic Software Detection of CPT Transition Zones." *Geotechnical News*, 29(2), 33.

Robertson, P., and Wride, C. (1998). "Evaluating cyclic liquefaction potential using the cone penetration test." *Canadian Geotechnical Journal*, 35(3), 442-459.

Robertson, P. K. (1990). "Soil classification using the cone penetration test." *Canadian Geotechnical Journal*, 27.

Sasaki, Y., Tokida, K.-i., Matsumoto, H., and Saya, S. "Shake table tests on lateral ground flow induced by soil liquefaction." *Proc., Proc., 3rd Japan-US Workshop on Earthquake Resistant Design of Lifeline Facilities and Countermeasures for Soil Liquefaction, San Francisco, CA*, National Center for Earthquake Engineering Research, SUNY-Buffalo, Buffalo, NY, 371-385.

Saygili, G., and Rathje, E. M. (2008). "Empirical predictive models for earthquake-induced sliding displacements of slopes." *Journal of Geotechnical and Geoenvironmental Engineering*, 134(6), 790-803.

Seed, H. B. (1979). "SOIL LIQUEFACTION AND CYCLIC MOBILITY EVALUTION FOR LEVEL GROUND DURING EARTHQUAKES." *Journal of Geotechnical and Geoenvironmental Engineering*, 105(ASCE 14380).

Seed, H. B., and Idriss, I. M. (1971). "Simplified procedure for evaluating soil liquefaction potential." *Journal of Soil Mechanics & Foundations Div*.

Seed, H. B., and Idriss, I. M. (1982). *Ground motions and soil liquefaction during earthquakes*, Earthquake Engineering Research Institute.

Shamoto, Y., Zhang, J.-M., and Goto, S. (1997). "Mechanism of large post-liquefaction deformation in saturated sand." *Soils and Foundations*, 37(2), 71-80.

Shiomi, T., Tsukuni, S., Hatanaka, M., Tanaka, Y., Suzuki, Y., and Hirose, T. (1987). "Simulation analysis of ground liquefaction induced by earthquake." *Computers and geotechnics*, 4(4), 221-245.

Singh, J. P. (1985). "Earthquake ground motions: Implications for designing structures and reconciling structural damage." *Earthquake Spectra*, 1(2), 239-270.

Taboada-Urtuzuastegui, V. M., and Dobry, R. (1998). "Centrifuge modeling of earthquake-induced lateral spreading in sand." *Journal of geotechnical and geoenvironmental engineering*, 124(12), 1195-1206.

Taboada, V., Abdoun, T., and Dobry, R. "Prediction of liquefaction-induced lateral spreading by dilatant sliding block model calibrated by centrifuge tests." *Proc., Proc., 11th World Conf. on Earthquake Engineering*, Pergamon Oxford, UK.

Tatsuoka, F., Zhou, S., Sato, T., and Shibuya, S. (1990). "Evaluation method of liquefaction potential and its application." *Report on seismic hazards on the ground in urban areas. Ministry of Education of Japan, Tokyo*, 75-109.

Towhata, I., Sasaki, Y., Tokida, K., MATSUMOTO, H., TAMARI, Y., and Yamada, K. (1992). "Prediction of permanent displacement of liquefied ground by means of minimum energy principle." *Soils and Foundations*, 32(3), 97-116.

Towhata, I., Tokida, K., Tamari, Y., Matsumoto, H., and Yamada, K. "Prediction of permanent lateral displacement of liquefied ground by means of variational principle." *Proc., Proc., 3rd Japan-US Workshop on Earthquake Resistant Design of Lifeline Facilities and Countermeasures for Soil Liquefaction, Technical Report NCEER-91-0001, NCEER*, 237-251.

Treadwell, D. D. (1976). *The influence of gravity, prestess, compressibility, and layering on soil resistance to static penetration*, University of California, Berkeley.

Valsamis, A. I., Bouckovalas, G. D., and Papadimitriou, A. G. (2010). "Parametric investigation of lateral spreading of gently sloping liquefied ground." *Soil Dynamics and Earthquake Engineering*, 30(6), 490-508.

Vidale, J. E., and Helmberger, D. V. (1988). "Elastic finite difference of the 1971 San Fernando earthquake." *Bulletin of the Seismological Society of America*, 78(1), 122-141.

Wang, W. (1979). *Some findings in soil liquefaction*, Earthquake Engineering Department, Water Conservancy and Hydroelectric Power Scientific Research Institute.

Wells, D. L., and Coppersmith, K. J. (1994). "New empirical relationships among magnitude, rupture length, rupture width, rupture area, and surface displacement." *Bulletin of the seismological Society of America*, 84(4), 974-1002.

Wong, T., Seed, H., and Chan, C. (1974). "Liquefaction of Gravelly Soils Under Cyclic Loading Conditions, University of California." *Earthquake Engineering Research Center, EERC Report*(74-11).

Wu, J. (2002). *Liquefaction triggering and post-liquefaction deformation of Monterey 0/30 sand under uni-directional cyclic simple shear loading*, University of California, Berkeley.

Yang, Z. (2000). "Numerical modeling of earthquake site response including dilation and liquefaction."

Yang, Z., Elgamal, A., and Parra, E. (2003). "Computational model for cyclic mobility and associated shear deformation." *Journal of Geotechnical and Geoenvironmental Engineering*, 129(12), 1119-1127.

Yasuda, S., Masuda, T., Yoshida, N., Nagase, H., Kiku, H., Itafuji, S., Mine, K., and Sato, K. (1994). "Torsional chear and triaxial compression tests on deformation characters of sands before and after liquefaction." *Technical Report NCEER*, US National Center for Earthquake Engineering Research (NCEER), 249-265.

Yasuda, S., Nagase, H., Kiku, H., and Uchida, Y. "A simplified procedure for the analysis of the permanent ground displacement." *Proc., Proceedings of the 3rd Japan–US Workshop on Earthquake Resistant Design of Lifelines Facilities and Countermeasures for Soil Liquefaction, San Francisco, Calif*, 17-19.

Youd, L. (2001). "Liquefaction Resistance of Soils: Summary Report from the 1996 NCEER and 1998/NSF Workshops on Evaluation of Liquefaction Resistance of Soils." *Journal of Geotechnical and Geoenvironmental Engineering*, 127(4).

Youd, T. L. "Recurrence of liquefaction at the same site." *Proc., 8th World Conference on Earthquake Engineering*, 231-238.

Youd, T. L., Hansen, C. M., and Bartlett, S. F. (2002). "Revised multilinear regression equations for prediction of lateral spread displacement." *Journal of Geotechnical and Geoenvironmental Engineering*, 128(12), 1007-1017.

Youd, T. L., and Hoose, S. N. "Liquefaction susceptibility and geologic setting." *Proc., 6th World Conference on Earthquake Engineering*, Prentice-Hall.

Youd, T. L., and Hoose, S. N. (1978). *Historic ground failures in northern California triggered by earthquakes*, US Govt. Print. Off.

Zhang, G., Robertson, P. K., and Brachman, R. (2004). "Estimating liquefaction-induced lateral displacements using the standard penetration test or cone penetration test." *Journal of Geotechnical and Geoenvironmental Engineering*, 130(8), 861-871.

Zhang, J.-M., and Wang, G. (2012). "Large post-liquefaction deformation of sand, part I: physical mechanism, constitutive description and numerical algorithm." *Acta Geotechnica*, 7(2), 69-113.

Zienkiewicz, O., Chang, C., and Hinton, E. (1978). "Non‐linear seismic response and liquefaction." *International Journal for Numerical and Analytical Methods in Geomechanics*, 2(4), 381-404.

Zienkiewicz, O., and Shiomi, T. (1984). "Dynamic behaviour of saturated porous media; the generalized Biot formulation and its numerical solution." *International journal for numerical and analytical methods in geomechanics*, 8(1), 71-96.

APPENDIX A: CPTLIQUEFY TUTORIAL

A.1 Introduction

CPTLiquefY was created for, and used extensively, by this study. As such, a tutorial is included to aid readers in using the program, or in understanding the context of the study when *CPTLiquefY* is mentioned. While CPTLiquefY was created to be user-friendly, this tutorial should aid in understanding its capabilities.

A.2 Tutorial

When the program is started a title page will appear, as shown in Figure A-1. To start, the user can navigate to the "Soil Info" tab, which is shown in the screenshot shown in Figure A-1.

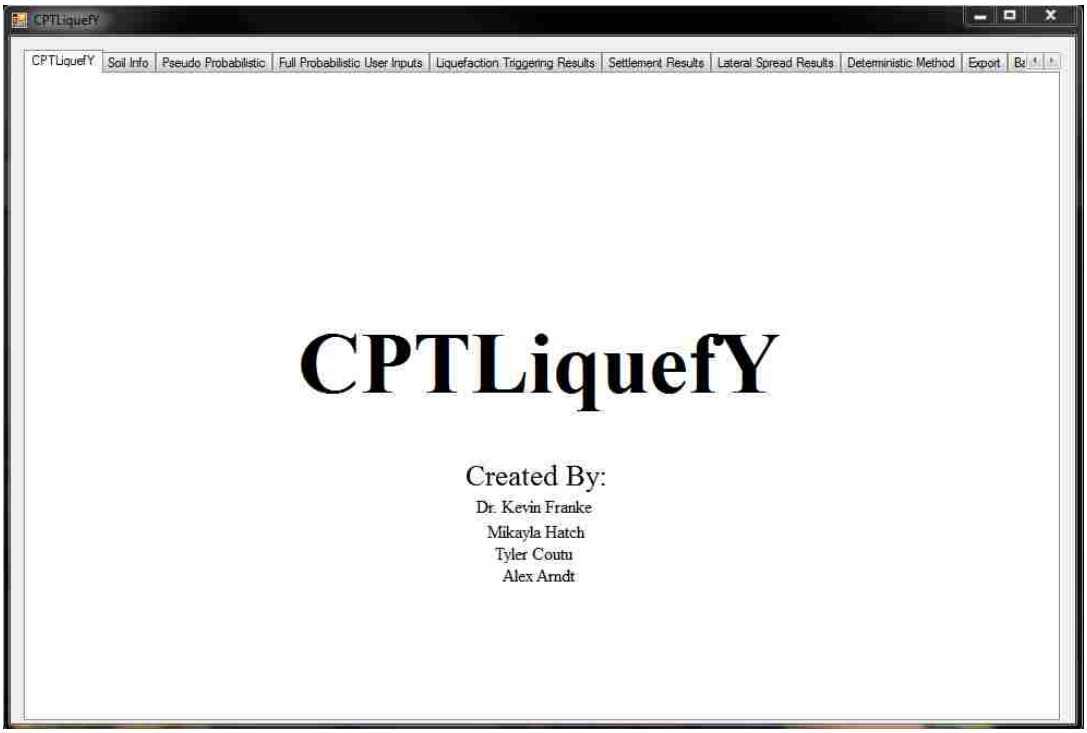

Figure A-1: Screenshot of title page of *CPTLiquefY*.

A.2.1 Soil Info Tab

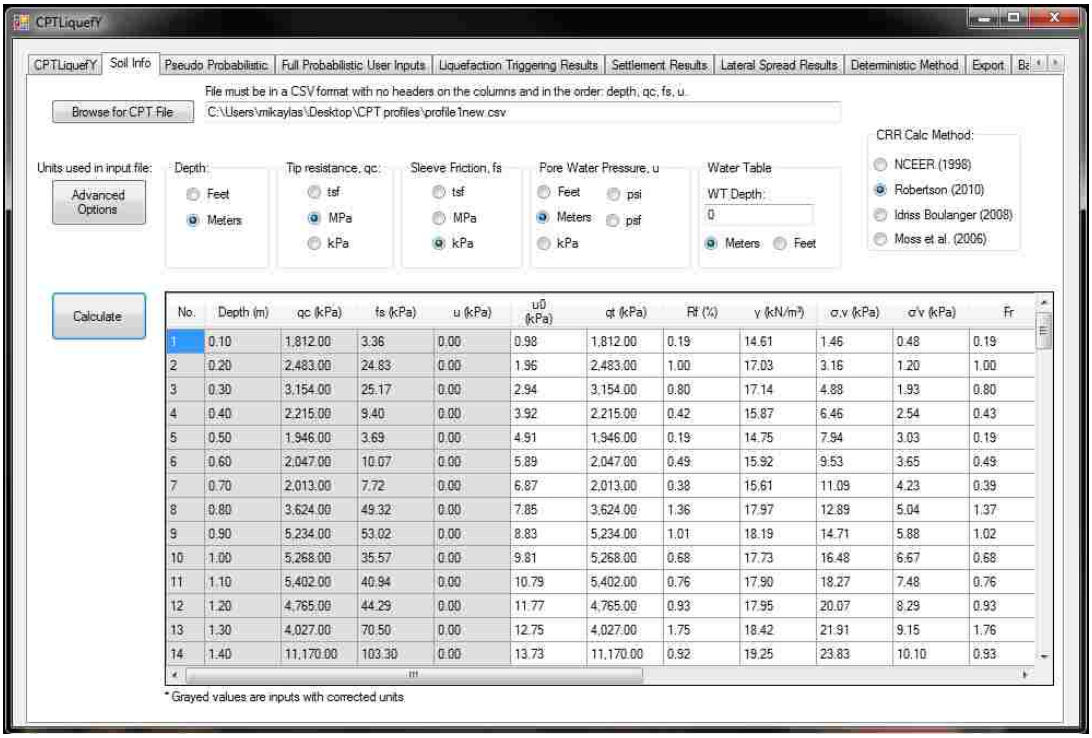

Figure A-2: Screenshot of "Soil Info" tab.

1. Click on "Soil Info" tab (Figure A-2).
2. To upload a CPT profile, click "Browse for CPT File" , The CPT profile must be in a Microsoft Excel ".csv" format. The recorded CPT depth, tip resistance, sleeve friction, and pore water pressure need to be in the first, second, third, and fourth columns, respectively.
3. The user must next select what input units the CPT data is currently in.
4. Next, fill out the water table information.

5. The user may adjust some advanced options by clicking the “Advanced Options” button. Adjustable options include, but are not limited to: Net Area Ratio, Reference Pressure, apply Kα, apply Kσ, apply depth correction factor, apply thin layer correction factor, etc.
6. To run preliminary calculations select the “Calculate” button. This button will run calculations all the way through the calculation of the CRR.

A.2.2 Pseudo Probabilistic Tab

Figure A-3: Screenshot of “Pseudo Probabilistic” tab.

1. Navigate to the “Pseudo Probabilistic” tab (Figure A-3).

2. Select all desired deaggregation options: Mean or Modal magnitude, Return period, USGS tool year, Latitude and Longitude, and if the location is within the western or central/eastern United States.
3. Select which models to run.
4. Enter in Lateral Spread geometry.
5. Select which amplification factor to use.
6. To run a pseudo-probabilistic analysis, select "Run Analysis." The results will be displayed in the data grid view on that tab.

A.2.3 Full Probabilistic User Inputs Tab

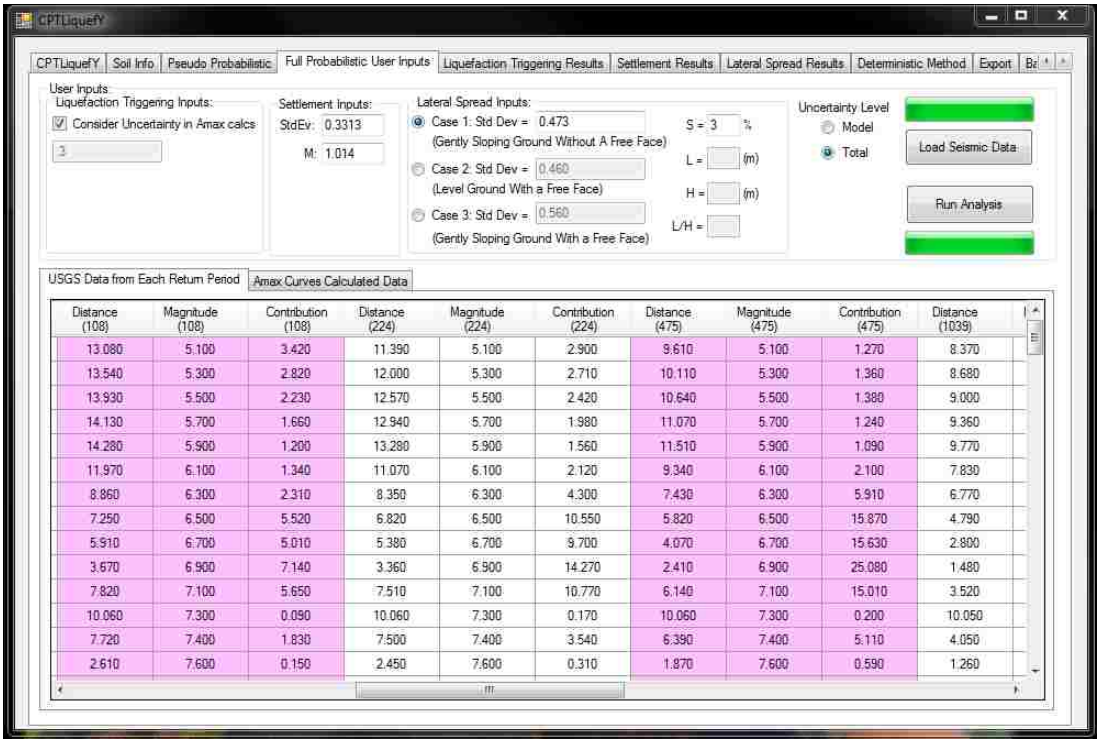

Figure A-4: Screenshot of "Full Probabilistic User Inputs" tab.

1. Navigate to the “Full-Probabilistic User Inputs” tab (Figure A-4).
2. On this tab, options for the full-probabilistic liquefaction triggering and post-liquefaction settlements and lateral spreading are available to be adjusted.
3. To collect all seismic data for the full-probabilistic analysis and to generate amax hazard curves to run the liquefaction triggering analysis click “Load Seismic Data.” This runs deaggregations for return periods: 10, 22, 50, 108, 224, 475, 1039, 2475, 4975, 9950, and 19990. *CPTLiquefY* collects the distance, magnitude, and contribution from each return period. At this point everything is ready to run the full-probabilistic analysis.
4. To run the fully-probabilistic liquefaction triggering, post-liquefaction settlements, and lateral spreading analyses click “Run Analysis.”
5. After the analysis is complete, results can be viewed in their respective tabs. To view liquefaction triggering results navigate to the “Liquefaction Triggering Results” tab. To view post-liquefaction settlement results, navigate to the “Settlement Results” tab. To view post-liquefaction lateral spreading results, navigate to the “Lateral Spread Results” tab.

A.2.4 Lateral Spread Results Inputs Tab

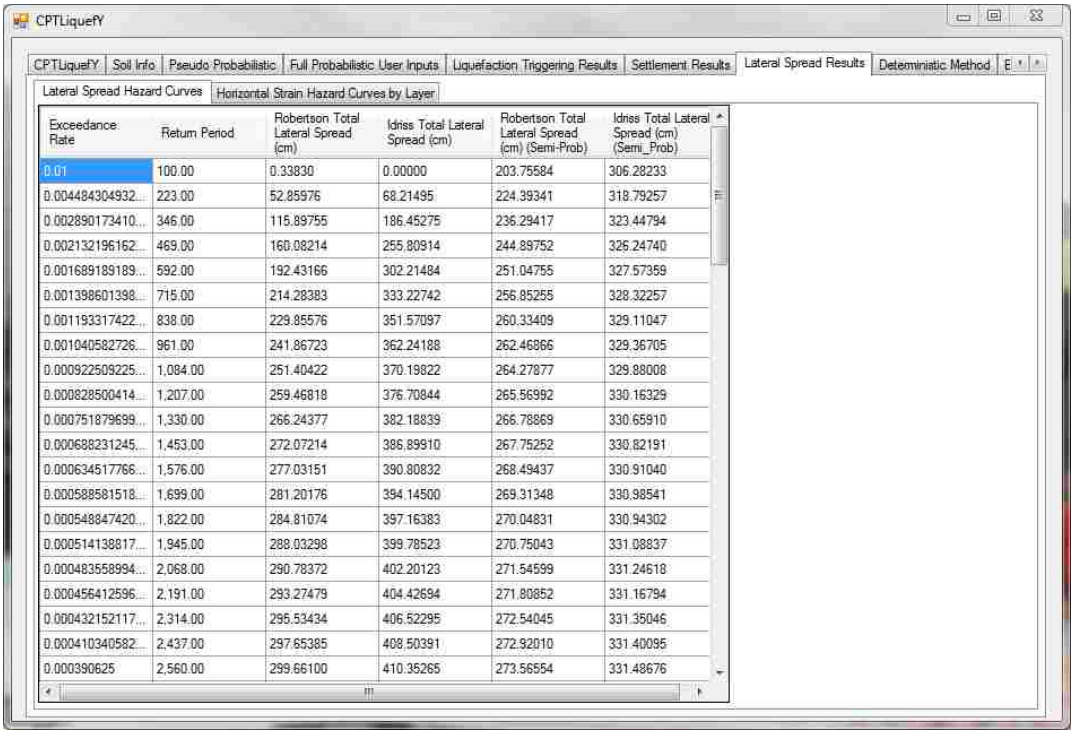

Exceedance Rate	Return Period	Robertson Total Lateral Spread (cm)	Idriss Total Lateral Spread (cm)	Robertson Total Lateral Spread (cm) (Semi-Prob)	Idriss Total Lateral Spread (cm) (Semi_Prob)
0.01	100.00	0.33830	0.00000	203.75584	306.28233
0.004484304932...	223.00	52.85976	68.21495	224.39341	318.79257
0.002890173410...	346.00	115.89755	186.45275	236.29417	323.44794
0.002132196162...	469.00	160.08214	255.80914	244.89752	326.24740
0.001689189189...	592.00	192.43166	302.21484	251.04755	327.57359
0.001398601398...	715.00	214.28383	333.22742	256.85255	328.32257
0.001193317422...	838.00	229.85576	351.57097	260.33409	329.11047
0.001040582726...	961.00	241.86723	362.24188	262.46866	329.36705
0.000922509225...	1,084.00	251.40422	370.19822	264.27877	329.88008
0.000828500414...	1,207.00	259.46818	376.70844	265.56992	330.16329
0.000751879699...	1,330.00	266.24377	382.18839	266.78869	330.65910
0.000688231245...	1,453.00	272.07214	386.89910	267.75252	330.82191
0.000634517766...	1,576.00	277.03151	390.80832	268.49437	330.91040
0.000588581518...	1,699.00	281.20176	394.14500	269.31348	330.98541
0.000548847420...	1,822.00	284.81074	397.16383	270.04831	330.94302
0.000514138817...	1,945.00	288.03298	399.78523	270.75043	331.08837
0.000483558994...	2,068.00	290.78372	402.20123	271.54599	331.24618
0.000456412596...	2,191.00	293.27479	404.42694	271.80852	331.16794
0.000432152117...	2,314.00	295.53434	406.52295	272.54045	331.35046
0.000410340582...	2,437.00	297.65385	408.50391	272.92010	331.40095
0.000390625	2,560.00	299.66100	410.35265	273.56554	331.48676

Figure A-5: Screenshot of "Lateral Spread Results" tab, part one.

1. Navigate to the "Lateral Spread Results" tab (Figure A-5).
2. The total lateral spread displacement for the full-probabilistic and semi-probabilistic methods are displayed for return periods ranging from 100 to 10,000 years.
3. This data can be easily copy-pasted into excel for plotting.
4. To view the horizontal strain hazard curves for each soil layer click the sub tab "Strain Hazard Curves by Layer" and enter the soil layer of interest (Figure A-6).

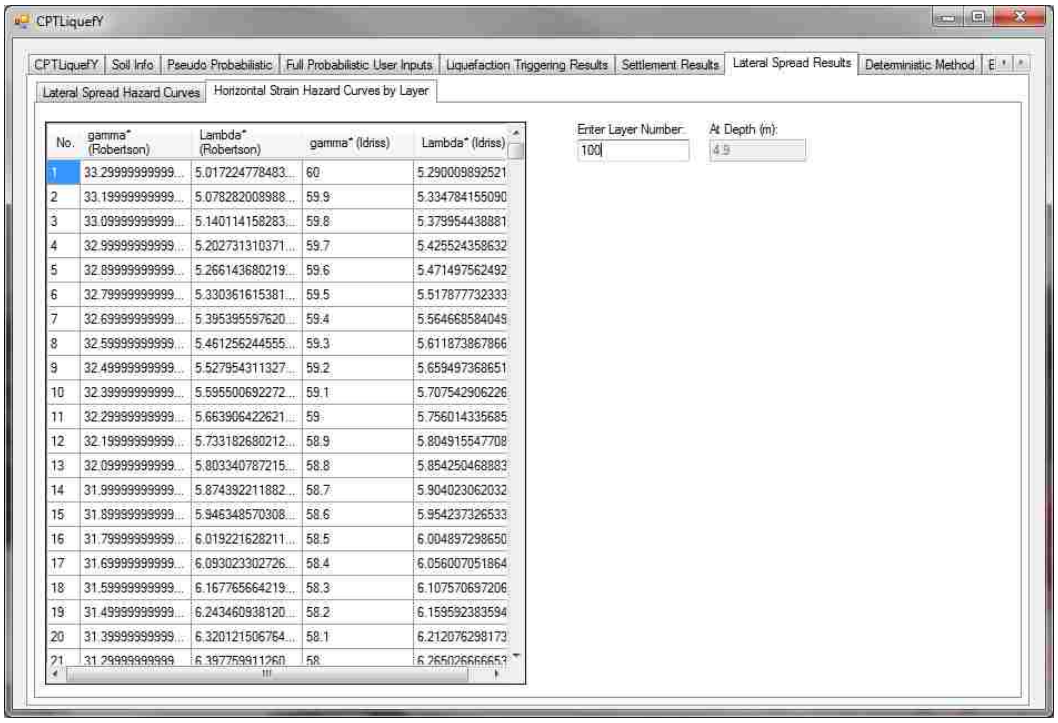

No.	gamma* (Robertson)	Lambda* (Robertson)	gamma* (Idriss)	Lambda* (Idriss)
1	33.29999999999...	5.017224778483...	60	5.290009892521
2	33.19999999999...	5.078282008988...	59.9	5.334784155090
3	33.09999999999...	5.140114158283...	59.8	5.379954438881
4	32.99999999999...	5.202731310371...	59.7	5.425524358632
5	32.89999999999...	5.266143680219...	59.6	5.471497562492
6	32.79999999999...	5.330361615381...	59.5	5.517877732333
7	32.69999999999...	5.395395597620...	59.4	5.564668584045
8	32.59999999999...	5.461256244555...	59.3	5.611873867866
9	32.49999999999...	5.527954311327...	59.2	5.659497368651
10	32.39999999999...	5.595500692272...	59.1	5.707542906226
11	32.29999999999...	5.663906422621...	59	5.756014335685
12	32.19999999999...	5.733182680212...	58.9	5.804915547708
13	32.09999999999...	5.803340787215...	58.8	5.854250468883
14	31.99999999999...	5.874392211882...	58.7	5.904023062032
15	31.89999999999...	5.946348570308...	58.6	5.954237326533
16	31.79999999999...	6.019221628211...	58.5	6.004897298650
17	31.69999999999...	6.093023302726...	58.4	6.056007051864
18	31.59999999999...	6.167765664219...	58.3	6.107570697206
19	31.49999999999...	6.243460938120...	58.2	6.159592383594
20	31.39999999999...	6.320121506764...	58.1	6.212076298173
21	31.29999999999...	6.397759911260...	58	6.265026666653

Figure A-6: Screenshot of "Lateral Spread Results" tab, part two.

A.2.5 Export Tab

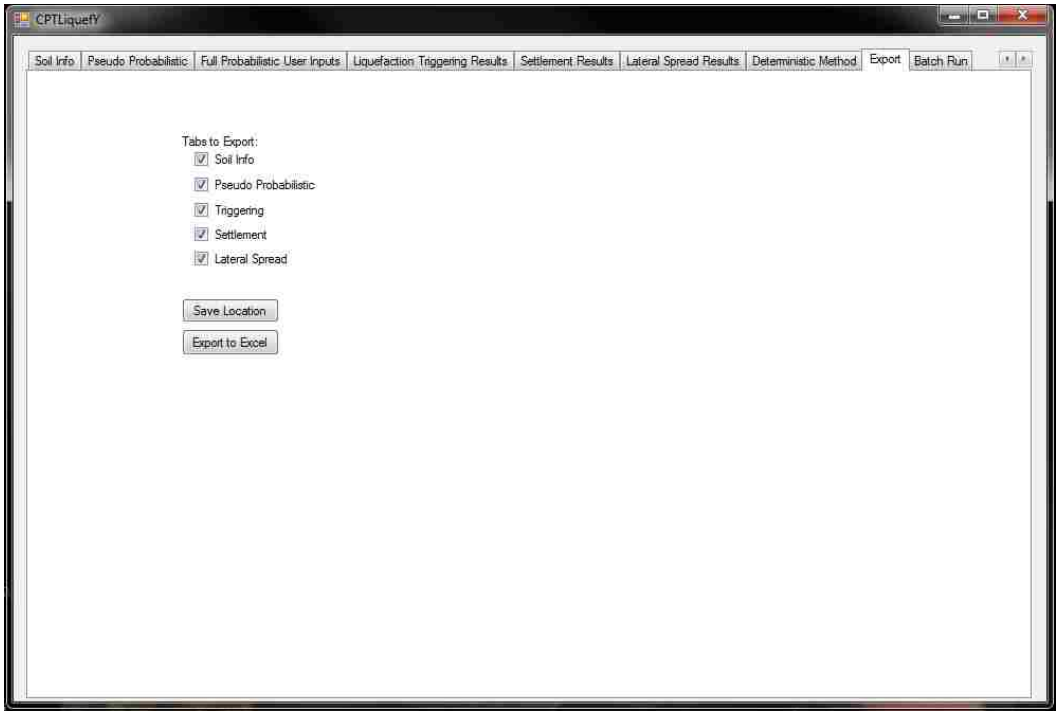

Figure A-7: Screenshot of "Export" tab.

1. All calculated data can be exported to an excel sheet by navigating to the "Export" tab (Figure A-7).
2. Select which data to export.
3. Select "Save Location" to choose the file name and where to save the file.
4. Click "Export to Excel" to export the file.

A.2.6 Batch Run Tab

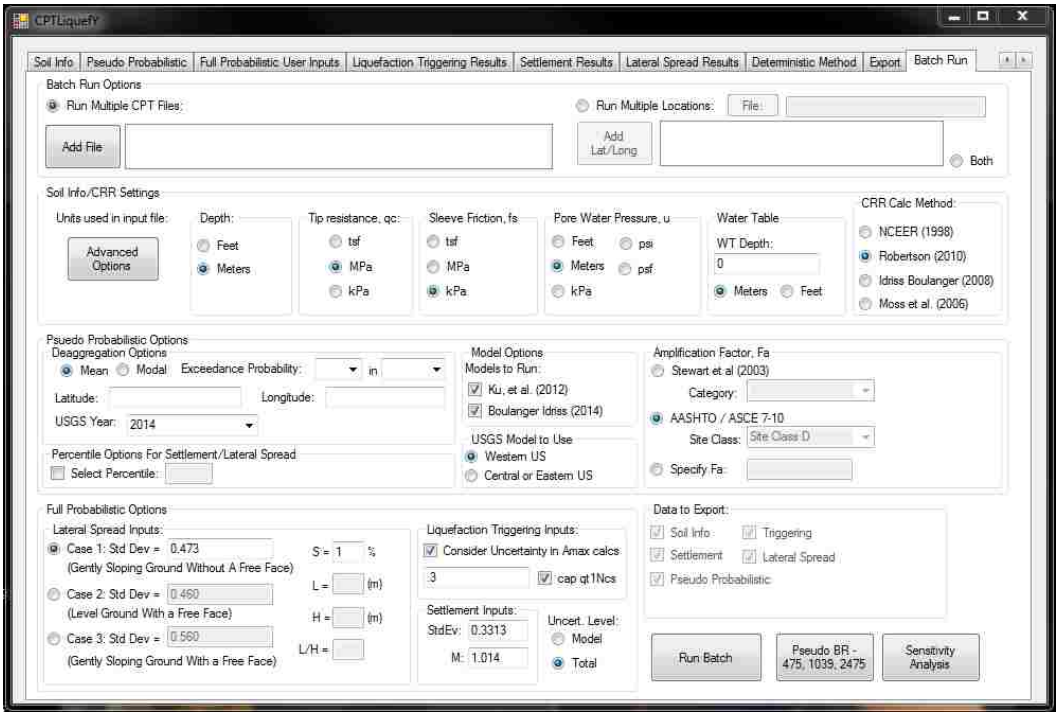

Figure A-8: Screenshot of "Batch Run" tab.

1. To run batch runs, navigate to the "Batch Run" tab (Figure A-8).
2. Here batches can be run for multiple soil profile files at one location, for multiple locations for one soil profile file, or for multiple files and locations.
3. After all options, for all the tabs, are selected on this page select "Run Batch." This button will run the Soil Info, Pseudo-Probabilistic, and Full-Probabilistic tabs automatically for all profiles and locations selected. The results are automatically exported into an excel sheet and saved in the same location as the soil profiles that are being ran.

APPENDIX B: LATERAL SPREAD GEOMETRY 2 COMPARISON PLOTS

Chapter 6 presented one-to-one plots were presented to compare the fully-probabilistic method to the conventional methods. Two lateral spread geometries were used in the analysis; however, it was found that both geometries displayed identical results, the only difference being that the results for lateral spread geometry 2 were scaled down. With such a minor difference, only the results from lateral spread geometry 1 were presented in Chapter 6. Figure B-1 to Figure B-18 are the one-to-one plots for lateral spread geometry 2.

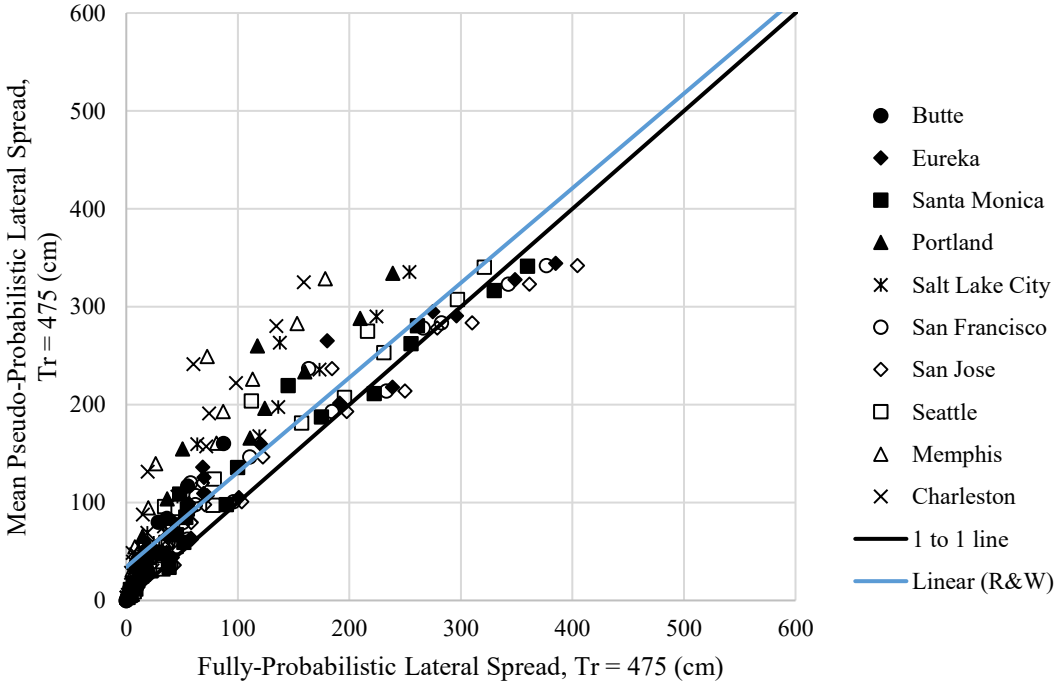

Figure B-1: Mean magnitude pseudo-probabilistic versus fully-probabilistic for the 475-year return period using the Robertson and Wride liquefaction triggering procedure.

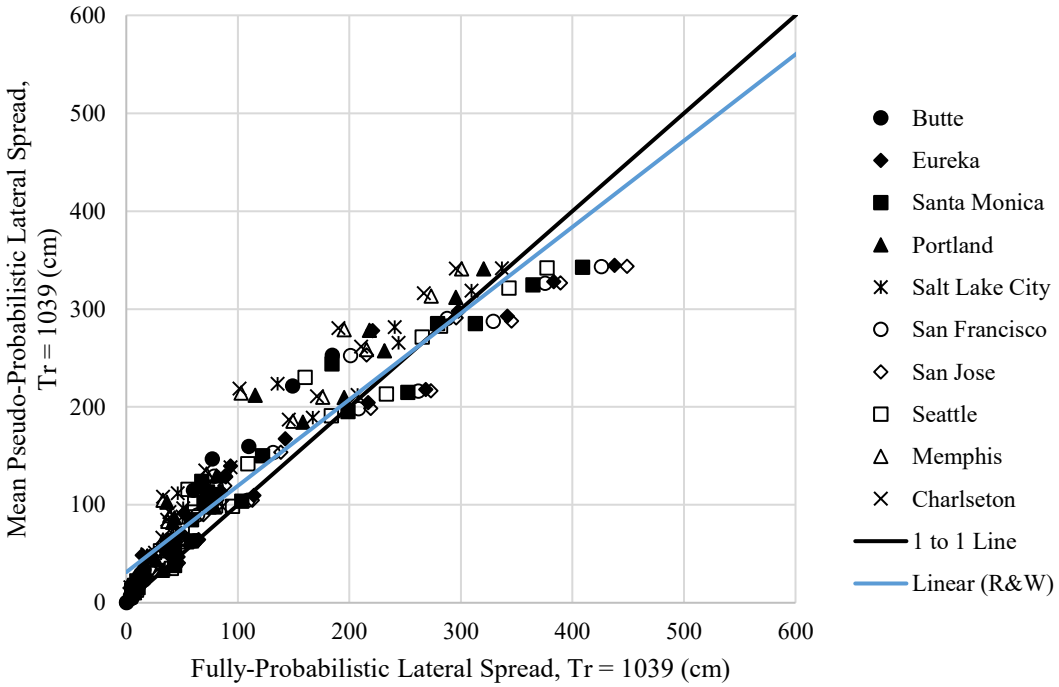

Figure B-2: Mean magnitude pseudo-probabilistic versus fully-probabilistic for the 1039-year return period using the Robertson and Wride liquefaction triggering procedure.

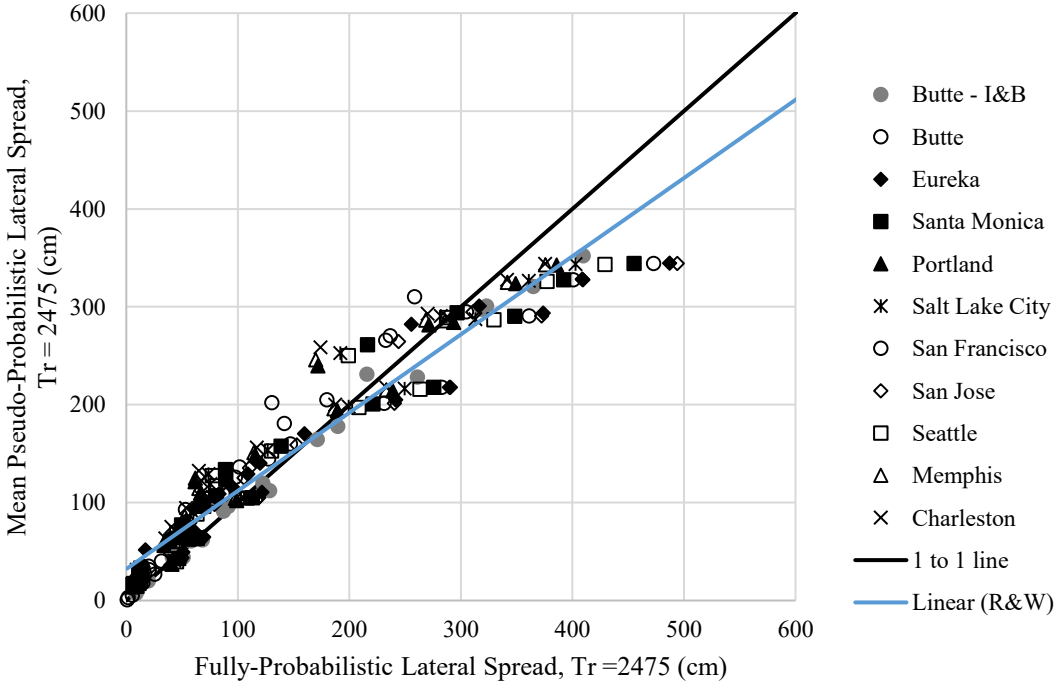

Figure B-3: Mean magnitude pseudo-probabilistic versus fully-probabilistic for the 2475-year return period using the Robertson and Wride liquefaction triggering procedure.

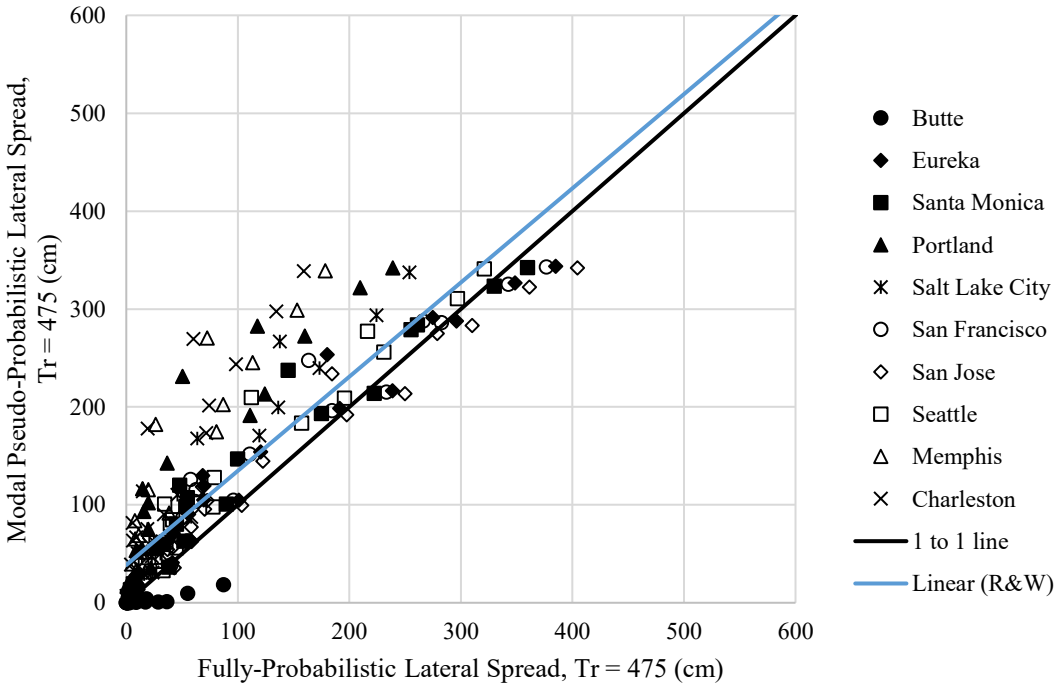

Figure B-4: Modal magnitude pseudo-probabilistic versus fully-probabilistic for the 475-year return period using the Robertson and Wride liquefaction triggering procedure.

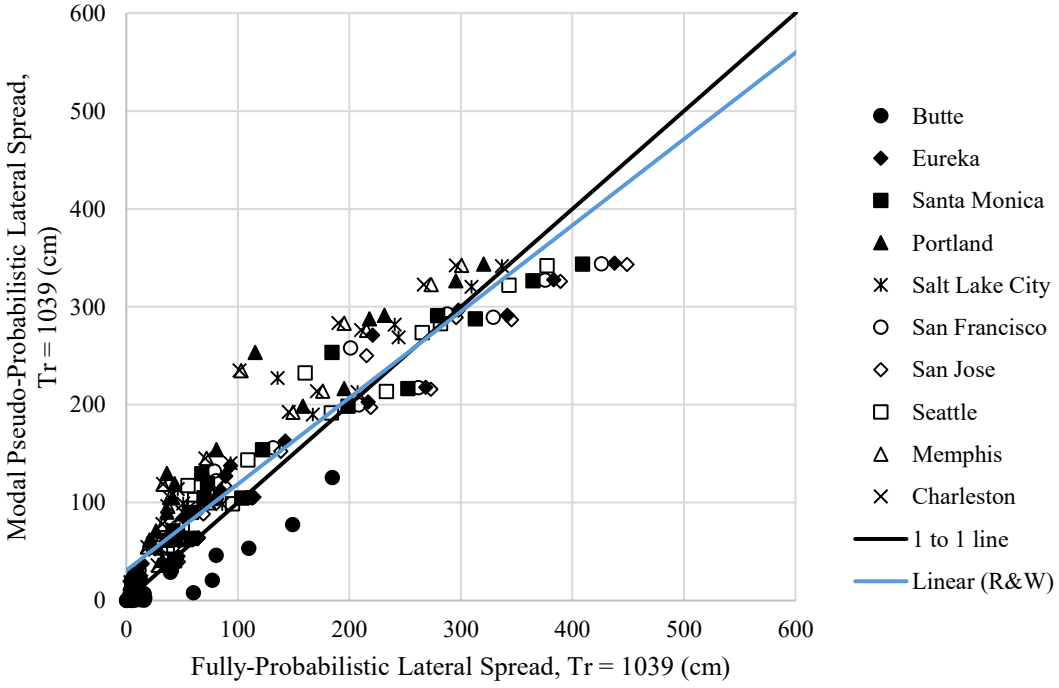

Figure B-5: Modal magnitude pseudo-probabilistic versus fully-probabilistic for the 1039-year return period using the Robertson and Wride liquefaction triggering procedure.

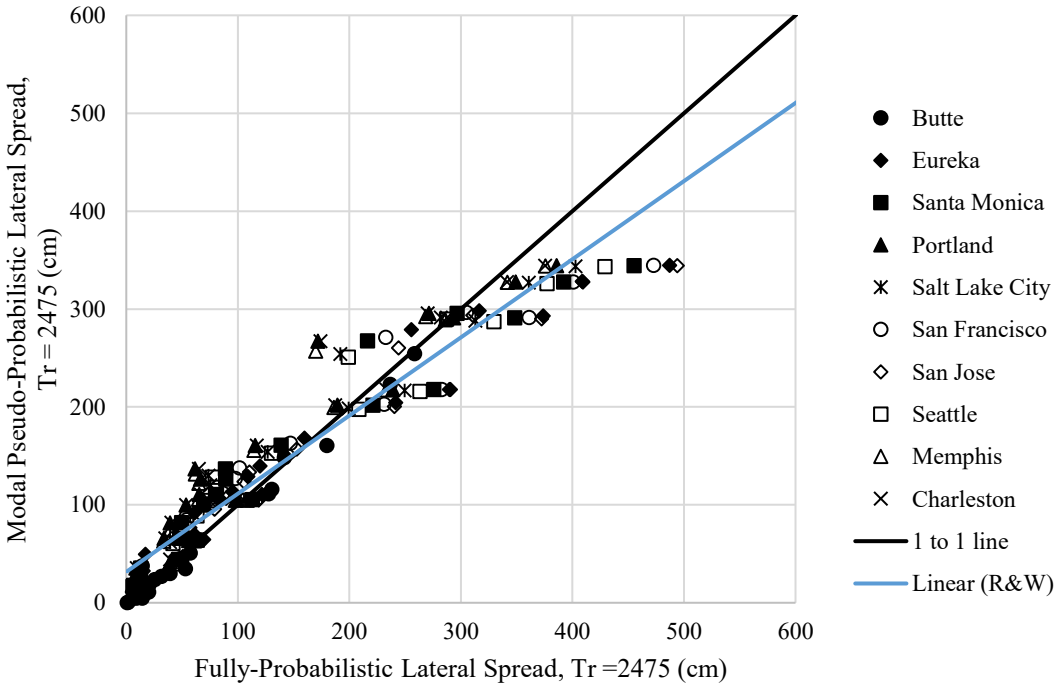

Figure B-6: Modal magnitude pseudo-probabilistic versus fully-probabilistic for the 2475-year return period using the Robertson and Wride liquefaction triggering procedure.

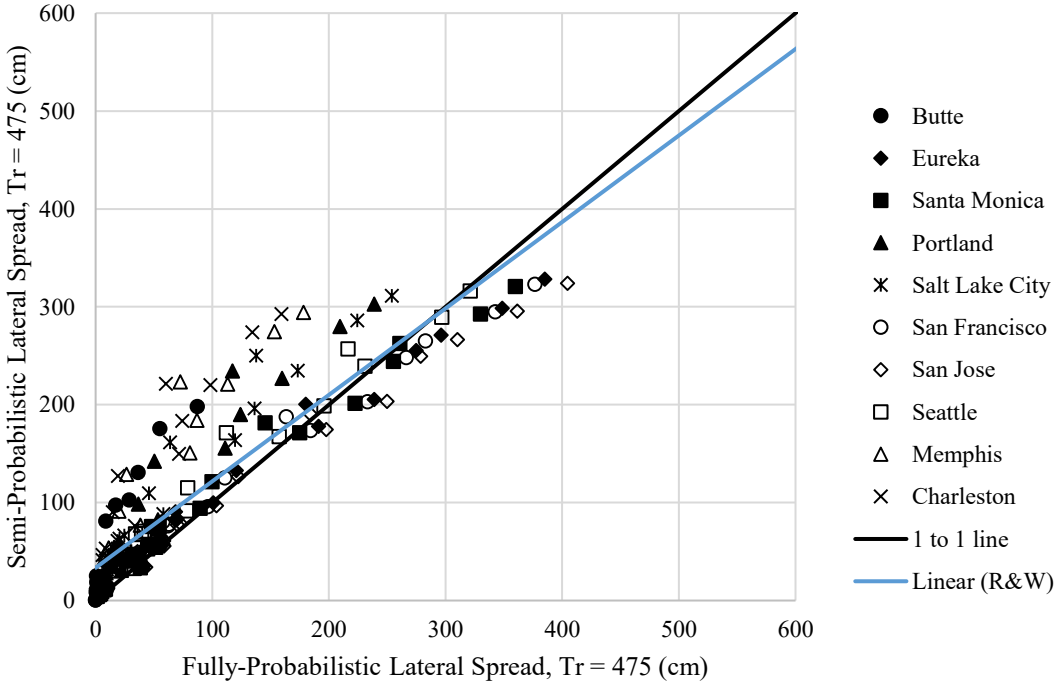

Figure B-7: Semi-probabilistic versus fully-probabilistic for the 475-year return period using the Robertson and Wride liquefaction triggering procedure.

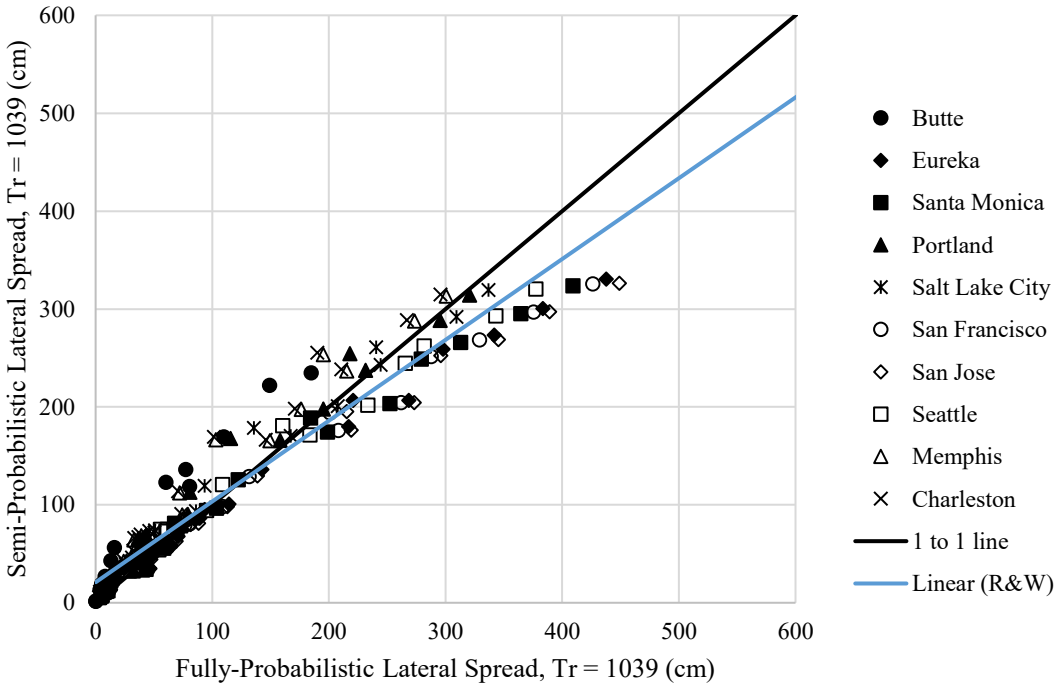

Figure B-8: Semi-probabilistic versus fully-probabilistic for the 1039-year return period using the Robertson and Wride liquefaction triggering procedure.

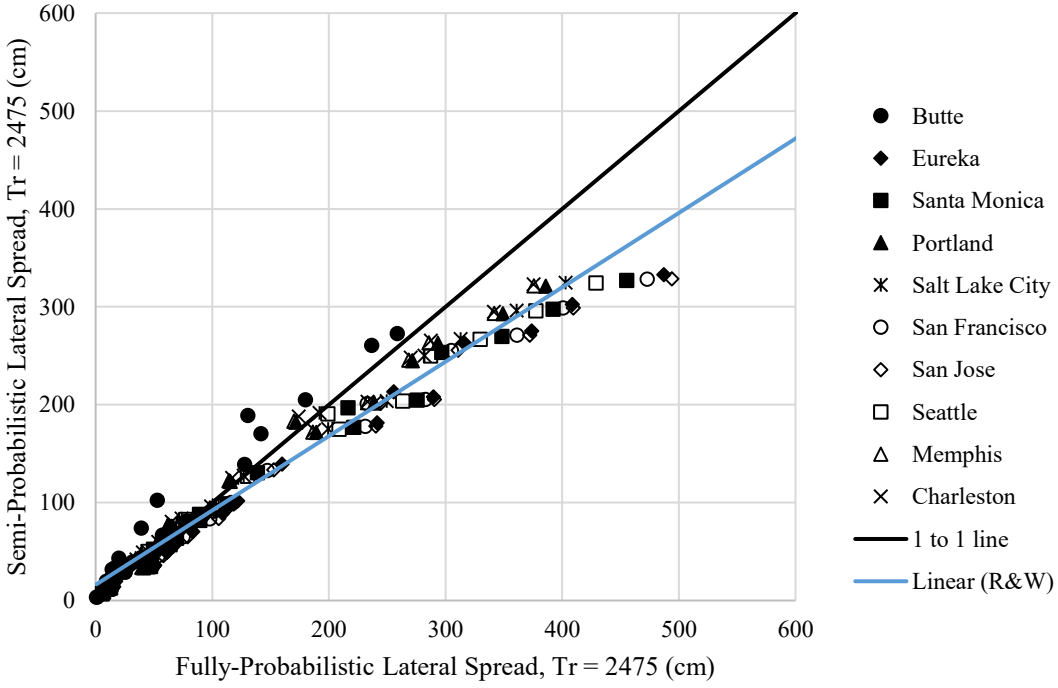

Figure B-9: Semi-probabilistic versus fully-probabilistic for the 2475-year return period using the Robertson and Wride liquefaction triggering procedure.

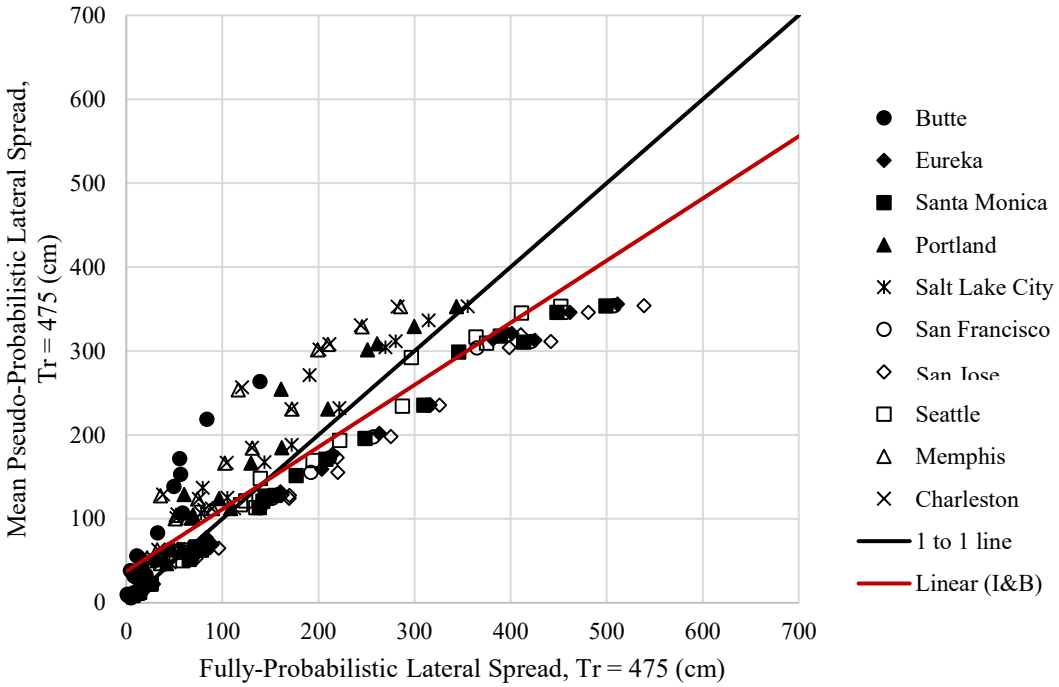

Figure B-10: Mean magnitude pseudo-probabilistic versus fully-probabilistic for the 475-year return period using the Boulanger and Idriss liquefaction triggering procedure.

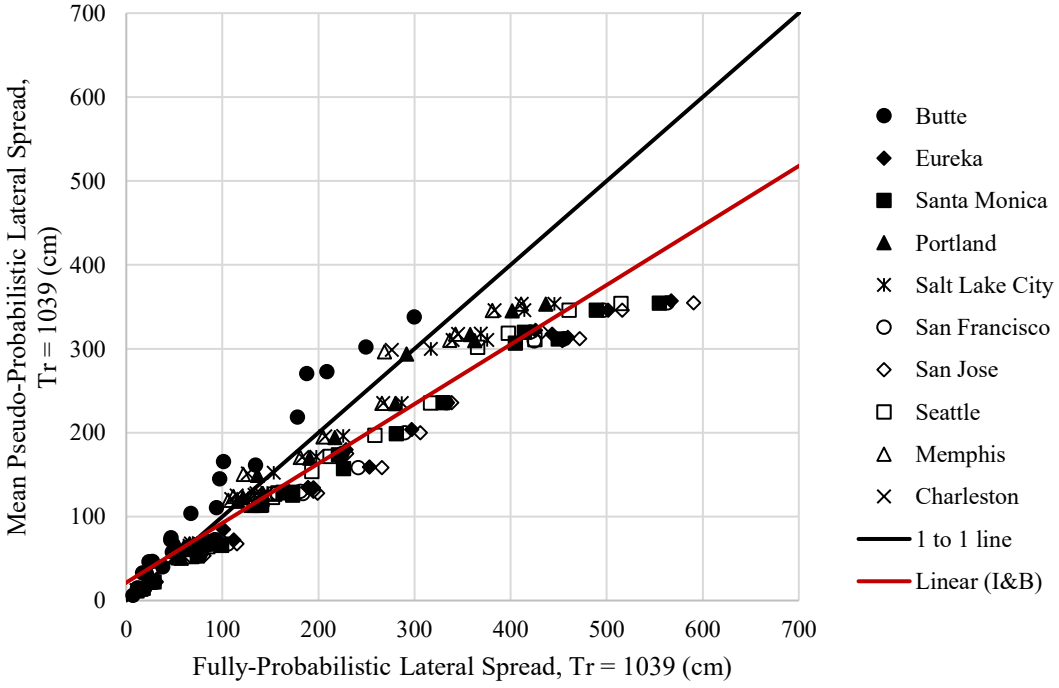

Figure B-11: Mean magnitude pseudo-probabilistic versus fully-probabilistic for the 1039-year return period using the Boulanger and Idriss liquefaction triggering procedure.

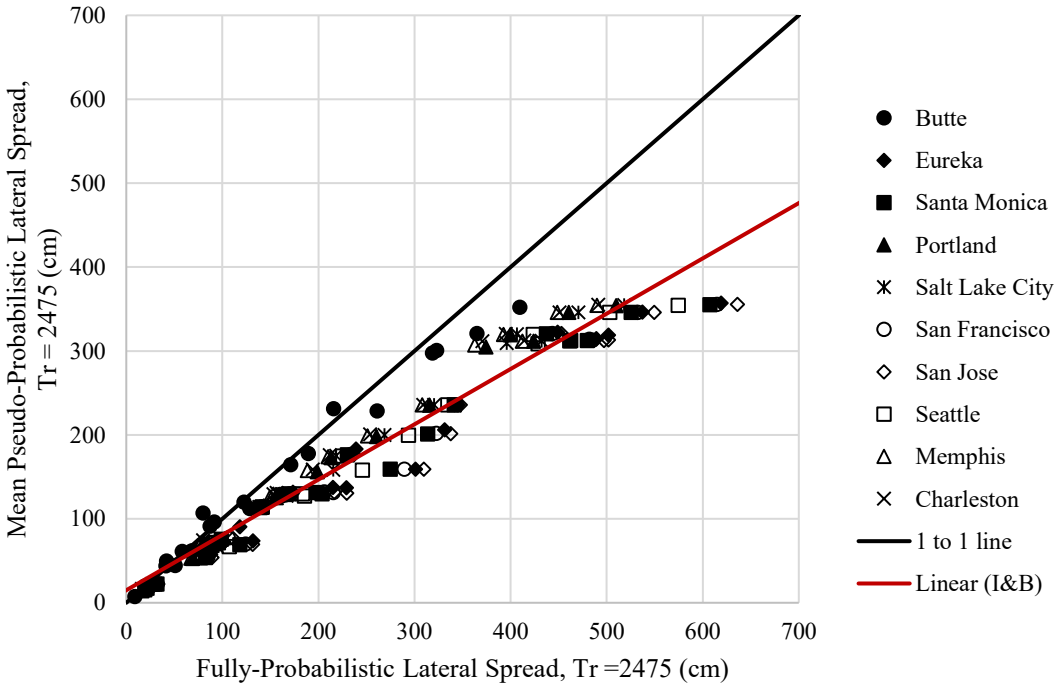

Figure B-12: Mean magnitude pseudo-probabilistic versus fully-probabilistic for the 2475-year return period using the Boulanger and Idriss liquefaction triggering procedure.

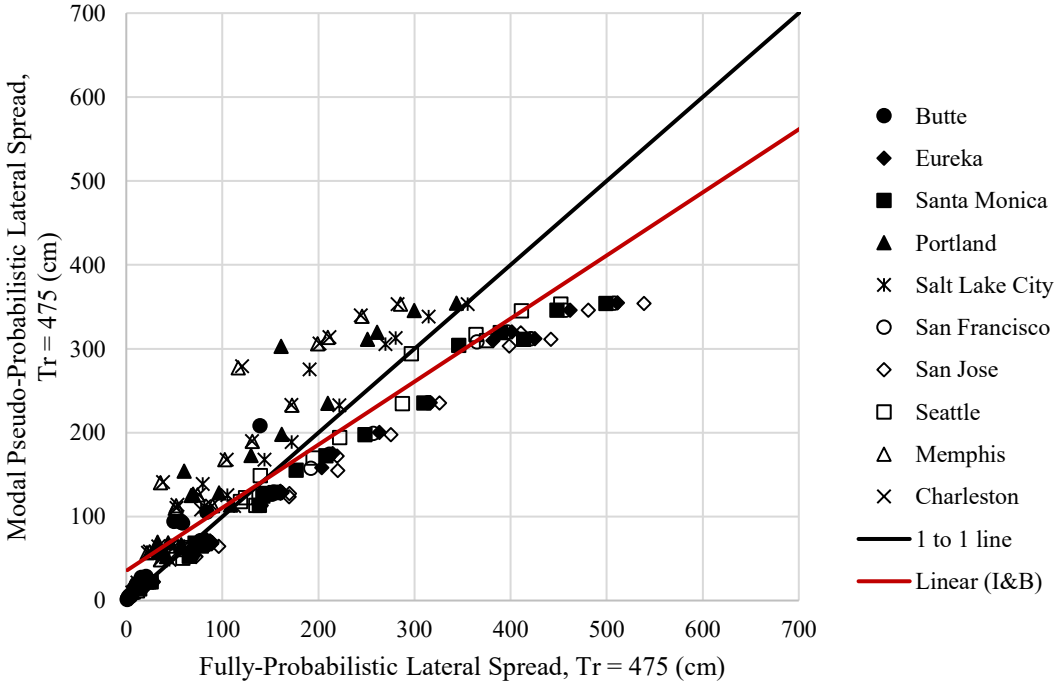

Figure B-13: Modal magnitude pseudo-probabilistic versus fully-probabilistic for the 475-year return period using the Boulanger and Idriss liquefaction triggering procedure.

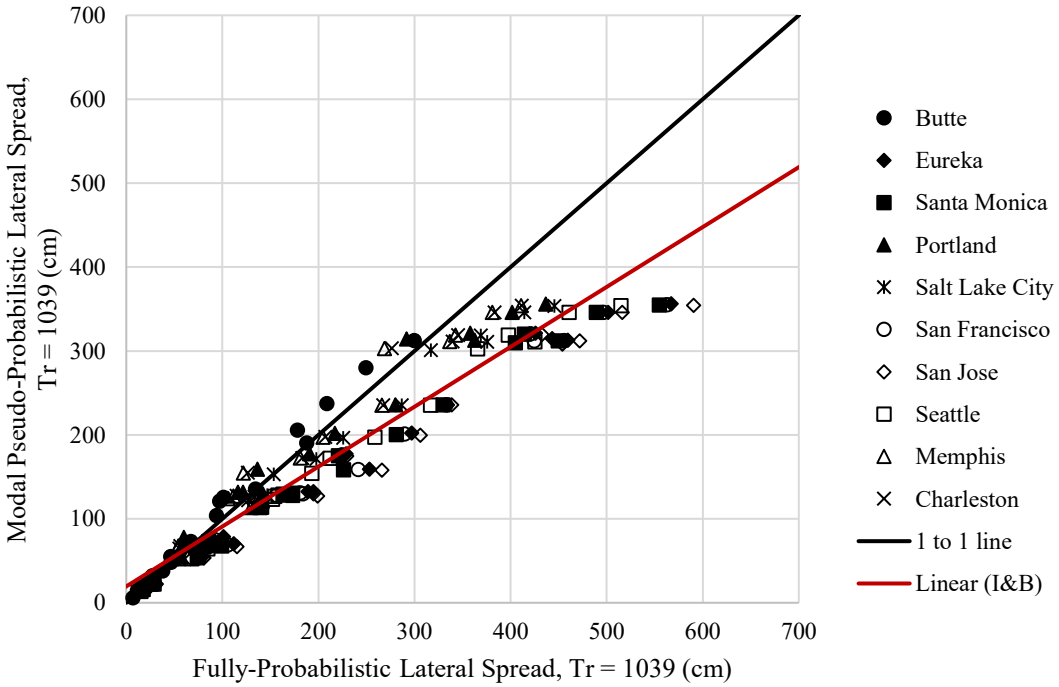

Figure B-14: Modal magnitude pseudo-probabilistic versus fully-probabilistic for the 1039-year return period using the Boulanger and Idriss liquefaction triggering procedure.

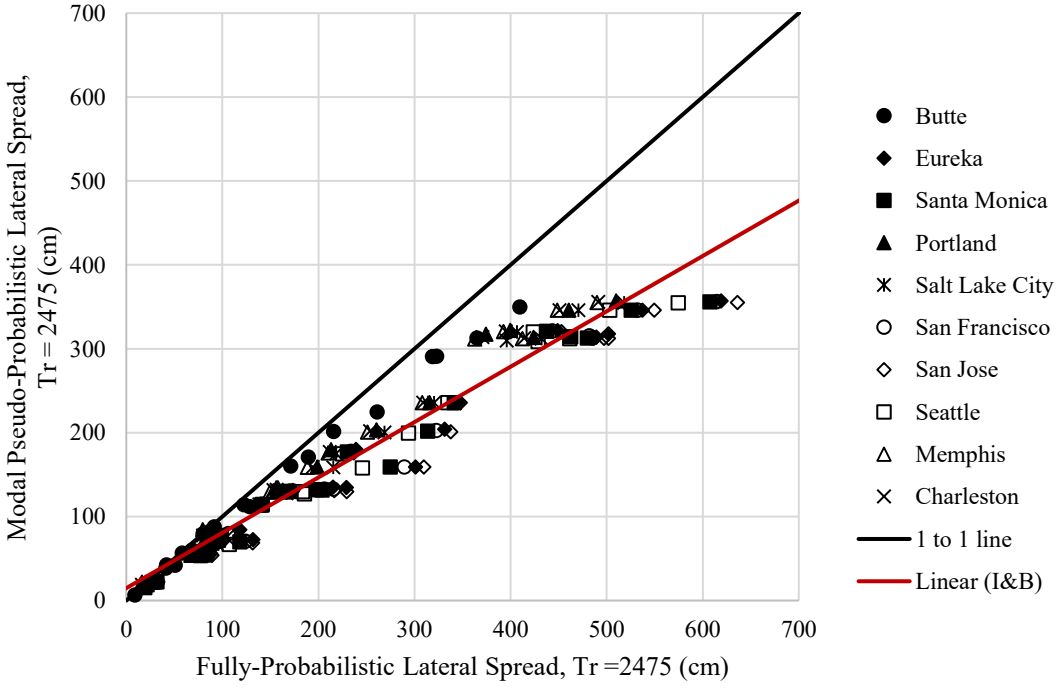

Figure B-15: Modal magnitude pseudo-probabilistic versus fully-probabilistic for the 2475-year return period using the Boulanger and Idriss liquefaction triggering procedure.

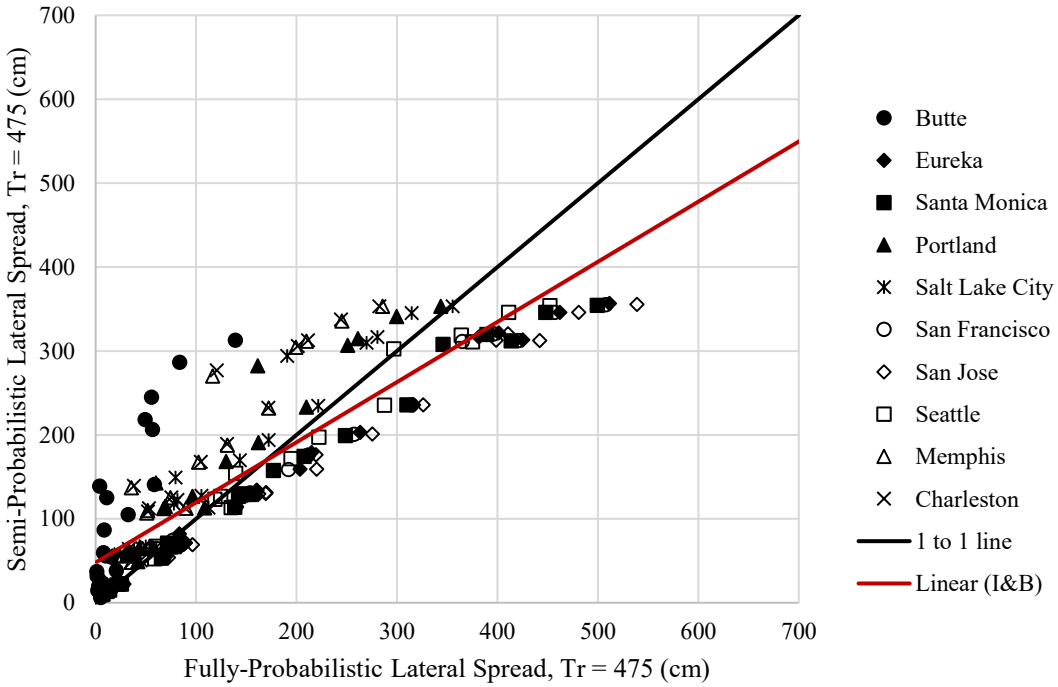

Figure B-16: Semi-probabilistic versus fully-probabilistic for the 475-year return period using the Boulanger and Idriss liquefaction triggering procedure.

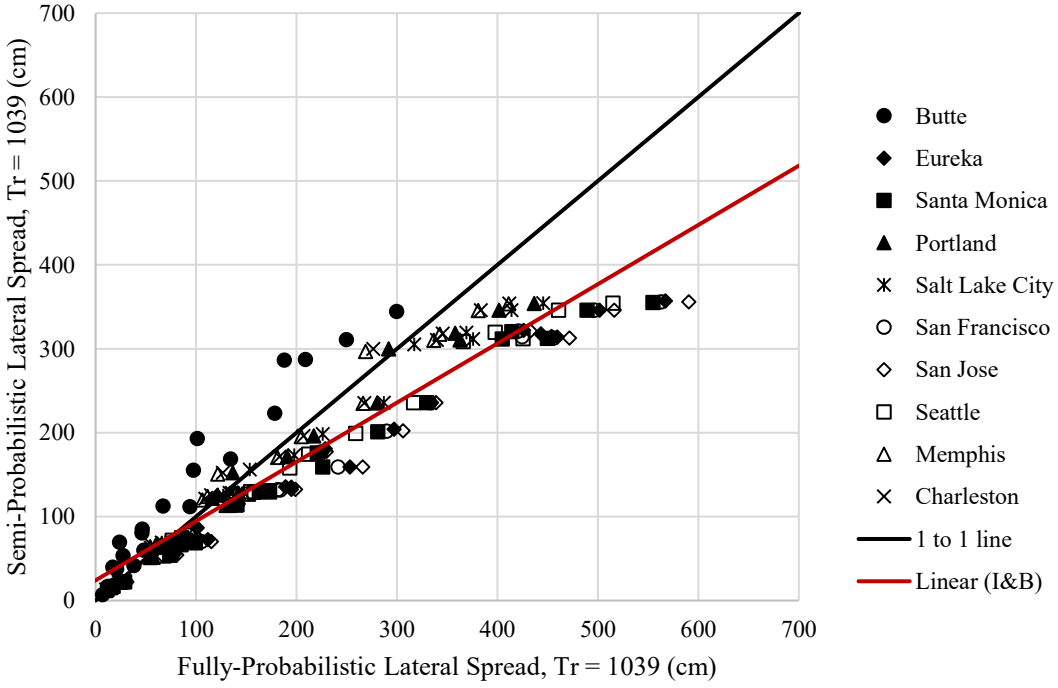

Figure B-17: Semi-probabilistic versus fully-probabilistic for the 1039-year return period using the Boulanger and Idriss liquefaction triggering procedure.

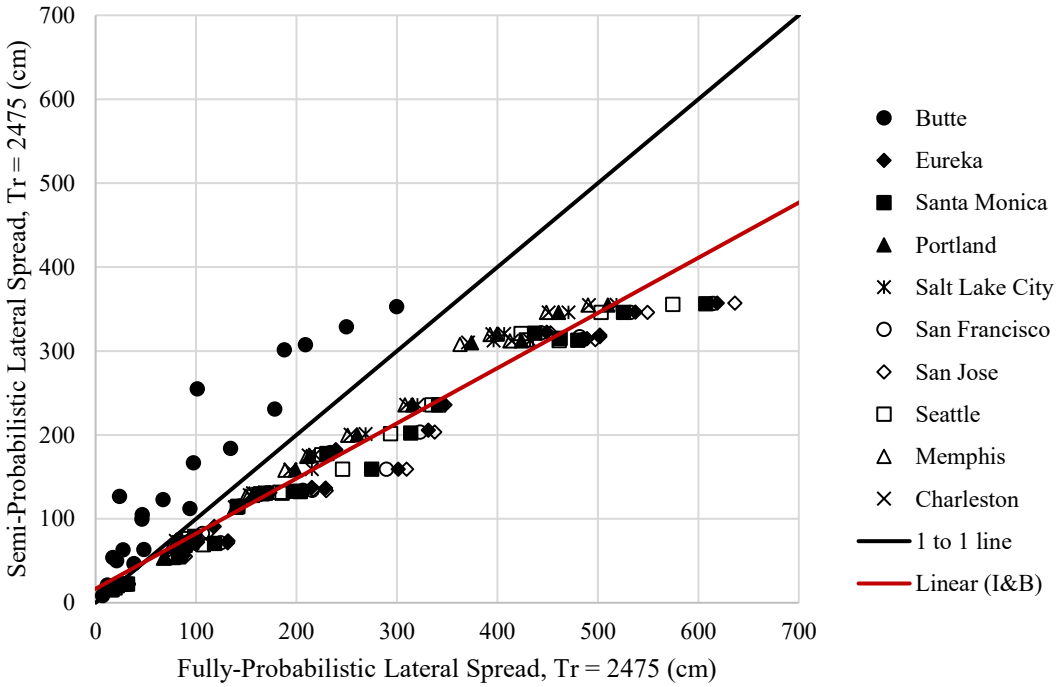

Figure B-18: Semi-probabilistic versus fully-probabilistic for the 2475-year return period using the Boulanger and Idriss liquefaction triggering procedure.

APPENDIX C: RETURN PERIOD BOX PLOT DATA

Chapter 6 presented box-and-whisker plots that compared the actual return period to the assumed return period, as calculated using the conventional methods. These actual return periods were back-calculated from the hazard curves of the fully-probabilistic procedure. The data used to create these plots are presented in Table C-1 to Table C-30. Only lateral spread geometry 1 was used for the return period analysis.

Table C-1: Actual Return Periods for Lateral Spread at Butte, MT (475)

		Actual T_R					
		Robertson and Wride (2009)			Idriss and Boulanger (2014)		
Profile	Assumed T_R	Mean	Modal	Semi	Mean	Modal	Semi
1	475	820.9	258.3	1162.3	829.5	636.4	1099.0
2	475	735.0	277.5	1502.6	793.2	663.4	1029.5
3	475	771.5	175.4	1273.0	826.3	558.9	1272.6
4	475	676.7	204.8	1381.9	796.3	624.5	1231.3
5	475	633.3	396.1	1772.0	658.8	503.3	1216.6
6	475	771.3	235.9	1288.0	845.8	507.3	1278.1
7	475	792.5	197.4	1436.0	914.1	585.8	1218.0
8	475	541.7	156.7	2177.4	765.0	538.1	1343.0
9	475	650.5	450.4	1825.1	635.8	620.0	751.8
10	475	638.1	228.5	1686.0	769.9	582.0	1255.5
11	475	508.6	223.5	2214.7	717.0	592.7	1150.8
12	475	600.6	163.5	1346.6	709.4	515.8	1406.7
13	475	721.0	205.3	1350.9	835.7	580.4	1283.8
14	475	433.1	223.0	1932.0	677.9	487.8	1224.1
15	475	793.9	267.0	1132.0	860.7	611.3	1216.1
16	475	415.6	346.0	1254.5	839.4	535.1	1400.0
17	475	793.2	196.7	1363.4	688.7	510.3	1347.5
18	475	475.6	469.0	2733.8	653.5	458.9	1338.2
19	475	996.9	224.3	1471.9	770.0	667.7	1106.7
20	475	536.1	186.2	1327.7	648.3	464.1	1382.6

Table C-2: Actual Return Periods for Lateral Spread at Butte, MT (1039)

		Actual T_R					
		Robertson and Wride (2009)			Idriss and Boulanger (2014)		
Profile	Assumed T_R	Mean	Modal	Semi	Mean	Modal	Semi
1	1039	2152.4	622.5	1718.9	1256.2	1078.1	1321.0
2	1039	1939.3	465.0	2356.6	1130.6	1007.8	1247.5
3	1039	1752.9	557.3	2125.7	1471.9	1181.2	1656.6
4	1039	1975.9	438.7	2247.3	1601.2	1020.4	1828.1
5	1039	1441.7	496.4	4001.6	1598.0	1015.0	2072.3
6	1039	1947.4	560.6	2029.8	1390.6	1206.4	1481.9
7	1039	1791.5	444.0	2254.9	1335.5	1174.3	1437.1
8	1039	1243.8	386.3	3795.9	1677.1	1189.6	2060.4
9	1039	1186.6	537.9	4930.8	768.7	655.3	1023.4
10	1039	1966.9	526.9	3505.0	1669.6	1033.9	2121.2
11	1039	1199.3	375.3	4181.6	1722.3	1080.8	2266.8
12	1039	1747.8	409.1	2781.1	1655.0	1275.7	1905.2
13	1039	2528.1	486.0	2238.2	1396.9	1249.7	1463.8
14	1039	948.0	363.6	3561.9	1480.7	983.5	2172.5
15	1039	1571.1	681.4	1791.3	1324.2	1181.2	1358.6
16	1039	1103.6	368.9	2864.1	1449.6	1352.0	1696.1
17	1039	1404.5	458.2	2311.6	1683.4	1076.8	1978.6
18	1039	620.0	469.0	4067.4	1684.4	1139.0	2117.7
19	1039	1642.6	586.8	1942.3	1385.4	1014.4	1612.0
20	1039	1560.5	403.5	2693.2	1627.7	1210.7	2048.5

Table C-3: Actual Return Periods for Lateral Spread at Butte, MT (2475)

		Actual T_R					
		Robertson and Wride (2009)			Idriss and Boulanger (2014)		
Profile	Assumed T_R	Mean	Modal	Semi	Mean	Modal	Semi
1	2475	5317.5	2206.9	3009.8	1381.9	1358.0	1391.0
2	2475	2735.0	1963.7	3301.4	1421.3	1257.3	1708.7
3	2475	3714.7	1780.2	3919.7	1823.2	1682.6	1966.5
4	2475	5948.3	1998.1	5216.4	1966.7	1859.9	2042.4
5	2475	3360.1	1474.3	9956.0	2669.9	2095.3	3900.0
6	2475	3820.3	1981.9	3375.0	1574.6	1491.6	1683.7
7	2475	5062.3	1811.1	4946.0	1546.6	1444.5	1664.5
8	2475	6071.3	1276.2	9895.0	2605.7	2086.8	3381.5
9	2475	2217.4	1193.3	9931.0	1305.7	926.1	2169.5
10	2475	5927.3	2020.2	8992.6	2613.4	2178.5	3310.8
11	2475	5192.8	1220.8	9911.0	3142.2	2396.9	3715.4
12	2475	4683.9	1776.6	7551.9	2120.8	1991.2	2205.8
13	2475	4601.8	2582.6	3855.0	1533.5	1481.1	1573.1
14	2475	5716.5	968.6	9715.7	3517.1	2354.1	4999.7
15	2475	4179.3	1613.9	4527.4	1363.2	1357.8	1373.7
16	2475	5839.0	1169.4	9944.0	2462.1	1766.1	3183.4
17	2475	4592.5	1426.0	7696.6	2235.9	2007.4	2416.6
18	2475	2201.3	627.5	9913.0	2646.7	2249.4	2922.2
19	2475	4447.6	1659.1	3810.5	1877.2	1648.6	2149.1
20	2475	5552.9	1600.7	7444.7	2719.3	2110.5	3674.7

Table C-4: Actual Return Periods for Lateral Spread at Eureka, CA (475)

		Actual T_R					
		Robertson and Wride (2009)			Idriss and Boulanger (2014)		
Profile	Assumed T_R	Mean	Modal	Semi	Mean	Modal	Semi
1	475	282.1	279.6	231.3	97.0	96.7	97.3
2	475	661.3	442.6	267.4	177.3	171.4	183.5
3	475	882.9	770.5	315.5	153.0	151.6	154.0
4	475	434.3	420.9	344.0	145.1	144.4	146.0
5	475	9957.0	6946.4	1155.1	364.0	310.3	443.6
6	475	326.5	323.3	221.4	129.1	129.1	129.2
7	475	872.0	825.7	451.5	158.0	155.2	158.0
8	475	4843.3	3658.6	774.7	257.7	237.4	270.2
9	475	9989.0	6114.8	1055.3	529.5	348.2	745.4
10	475	7872.4	3955.0	714.1	236.9	226.4	249.4
11	475	3157.7	2399.4	841.6	264.7	246.5	278.6
12	475	2242.0	1684.4	684.6	179.3	175.3	183.8
13	475	309.5	303.3	252.0	117.7	117.7	117.7
14	475	3830.2	3110.9	926.4	257.0	254.6	257.4
15	475	561.8	551.1	445.2	98.4	97.8	98.8
16	475	9978.0	9913.0	2211.1	194.4	194.4	194.4
17	475	9984.0	6814.5	869.9	171.5	169.7	174.5
18	475	9996.0	9892.0	2130.3	210.3	206.7	212.6
19	475	606.4	558.9	329.7	161.6	158.0	165.2
20	475	2965.8	2156.9	657.5	232.9	222.4	240.6

Table C-5: Actual Return Periods for Lateral Spread at Eureka, CA (1039)

		Actual T_R					
		Robertson and Wride (2009)			Idriss and Boulanger (2014)		
Profile	Assumed T_R	Mean	Modal	Semi	Mean	Modal	Semi
1	2475	283.2	283.1	245.7	97.4	97.4	97.4
2	2475	1709.5	1152.2	292.1	204.8	193.5	201.4
3	2475	1108.9	1004.7	352.0	155.4	154.2	155.3
4	2475	447.7	444.3	362.3	147.7	146.8	147.6
5	2475	9913.0	9955.0	1753.6	624.4	478.7	632.2
6	2475	329.1	328.5	232.9	129.4	129.3	129.4
7	2475	985.9	944.7	536.2	158.0	158.0	158.0
8	2475	5684.3	5558.1	980.7	287.1	276.3	286.0
9	2475	9990.0	9977.0	1508.6	935.2	786.0	959.0
10	2475	9964.0	9894.0	968.0	271.1	256.2	272.0
11	2475	4834.2	4487.6	1048.3	296.9	285.9	296.1
12	2475	4241.2	3710.0	886.5	193.3	186.4	192.0
13	2475	309.6	309.6	263.6	117.7	117.7	117.7
14	2475	4388.8	4316.8	1218.1	257.4	257.4	257.4
15	2475	752.0	749.2	477.3	99.1	98.9	99.2
16	2475	9876.0	9949.0	5761.7	194.4	194.4	194.4
17	2475	9939.0	9983.0	1278.2	176.4	176.1	175.9
18	2475	9886.0	9950.0	5088.1	213.2	212.9	213.5
19	2475	671.3	665.1	360.1	171.9	167.3	170.9
20	2475	4832.5	4364.2	840.6	245.8	243.1	245.6

Table C-6: Actual Return Periods for Lateral Spread at Eureka, CA (2475)

		Actual T_R					
		Robertson and Wride (2009)			Idriss and Boulanger (2014)		
Profile	Assumed T_R	Mean	Modal	Semi	Mean	Modal	Semi
1	1039	283.0	282.6	238.3	97.4	97.1	97.4
2	1039	1087.4	792.8	279.8	187.6	178.9	192.2
3	1039	984.9	939.2	331.7	154.4	153.1	154.6
4	1039	443.4	437.4	353.2	146.3	145.4	146.6
5	1039	9936.0	9914.0	1422.2	486.0	381.6	536.8
6	1039	328.2	326.9	225.5	129.2	129.1	129.2
7	1039	941.4	907.2	495.2	158.0	158.0	158.0
8	1039	5508.8	5149.0	870.0	273.6	261.7	276.9
9	1039	9958.0	9895.0	1253.0	790.4	595.9	863.4
10	1039	9960.0	9676.3	830.1	254.4	240.7	260.6
11	1039	4356.6	3556.2	942.0	282.5	268.8	287.1
12	1039	3516.0	2675.8	762.2	185.9	180.2	187.8
13	1039	309.6	309.6	257.8	117.7	117.7	117.7
14	1039	4278.1	4025.5	1065.5	257.4	257.4	257.4
15	1039	702.3	573.3	464.0	98.9	98.8	98.9
16	1039	9891.0	9982.0	3473.9	194.4	194.4	194.4
17	1039	9923.0	9954.0	1042.0	175.4	172.7	175.7
18	1039	10000.0	9966.0	3182.1	212.8	211.3	212.9
19	1039	661.7	630.0	341.6	166.3	162.6	167.9
20	1039	4252.9	3466.8	741.3	242.2	234.7	243.6

Table C-7: Actual Return Periods for Lateral Spread at Santa Monica, CA (475)

		Actual T_R					
		Robertson and Wride (2009)			Idriss and Boulanger (2014)		
Profile	Assumed T_R	Mean	Modal	Semi	Mean	Modal	Semi
1	475	349.1	354.6	277.2	107.4	108.1	108.8
2	475	302.1	374.7	294.3	178.5	187.9	193.9
3	475	546.2	945.1	356.7	174.2	176.1	177.0
4	475	583.8	607.5	464.8	166.6	167.6	168.2
5	475	1890.2	7123.7	1770.7	329.6	389.4	462.9
6	475	361.8	408.1	265.2	156.4	156.7	156.7
7	475	1106.3	1837.5	602.2	168.9	172.4	181.1
8	475	2722.4	5506.1	1104.6	285.5	307.3	322.5
9	475	1497.8	3545.9	1463.3	326.1	450.5	611.1
10	475	1834.3	5812.4	930.9	279.7	295.6	310.3
11	475	2531.5	4069.1	1275.7	276.8	298.0	314.9
12	475	1861.4	3613.9	961.5	184.5	188.0	192.5
13	475	357.7	381.7	309.5	140.4	140.9	141.5
14	475	4807.3	7586.7	1349.8	321.1	335.0	345.1
15	475	694.8	819.0	570.5	116.3	116.8	118.1
16	475	9992.0	10000.0	2926.0	215.1	215.1	215.1
17	475	3519.3	9902.0	1267.1	190.2	192.0	193.7
18	475	9052.7	9939.0	2669.2	217.7	223.9	243.1
19	475	661.8	793.9	415.5	179.6	184.5	188.4
20	475	2423.5	4115.2	928.3	281.4	295.8	308.9

Table C-8: Actual Return Periods for Lateral Spread at Santa Monica, CA (1039)

		Actual T_R					
		Robertson and Wride (2009)			Idriss and Boulanger (2014)		
Profile	Assumed T_R	Mean	Modal	Semi	Mean	Modal	Semi
1	1039	357.2	361.5	288.1	108.4	109.0	109.9
2	1039	435.6	625.1	308.6	191.4	195.4	199.1
3	1039	1254.9	1656.0	398.4	176.7	177.2	177.8
4	1039	621.6	645.2	486.2	168.1	168.5	168.7
5	1039	9983.0	9956.0	2270.0	429.0	491.1	556.1
6	1039	416.5	431.5	274.8	156.7	156.7	156.7
7	1039	1957.9	2051.8	696.7	177.4	182.6	185.8
8	1039	7577.0	9955.0	1305.2	314.7	328.1	339.3
9	1039	6528.5	9989.0	1802.2	528.2	678.0	862.7
10	1039	9141.3	9994.0	1142.9	303.7	313.1	318.5
11	1039	4975.5	7172.3	1496.6	307.0	323.2	337.0
12	1039	4469.8	5835.4	1164.1	190.3	193.4	195.5
13	1039	388.3	403.4	317.5	141.5	141.5	141.5
14	1039	8785.5	9937.0	1663.0	342.4	347.6	350.2
15	1039	970.6	1040.5	650.3	117.2	118.2	119.9
16	1039	9901.0	9942.0	5616.3	215.1	215.1	215.1
17	1039	9932.0	9972.0	1642.8	193.1	193.9	194.8
18	1039	9980.0	9955.0	4823.6	236.2	247.7	254.7
19	1039	845.0	946.8	450.4	186.8	190.4	192.3
20	1039	5101.6	7039.1	1092.7	303.3	312.3	319.8

Table C-9: Actual Return Periods for Lateral Spread at Santa Monica, CA (2475)

		Actual T_R					
		Robertson and Wride (2009)			Idriss and Boulanger (2014)		
Profile	Assumed T_R	Mean	Modal	Semi	Mean	Modal	Semi
1	2475	365.6	366.4	299.1	109.8	110.4	111.4
2	2475	922.4	1216.1	324.6	199.2	201.9	204.6
3	2475	1895.8	2078.6	441.7	177.9	178.4	178.8
4	2475	667.8	674.7	510.7	168.8	169.1	169.5
5	2475	9917.0	9912.0	3244.4	556.9	621.5	690.7
6	2475	437.3	438.3	283.6	156.7	156.7	156.7
7	2475	2179.9	2321.0	817.6	185.8	185.8	185.8
8	2475	9982.0	9922.0	1551.2	340.0	352.9	363.2
9	2475	9940.0	9943.0	2338.1	880.5	1254.3	1835.2
10	2475	9992.0	9965.0	1454.5	318.5	323.9	330.7
11	2475	9078.9	9904.0	1767.5	336.6	344.1	354.6
12	2475	7635.5	9762.4	1460.0	195.3	197.0	199.1
13	2475	414.2	415.6	323.9	141.5	141.5	141.5
14	2475	9927.0	9960.0	2178.8	350.4	351.9	352.1
15	2475	1058.4	1081.7	736.1	120.1	122.7	124.7
16	2475	9884.0	9955.0	9923.0	215.1	215.1	215.1
17	2475	9893.0	9934.0	2277.8	194.8	195.8	197.3
18	2475	9996.0	9906.0	9964.0	254.5	260.1	263.5
19	2475	1026.5	1075.1	484.0	192.6	194.2	196.0
20	2475	9399.4	9911.0	1342.9	319.8	324.2	327.6

Table C-10: Actual Return Periods for Lateral Spread at Salt Lake City, UT (475)

		Actual T_R					
		Robertson and Wride (2009)			Idriss and Boulanger (2014)		
Profile	Assumed T_R	Mean	Modal	Semi	Mean	Modal	Semi
1	475	1015.9	1038.6	781.9	466.9	467.0	467.3
2	475	776.5	794.8	861.2	543.7	549.3	590.8
3	475	910.8	958.0	896.3	568.0	570.9	582.7
4	475	1297.1	1347.4	1131.9	578.5	581.1	594.5
5	475	811.6	925.7	1833.0	733.5	765.8	947.7
6	475	822.1	850.3	788.9	537.7	542.4	562.6
7	475	1060.6	1091.2	1120.0	535.3	538.7	556.6
8	475	1356.6	1526.6	1751.6	712.6	735.3	871.0
9	475	624.8	681.9	1858.2	612.3	632.9	860.9
10	475	1186.4	1315.4	1514.8	701.3	716.3	843.6
11	475	1877.6	2112.6	1714.4	759.7	772.1	876.8
12	475	1360.8	1496.4	1469.5	608.5	610.5	627.1
13	475	896.8	918.7	881.0	518.0	519.7	528.2
14	475	2089.8	2545.0	1613.2	845.0	865.6	978.0
15	475	1055.7	1105.0	1129.3	476.5	477.5	483.4
16	475	855.0	906.7	1331.3	654.9	660.8	699.0
17	475	1205.7	1392.4	1572.5	623.5	628.2	648.7
18	475	993.1	1068.3	2147.1	674.4	680.0	742.2
19	475	1048.7	1118.4	946.8	566.7	571.8	607.2
20	475	1424.2	1612.7	1467.1	722.8	744.9	846.7

Table C-11: Actual Return Periods for Lateral Spread at Salt Lake City, UT (1039)

		Actual T_R					
		Robertson and Wride (2009)			Idriss and Boulanger (2014)		
Profile	Assumed T_R	Mean	Modal	Semi	Mean	Modal	Semi
1	1039	1084.9	1087.4	848.6	468.1	468.2	469.0
2	1039	1032.6	1060.9	946.7	635.6	641.4	665.3
3	1039	1548.1	1666.6	1009.7	586.8	587.7	589.9
4	1039	1584.7	1593.0	1265.1	598.8	599.5	603.0
5	1039	4236.8	5172.6	2896.8	1014.9	1035.6	1170.6
6	1039	1160.3	1183.7	834.3	564.4	564.5	564.9
7	1039	2683.5	2938.8	1390.2	560.2	561.1	569.3
8	1039	6169.6	6919.0	2288.4	934.2	944.8	994.8
9	1039	3708.2	4207.0	2780.7	1072.5	1122.0	1343.3
10	1039	4277.4	5025.8	2013.3	894.7	902.2	935.1
11	1039	5346.3	5748.0	2492.0	939.0	950.9	1001.7
12	1039	3835.7	4193.3	1921.1	637.6	639.4	651.4
13	1039	1108.1	1116.8	934.9	531.4	531.6	532.9
14	1039	8747.9	9415.5	2392.4	1020.7	1029.0	1066.7
15	1039	1707.2	1718.2	1381.8	483.7	483.9	485.0
16	1039	9905.0	9937.0	2798.2	701.2	701.2	701.2
17	1039	6375.3	7992.0	2205.6	654.9	655.8	661.3
18	1039	9891.0	9961.0	3602.3	771.8	777.4	806.7
19	1039	1796.6	1848.1	1109.4	628.9	632.7	649.3
20	1039	4924.8	5384.0	1921.0	891.0	898.3	930.4

Table C-12: Actual Return Periods for Lateral Spread at Salt Lake City, UT (2475)

		Actual T_R					
		Robertson and Wride (2009)			Idriss and Boulanger (2014)		
Profile	Assumed T_R	Mean	Modal	Semi	Mean	Modal	Semi
1	2475	1110.0	1111.5	901.8	470.7	471.0	472.8
2	2475	1772.3	1861.0	1025.3	686.1	686.3	699.7
3	2475	3367.6	3470.6	1139.0	592.1	592.5	595.0
4	2475	1700.1	1708.8	1351.0	605.2	605.6	606.9
5	2475	9970.0	9918.0	4223.6	1352.1	1374.9	1489.6
6	2475	1292.4	1298.3	876.9	565.0	565.0	565.0
7	2475	3741.7	3757.1	1660.6	584.7	586.0	589.3
8	2475	9981.0	9896.0	2902.8	1045.7	1052.4	1087.9
9	2475	9968.0	9979.0	3933.5	1641.5	1688.7	2101.0
10	2475	9918.0	9940.0	2590.6	969.8	973.7	990.0
11	2475	9972.0	9968.0	3138.5	1063.3	1072.1	1111.9
12	2475	8311.9	8549.2	2493.8	666.8	668.5	675.2
13	2475	1185.7	1191.8	972.8	533.7	533.7	533.7
14	2475	9900.0	9906.0	3366.6	1100.1	1102.0	1107.6
15	2475	2322.5	2326.3	1622.1	487.2	487.6	490.4
16	2475	9932.0	9919.0	6541.5	701.2	701.2	701.2
17	2475	9927.0	9893.0	3106.0	666.6	667.2	670.3
18	2475	9969.0	9942.0	6649.1	839.8	842.6	856.9
19	2475	2327.9	2355.3	1252.8	667.6	670.3	678.2
20	2475	9980.0	9885.0	2421.5	964.0	968.9	990.6

Table C-13: Actual Return Periods for Lateral Spread at San Jose, CA (475)

		Actual T_R					
		Robertson and Wride (2009)			Idriss and Boulanger (2014)		
Profile	Assumed T_R	Mean	Modal	Semi	Mean	Modal	Semi
1	475	200.1	199.8	167.3	86.3	86.3	86.6
2	475	211.3	203.5	183.2	99.6	99.3	110.9
3	475	459.8	411.4	213.4	94.8	94.7	95.2
4	475	317.7	315.6	257.0	94.1	94.0	94.4
5	475	3045.3	2361.9	1050.9	210.5	205.1	297.0
6	475	218.1	216.4	165.2	92.2	92.2	92.2
7	475	834.8	800.5	336.7	94.2	94.0	96.3
8	475	2491.8	2165.3	628.0	178.0	176.0	195.3
9	475	1635.7	1349.0	882.0	235.7	221.9	434.5
10	475	2476.3	1934.3	548.4	175.2	174.1	186.3
11	475	1850.2	1677.7	705.0	173.7	172.0	194.1
12	475	1585.6	1406.7	555.5	97.3	97.0	99.3
13	475	210.7	209.8	187.1	89.2	89.2	89.3
14	475	3325.0	3096.7	792.7	191.7	190.3	198.6
15	475	403.4	374.5	325.8	87.7	87.7	88.1
16	475	9899.0	9884.0	2258.7	122.8	122.8	122.8
17	475	7174.7	5024.0	747.0	98.2	98.1	99.0
18	475	9991.0	8897.0	2015.8	142.6	140.9	157.5
19	475	404.8	391.0	232.9	98.8	98.6	102.4
20	475	1847.8	1686.1	533.2	174.3	172.9	186.4

Table C-14: Actual Return Periods for Lateral Spread at San Jose, CA (1039)

		Actual T_R					
		Robertson and Wride (2009)			Idriss and Boulanger (2014)		
Profile	Assumed T_R	Mean	Modal	Semi	Mean	Modal	Semi
1	1039	202.3	201.8	171.2	86.5	86.4	86.8
2	1039	331.6	295.1	189.3	106.4	105.0	115.9
3	1039	785.1	718.5	220.1	95.1	95.0	95.4
4	1039	331.7	328.4	265.9	94.3	94.2	94.5
5	1039	9945.0	9999.0	1276.8	257.3	242.3	336.5
6	1039	227.4	223.6	168.2	92.2	92.2	92.2
7	1039	927.5	917.1	376.4	95.9	95.6	96.4
8	1039	4712.1	4207.0	697.0	188.3	185.8	202.5
9	1039	9896.0	7124.1	1036.1	334.7	310.4	660.8
10	1039	6346.5	5425.8	633.6	183.1	181.7	190.1
11	1039	3177.0	2784.7	785.8	186.5	183.0	199.4
12	1039	2489.9	2282.0	635.1	98.6	98.3	99.8
13	1039	216.2	214.5	189.4	89.3	89.3	89.3
14	1039	4806.2	4458.1	918.7	197.5	196.8	199.2
15	1039	502.4	500.3	346.0	87.9	87.8	88.7
16	1039	9928.0	9956.0	3399.9	122.8	122.8	122.8
17	1039	9931.0	9978.0	897.7	98.7	98.6	99.4
18	1039	9971.0	9979.0	3118.2	153.5	151.8	160.2
19	1039	472.9	456.1	247.2	99.9	99.6	105.1
20	1039	3067.3	2783.8	592.9	182.0	180.3	188.9

Table C-15: Actual Return Periods for Lateral Spread at San Jose, CA (2475)

		Actual T_R					
		Robertson and Wride (2009)			Idriss and Boulanger (2014)		
Profile	Assumed T_R	Mean	Modal	Semi	Mean	Modal	Semi
1	2475	203.8	203.5	175.4	86.7	86.6	87.0
2	2475	534.6	448.6	194.9	112.2	110.6	124.2
3	2475	932.1	880.3	239.7	95.3	95.2	95.6
4	2475	341.9	339.8	273.6	94.4	94.3	94.7
5	2475	9921.0	9942.0	1623.0	304.0	287.4	410.3
6	2475	232.4	232.1	171.3	92.2	92.2	92.2
7	2475	1004.6	969.4	421.1	96.4	96.4	96.4
8	2475	6448.8	5893.5	793.7	197.3	194.3	207.1
9	2475	9885.0	9917.0	1237.6	504.8	421.7	997.2
10	2475	9996.0	9897.0	746.7	187.6	185.6	195.7
11	2475	4323.3	3911.1	892.7	195.9	193.0	205.7
12	2475	3587.8	3144.1	761.7	99.3	99.1	105.9
13	2475	219.4	219.0	191.6	89.3	89.3	89.3
14	2475	6057.7	5576.1	1102.8	198.9	198.5	199.2
15	2475	516.3	510.1	383.6	88.3	88.1	88.9
16	2475	9993.0	9994.0	6479.9	122.8	122.8	122.8
17	2475	9948.0	9921.0	1149.3	99.1	98.9	100.1
18	2475	9916.0	9918.0	5201.4	158.1	156.6	162.8
19	2475	526.2	510.1	261.9	103.2	102.0	108.5
20	2475	4532.5	3936.9	692.0	187.1	185.6	192.1

Table C-16: Actual Return Periods for Lateral Spread at San Francisco, CA (475)

		Actual T_R					
		Robertson and Wride (2009)			Idriss and Boulanger (2014)		
Profile	Assumed T_R	Mean	Modal	Semi	Mean	Modal	Semi
1	475	299.3	302.0	233.0	98.3	98.5	98.7
2	475	317.0	404.0	257.4	175.3	180.1	184.2
3	475	687.0	998.8	314.2	161.8	162.8	163.6
4	475	471.8	489.5	381.2	153.5	154.1	154.6
5	475	4192.2	9908.0	1394.8	315.8	361.9	420.9
6	475	333.3	341.7	222.1	140.9	140.9	140.9
7	475	1217.6	1319.8	490.3	156.1	161.7	169.4
8	475	3609.0	5562.6	890.8	259.7	273.7	287.6
9	475	2365.3	6685.6	1192.9	346.3	457.3	582.2
10	475	3514.1	6796.7	767.7	251.7	263.1	272.3
11	475	2678.4	3665.7	991.0	257.7	272.5	289.6
12	475	2257.2	3044.4	779.9	177.6	181.5	184.7
13	475	316.4	322.6	262.7	127.2	127.8	127.9
14	475	4692.8	5905.1	1070.7	285.5	294.5	299.0
15	475	596.0	743.5	465.6	99.3	99.4	99.6
16	475	9926.0	9907.0	2432.5	204.3	204.3	204.3
17	475	9515.2	9980.0	993.7	177.9	179.3	180.6
18	475	9910.0	9879.0	2276.3	210.0	215.3	219.6
19	475	604.1	671.3	344.6	166.1	169.8	173.6
20	475	2643.4	3630.6	742.1	248.3	260.6	269.8

Table C-17: Actual Return Periods for Lateral Spread at San Francisco, CA (1039)

		Actual T_R					
		Robertson and Wride (2009)			Idriss and Boulanger (2014)		
Profile	Assumed T_R	Mean	Modal	Semi	Mean	Modal	Semi
1	1039	303.2	305.1	242.4	98.5	98.7	98.8
2	1039	469.5	613.8	270.4	182.7	186.2	189.5
3	1039	1129.5	1251.4	332.7	162.9	163.7	164.4
4	1039	498.8	513.1	396.4	154.3	154.7	155.1
5	1039	9890.0	9913.0	1704.5	384.1	432.5	492.6
6	1039	345.9	353.4	228.4	140.9	140.9	140.9
7	1039	1337.5	1388.0	549.2	166.2	169.9	170.9
8	1039	6605.6	7948.0	1009.7	278.9	291.4	303.3
9	1039	9992.0	9993.0	1460.5	489.0	624.7	950.5
10	1039	8573.1	9943.0	907.9	268.2	273.3	281.1
11	1039	4378.2	5293.2	1131.1	280.3	293.3	303.6
12	1039	3398.3	4082.4	895.1	183.1	185.4	187.6
13	1039	327.4	333.7	269.1	127.9	127.9	127.9
14	1039	6643.9	7440.9	1283.9	297.2	299.3	300.8
15	1039	747.4	755.3	522.1	99.5	99.7	102.6
16	1039	9883.0	9880.0	3982.6	204.3	204.3	204.3
17	1039	9957.0	9941.0	1229.3	179.9	180.7	182.3
18	1039	9893.0	9982.0	3783.7	217.6	219.7	222.4
19	1039	706.4	752.2	369.5	171.6	173.9	176.1
20	1039	4219.0	5095.9	848.4	264.3	272.0	277.6

Table C-18: Actual Return Periods for Lateral Spread at San Francisco, CA (2475)

		Actual T_R					
		Robertson and Wride (2009)			Idriss and Boulanger (2014)		
Profile	Assumed T_R	Mean	Modal	Semi	Mean	Modal	Semi
1	2475	306.4	306.9	251.5	98.8	99.0	99.1
2	2475	855.0	1067.4	283.5	188.1	191.8	195.5
3	2475	1393.5	1502.9	359.3	164.2	164.8	165.2
4	2475	523.5	528.1	409.4	155.0	155.4	155.9
5	2475	9991.0	9895.0	2263.4	472.1	539.5	607.4
6	2475	354.7	355.5	236.2	140.9	140.9	140.9
7	2475	1475.2	1569.5	616.6	170.9	170.9	170.9
8	2475	9430.5	9885.0	1161.5	300.6	309.6	315.1
9	2475	9884.0	9914.0	1763.3	820.8	1215.0	1406.9
10	2475	9976.0	9994.0	1086.7	279.4	286.5	292.9
11	2475	6371.5	7235.7	1304.4	301.4	309.7	317.1
12	2475	5289.9	6596.5	1074.8	186.9	189.3	191.8
13	2475	335.7	335.7	274.9	127.9	127.9	127.9
14	2475	8721.0	9200.4	1587.4	300.5	300.9	300.9
15	2475	772.1	795.1	573.2	100.9	103.9	104.2
16	2475	9984.0	9936.0	8143.6	204.3	204.3	204.3
17	2475	9995.0	9932.0	1601.2	181.8	183.3	185.0
18	2475	9981.0	9939.0	6909.5	221.6	223.2	226.5
19	2475	796.7	826.9	392.4	175.5	177.8	179.5
20	2475	6636.6	7997.1	1006.8	276.7	281.4	285.5

Table C-19: Actual Return Periods for Lateral Spread at Seattle, WA (475)

		Actual T_R					
		Robertson and Wride (2009)			Idriss and Boulanger (2014)		
Profile	Assumed T_R	Mean	Modal	Semi	Mean	Modal	Semi
1	475	600.4	602.0	445.2	203.3	203.4	203.8
2	475	438.0	454.1	456.7	273.2	277.6	309.2
3	475	734.6	786.1	552.4	271.2	272.4	277.6
4	475	932.1	956.6	746.6	269.2	270.1	273.0
5	475	1355.1	1723.1	2100.5	525.0	538.6	645.3
6	475	544.0	567.5	431.4	245.2	245.9	247.8
7	475	1089.5	1226.8	878.3	240.6	241.5	249.5
8	475	2351.3	2937.1	1514.0	450.4	462.1	522.6
9	475	954.8	1319.2	1871.4	426.5	455.8	698.9
10	475	1742.3	2071.6	1248.6	446.0	453.9	501.6
11	475	2902.0	3359.1	1737.4	446.9	455.3	510.3
12	475	1793.5	2107.2	1265.5	292.3	294.0	301.6
13	475	575.9	587.9	496.8	218.5	218.8	219.7
14	475	4939.2	5973.6	1670.5	533.4	540.7	579.2
15	475	1143.7	1185.4	851.3	206.3	206.3	206.6
16	475	1060.4	1609.9	2076.0	356.2	358.6	361.3
17	475	2685.5	3583.6	1533.4	304.8	305.3	310.3
18	475	2595.8	4258.1	2755.0	355.5	362.0	398.8
19	475	938.5	1002.1	628.1	285.3	288.4	303.6
20	475	2662.6	3106.9	1256.4	455.4	461.4	505.4

Table C-20: Actual Return Periods for Lateral Spread at Seattle, WA (1039)

		Actual T_R					
		Robertson and Wride (2009)			Idriss and Boulanger (2014)		
Profile	Assumed T_R	Mean	Modal	Semi	Mean	Modal	Semi
1	1039	611.4	612.9	465.7	203.8	203.8	204.3
2	1039	570.4	587.1	486.7	307.4	310.4	325.8
3	1039	1213.9	1308.5	606.3	277.1	277.6	280.4
4	1039	1027.1	1033.6	796.1	272.8	273.0	274.7
5	1039	6754.6	8050.1	2953.9	616.2	630.7	802.4
6	1039	674.3	682.5	448.0	247.6	247.7	248.0
7	1039	2715.7	2891.4	1021.2	248.9	250.0	268.9
8	1039	6916.4	7546.9	1839.7	515.7	522.1	562.4
9	1039	4054.9	4535.3	2443.4	682.8	712.6	1050.7
10	1039	5652.5	6622.3	1547.6	499.1	503.5	538.9
11	1039	5635.4	5972.1	2174.2	507.2	511.8	549.1
12	1039	4610.7	5075.2	1564.1	301.0	302.0	311.7
13	1039	642.9	647.2	522.8	219.7	219.7	220.2
14	1039	9992.0	9971.0	2193.1	574.4	578.3	610.0
15	1039	1228.6	1247.2	980.4	206.5	206.5	207.0
16	1039	9954.0	9989.0	4417.5	361.3	361.3	361.3
17	1039	9944.0	9970.0	2078.7	310.1	310.5	314.2
18	1039	9886.0	9881.0	4159.7	394.5	397.9	429.5
19	1039	1260.2	1290.2	703.0	301.7	303.1	313.6
20	1039	5690.6	6113.1	1539.5	498.9	502.8	536.0

Table C-21: Actual Return Periods for Lateral Spread at Seattle, WA (2475)

		Actual T_R					
		Robertson and Wride (2009)			Idriss and Boulanger (2014)		
Profile	Assumed T_R	Mean	Modal	Semi	Mean	Modal	Semi
1	2475	622.6	623.1	490.6	204.3	204.3	205.1
2	2475	878.0	903.5	526.0	326.7	327.1	337.9
3	2475	2543.6	2596.6	683.5	280.4	280.5	282.7
4	2475	1086.3	1089.2	837.7	274.8	274.8	276.1
5	2475	9892.0	9907.0	4078.7	796.4	804.3	1015.9
6	2475	725.0	727.4	462.9	248.0	248.0	248.0
7	2475	3512.8	3522.3	1204.9	271.0	271.8	283.8
8	2475	9929.0	9894.0	2284.9	563.2	564.8	608.8
9	2475	9923.0	9925.0	3231.2	1044.8	1063.1	1679.7
10	2475	9913.0	9952.0	2008.9	538.1	539.4	561.7
11	2475	9911.0	9901.0	2614.6	553.3	555.7	600.2
12	2475	9081.6	9303.9	2049.1	311.4	311.8	318.5
13	2475	676.0	677.9	542.2	220.2	220.2	220.2
14	2475	9950.0	9983.0	2960.2	610.3	611.1	620.7
15	2475	1788.9	1790.4	1130.0	207.0	207.1	208.2
16	2475	9935.0	9946.0	9958.0	361.3	361.3	361.3
17	2475	9971.0	9941.0	2936.4	314.2	314.3	317.1
18	2475	9975.0	9907.0	9303.8	430.3	431.4	448.0
19	2475	1546.3	1560.1	779.6	314.1	314.6	323.4
20	2475	9975.0	9999.0	1924.4	534.8	536.1	562.0

Table C-22: Actual Return Periods for Lateral Spread at Charleston, SC (475)

		Actual T_R					
		Robertson and Wride (2009)			Idriss and Boulanger (2014)		
Profile	Assumed T_R	Mean	Modal	Semi	Mean	Modal	Semi
1	475	1377.6	1589.6	1011.1	669.9	671.2	671.1
2	475	1114.1	1285.8	1185.9	728.7	783.6	778.4
3	475	1169.0	1523.2	1145.7	780.5	805.5	800.2
4	475	1545.7	2022.3	1301.8	800.3	820.4	817.9
5	475	944.3	1572.2	1526.2	894.0	1105.7	1056.8
6	475	1164.1	1370.8	1096.1	730.0	769.7	761.4
7	475	1245.8	1694.8	1199.5	728.7	763.5	758.4
8	475	1327.4	2453.9	1564.7	913.9	1057.9	1027.4
9	475	778.9	1133.0	1652.5	735.1	920.8	915.4
10	475	1290.3	2141.4	1441.7	912.7	1029.0	1007.6
11	475	1687.3	3190.7	1388.5	1007.1	1094.6	1075.9
12	475	1365.3	2281.5	1419.6	840.4	855.1	854.5
13	475	1278.0	1439.7	1173.8	719.5	732.4	728.2
14	475	1549.5	4102.5	1276.9	1069.6	1227.8	1200.0
15	475	1095.2	1731.0	1112.9	676.0	681.2	679.9
16	475	1118.5	1401.5	1467.7	886.9	922.6	918.3
17	475	1115.6	2212.4	1311.9	852.4	885.9	880.4
18	475	907.9	1615.6	1299.8	924.3	957.0	950.5
19	475	1222.9	1745.8	1082.2	763.3	808.7	802.6
20	475	1428.2	2619.8	1356.2	929.0	1057.7	1037.5

Table C-23: Actual Return Periods for Lateral Spread at Charleston, SC (1039)

		Actual T_R					
		Robertson and Wride (2009)			Idriss and Boulanger (2014)		
Profile	Assumed T_R	Mean	Modal	Semi	Mean	Modal	Semi
1	1039	1635.2	1651.3	1240.7	672.4	674.0	673.4
2	1039	1549.7	1803.8	1411.5	882.8	920.0	890.4
3	1039	2046.2	2842.5	1413.0	822.9	828.3	824.3
4	1039	2270.3	2339.3	1756.5	838.8	843.4	840.3
5	1039	4254.4	9916.0	2962.5	1361.3	1521.0	1402.0
6	1039	1698.1	1847.3	1256.1	795.5	796.2	795.2
7	1039	3017.2	4483.8	1769.1	786.7	794.6	788.9
8	1039	6803.2	9912.0	2695.9	1275.2	1351.4	1290.2
9	1039	4055.4	7757.5	3084.5	1396.5	1710.5	1435.4
10	1039	4645.1	9779.9	2372.0	1225.4	1277.8	1230.9
11	1039	6283.9	8951.4	2826.0	1281.8	1358.7	1301.2
12	1039	4355.8	6872.0	2274.1	884.6	899.1	888.7
13	1039	1639.8	1707.3	1382.4	746.6	748.1	746.9
14	1039	9732.1	9987.0	2549.2	1398.7	1453.9	1409.3
15	1039	2358.2	2580.7	1761.3	686.3	687.1	686.6
16	1039	9909.0	9879.0	2260.1	968.4	968.4	968.4
17	1039	5978.3	9963.0	2478.4	912.4	919.7	914.3
18	1039	9954.0	9891.0	3364.9	1062.1	1097.3	1065.7
19	1039	2448.6	2814.7	1485.5	871.9	897.0	876.0
20	1039	5678.2	8393.1	2285.3	1218.9	1267.7	1223.3

Table C-24: Actual Return Periods for Lateral Spread at Charleston, SC (2475)

		Actual T_R					
		Robertson and Wride (2009)			Idriss and Boulanger (2014)		
Profile	Assumed T_R	Mean	Modal	Semi	Mean	Modal	Semi
1	2475	1684.5	1690.8	1345.2	677.9	680.2	677.0
2	2475	3201.1	4213.9	1562.1	974.6	993.3	958.9
3	2475	4913.5	5423.9	1622.5	833.9	836.6	833.0
4	2475	2510.0	2548.7	1934.7	849.7	852.2	849.0
5	2475	9878.0	9883.0	4722.6	1983.6	2233.3	1893.1
6	2475	1971.0	1975.8	1330.8	796.4	796.4	796.4
7	2475	5002.1	5241.2	2173.3	831.1	831.1	825.7
8	2475	9918.0	9989.0	3612.5	1493.1	1559.2	1461.0
9	2475	9946.0	9931.0	4641.9	2567.5	3582.3	2340.2
10	2475	9983.0	9892.0	3267.7	1364.1	1394.7	1353.8
11	2475	9897.0	9911.0	3872.6	1528.2	1582.8	1491.5
12	2475	9953.0	9897.0	3052.1	935.7	946.0	931.2
13	2475	1812.4	1820.9	1467.1	750.4	750.4	750.4
14	2475	9884.0	9916.0	3926.8	1531.0	1537.4	1524.1
15	2475	3227.6	3288.8	2166.3	692.5	698.5	690.8
16	2475	9885.0	9964.0	5813.6	968.4	968.4	968.4
17	2475	9957.0	9942.0	3591.0	933.3	939.4	931.2
18	2475	9889.0	9937.0	6061.4	1189.1	1210.6	1177.3
19	2475	3460.1	3644.3	1757.7	940.3	953.3	932.6
20	2475	9992.0	9883.0	3036.4	1363.9	1392.5	1342.5

Table C-25: Actual Return Periods for Lateral Spread at Portland, OR (475)

		Actual T_R					
		Robertson and Wride (2009)			Idriss and Boulanger (2014)		
Profile	Assumed T_R	Mean	Modal	Semi	Mean	Modal	Semi
1	475	1207.4	1326.0	842.3	504.4	509.8	505.4
2	475	872.9	1307.5	914.9	577.2	755.6	643.7
3	475	1066.8	2494.0	961.8	626.4	677.7	654.8
4	475	1601.0	2094.6	1208.9	637.9	678.1	659.9
5	475	942.1	9900.0	1773.4	795.4	1530.4	1056.7
6	475	942.4	1464.2	857.0	561.9	621.1	599.9
7	475	1313.3	5076.2	1156.3	565.5	619.9	593.7
8	475	1692.8	9898.0	1826.0	784.7	1228.8	956.1
9	475	723.5	8146.4	1918.7	646.6	1908.2	849.4
10	475	1487.8	9876.0	1569.5	780.2	1142.0	921.7
11	475	2571.0	9879.0	1659.0	883.9	1226.1	987.8
12	475	1730.3	8400.0	1513.7	691.6	748.7	705.1
13	475	1048.9	1377.1	957.9	559.5	577.2	569.9
14	475	2828.7	9970.0	1512.8	947.3	1298.2	1124.5
15	475	1292.7	2400.9	1164.1	511.6	523.7	517.5
16	475	1042.5	9904.0	1513.1	751.2	859.6	811.1
17	475	1470.8	9926.0	1579.7	693.1	741.3	719.7
18	475	1256.8	9907.0	1784.8	777.6	942.8	818.4
19	475	1264.2	2561.1	964.5	601.7	737.8	663.9
20	475	1813.3	9926.0	1487.2	792.6	1146.1	955.8

Table C-26: Actual Return Periods for Lateral Spread at Portland, OR (1039)

		Actual T_R					
		Robertson and Wride (2009)			Idriss and Boulanger (2014)		
Profile	Assumed T_R	Mean	Modal	Semi	Mean	Modal	Semi
1	1039	1309.6	1351.8	956.5	506.0	514.3	507.7
2	1039	1080.6	2290.8	1027.2	685.4	852.3	732.6
3	1039	1672.4	5313.1	1139.2	664.8	684.4	671.6
4	1039	1982.2	2243.8	1499.8	671.6	684.1	675.8
5	1039	3643.9	9901.0	3353.9	1193.5	2259.3	1304.9
6	1039	1274.1	1584.7	944.0	618.7	622.4	621.5
7	1039	2559.4	6204.9	1584.9	610.1	662.2	616.5
8	1039	6168.0	9953.0	2716.2	1072.9	1410.9	1156.1
9	1039	3016.0	9973.0	3298.5	1060.4	3943.9	1360.6
10	1039	4257.4	9891.0	2293.0	1050.8	1275.6	1119.7
11	1039	6516.7	9947.0	3012.3	1080.1	1422.3	1164.5
12	1039	4198.3	9912.0	2253.7	716.1	796.2	731.5
13	1039	1290.3	1464.1	1067.3	575.1	580.5	577.9
14	1039	9915.0	9929.0	2786.9	1216.9	1386.8	1271.2
15	1039	2316.9	3372.6	1599.3	521.7	530.2	522.3
16	1039	4379.4	9946.0	2546.6	856.0	862.2	862.2
17	1039	7091.8	9920.0	2555.0	729.7	763.5	738.3
18	1039	9906.0	9980.0	4118.4	879.4	1058.3	922.2
19	1039	2105.3	3218.1	1259.4	696.4	790.7	717.4
20	1039	6055.1	9915.0	2276.0	1056.8	1272.7	1114.7

Table C-27: Actual Return Periods for Lateral Spread at Portland, OR (2475)

		Actual T_R					
		Robertson and Wride (2009)			Idriss and Boulanger (2014)		
Profile	Assumed T_R	Mean	Modal	Semi	Mean	Modal	Semi
1	2475	1333.2	1366.4	1034.9	508.6	518.1	510.6
2	2475	1527.1	4076.1	1122.6	778.3	905.4	812.6
3	2475	3476.6	6468.6	1294.8	676.1	687.1	678.8
4	2475	2140.8	2338.7	1650.5	679.5	687.7	681.8
5	2475	9961.0	9886.0	5361.5	1503.6	3043.6	1772.6
6	2475	1510.4	1610.6	999.7	622.5	622.6	622.4
7	2475	5798.1	6951.2	2010.7	629.6	671.3	655.4
8	2475	9876.0	9893.0	3573.5	1228.2	1488.5	1297.1
9	2475	9930.0	9933.0	4715.7	1732.8	6651.5	2258.3
10	2475	9962.0	9931.0	3079.3	1176.6	1348.6	1229.7
11	2475	9969.0	9904.0	4066.9	1233.1	1509.7	1317.9
12	2475	9929.0	9923.0	3047.8	749.0	821.1	771.4
13	2475	1403.5	1506.2	1138.5	579.3	580.5	580.5
14	2475	9954.0	9961.0	4180.7	1330.1	1392.9	1373.7
15	2475	2862.3	3500.2	1941.6	523.2	538.1	525.2
16	2475	9980.0	9979.0	7512.4	862.2	862.2	862.2
17	2475	9907.0	9895.0	3824.7	747.5	778.6	755.6
18	2475	9984.0	9902.0	7338.4	966.3	1091.4	1028.0
19	2475	2791.9	3610.2	1468.2	741.9	809.9	766.6
20	2475	9966.0	10000.0	2983.8	1166.4	1310.1	1218.0

Table C-28: Actual Return Periods for Lateral Spread at Memphis, TN (475)

		Actual T_R					
		Robertson and Wride (2009)			Idriss and Boulanger (2014)		
Profile	Assumed T_R	Mean	Modal	Semi	Mean	Modal	Semi
1	475	1384.3	1552.8	970.9	664.3	666.0	665.7
2	475	1080.9	1228.5	1130.5	724.0	791.5	775.2
3	475	1173.6	1531.0	1105.4	789.7	816.1	806.8
4	475	1644.4	2043.6	1292.9	809.7	830.1	824.7
5	475	945.6	1724.7	1599.6	931.0	1163.0	1088.1
6	475	1132.5	1336.2	1045.4	727.3	771.1	756.7
7	475	1326.1	1765.9	1184.8	729.2	767.0	754.4
8	475	1494.0	2759.4	1652.5	939.6	1102.2	1044.6
9	475	775.4	1211.5	1762.8	755.4	980.6	914.3
10	475	1418.2	2370.4	1485.5	935.6	1059.7	1017.0
11	475	2056.8	3737.3	1469.0	1047.7	1148.7	1116.8
12	475	1543.0	2514.3	1451.7	860.2	876.0	872.4
13	475	1246.8	1404.7	1128.4	719.4	733.3	728.6
14	475	1979.0	5137.8	1340.9	1112.0	1292.4	1241.4
15	475	1182.9	1873.7	1118.4	670.4	675.5	673.5
16	475	1129.3	1492.5	1531.0	910.9	941.7	932.4
17	475	1239.5	2499.5	1371.0	872.1	904.5	892.8
18	475	1035.5	1842.2	1398.8	950.1	987.3	975.8
19	475	1286.9	1799.4	1053.0	768.6	821.5	803.4
20	475	1589.1	3013.2	1392.9	951.0	1093.8	1047.3

Table C-29: Actual Return Periods for Lateral Spread at Memphis, TN (1039)

		Actual T_R					
		Robertson and Wride (2009)			Idriss and Boulanger (2014)		
Profile	Assumed T_R	Mean	Modal	Semi	Mean	Modal	Semi
1	1039	1585.0	1606.3	1174.1	666.6	668.8	667.6
2	1039	1425.4	1723.6	1318.4	873.9	937.8	878.5
3	1039	1940.4	2940.8	1346.2	833.0	841.9	833.7
4	1039	2253.5	2365.2	1707.7	854.4	860.3	854.9
5	1039	3908.5	9927.0	3079.0	1428.6	1645.0	1450.9
6	1039	1589.2	1796.6	1184.2	801.0	802.8	801.0
7	1039	2827.0	5081.0	1713.8	790.6	799.4	792.2
8	1039	6600.8	9980.0	2741.3	1319.0	1432.6	1329.9
9	1039	3486.4	8999.8	3197.5	1371.6	1873.4	1399.6
10	1039	4506.6	9917.0	2393.7	1273.2	1351.5	1276.0
11	1039	6543.6	9916.0	2930.2	1319.4	1434.1	1340.6
12	1039	4345.3	8379.5	2310.3	901.1	920.3	902.4
13	1039	1570.0	1663.9	1314.9	748.1	750.2	747.8
14	1039	9892.0	9972.0	2656.4	1465.4	1544.5	1471.8
15	1039	2472.8	2711.2	1729.1	681.1	682.1	681.3
16	1039	6237.1	9891.0	2238.2	1016.0	1016.0	1015.4
17	1039	6539.2	9947.0	2513.8	928.1	938.9	930.8
18	1039	9918.0	9981.0	3559.9	1084.1	1143.6	1090.3
19	1039	2395.8	2892.4	1436.1	889.8	922.0	891.7
20	1039	5959.0	10000.0	2322.2	1273.4	1344.9	1277.0

Table C-30: Actual Return Periods for Lateral Spread at Memphis, TN (2475)

		Actual T_R					
		Robertson and Wride (2009)			Idriss and Boulanger (2014)		
Profile	Assumed T_R	Mean	Modal	Semi	Mean	Modal	Semi
1	2475	1620.3	1637.9	1275.8	670.0	672.6	670.9
2	2475	2162.5	3061.1	1456.3	968.0	1007.3	977.7
3	2475	4294.9	5413.8	1539.2	847.0	851.8	847.8
4	2475	2432.7	2533.2	1895.8	864.1	866.7	864.8
5	2475	9966.0	9971.0	5023.0	1864.2	2193.7	1944.4
6	2475	1858.3	1922.9	1257.7	803.2	803.2	803.2
7	2475	5538.3	5742.8	2153.6	819.8	836.4	824.7
8	2475	9983.0	9980.0	3658.4	1495.6	1591.1	1519.3
9	2475	9963.0	9941.0	4776.9	2240.5	2984.1	2397.8
10	2475	9936.0	9896.0	3216.4	1408.0	1449.8	1420.8
11	2475	9924.0	9898.0	4052.6	1506.6	1616.5	1531.7
12	2475	9887.0	9952.0	3086.9	937.1	957.4	942.7
13	2475	1697.5	1766.8	1399.6	753.2	753.0	753.2
14	2475	9906.0	9966.0	4042.9	1606.5	1633.3	1613.8
15	2475	3401.3	3458.4	2127.5	683.4	686.6	684.2
16	2475	9905.0	9906.0	6078.7	1016.0	1016.0	1016.0
17	2475	9910.0	9890.0	3675.7	947.4	953.2	948.9
18	2475	9951.0	9944.0	6404.1	1199.5	1245.7	1214.3
19	2475	3193.5	3560.2	1690.4	943.3	968.9	949.6
20	2475	9954.0	9913.0	3060.5	1397.4	1451.7	1407.2